

School of Electrical Engineering, Computing and  
Mathematical Sciences

**Towards More Realistic Reionisation Studies and  
Experiments**

Ainunabilah Nasirudin  
0000-0003-2213-4547

This thesis is presented for the Degree of  
Doctor of Philosophy  
of  
Curtin University of Technology

August 2020



## Author's Declaration

To the best of my knowledge and belief this thesis contains no material previously published by any other person except where due acknowledgement has been made. This thesis contains no material which has been accepted for the award of any other degree or diploma in any university.

Ainunabilah Nasirudin

11 August 2020



# Statement of Contributions

The contents of Chapter 3 are my own work based on the paper titled “Modelling the stochasticity of high-redshift halo bias”, which was published in the *Monthly Notices of the Royal Astronomical Society*, Volume 494, Issue 3, pp.3294-3309. DOI: 10.1093/mnras/staa853. I developed and ran the pipeline to model the stochasticity of low-mass dark matter haloes that are temporally-biased, compared them to the numerical results, made the codes that generated Figures 3.2 - 3.17, and wrote the draft manuscripts for publication. The input data used in this work is obtained from the suite of  $N$ -body simulation, which was provided by I. T. Iliev. K. Ahn had minor contributions to the introduction and discussion. All co-authors provided comments which I incorporated into the manuscript.

The contents of Chapter 4 are also my work based on the paper titled “The Impact of Realistic Foreground and Instrument Models on 21 cm Epoch of Reionisation Experiments”, which was published in the *Astrophysical Journal*, Volume 893, Issue 2, id.118, DOI:10.3847/1538-4357/ab8003. The pipeline used to coherently include foregrounds and instrumental effects was developed by myself. I ran the pipeline and MCMC, produced all the plots in the chapter and wrote the resulting paper, which incorporated minor comments from all co-authors. S. G. Murray and B. Greig made major adjustments in the existing version of 21CMMC to accommodate for the inclusion of my pipeline. C. M. Trott and C. Power provided necessary computing time on supercomputers for this work and R. C. Joseph made useful suggestions that aided in the interpretation of the results. S. G. Murray derived the variance of the cross-power in Appendix B.



# Acknowledgements

First and foremost, I would like to thank my PhD supervisors, Cath and Steven, for their guidance throughout my PhD journey. Thank you so much for this opportunity, for patiently explaining concepts in signal processing and 21 cm experiments, for their willingness to go bug hunting through my codes with me, and for meticulousness when going through my writings, among other things.

I would also like to thank my MSc supervisor, Ilian, who first introduced me to the Epoch of Reionisation. Thank you for having faith in me and accepting me as an MSc student, even though I did not have a physics background.

Thank you to all the friends I have made in Perth. Ronniy, for all the extremely helpful discussions, input, and Q&A sessions about power spectrum and 21 cm experiments; Mike, for the useful distractions from work and sharing of Indo/Malay cuisine; the EoR group, for the friendly banter and discussions; the badminton group, for the much-needed stress relief; and the boardgame gang (in alphabetical order): Garima, Josh, Lilian and Lucie, for their friendship and time for the past few years.

Of course, thank you to my family for their love and encouragement. Apak and Mama, for supporting me when I wanted to pursue astrophysics after my Math degree. My siblings, whose prayers helped me through rough times. And Opah, who is dearly missed.

And last but not least, thank you to my amazing husband, Rhys, for being there for me through thick and thin. My PhD journey would have been a lot more difficult and stressful if it weren't for his undying patience and support.



# Abstract

The detection of signal from the Epoch of Reionisation (EoR) is the next frontier of observational cosmology and will revolutionise galaxy formation studies. However, because of the extreme challenges that have to be overcome to detect the 21 cm signal, understanding the process of reionisation of the universe via simulation is of utmost importance to help narrow down the search. Large-scale simulations that model the formation and evolution of galaxies and their effects on the IGM have been extensively used to study this elusive epoch. It is, therefore, imperative that the results from both semi-numerical models and complete, hydrodynamical simulations match well and that their components are as realistic as possible in order to probe different aspects of the EoR. The ultimate goal of this PhD thesis, thus, is to explore and enhance different areas of reionisation studies to help supplement future 21 cm observations.

One main limitation of large-scale simulations is that they suffer from limited resolution due to the vast volume used, hence the role of small, low mass galaxies in the early stages of reionisation has often been neglected. To alleviate this problem, I modelled low-mass haloes from cosmological simulations using the instantaneous binned distribution of the number or mass of haloes that is approximated by a log-normal distribution. In addition to the deterministic halo bias that captures the average property, I modelled its stochasticity and its correlation in time. I tested the robustness of our new scheme against various statistical measures, and showed that temporally-correlated stochasticity generates mock halo data that matches the real N-body data better than that from temporally-uncorrelated stochasticity.

In addition to the resolution limitation, the effects of realistic foregrounds have not been well studied in works aiming to constrain the astrophysical parameters that influence cosmic reionisation. To move towards more realistic scenarios, I

explored the effects of applying more realistic foreground and instrument models to the 21cm signal, and gauged the ability to estimate astrophysical parameters with these additional complexities. A highly-optimized version of 21CMFAST that is integrated into 21CMMC was used to generate lightcones of the brightness temperature fluctuation for Bayesian parameter estimation. Next, a statistical point-source foreground model and an instrument model were included. I found that the inclusion of realistic foregrounds and instrumental components biases the parameter constraints due to unaccounted cross-power between the EoR signal, foregrounds and thermal noise.

Finally, current EoR research has not considered the possibility that there is a correlation between the EoR signal and the foreground sources, even though the foregrounds are the evolutionary descendants of the sources that reionised the universe. To explore this possible correlation, I used the GENESIS N-body simulation coupled with the semi-analytic model MERAXES to study self-consistent reionisation and foregrounds. I compared the luminosity function of the foregrounds generated by MERAXES to the observed foregrounds at 1.4 GHz and employed an extreme reionisation model and investigated its effects on the foregrounds in the power spectrum space. I found that the ratio of the foreground power between the extreme model and the default reionisation model is consistent within uncertainties of unity, even with implemented variance arising from the spectral index and lightcone-generation randomization.

The results of the research presented in this thesis have illuminated areas of EoR studies that have not been properly explored before. These will be useful for future 21 cm experiments, especially in the era of the next-generation interferometers such as the Square Kilometre Array.

# Contents

<b>Statement of Contributions</b>	<b>v</b>
<b>Acknowledgements</b>	<b>vii</b>
<b>Abstract</b>	<b>ix</b>
<b>1 Introduction</b>	<b>1</b>
1.1 General Overview . . . . .	1
1.1.1 The History . . . . .	1
1.1.2 The Consensus . . . . .	3
1.2 Reionisation of the Universe . . . . .	5
1.2.1 Sources of Reionisation . . . . .	6
1.2.2 Physics of Reionisation . . . . .	7
1.2.3 Modelling the Universe . . . . .	10
1.3 Reionisation Probes . . . . .	13
1.3.1 Cosmic Microwave Background . . . . .	13
1.3.2 Quasars . . . . .	15
1.3.3 High Redshift Galaxies . . . . .	17
1.3.4 Neutral Hydrogen (HI) . . . . .	18
1.4 21 cm Experiments . . . . .	23
1.4.1 Murchison Widefield Array (MWA) . . . . .	27
1.4.2 Low Frequency Array (LOFAR) . . . . .	28
1.4.3 Giant Metrewave Radio Telescope (GMRT) . . . . .	29

1.4.4	Precision Array for Probing the Epoch of Reionization (PA- PER) . . . . .	30
1.4.5	Hydrogen Epoch of Reionization Array (HERA) . . . . .	31
1.4.6	Next Generation Radio Interferometer . . . . .	32
1.4.7	Global 21 cm Experiments . . . . .	32
1.4.8	Current Results and Limits . . . . .	33
1.5	Challenges in 21 cm EoR Experiments . . . . .	35
1.5.1	Foregrounds . . . . .	36
1.5.2	Instrumental Systematics . . . . .	42
1.5.3	Radio Frequency Interference (RFI) . . . . .	43
1.5.4	Ionosphere . . . . .	44
1.6	Thesis Motivation . . . . .	45
<b>2</b>	<b>Methodology</b>	<b>47</b>
2.1	Simulation Software . . . . .	47
2.1.1	CUBEP <sup>3</sup> M . . . . .	48
2.1.2	GADGET-2 . . . . .	51
2.1.3	21cmFAST . . . . .	52
2.1.4	MERAXES . . . . .	55
2.2	Power Spectrum . . . . .	59
2.3	Parameter Estimation . . . . .	64
2.3.1	Markov Chain Monte Carlo . . . . .	64
2.3.2	21cmMC . . . . .	66
2.4	Summary of Methods . . . . .	68
<b>3</b>	<b>Modelling the stochasticity of high-redshift halo bias</b>	<b>71</b>
3.1	Abstract . . . . .	71
3.2	Introduction . . . . .	72
3.3	Methodology . . . . .	76

3.3.1	<i>N</i> -body simulation data . . . . .	76
3.3.2	Instantaneous halo bias in <i>N</i> -body simulation . . . . .	82
3.3.3	Implementing instantaneous halo bias . . . . .	84
3.3.4	Temporal halo bias in <i>N</i> -body simulation . . . . .	85
3.3.5	Implementing temporal halo bias . . . . .	87
3.4	Results . . . . .	89
3.4.1	Testing the method . . . . .	91
3.4.2	Sub-grid Modelling of Temporal Stochasticity in Multi-Scale Reionisation . . . . .	96
3.5	Summary and Discussion . . . . .	98
3.6	Acknowledgment . . . . .	101
<b>4</b>	<b>The Impact of Realistic Foreground and Instrument Models on 21 cm Epoch of Reionisation Experiments</b>	<b>103</b>
4.1	Abstract . . . . .	103
4.2	Introduction . . . . .	104
4.3	Mathematical Framework . . . . .	107
4.3.1	Interferometric Visibilities . . . . .	107
4.3.2	Brightness Temperature and Power Spectrum . . . . .	108
4.3.3	Components of Observable Signal . . . . .	110
4.3.3.1	EoR Lightcones and Parameters . . . . .	110
4.3.3.2	Point-Source Foreground Model . . . . .	111
4.3.3.3	MWA and SKA-based Instrument Model . . . . .	112
4.3.3.4	2-D Power Spectrum . . . . .	114
4.3.4	Bayesian Parameter Estimation . . . . .	115
4.3.4.1	3-D Isotropic Uncertainties . . . . .	117
4.3.4.2	Gaussianity and Independence of Instrument-Convolved Foregrounds . . . . .	117

4.3.5	Extensions to 21CMMC . . . . .	121
4.3.6	Comparison to Existing Framework . . . . .	122
4.4	Observational Effects on EoR Lightcones . . . . .	125
4.5	MCMC Analysis . . . . .	127
4.6	Parameter Estimation Results . . . . .	130
4.7	Discussion and Conclusion . . . . .	139
4.8	Appendix . . . . .	141
4.8.1	Fourier Conventions . . . . .	141
4.8.2	Variance of Residual . . . . .	142
<b>5</b>	<b>The Correlation between Self-Consistent Foregrounds and Cos-</b>	
	<b>mic Reionisation</b> . . . . .	<b>145</b>
5.1	Introduction . . . . .	145
5.2	Methodology . . . . .	147
5.2.1	Luminosity Scaling Relation . . . . .	148
5.2.2	Source Count Distribution . . . . .	149
5.2.3	Power Spectrum . . . . .	150
5.3	Results . . . . .	151
5.4	Discussion and Conclusion . . . . .	160
<b>6</b>	<b>Conclusion</b> . . . . .	<b>163</b>
	<b>Appendices</b> . . . . .	<b>169</b>
<b>A</b>	<b>Co-author Agreements</b> . . . . .	<b>171</b>
A.1	Statement of Originality . . . . .	171
A.2	Co-Author Responses . . . . .	172
<b>B</b>	<b>Copyright Information</b> . . . . .	<b>175</b>
B.1	Copyright for Chapter 3 . . . . .	175

B.2 Copyright for Chapter 4 . . . . .	176
<b>Bibliography</b>	<b>177</b>

# List of Figures

1.1	The evolutionary timeline of the universe from the Big Bang to the present day. Credit NASA and WMAP team. . . . .	4
1.2	The anisotropies of CMB radiation from the Wilkinson Microwave Anisotropy Probe (WMAP) satellite. Credit: NASA and WMAP team. . . . .	13
1.3	The spectra from a few high-redshift quasars from Fan et al. (2006). The Gunn-Peterson trough is clearly visible in the spectra of QSOs at $z > 6$ . . . . .	16
1.4	An example of the evolution of the 21 cm signal across redshift. The panels show the lightcone evolution of $\delta T_B$ (top panel), the sky-averaged or global brightness temperature, $\delta \bar{T}_B$ (middle panel), and the dimensionless 1-D power spectrum of $\delta \bar{T}_B$ ( $\delta \bar{T}_B \Delta_{21}^2$ ) at $k = 0.1$ and $k = 0.5 \text{ Mpc}^{-1}$ as labelled (bottom panel) versus redshift from Mesinger et al. (2016). . . . .	21
1.5	The MWA Phase II tiles at the MRO in Western Australia. . . . .	27
1.6	The LOFAR Superterp stations in Dwingeloo, Netherlands from van Haarlem et al. (2013). . . . .	29
1.7	A lit-up GMRT dish in Pune, India. Credit: SKA. . . . .	30
1.8	A PAPER antenna element that is mounted on a grounding structure. Credit: SKA Africa. . . . .	31
1.9	The flattened absorption lines from cosmic dawn as reported by Bowman et al. (2018). The different colors correspond to the different hardware configurations used to verify the finding. . . . .	34
1.10	Current lowest EoR limits with respect to wavenumber (left panel) and redshift (right panel) from PAPER by Kolopanis et al. (2019)	

(blue square), MWA by Li et al. (2019a), Barry et al. (2019) and Trott et al. (2020) (green circles, red pentagon, and purple triangle respectively), LOFAR by Mertens et al. (2020) (yellow diamond), and GMRT by Paciga et al. (2013) (black star). The various possible reionisation models from 21CMFAST (Mesinger et al., 2011) (grey lines) are also included for comparison. Credit: R.C. Joseph<sup>1</sup>. 36

1.11 The Euclidean-normalized differential source count distribution of AGN (black circle) and star forming galaxies (white circle) from Mauch & Sadler (2007). . . . . 38

1.12 The left panel shows the foreground contamination (darker grey region) due to instrumental effects in 3-D and the right panel shows the same region after 2-D averaging from Thyagarajan et al. (2013). 40

2.1 2-D depiction of the CUBEP<sup>3</sup>M code sub-volume decomposition process in each MPI node from Harnois-Déraps et al. (2013). Here, `nf_physical_node_dim`, `nf_physical_tile_dim`, and `nf_buff` are the fine-mesh cells in the entire node, fine-mesh cells in the tile, and the buffer region corresponding to 24 fine cells respectively. . 50

2.2 2-D depiction of the gridding process involving a Gaussian gridding kernel for  $4^2$  grid cells with 2 baselines. The different coloured regions correspond to the visibilities convolved with the normalized gridding kernel, with the actual position of the baseline represented by the coloured circles. The centre of cells that receive contributions from the convolved visibility are shown by the black crosses. At the centre of the cell in which both baselines contribute to the visibility (diamond marker), the convolved values are coherently averaged to give the final visibility of that cell, based on Equation 2.27. . . . . 62

2.3 A summary of the relationship between the tools we have presented that are used to achieve the final goal of reionisation studies: parameter estimation. Note that not all of these tools are actually used to constrain reionisation parameters in this thesis; only those

	that are within the dashed blue lines are used in Chapter 4. The other tools are used in Chapter 3 and 5 to address the resolution issues affecting low-mass haloes in $N$ -body simulations (enclosed in green dash line) and the relationship between foregrounds and cosmic reionisation (enclosed in orange dash line), respectively. . . . .	69
3.1	Halo mass functions in $N$ -body simulations, with the box size of $6.3 h^{-1}$ Mpc (top) and $114 h^{-1}$ Mpc (bottom). The $N$ -body halo data is plotted as points and compared to the Sheth-Tormen mass function (solid lines) at different redshifts (decreasing from top to bottom). . . . .	77
3.2	PDF of the number of MHs, $N_{5;8}$ , contained within cells of given overdensity $\delta$ on our $14^3$ -grid $6.3 h^{-1}$ Mpc-box. $\delta$ is shown on top of each subplot while redshifts are shown on the left. The PDF of the $N$ -body halo data (black solid) is fit by a log-normal distribution (red dashed). . . . .	78
3.3	Same as in Fig. 3.2, but with the number of haloes sampled on a $44^3$ grid. . . . .	78
3.4	PDF of the LMACH collapsed fraction, $f_{\text{coll},8;9}$ , contained within cells of given overdensity $\delta$ on our $64^3$ -grid $114 h^{-1}$ Mpc-box. Plotting convention is the same as in Figure 3.2. . . . .	79
3.5	Same as in Fig. 3.4, but with the collapsed fraction sampled on a $128^3$ grid. . . . .	79
3.6	The evolution of $\mu$ with respect to overdensity for the $6.3 \text{ Mpc } h^{-1}$ (top panels) and $114 \text{ Mpc } h^{-1}$ box(bottom panels) $14^3$ , $44^3$ , $128^3$ and $64^3$ grid for several representative redshifts, all as labelled. . . . .	80
3.7	The evolution of $\sigma$ with respect to overdensity for the $6.3 \text{ Mpc } h^{-1}$ (top panels) and $114 \text{ Mpc } h^{-1}$ box(bottom panels) with $14^3$ , $44^3$ , $128^3$ and $64^3$ grid for several representative redshifts, all as labelled. . . . .	80
3.8	Number of MHs, $N_{5;8}$ , per cell vs cell overdensity $\delta$ at $z = 17.215$ (upper panel) and $z = 10.110$ (lower panel) for $6.3 \text{ Mpc}/h$ box and $14^3$ grid (cell size $450 h^{-1} \text{ kpc}$ ). Shown are the $N$ -body halo data (left panels), the instantaneous mock halo (middle panels), and temporal mock halo (right panels). Data points are projected onto a 2-dimensional uniform . . . . .	

	grid of $\log_{10}(1 + \delta)$ and $\log_{10}(N_{5:8})$ , and are then shown collectively as the ratio of the number of data points on each grid cell (color map) to the total number of data points. The data is compared to the mean deterministic bias (solid line) by Ahn et al. (2015). . . . .	86
3.9	Same as Fig. 3.8, but for $44^3$ grid (cell size $143 h^{-1}\text{kpc}$ ). . . . .	87
3.10	LMACHs collapsed fraction, $f_{\text{coll},8:9}$ , per cell vs cell overdensity $\delta$ at $z = 12.603$ (upper panel) and $z = 7.570$ (lower panel) for $114 \text{Mpc } h^{-1}$ box and $64^3$ grid (cell size $1.781 h^{-1}\text{Mpc}$ ). Shown are the $N$ -body halo data (left panels), the instantaneous mock haloes (middle), and the temporal mock haloes (right). Data points are projected onto a 2-dimensional uniform grid of $\log_{10}(1 + \delta)$ and $\log_{10}(f_{\text{coll},5:8})$ , and are shown collectively as the ratio of the number of data points on each grid cell (color map) to the total number of data points. The data is compared to the mean deterministic bias (solid line) by Ahn et al. (2015). . . . .	90
3.11	Same as in Fig. 3.10, but for $128^3$ grid (cell size $0.891 \text{Mpc } h^{-1}$ ). . . . .	91
3.12	Evolution of the absolute value of the percentage difference between the $N$ -body data and the total number of MHs, $N_{5:8}$ , (upper panels) and the LMACH collapsed fraction, $f_{\text{coll},8:9}$ , summed over the grid (lower panels) vs. redshift, $z$ , for the $6.3 \text{Mpc } h^{-1}$ and $114 \text{Mpc } h^{-1}$ box respectively. Plotted are the difference between the $N$ -body data and the instantaneous mock haloes (triangles) and the temporal mock haloes (squares) for the $14^3$ , $44^3$ , $128^3$ and $64^3$ grid, as labelled. . . . .	93
3.13	Pearson correlation coefficient between consecutive time slices vs redshift $z$ for: (top) $6.3 \text{Mpc } h^{-1}$ box with (left) grids of $14^3$ , and (right) $44^3$ , for the simulation data, and realisations of instantaneous mock and temporal mock haloes as labelled; (bottom) same as the top panels, but for $114 \text{Mpc } h^{-1}$ box with (left) grids of $64^3$ and (right) $128^3$ . . . . .	94
3.14	The lower panels show the $P(k)$ and the upper panels show the percentage of absolute difference of the $P(k)$ between the $N$ -body data and the mock realisations for the respective grids at $z = 12.903$ . The	

	black dash-dot line corresponds to the $N$ -body data, the cyan solid line corresponds to the generated instantaneous mock haloes and the magenta dash line corresponds to the generated temporal mock haloes. The percentage in the upper panel is capped at 50%. . . . .	95
3.15	Same as Figure 3.14 but for $z = 8.283$ . . . . .	96
3.16	The figure shows the LMACH collapsed fraction $f_{\text{coll},8:9}$ per cell with respect to $\delta$ at $z = 17.848, 10.110$ and $7.570$ (left to right). The top panels correspond to the actual $N$ -body simulation data from our $114 h^{-1}$ Mpc box on a $64^3$ grid, while the bottom panels show the generated mock haloes with temporal bias for $500 h^{-1}$ Mpc box on a $300^3$ grid. The plotting convention is the same as in Figure 3.10. . . . .	97
3.17	The lower panels show the $P(k)$ and the upper panels show the percentage of absolute difference of the $P(k)$ of $f_{\text{coll},8:9}$ at the indicated redshift between the $N$ -body ( $114 \text{ Mpc } h^{-1}$ , $64^3$ grid, black dotted in lower panel) and mock data ( $500 \text{ Mpc } h^{-1}$ , $300^3$ grid; magenta dashed). . . . .	99
4.1	A summary of our instrumental algorithm. . . . .	115
4.2	The skewness of the 2-D PS of the instrument-convolved point source foregrounds. The bins are predominantly close to Gaussian over the primary range of interest ( $0.1$ to $1 h \text{ Mpc}^{-1}$ ). . . . .	118
4.3	The correlation coefficient of the 2-D PS of the instrument-convolved foregrounds between a single cell with all other cells. The horizontal and vertical plots show cuts through the 2-D space at the chosen single cell locations, demonstrating the degree of correlation in the angular and line-of-sight modes. Each chosen $(k_{\perp}, k_{\parallel})$ bin is completely correlated with itself (black cell in main panels corresponding to highest point in the smaller side panels). However, also note that the bin is highly correlated over $k_{\parallel}$ and the correlation spills over to the two $k_{\perp}$ bins adjacent to the chosen bin. . . . .	119
4.4	The total uncertainty from 21CMSENSE (red solid line) compared to the total uncertainty from our framework (black dash line) with $T_{\text{sys}} = 240$ K and $\Delta t = 2 \times 10^5$ hours. . . . .	124

4.5	Comparison of the 1-D PS of the 7.5 Gpc box (red), the stitched 1.5 Gpc box (green dotted), and the stitched 1.5 Gpc coarsened to a resolution of 15 Mpc (blue dash-dot). The 7.5 Gpc box and the stitched 1.5 Gpc box agree very well on most scales, but the 1-D PS of the stitched and coarsened box differs from the 1.5 Gpc box at high $k$ due to finite resolution. . . . .	125
4.6	A corner plot comparing the constraints our systematic tests: uniform $uv$ sampling with no thermal noise or foregrounds (blue); uniform $uv$ sampling with point-source foregrounds but no thermal noise (orange); uniform $uv$ sampling with 1000 hours of thermal noise with the MWA but no foregrounds (green); MWA baseline sampling with $2 \times 10^5$ hours of thermal noise with the MWA but no foregrounds (red); MWA baseline sampling with $2 \times 10^5$ hours of thermal noise with the MWA and point-source foregrounds (purple). The use of $2 \times 10^5$ hours of thermal noise with the MWA is comparable to the noise level of 1000 hours with the SKA. The artificial “uniform” $uv$ sampling unnecessarily inflates the impact of thermal noise (green) as it restricts the number of baselines per $uv$ cell to one and the small collecting area of the MWA gives a signal-to-noise ratio of order unity; both of these factors results in a biased estimate. With the addition of baselines sampling and the use of SKA sensitivity, the constraints are remain unbiased (purple and red) although the final test (red) gives a really inflated constraint compared to the other tests. Note that these constraints still have the burn-in phase included. . . . .	128
4.7	The power spectra of the EoR signal (left) and the thermal noise with the MWA sensitivity (right) in unit of $\text{Jy}^2\text{Hz}^2$ . With the uniform $uv$ sampling, the signal to noise ratio is of order unity for 1000 hours of observation time due to the small collecting area of the MWA. While this is enough for an EoR signal detection over the slope of the 1-D PS, it is not sensitive enough for EoR parameter estimation with the MWA.	129

4.8	An example trace plot from the 160–170 MHz band with thermal noise and foregrounds. The blue lines show the true value of the parameter while the black lines show the progression of the parameter estimation at each iteration. In this particular case, we have ignored the walkers with $\ln \mathcal{L} < -4000$ . . . . .	131
4.9	A corner plot comparing the constraints of EoR parameters in the presence of instrumental noise and foregrounds in the different frequency bands: 150–160 (orange), 160–170 (green), and 170–180 (blue) MHz. . . . .	133
4.10	The 2-D power spectra of the EoR signal (i.e. without foregrounds or thermal noise) in the 160–170 MHz band for the true values (left) and the MCMC values (middle) – the median values of $\zeta = 21.13$ , $\log_{10}(T_{vir}) = 4.52$ , $L_X/\text{SFR} = 40.00$ , and $E_0=0.656$ keV– along with their ratio. The true parameters give a maximum power that is up to 6 times higher than the MCMC parameters in the EoR window, suggesting that it is deceptively easy to discriminate between the two models. . . . .	134
4.11	The 2-D power spectra of the data i.e. EoR signal, foregrounds and thermal noise (left) and the EoR signal (middle) in the 160–170 MHz band along with their difference (right). The negative power (white region) in the right panel is caused by the unaccounted contribution of the cross-power terms between the EoR signal and the foregrounds and thermal noise. . . . .	135
4.12	The ratio of the variance of the $P_D - P_M$ to the actual total variance, $\sigma_T$ .	136
4.13	$-\hat{\mathcal{L}}$ for the true (left) and MCMC (right) parameters. $-\hat{\mathcal{L}}$ is overall greater for the true parameters, as apparent from the overwhelming red region in the left panel coinciding with low u. . . . .	137
4.14	The $\Delta\chi^2$ contours for the three bands using the best fitting parameters from our framework which are presented in Table 4.3. With $df = 2996$ , the $1\sigma$ level is $\sim 77$ . Because the constraints for $L_X/\text{SFR}$ and $E_0$ from the MCMC look reasonably inflated, we only focus on examining the	

$\Delta\chi^2$  contours for  $\zeta$  and  $T_{\text{vir}}$ . . . . . 138

5.1 The luminosity function of the foregrounds at 1.4 GHz, in which the AGN and SFG from MERAXES are given by the solid red and cyan lines respectively, the AGN observations by Smolčić et al. (2017) is given by the black dash line, and the SFG observations by Mauch & Sadler (2007) and Upjohn et al. (2019) are given by the yellow dotted and magenta dash dot lines respectively. Note that AGN observations from Smolčić et al. (2017) are within  $0 < z < 5.5$ , but the SFG observations from Mauch & Sadler (2007) and Upjohn et al. (2019) are between  $0 < z < 0.3$  and  $0 < z < 1.3$  respectively; as such, the AGN and SFG from MERAXES are presented over the same  $z$  ranges as the observations ( $0 < z < 1.3$  for the SFG). The overall magnitude and shape of the SFG luminosity function from our framework is consistent with both SFG observations at  $\log_{10}(L_\nu) < 25$ . For the AGN, however, there is a discrepancy in both the magnitude and shape of the luminosity function across  $\log_{10}(L_\nu)$ . There is no flattening in the AGN luminosity function from MERAXES at  $\log_{10}(L_\nu) > 25$  and the discrepancy is as high as 2 orders of magnitude. . . . . 151

5.2  $P(k_\perp, k_\parallel)$  of the EoR, self-consistent foregrounds and the foreground model with respect to  $k_\parallel$  for some  $k_\perp$ . The red region shows the foreground-contaminated region because most of the foreground power is contained in the first four  $k_\parallel$  cells, which is the width of the Blackman-Harris taper. The EoR signal (black line) dominates in the EoR window compared to the observed Intema foregrounds (cyan line). However, the self-consistent MERAXES foreground power (orange line) dominates all regions of the 2D power spectrum space and is up to  $\sim 8$  orders of magnitude brighter than the empirically observed foregrounds from (Intema et al., 2011) across all  $k_\parallel$ . . . . . 153

5.3 From top to bottom, the  $T_B$  field lightcone from the implementation of extreme reionisation models with  $f_{\text{esc}|z=5} \in [0.06, 1e^{-4}, 1.0]$ , dubbed as default, late, and early respectively. The use of a lower/higher  $f_{\text{esc}|z=5}$

	value (middle/bottom panel) results in a(an) later/earlier completion of reionisation, as expected. . . . .	154
5.4	The ratio of the $P(k_{\perp}, k_{\parallel})$ of EoR signal (top panels) and foregrounds (bottom panels) of the late model (left panels) and early model (right panels) to the default model. Note that the top right panel is completely empty because for the early model as shown in Figure 5.3, reionisation has ended in the frequency range that we are interested in ( $150 \leq \nu \leq 160$ MHz corresponds to $\sim 7.8 \leq z \leq 8.5$ ). In the top left panel, the ratio of the EoR signal for the late model is as high as $\sim 90\%$ greater than the default, which is expected because reionisation of HI is still ongoing. Furthermore, the lower panels show that the ratios of foreground power of the two models to the default also differ by as high as $\sim 90\%$ and $\sim 25\%$ in the foreground-dominated region of the power spectrum, and as low as $\sim 50\%$ and $\sim 10\%$ in the rest of the power spectrum space. . . . .	156
5.5	The evolution of the ratio of the foregrounds $P(k_{\perp}, k_{\parallel})$ with the different EoR models to the default model in some $k_{\perp}$ cells with respect to $k_{\parallel}$ . The cyan, red, and green regions represent the ratio of uncertainties of $P(k_{\perp}, k_{\parallel})$ for the late, early, and default MERAXES runs respectively, in which the uncertainty arises from the lightcone generation and spectral index variance. The dashed cyan line and dotted red line represent the mean $P(k_{\perp}, k_{\parallel})$ ratio of the late and early model to the default model. . . . .	157
5.6	The mean Euclidean-normalized differential source count and uncertainty from the default, early, and late runs (square, triangle and circle markers respectively with colours as labelled), the foregrounds model based on Intema et al. (2011) (orange solid line), and the mean value (black dash line) and uncertainty (grey region) from multiple AGN simulations based on Amaratidis et al. (2019), which is what we use for our AGN scaling relation as described in §5.2.1. . . . .	159

# Chapter 1

## Introduction

### 1.1 General Overview

The last century has seen many exciting discoveries in the field of astronomy and cosmology. Different studies and findings combine together to provide a more coherent overview of the universe, from the very beginning to the present day.

#### 1.1.1 The History

At the end of the 19th century, the discovery of the relationship between the frequency of a wave and its velocity in an effect known as the Doppler shift led to the finding of spectral lines from stars that have been Doppler shifted (Doppler, 1842; Hearnshaw, 1992). This provided the first hint to the real state of our Universe, which at that time was believed to be in an ethereal steady-state whereby matter is continuously created, without beginning or end. The effect of the lengthening of the wavelength of celestial sources came to be known as redshift, a term that is important in astronomy and cosmology, whereby the redshift,  $z$ , is given by

$$z = \frac{\lambda_o}{\lambda_e} - 1, \quad (1.1)$$

with  $\lambda_o$  and  $\lambda_e$  being the observed and emitted wavelengths respectively.

Increasing findings of redshifted objects resulted in an understanding that the universe is actually expanding. This idea was first discussed by Georges Lemaître in his publication entitled “*Un Univers homogène de masse constante et de rayon croissant rendant compte de la vitesse radiale des nébuleuses extra-*

*galactiques*” (“A homogeneous universe of constant mass and increasing radius accounting for the radial velocity of extra-galactic nebulae”) (Lemaître, 1927). In this paper, Lemaître reported that the velocity of a celestial object is proportional to its distance and presented the value of the proportionality constant. He even hypothesized that the universe started from a singular point which then expanded over time – an idea that directly opposed the widely-accepted view of a steady-state universe. Lemaître’s work, however, did not gain enough attention from the scientific community, possibly because it was written in French hence limiting its pool of readers.

It was not until two years later when the American Edwin Hubble published his research on the recessional velocity of extra-galactic nebulae (Hubble, 1929) that the scientific community began to accept the idea that the universe is expanding. Hubble’s observation reported the relation between the recessional velocity and distance of an object, along with an updated value of the proportionality constant, both previously found by Lemaître. These two findings – respectively known as the Hubble’s law<sup>1</sup> and Hubble’s constant – provided the foundations for modern cosmology.

A few years after, in 1933, the discovery of extra-terrestrial radio signals from the depths of the Milky Way by Karl Jansky (1933) pioneered the field of radio astronomy. This opened up the possibility of studying objects from the early universe, whose radiation emits in, or has been redshifted to, the radio regime. Radio astronomy was further revolutionised in 1964 via the accidental discovery of the Cosmic Microwave Background (CMB) by Penzias & Wilson (1965). The steady-state universe theory was unable to explain the presence of CMB radiation, hence a new theory gained popularity: the Big Bang theory. This theory suggested that the universe started from singularity before cosmic expansion and that the CMB is a remnant of this “explosion”.

During the same year of Jansky’s discovery and the birth of radio astronomy, Fritz Zwicky first postulated the existence of the exotic, unknown substance dubbed as dark matter based on his observation of the velocity dispersion of galax-

---

<sup>1</sup>It is now called the Hubble-Lemaître Law by the International Astronomical Union (IAU)

ies in the Coma cluster (Zwicky, 1933). However, much like Lemaître’s work in 1927, Zwicky’s finding was not well known. It was not until the 1970’s when Vera Rubin and Kent Ford studied the rotation curves of spiral galaxies (Rubin & Ford Jr, 1970; Rubin et al., 1978) that the theory of dark matter became widely accepted. In the next decade, other observations, particularly of the anisotropies of the CMB, further supported the existence of dark matter.

Finally, at the end of the previous century, independent studies of distant type Ia supernovae showed that cosmic expansion is in fact accelerating (Riess et al., 1998; Perlmutter et al., 1999). These studies led to the discovery of the last missing piece of the cosmological model puzzle: dark energy. The cosmological constant,  $\Lambda$ , which was introduced by Einstein in his general relativity model denotes the energy density of empty space (Einstein, 1917) and is used to represent dark energy. Not much is known about dark energy except that it drives the acceleration of the expansion of the universe, however it is commonly assumed to be a characteristic energy of the vacuum.

### 1.1.2 The Consensus

The current consensus on the standard paradigm of the universe is the Lambda Cold Dark Matter ( $\Lambda$ CDM) model, in which the Big Bang is governed by dark energy and cold dark matter, in addition to normal matter. The composition of these components in the universe is: 68% dark energy, 27% dark matter, and 5% ordinary matter. As suggested by the term “dark”, the nature of the first two components are still being debated. Dark matter takes up almost 85% of matter in the universe, thereby dominating the mass in the universe.

The evolution of the universe as we know it is summarized in Figure 1.1. The birth of our universe happened approximately 13.8 billion years ago from an energetic “explosion” of space from a primordial singularity in an event known as the Big Bang. This was instantaneously followed by a brief exponential expansion of space during cosmic inflation, which caused density fluctuations to amplify (Vilenkin, 1985). The heating of the universe resumed at the end of inflation until the temperature was hot enough for the continuous creation and destruction of

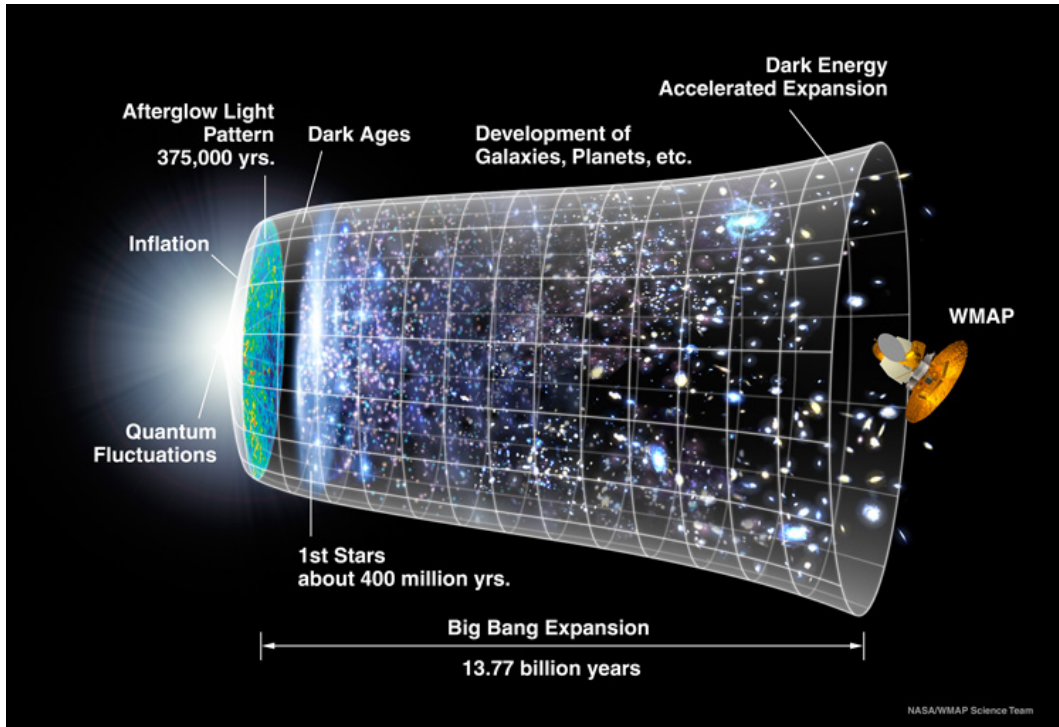


Figure 1.1: The evolutionary timeline of the universe from the Big Bang to the present day. Credit NASA and WMAP team.

fundamental particles and their antiparticles. At this time, radiation dominated the processes in the early universe (Peacock, 1999).

As the universe expanded, the temperature dropped, and hence production of matter ceased. This, in turn, triggered the annihilation of anti-matter until an excess of matter was left, in a process called baryogenesis. The loss of energy further led to the creation of light atomic nuclei during primordial nucleosynthesis a few minutes after the Big Bang (Kolb & Turner, 1981). Matter existed as an opaque plasma until the universe cooled down sufficiently for the baryons to combine together, thus forming neutral atoms around 370,000 years later. The event known as the epoch of recombination allowed photons to decouple from matter, thus producing what we now call the CMB. It lasted for around 10,000 years before the last scattering of photons occurred. Due to the lack of standard sources of photon emission, the succeeding period is called the cosmic dark ages (Furlanetto et al., 2006b; Barkana & Loeb, 2001).

Formation of structure in the universe is believed to have stemmed from minuscule Gaussian density perturbations that occurred during cosmic inflation of

the universe. These fluctuations are large at small scale but homogeneous and isotropic at large scale. Over time, they were amplified via gravitational instability until their self-gravity started to dominate; this resulted in the collapse of matter to form gravitationally bound systems and the first ionising sources (Kolb & Turner, 1981; Barkana & Loeb, 2001).

These luminous sources gave out radiation that illuminated the cold, dark universe during the Cosmic Dawn, thus ending the cosmic dark ages. The photons were then absorbed by the surrounding neutral hydrogen in the IGM, forming bubbles of ionised hydrogen. At the end of their lifetimes, these sources emitted X-ray radiation that pre-heated the neutral hydrogen IGM, with no large-scale reionisation actually occurring, and recombination dominated. During the subsequent period, called the Epoch of Reionisation, as more and larger structures were formed, reionisation of the universe began in earnest. The bubbles of reionised regions intercepted with each other, eventually reionising the entire universe to what we see today (Furlanetto et al., 2006b; Morales & Wyithe, 2010).

## 1.2 Reionisation of the Universe

Studies of the cosmic dawn and the succeeding Epoch of Reionisation (hereafter EoR) of hydrogen are key to understanding the universe. For one, the formation of the first cosmic structures signifies the transition of the gravitational growth of the universe from the linear to non-linear regime (Furlanetto et al., 2006b) i.e. from a homogeneous and isotropic state to the complex web-like form that we see today. Reionisation thus provides a platform to study the initial conditions of the density perturbations which gave birth to the primordial luminous sources, and more importantly, to understand galaxy and star formation processes (Barkana & Loeb, 2001), without the need to have complete details on the cosmology. Indeed, to further understand the cosmology of the early universe, we need to probe the dark ages and cosmic dawn, but because these periods are earlier than the EoR, the need for cutting-edge instruments with high-sensitivity means that

their detection may be currently out of our reach<sup>2</sup>. Therefore detection of the EoR signal is one of the most important frontiers in observational cosmology and galaxy formation.

### 1.2.1 Sources of Reionisation

Although the results remain inconclusive due to lack of observation, the main sources of reionisation radiation are believed to be the first stars and their descendants. Based on theoretical work, minihaloes – dark matter haloes with low mass – are generally conceived to host the first stars (Population III stars) responsible for the early stages of cosmic dawn at around  $z \sim 20$  (Bromm et al., 2009). These stars are believed to be unusually massive and metal poor because of the pristine matter environment, presence of background radiation, and absence of substructures in the early universe (Silk, 1977). Simulations of EoR sources have demonstrated that heating of the IGM reduces the cooling of baryons, which is necessary for cosmological dark matter halos to collapse and form stars hence potentially delaying cosmic reionisation (Simpson et al., 2013; Ocvirk et al., 2016). In addition, studies also show that the mechanism of radiative feedback can suppress the formation of stars in dwarf galaxies due to intense photoionising UV radiation, hence they are less likely to contribute photons for reionisation of the IGM (Dixon et al., 2016). The effects of these phenomena occurring during the early stages of EoR, however, are not fully understood.

After their death, these first stars continue to contribute to reionisation by emitting X-ray radiation either through supernovae explosion or through the formation of blackholes (Johnson & Bromm, 2007). Several studies have shown that they may have helped in pre-ionising large volumes of the IGM unreachable by UV radiation from stars. However, X-ray radiation could influence reionisation by suppressing small-scale structure formation and by heating of the IGM, both of which could affect star formation in dwarf galaxies (Ricotti & Ostriker, 2004; Madau et al., 2004; Knevitt et al., 2014). In addition, if X-ray radiation were the main cause of reionisation, the tomography of the expected reionisation bubbles

---

<sup>2</sup>A claimed detection of the cosmic dawn has been reported and will be discussed in detail in §1.4.8.

in the universe would be affected.

## 1.2.2 Physics of Reionisation

Simulations of the first generations of reionisation sources are highly dependent on processes governing star formation. Due to its overwhelming abundance in the universe, dark matter is a key driver in the formation of structures.

Dark matter particles interact with each other only through gravity, forming dark matter halos. This cycle continues, causing the halos to grow in size and mass until a critical overdensity threshold,  $\Delta$ , is reached. The dark matter halo then collapses, pulling the baryons and heating them to the virial temperature ( $T_{\text{vir}}$ ), corresponding to a certain mass threshold ( $M_{\text{min}}$ ), following the virial theorem

$$\frac{3}{2m_p}k_B T_{\text{vir}} = \frac{3}{5} \frac{GM}{2R_{\text{vir}}}. \quad (1.2)$$

Here,  $m_p$  is the mass of a proton,  $k_B$  is the Boltzmann constant,  $G$  is the gravitational constant, and  $M$  is the cumulative gravitating mass of the halo within radius  $R_{\text{vir}}$ . The equation represents the equilibrium between the kinetic and the gravitational energy of a halo, where a halo will only collapse and form stars through the cooling and condensation of gas if it has reached  $M_{\text{min}}$ .

Since primordial baryonic matter is predominantly composed of hydrogen, the minimum  $T_{\text{vir}}$  that allows the heated hydrogen gas to emit photons is  $10^4$  K, based on the atomic cooling property of hydrogen (Oh & Haiman, 2002; Osterbrock & Ferland, 2006). The emitted photons then escape the halo, cooling down the gas, which in turn, allows the gas to condense and form stars. The  $M_{\text{min}}$  that corresponds to this value of  $T_{\text{vir}}$  is presumed to be  $\sim 10^8 M_{\odot}$  at  $z \sim 10$  (Johnson et al., 2008; Lidz, 2016).

Assuming that every dark matter halo above  $M_{\text{min}}$  hosts a star-forming galaxy, the average number of ionising photons emitted per hydrogen atom, ( $n_{\gamma}/n_H$ ), is given by

$$\frac{n_{\gamma}}{n_H} = \zeta f_{\text{coll}}(M > M_{\text{min}}). \quad (1.3)$$

$\zeta$  is the efficiency of the production of ionising photons by baryons that have

collapsed into stars, where  $\zeta = A_{\text{He}} f_{\text{esc}} f_{\star} N_{\gamma}$  for  $A_{\text{He}} = 4/(4 - 3Y_{\text{He}})$  in which  $Y_{\text{He}}$  is the mass fraction of helium,  $f_{\text{esc}}$  is the fraction of ionising photons escaping into the IGM,  $f_{\star}$  is the fraction of baryonic matter in stars,  $N_{\gamma}$  is the number of ionising photons produced per baryon in the stars, and  $f_{\text{coll}}$  is the collapse fraction of matter into a star-forming galaxy (Furlanetto et al., 2006a). The radius for propagating ionising photons (local mean free path) inside the cosmic HII regions is postulated to be short as the photons do not have to travel far before encountering the neutral gas.

After the gas in the IGM has been reionised, a key parameter that ensures the gas stays ionised is its average recombination time,  $\bar{t}_{\text{rec}}$ . Recombination time is dependent on the clumping factor of the reionised gas in the IGM,  $C$ , which measures the average ratio of ionised hydrogen to the hydrogen gas in the IGM, following

$$C = \frac{\langle \rho_{g;\text{ionised}}^2 \rangle}{\langle \rho_g \rangle^2}, \quad (1.4)$$

with  $\rho_g$  and  $\rho_{g;\text{ionised}}$  being the density of hydrogen gas and density of ionised hydrogen gas in the IGM, respectively (Furlanetto et al., 2006b). In the early universe, it is reasonable to assume the case-B recombination rate at which the recombination directly to the ground state has been excluded and photons are not re-absorbed. At a temperature of  $T_0 = 2 \times 10^4$  K, this yields

$$\bar{t}_{\text{rec}} = 0.93 \frac{3}{C} \left( \frac{1+z}{7} \right)^{-3} \frac{T_0^{0.7}}{2 \times 10^4} \text{ [Gyr]}. \quad (1.5)$$

Because  $\bar{t}_{\text{rec}}$  is fairly long, it is believed that the ionised fraction during the EoR is reflective of the total photons output from all reionising sources, inclusive of smaller, dimmer objects (Lidz, 2016).

The previous parameters are combined together to give the mean fraction of the IGM volume in each of the ionised and neutral phases as a function of time, which is described by Lidz (2016) as

$$\frac{d\langle x_i \rangle}{dt} = \frac{d(n_{\gamma}/n_H)}{dt} - \frac{\langle x_i \rangle}{\bar{t}_{\text{rec}}}, \quad (1.6)$$

where  $\langle x_i \rangle$  denotes the volume-averaged ionised fraction. This differential equa-

tion gives the quantity of newly ionised atoms which increases proportional to the number of new ionising photons, but decreases proportionally to the current amount of ionised hydrogen due to recombination. A few caveats of this equality, however, include the dependence of  $\bar{t}_{\text{rec}}$  on the degree of clumping of the IGM, the inclusion of certain regions in  $\langle x_i \rangle$ , the disregard of spatial bias between the ionising sources and photons, the assumption that the photons are immediately absorbed by the IGM, and the neglect of spatial bias in the clumping factor.

As mentioned earlier, the first generations of metal-free and metal-poor Population III stars are believed to have driven reionisation of the IGM in the early universe due to feedback processes. Galaxy stellar mass,  $M_\star$ , is assumed to be related to the mass of the host halos,  $M_h$ , that are larger than a critical mass,  $M_{\text{crit}}$  ( $M_h > M_{\text{crit}}$ ), following a simple scaling relation (Mirocha, 2019):

$$M_\star(z, M_h) = \tilde{f}_\star(z, M_h)M_h(z); \quad (1.7)$$

or, for the star formation rate,  $\dot{M}_\star$ , and mass accretion rate,  $\dot{M}_h$ :

$$\dot{M}_\star(z, M_h) = f_\star(z, \dot{M}_h)\dot{M}_h(z, M_h). \quad (1.8)$$

Here,  $\tilde{f}_\star$  and  $f_\star$  are the star formation efficiencies that are dependent on  $M_h$  and  $\dot{M}_h$  respectively. Although  $M_{\text{crit}}$  is very uncertain at high redshift, for the formation of Population III stars in minihaloes (Visbal et al., 2014),

$$M_{\text{crit}} = 2.5 \times 10^5 \left( \frac{1+z}{26} \right)^{-3/2} (1 + 6.96(4\pi J_{\text{LW}})^{0.47}) M_\odot, \quad (1.9)$$

where  $J_{\text{LW}}$  [ $10^{-21} \text{ergs}^{-1} \text{cm}^{-2} \text{Hz}^{-1} \text{sr}^{-1}$ ] is the Lyman-Werner background intensity, corresponding to photons with energy 11.2 - 13.6 keV.

Furthermore, X-ray emission is expected to help pre-ionise regions of the IGM unreachable by UV radiation from stars after the cosmic dawn. The correlation between X-ray luminosity in the photon energy range of 0.5-8 keV,  $L_X$ , and  $\dot{M}_\star$  is given by (Furlanetto et al., 2006b)

$$L_X = 3 \times 10^{39} f_X \frac{\dot{M}_*}{M_\odot \text{yr}^{-1}} [\text{ergs}^{-1}], \quad (1.10)$$

where  $f_X$  is the unknown X-ray renormalization factor at high redshift, which is assumed to be proportional to  $\langle x_i \rangle$ .

### 1.2.3 Modelling the Universe

Exploration of a physical understanding of the EoR is conducted through comprehensive modelling of the luminous sources and their evolution during the EoR, which are dependent on these astrophysical processes:

- gas cooling - molecular hydrogen, Lyman- $\alpha$ , bremsstrahlung, recombination and collisional ionisations;
- star formation - pressure from turbulence, magnetic fields, and gravity causes the core to collapse;
- radiative emission - causes ionisation of hydrogen and helium and heating of gas;
- supernova - explosions produce hot gas suppressing further star formation, while ejecta and galactic winds transfer mass into the IGM;
- gas and energy feedback - cycle of matter from and into the IGM.

Simulating these processes relies heavily on modelling the key driver of structure formation: the dark matter particles. By doing dark matter only  $N$ -body simulations, we get an understanding of galaxy formation and clustering in the universe because the dark matter haloes act as a cosmic scaffolding for the formation of cosmic structures (Dayal & Ferrara, 2018). The latest generation of  $N$ -body simulations use billions of mass elements to trace galaxy evolution in a volume of space in which each mass element is treated as a collection of particles of dark matter with a given mass.

In general,  $N$ -body simulations determine the force on each element  $i$ ,  $\vec{F}_i$ , following the equation

$$\vec{F}_i = - \sum_{j \neq i} G \frac{m_i m_j (\vec{r}_i - \vec{r}_j)}{|\vec{r}_i - \vec{r}_j|^3} - \vec{\nabla} \cdot \phi_{ext}(\vec{r}_i), \quad (1.11)$$

where  $m_i$  is the mass of particle  $i$ ,  $\phi_{ext}(\vec{r}_i)$  is the external potential at  $\vec{r}_i$  and  $\vec{r}_i - \vec{r}_j$  is the relative distances between the masses (Trenti & Hut, 2008). Using methods such as the particle-based (Barnes & Hut, 1986), particle-mesh based (Hockney & Eastwood, 1988) or a hybrid of both (Springel, 2005), Equation 1.11 is solved to determine the forces on each element from all other particles for each discrete time step, referred to as ‘snapshot’, within a comoving frame. Based on the hierarchical structure formation ansatz that galaxies form inside clumps of dark matter, sophisticated codes are then used to identify the clumps, which are known as dark matter ‘haloes’, and construct their merger history for a complete halo catalogue.

Although  $N$ -body simulation is an excellent tool to study large-scale structure formation, it is not physically motivated because of the absence of an important component: baryonic matter. Unlike dark matter, baryons are able to dissipate energy through radiative processes. This is the motivation behind hydrodynamical or cosmological simulations in which primordial baryons are coupled with dark matter and goes through complicated but rigorous gas dynamic processes to form cosmic structures. Equations of gravity, hydrodynamics and thermodynamics are simultaneously solved either using Euler, Lagrangian or Euler-Lagrangian methods for particles and/or grid cells representing dark matter, gas and stars (Somerville & Davé, 2015). The specifics of these methods are beyond the scope of this thesis but they essentially decide how clumps of particles are defined and which time frame (fixed vs fluid frame) is used to calculate their properties such as mass and temperature (Dayal & Ferrara, 2018).

Cosmological simulation involving more than one single galaxy, however, still lacks the resolution to model small scale processes that are involved in star formation. Because of this, sub-grid modelling of the interstellar medium is done

numerically whereby converging clumps of gas are assigned a value of  $\dot{M}_\star$  that is proportional to the density of gas,  $\rho_{gas}$ , (Schmidt, 1959; Katz, 1992) if  $\rho_{gas}$  exceeds a certain threshold (Springel, 2005). Moreover, increasing interest in studying the EoR gave rise to numerical and semi-numerical models for sub-grid physics in which more resolved models of galaxy formation that are run on the base of  $N$ -body simulations are coupled with radiative transfer models which describe the interactions and propagation of radiation (Trac & Gnedin, 2011) via emission, absorption and scattering processes. The coupling enables realization of both small scale and large scale structures that are necessary for reionisation studies (Iliev et al., 2014). Nevertheless, despite being a more accurate representation of the physical processes involved, hydrodynamical simulation is computationally expensive and time-consuming (Thoul & Weinberg 1995; Tormen 1996).

Because of this disadvantage, semi-analytical simulations were developed. With this type of simulation, the dark matter component is modelled separately to produce dark matter merger trees via  $N$ -body simulations or analytical prescriptions such as the Press-Schechter (PS; Press & Schechter, 1974) or excursion set formalism (Bond et al., 1991). They are then combined with various analytical recipes for baryonic processes such as the ones listed earlier. As the baryons are treated using equations, semi-analytic models generally output average baryonic properties over a given halo, thus lacking sub-grid resolution. However, the use of a Monte Carlo approach to study individual objects or global quantities provides an efficient way of exploring a large parameter space that are occupied by the unknown, which helps reduce computational load and enables galaxies with much more complexity to be simulated (Somerville & Primack, 1999). This is why semi-analytic models are generally used to generate results that match with observation, especially for large and surveys, before a complete hydrodynamical simulation is run to understand the full physics; the use of SAMs thus complements the use of hydrodynamical simulations.

## 1.3 Reionisation Probes

The EoR happened 150 million to one billion years after the Big Bang. Though it is very challenging to look back so far in the past, there are a few tools that can be used to observe and study cosmic reionisation.

### 1.3.1 Cosmic Microwave Background

The Cosmic Microwave Background (CMB) is one potential probe of the reionisation of the IGM. It is the earliest radiation that can be observed, revealing the Last Scattering Surface of photons from the Big Bang. These photons had to propagate through the ever-expanding universe, causing their wavelength to increase and energy to decrease. This relic radiation comprises of plasma fluctuations which were rapidly cooled down by cosmic inflation and thus were frozen in the CMB map, as shown in Figure 1.2. Although the CMB only provides angular spatial information, observation of the CMB has managed to provide two reionisation constrains thus far, which we will present in this section. These constrains arise from the optical depth of the Thomson scattering of free electrons and from the kinematic Sunyaev-Zel'dovich effect of inverse Compton scattering which distorts the CMB.

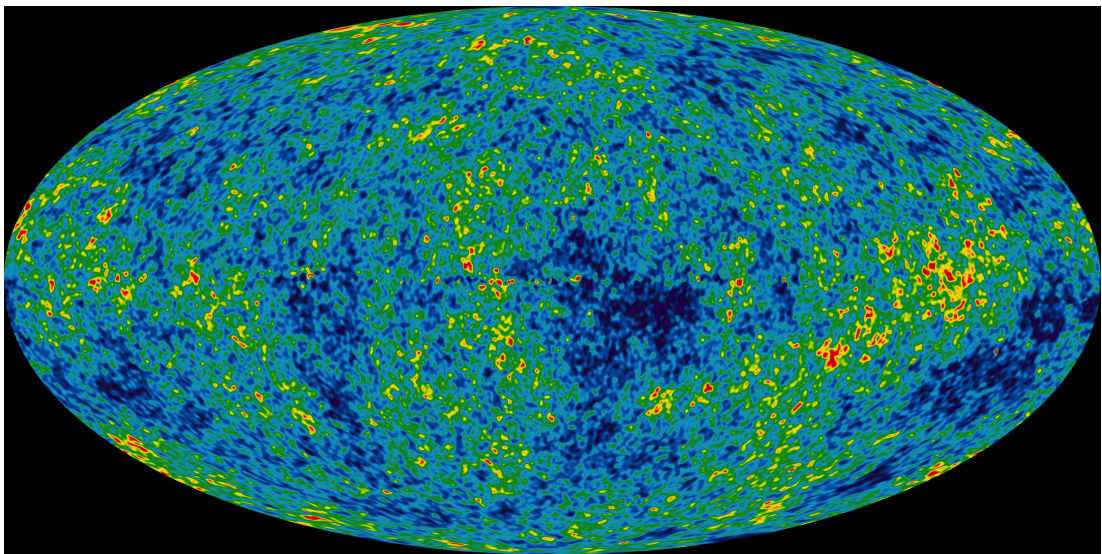


Figure 1.2: The anisotropies of CMB radiation from the Wilkinson Microwave Anisotropy Probe (WMAP) satellite. Credit: NASA and WMAP team.

The evolution of the IGM from a neutral to an ionised environment provides an increase in the number of free electrons available for Thomson scattering. The optical depth  $\tau$  of this process given by Reichardt (2016) is

$$\tau = \int n_e \sigma_T dl, \quad (1.12)$$

with  $n_e$  and  $\sigma_T$  being the number of electrons and the Thomson cross-section respectively, and  $l$  is the line-of-sight distance.  $\tau$  is insensitive to the progression of  $\langle x_i \rangle$  because of its integral nature, but it is useful to constrain the redshift of reionisation as the column depth of electrons, and consequently  $\tau$ , increases with respect to redshift.

In addition, the CMB is also polarized when the IGM is reionised. This is because reionisation causes the free electrons to scatter radiation in a quadrupole radiation field, resulting in linear polarization of the CMB. The amplitude of the polarized signal scales as  $\tau$  and so its power scales as  $\tau^2$ . The polarization signal from reionisation of the Universe, also known as the “reionisation bump”, was first detected by the Wilkinson Microwave Anisotropy Probe (WMAP) satellite from its measurement of temperature-polarization correlation (Kogut et al., 2003). The bump is unique to  $\tau$  and is not shared by any of the other five standard  $\Lambda$ CDM parameters. Current optical depth constraints were published by Planck 2015 whereby  $\tau = 0.058 \pm 0.012$  (Adam et al., 2016).

The kinematic Sunyaev-Zel’dovich (kSZ) effect is essentially a Doppler shift effect on scattered photons due to the velocity of the free electrons relative to the CMB. The kSZ differential temperature signal following Reichardt (2016) is given by

$$\frac{\Delta T_{\text{kSZ}}}{T_{\text{CMB}}}(\hat{\mathbf{n}}) = \bar{n}_{e,0} \sigma_T \int a(\eta)^{-2} e^{-\tau(\eta)} \bar{x}_e(\eta) (1 + \delta_x)(1 + \delta_b) (-\hat{\mathbf{n}} \cdot \mathbf{v}) d\eta. \quad (1.13)$$

Here,  $\tau(\eta)$  is the optical depth from observer to conformal time,  $\bar{x}_e(\eta)$  is the mean ionisation fraction at  $\eta$ ,  $a$  is the scale factor at  $\eta$ ,  $\bar{n}_{e,0}$  is the mean electron density at  $z = 0$ ,  $\delta_b$  and  $\delta_x$  are perturbations in the baryon density and ionisation fraction respectively,  $\hat{\mathbf{n}}$  is the line-of-sight unit vector and  $\mathbf{v}$  is the peculiar ve-

locity of free electrons at  $\eta$  (Reichardt, 2016). For non-relativistic kSZ effect, the observed CMB temperature scales as  $(v/c)n_e$  where  $v$  is the line-of-sight velocity of electrons, and  $n_e$  is the density of free electrons.

The main contribution to the kSZ signal comes from  $\delta_b$ , which gives a homogeneous signal, and  $\delta_x$ , which gives a patchy signal. The latter’s amplitude and power depends on reionisation duration and bubble size respectively. The power of the homogeneous and inhomogeneous (“patchy”) kSZ contributions are expected to be comparable and cannot be differentiated in current data due to the signal’s angular and spectral dependence (Reichardt, 2016). Current constraint on the kSZ power,  $D_{\text{kSZ}}$ , is  $D_{\text{kSZ}} = 2.9 \pm 1.3 \mu\text{K}^2$  at multipole moment,  $l$ , of 300 obtained by the South Pole Telescope Sunyaev-Zel’dovich (SPT-SZ) effect survey (George et al., 2015).

### 1.3.2 Quasars

Quasars, commonly referred to as Quasi-Stellar Objects (QSO), are ultra-luminous Active Galactic Nuclei (AGNs) believed to host a supermassive blackhole in their centers, which are surrounded by a gaseous accretion disk. Quasars are one of the most distant objects that have been currently observed, seen as unresolved point-sources mostly in optical or near-infrared (NIR) observation (although there are a few radio-loud quasars being detected in radio observation). Quasars are extremely rare and only 500 have been detected so far (Mortlock, 2016). However, those formed before the completion of the reionisation of the Universe provide a direct probe to the EoR because they provide photons which are believed to have helped reionise the universe and act as beacons to study the IGM line-of-sight to them.

These photons can undergo a few different mechanisms such as scattering and damping before being absorbed by neutral hydrogen in the IGM. The scattering of photons by a neutral hydrogen atom is dependent on the sum of the cross-sections of Rayleigh, Raman and photo-ionisation scattering. Out of these three, the Rayleigh scattering cross-section is dominant, in which it is affected by the resonant Lyman series peaks and the damping wing at long wavelength (Mortlock,

2016).

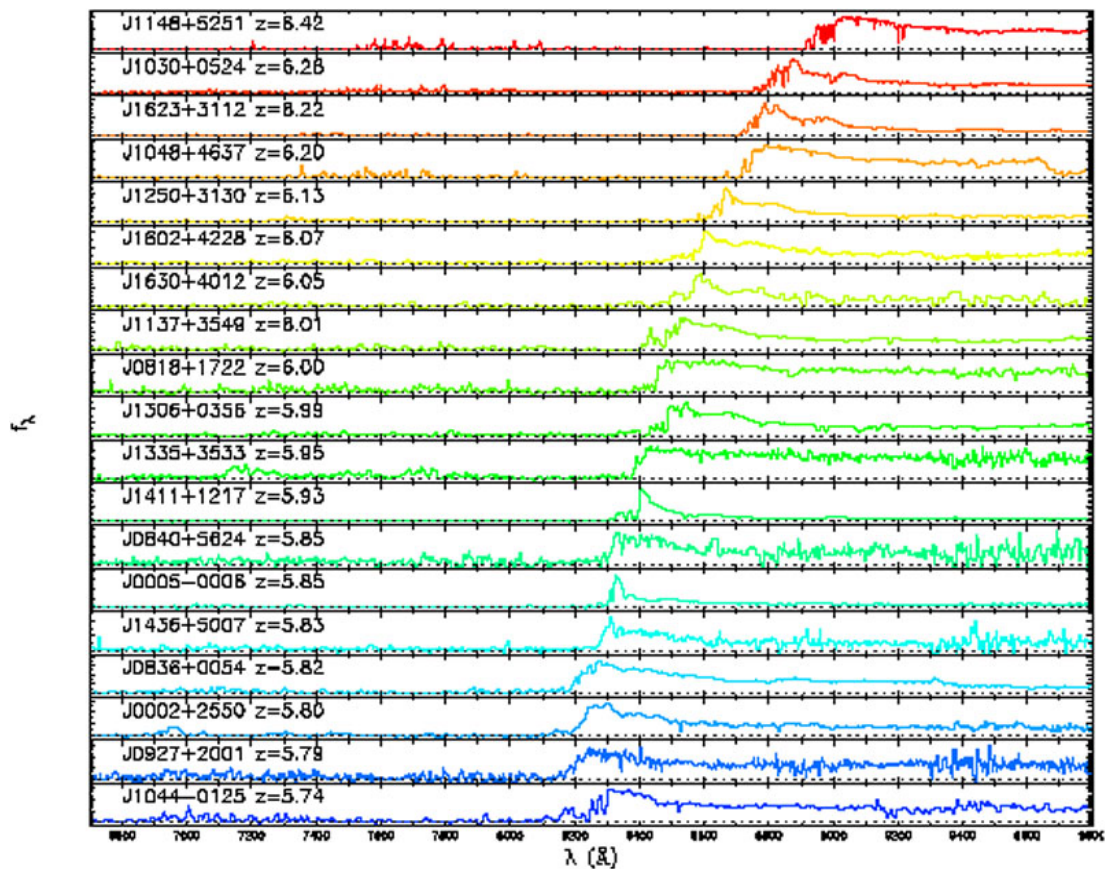


Figure 1.3: The spectra from a few high-redshift quasars from Fan et al. (2006). The Gunn-Peterson trough is clearly visible in the spectra of QSOs at  $z > 6$ .

One important tool in the study of quasars is the Lyman- $\alpha$  absorption line, which originates from electrons in hydrogen being excited from the ground state to the second lowest quantum energy state. The energy difference between the two levels corresponds to absorption of a photon with a wavelength of 1216 Angstroms ( $\text{\AA}$ ). More energetic photons are initially emitted by quasars, but because of the expansion of the universe, they are redshifted, and thus their wavelengths are stretched. When the wavelength coincides with 1216  $\text{\AA}$ , the photons are absorbed by neutral hydrogen, thus producing the absorption lines in the spectrum. The series of quasar absorption lines along the LOS to a quasar are collectively known as the Lyman- $\alpha$  forest.

At high redshift, these absorption lines get more and more dense due to increasing amount of neutral hydrogen, until the lines finally overlap. During the EoR, more energetic photons with energy bluer than Lyman- $\alpha$  are absorbed by

neutral hydrogen atoms while the rest are scattered. After reionisation has been completed, there are no more neutral hydrogen regions hence these photons are no longer affected and can travel freely in the IGM. In between these two epochs, there is a region where the intrinsic flux blueward of Lyman- $\alpha$  is mostly zero. This region is called the Gunn-Peterson trough. An example of QSO spectra with the Gunn-Peterson trough visible at  $z \geq 6$  are shown in Figure 1.3.

The Gunn-Peterson optical depth,  $\tau_{\text{GP}}$ , gives the optical depth of the IGM in the presence of neutral hydrogen related to the Lyman series resonance scattering, as derived by Gunn & Peterson (1965). It is given by

$$\tau_{\text{GP}} = \int_0^{z_e} \sigma_{\alpha} [\nu_o(1+z)] n_{\text{HI}}(z) \frac{dl}{dz} dz, \quad (1.14)$$

where  $z_e$  is the redshift of the emitted photon that is blueward of, i.e. with shorter wavelength than, the Lyman- $\alpha$  line,  $\nu_o$  is the observed frequency,  $dl$  is the proper length interval, and  $\sigma_{\alpha}$  is the cross-section for the Lyman- $\alpha$  transition. The discovery of a  $z = 2.1$  quasar by Schmidt (1965) confirmed this calculation by Gunn & Peterson (1965).  $\tau_{\text{GP}}$ , however, is expected to saturate ( $\gg 1$ ) at  $z \geq 6$  because HI is more dense earlier in the universe, hence the Gunn-Peterson effect is only suitable to probe the end of cosmic reionisation (Mortlock, 2016).

### 1.3.3 High Redshift Galaxies

Another possible probe of the EoR is high redshift galaxies. Detection of these galaxies, similar to quasars, are dependent on the Lyman- $\alpha$  process. However, instead of the absorption line, high redshift galaxy studies make use of the Lyman- $\alpha$  emission line. Galaxies emitting strong Lyman- $\alpha$  lines with a certain minimum rest frame Equivalent Width (EW) are known as Lyman- $\alpha$  Emitters (LAEs). For a galaxy to be deemed an LAE, its EW needs to be  $> 20 \text{ \AA}$ , although the EW threshold may sometimes be higher (Dijkstra, 2016).

Another type of distant galaxy that can be used to study the EoR is Lyman Break Galaxies (LBGs). They refer to Lyman- $\alpha$  emitting galaxies whose spectra drop-out or break at wavelengths shorter than  $912 \text{ \AA}$ , but are bright at longer

wavelengths. The drop-out happens due to radiation at higher frequencies being completely absorbed by the neutral hydrogen gas in regions close to the galaxy known as the Circum-Galactic Medium (CGM). The Lyman- $\alpha$  fractions from LBGs increases from  $2 < z < 6$  (Stark et al., 2010, 2011), but suddenly decreases at  $z \sim 7$  (Fontana et al., 2010; Ono et al., 2011).

The transfer of Lyman- $\alpha$  photons from a galaxy to the foreground CGM and IGM is complicated and highly dependent on radiative transfer processes. In the ISM, the escape fraction of Lyman- $\alpha$  is anti-correlated to the dust content, but is assisted by outflows and low column density perforation (Jensen et al., 2013; Dijkstra, 2014). In the IGM, the scattering and suppression of Lyman- $\alpha$  photons are dependent on the velocity field and density of the CGM. The reduced observation of Lyman- $\alpha$  flux from galaxies at  $z > 6$  provides constraints not only on the redshift of reionisation, but also on the  $\langle x_i \rangle$  at  $z = 7$ , which is found to be  $\leq 0.5$  based on comparison with simulations (Dijkstra et al., 2011; Jensen et al., 2013).

### 1.3.4 Neutral Hydrogen (HI)

The 21 cm radiation from the spin-flip, hyperfine transition of neutral hydrogen (HI) is a forbidden transition that rarely occurs spontaneously. However, because HI is so prevalent in the Universe, its signal is commonly observed from space. In addition, because the transition has a long average lifetime i.e taking a few million years before the transition finally happens, the emission line has an extremely narrow natural width, which is mostly unaffected by broadening effects except from Doppler shift. Although the 21 cm line is very weak, it is a promising probe of reionisation because of the abundance of neutral hydrogen in the early universe. It can be observed in all directions, hence potentially allowing for the study of the tomography of the IGM in the early universe (Madau et al., 1997).

As the CMB radiation from the epoch of recombination precedes the 21 cm signal from the EoR, it can hence be used as a background radiation field of reference because of its near-isotropic nature, with variations of only up to  $10^{-5}$  of  $T_{\text{CMB}}$  (Pritchard & Loeb, 2012). Observation of variations in the brightness tem-

perature,  $T_B$  – the temperature of a radiating blackbody with the same intensity,  $I_\nu$  – can thus be attributed to the reionisation process itself.

An important quantity that determines the 21 cm  $T_B$  is the spin temperature of HI,  $T_S$ . It is not a physical temperature; rather, it relates to the proportion of the two populations of spin states of HI atoms.  $T_S$  is driven by the interaction of HI with CMB photons, the collision with electrons and other particles, and the scattering of UV photons. The first process pushes the spin states to reach thermal equilibrium with the CMB, while the other two processes disrupt this coupling. Which effect ends up dominating  $T_S$  is dependent on both the expansion of the universe and the radiation from the primordial reionising sources (Pritchard & Loeb, 2012). With the CMB as a background, the radiative transfer equation along the line-of-sight passing through a cloud with  $T_S$  and optical depth,  $\tau_\nu$ , is given by

$$T_B(\nu) = T_S(1 - e^{-\tau_\nu}) + T_{\text{CMB}}e^{-\tau_\nu}. \quad (1.15)$$

For a hydrogen cloud,  $\tau_\nu$  can be solved by integrating the profile of the 21 cm line multiplied by the number of atoms in the singlet state between the energy of the triplet and singlet states along the proper distance (Furlanetto et al., 2006b). The exact details of the derivation is beyond the scope of this thesis, but taking into account that the IGM gas expands uniformly with the Hubble flow and that the hydrogen column density depends on the neutral fraction of hydrogen,  $x_{\text{HI}}$ , at a certain reference frequency  $\nu_0$ ,

$$\tau_{\nu_0} \approx 0.0092(1 + \delta)(1 + z)^{3/2} \frac{x_{\text{HI}}}{T_S} \left[ \frac{H(z)}{dv_{\parallel}/dr_{\parallel}(1 + z)} \right]. \quad (1.16)$$

Here,  $\delta$  is the overdensity of baryons,  $dv_{\parallel}/dr_{\parallel}$  is the gradient of the line-of-sight velocity component, and  $H(z)$  is the Hubble's constant (Furlanetto et al., 2006b). Substituting Equation 1.16 into Equation 1.15 and subtracting by  $T_{\text{CMB}}$ , the differential brightness temperature  $\delta T_B$  can thus be quantified by

$$\delta T_B(\nu) \approx 9x_{\text{HI}}(1 + \delta)(1 + z)^{3/2} \left( 1 - \frac{T_{\text{CMB}}}{T_S} \right) \left[ \frac{H(z)}{dv_{\parallel}/dr_{\parallel}(1 + z)} \right] [\text{mK}]. \quad (1.17)$$

There are two distinct regimes of the  $\delta T_B$  field: absorption when  $T_S < T_{\text{CMB}}$ ,

and emission when  $T_S > T_{\text{CMB}}$ . The latter is expected to dominate during the reionisation era, in which  $\delta T_B$  will be saturated when  $T_S \gg T_{\text{CMB}}$  (Furlanetto et al., 2006b).

Because the 21 cm signal is very faint, the power spectrum is the primary metric used to characterise the EoR signal because the variance contains a significant majority of the information, and has far greater SNR since it averages over many modes which are independent in noise, but not in signal. The power spectrum measures the spatial variance of a signal over a spatial volume  $V$  (Nasirudin et al., 2020) and is defined as

$$P(k) \equiv \frac{|\langle \delta T_B^\dagger(\vec{k}) \delta T_B(\vec{k}) \rangle_{|\vec{k}|=k}|}{V} \quad [\text{mK}^2 \text{ Mpc}^{-3} h^3], \quad (1.18)$$

where  $k$  is the spatial scale in Fourier space. A related metric that is routinely used in current experiments is the dimensionless 1-D power spectrum, which is given by

$$\Delta_{21}^2(k) = \frac{k^3}{2\pi^2} P(k) \quad [\text{mK}^2]. \quad (1.19)$$

Although there is an increasing disquiet over the use of the power spectrum because of the loss of non-Gaussian information (e.g. Mondal et al. (2015, 2016, 2017); Majumdar et al. (2018); Shaw et al. (2019)), the power spectrum is still currently the main metric used in 21 cm experiments.

An example of the evolution of the globally-averaged amplitude of the 21 cm signal across redshift is presented in Figure 1.4. The panels show the lightcone evolution of  $\delta T_B$  (top panel), the sky-averaged or global brightness temperature,  $\delta \bar{T}_B$  (middle panel), and the dimensionless 1-D power spectrum of  $\delta \bar{T}_B$ , which is referred to as  $\delta \bar{T}_B \Delta_{21}^2$ <sup>3</sup>, at  $k = 0.1$  and  $k = 0.5 \text{ Mpc}^{-1}$  as labelled (bottom panel) versus redshift from Mesinger et al. (2016). The specific magnitude and timing of the trends in the global signal can greatly vary depending on the physics but in general, there are five critical phases in which the global signal is influenced by different astrophysical processes.

The first two phases happened during the cosmic dark ages. In the first

---

<sup>3</sup>This is now commonly denoted as  $\Delta_{21}$  with the unit of  $\text{mK}^2$ . However, for clarity and consistency, in this section, we use  $\delta \bar{T}_B \Delta_{21}^2$  when referring to Figure 1.4.

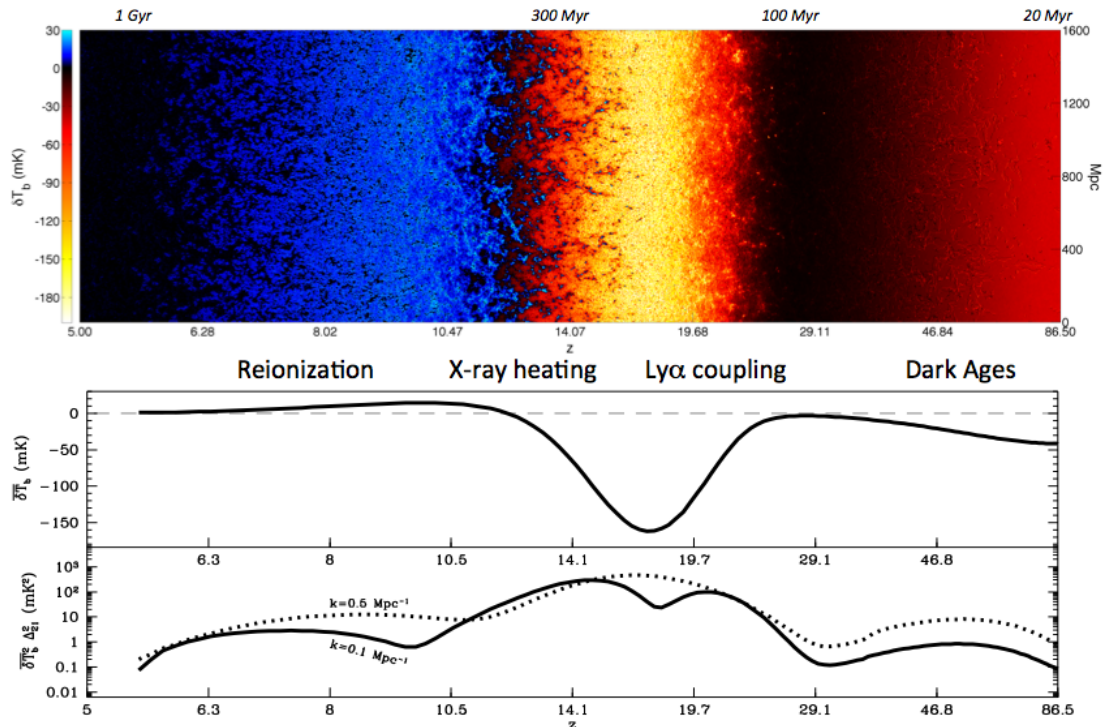


Figure 1.4: An example of the evolution of the 21 cm signal across redshift. The panels show the lightcone evolution of  $\delta T_B$  (top panel), the sky-averaged or global brightness temperature,  $\delta \bar{T}_B$  (middle panel), and the dimensionless 1-D power spectrum of  $\delta \bar{T}_B$  ( $\delta \bar{T}_B \Delta_{21}^2$ ) at  $k = 0.1$  and  $k = 0.5 \text{ Mpc}^{-1}$  as labelled (bottom panel) versus redshift from Mesinger et al. (2016).

phase,  $T_S$  was coupled to the kinetic temperature of the gas in the IGM,  $T_K$ , because of the high density of the IGM. The IGM decoupled from the CMB and cooled adiabatically following  $T_K \propto (1+z)^2$  while the cooling of the CMB was proportional to  $(1+z)$  (Furlanetto, 2016). The signal thus was in the absorption regime i.e negative in this phase, corresponding to the uniform red region in the leftmost part of the top panel of Figure 1.4. In principle, the signal from this phase provides a clear probe of the matter power spectrum, but it will be extremely difficult to observe (Furlanetto, 2016) because this phase happened in the very early universe, hence detection of this signal is beyond the sensitivity of current instruments.

In the second phase,  $z \sim 30$ , collisional coupling ended due to the decreasing density of the IGM with cosmological expansion. The spin states were driven to thermal equilibrium with the CMB due to the increasing inefficacy of collisional

coupling. This caused the IGM signal to dim over time until there was no signal left (Furlanetto, 2016), as shown in Figure 1.4 where the top panel goes from red to black.

The third phase kicked in when the primordial luminous sources formed. These first stars generated Lyman- $\alpha$  photons which helped re-couple  $T_S$  to  $T_K$  at the rate of dark matter halo collapse (Furlanetto, 2016). This phase marked the start of cosmic dawn and corresponds to the transition from black to yellow region in Figure 1.4, whereby the signal is in the absorption regime.

The fourth phase happened in the second half of cosmic dawn. The start of this phase corresponds to where  $\delta\bar{T}_B$  is at a minimum, which is when the IGM heating began to become significant. The death of the first luminous sources contributed to X-ray radiation, resulting in the heating of the IGM.  $T_S$  was increasingly driven to thermal equilibrium with  $T_K$  until they were coupled. The signal changed from absorption to emission when  $T_K$  surpassed  $T_{\text{CMB}}$ .  $\delta\bar{T}_B \Delta_{21}^2$  peaked during this phase due to the large fluctuations in the IGM temperature (Furlanetto, 2016), as evident from the transition from yellow to blue in the top panel of Figure 1.4.

The final phase happened during the EoR.  $T_K \gg T_{\text{CMB}}$  so the third term of Equation 4.2 saturated. The signal rapidly decreased once reionisation started, finally vanishing when reionisation completed (Furlanetto, 2016), as shown by the transition from blue to black in the plot.

Although the 21 cm signal is very faint, the availability of HI during the EoR makes up for this limitation. Its high sensitivity to the diffuse HI content in the IGM is also very useful because unlike the Gunn-Peterson optical depth which will saturate during cosmic reionisation, the IGM optical depth from the spin-flip transition is only  $\sim 1\%$  because of the low energy needed for the transition (Furlanetto, 2016). In addition, 21 cm line observations will enable a 3-D study of the neutral IGM in the early universe across cosmological redshift (Madau et al., 1997). The 21 cm line is thus the most promising probe for the EoR and its detection is one of the key scientific goals of current and future radio instruments.

## 1.4 21 cm Experiments

Detection of the 21 cm signal from the cosmic dawn and the succeeding EoR is considered to be one of the final frontiers of observational cosmology. Because the signal has been redshifted as a result of the expansion of the universe, it now lies in the low-frequency radio regime of the electromagnetic spectrum. The signal can be probed by the current and next generation of low-frequency radio telescopes.

Radio astronomy is a relatively new sub-field of astronomy that started in the 1930's with the detection of radio signals from the Milky Way by Karl G. Jansky (Jansky, 1933). Since then, radio observations have managed to capture new, non-thermal celestial objects such as quasars (Matthews & Sandage, 1963), pulsars (Hewish et al., 1968), and masers (Goldreich & Keeley, 1972), along with radio galaxies (Baade & Minkowski, 1954). It then gained popularity from the detection of the Cosmic Microwave Background (Penzias & Wilson, 1965) which supports the Big Bang theory. At the same time, radio instruments have also undergone major evolution since the first detection of astronomical radio signal in 1932. Because of the complexity of radio instruments, we only discuss some important first-order components that may affect cosmic dawn and EoR studies in this thesis.

Interferometric techniques were first explored in the optical regime by Michelson who measured the diameter of some close-by stars (Michelson, 1890; Michelson & Pease, 1921) and was later explored by Ryle & Vonberg who studied the sun in the radio regime (Ryle & Vonberg, 1946). Since then, the use of large steerable, single-dish radio antenna has been supplemented by the use of multiple linked antennas or dishes known as radio interferometers. The latter utilizes the displacement between the separate elements to resolve observations, as opposed to using the physical size of the antenna. This allows radio interferometers to obtain high angular resolution compared to other types of telescopes because the angular resolution of a telescope is proportional to  $\lambda/D$ , where  $D$  is the diameter of the observing element, and  $\lambda$  the wavelength. The popularity of “large- $N$ ”

interferometers is growing due to increased computer capacity.

The electric fields or voltages from a signal received at point  $\mathbf{x}$  as a function of  $\nu$ ,  $E(\mathbf{x}, \nu)$ <sup>4</sup>, captured by the pair of antennas  $(i, j)$  are then cross-correlated and averaged over time and source position, yielding the output,  $V(\mathbf{x}_i, \mathbf{x}_j, \nu)$ , given by

$$V(\mathbf{x}_i, \mathbf{x}_j, \nu) = \langle A_i E(\mathbf{x}_i, \nu) A_j^\dagger E^\dagger(\mathbf{x}_j, \nu) \rangle, \quad (1.20)$$

where the raised  $\dagger$  indicates the complex conjugate and  $A$  is the antenna response. Briefly, by taking into account the spatial incoherence of astronomical radiation, we can exchange the expectation with the integral and re-write the measured correlation of the electric fields between two antennas as

$$V(\mathbf{x}_i, \mathbf{x}_j, \nu) \approx \int B(\mathbf{s}, \nu) I(\mathbf{s}, \nu) e^{-2\pi i \nu \mathbf{s} \cdot (\mathbf{x}_i - \mathbf{x}_j)/c} d\Omega, \quad (1.21)$$

where  $B(\mathbf{s}, \nu) \approx A_i A_j^\dagger$ ,  $\mathbf{s}$  is the position of the astronomical sources,  $I(\mathbf{s}, \nu)$  is the observed intensity and  $d\Omega$  is the solid angle of the celestial sphere for the observation (Bridle et al., 1989).

For clarity, we can re-write the notations as follows:  $\mathbf{u}$  is the baseline displacements in Fourier space, which are defined as  $\mathbf{u} = (u, v, w) = (\frac{r_1}{\lambda}, \frac{r_2}{\lambda}, \frac{r_3}{\lambda})$ , where  $r_1$  and  $r_2$  are the physical, horizontal displacement between the baseline antennas and  $r_3$  is the vertical displacement of the baselines; and  $\mathbf{s}$  is transformed to 2-D coordinates  $\mathbf{l} = (l, m) = (\sin \theta \cos \phi, \sin \theta \sin \phi)$ , where  $\theta$  is the zenith angle,  $\phi$  the azimuthal angle around the zenith pole, and  $l^2 + m^2 < 1$ . Substituting these into Equation 1.21, in the presence of a beam attenuation, the measured correlation between the electric fields, formally known as the visibility  $V(u, v, w, \nu)$  in interferometry, is thus given by

$$V(u, v, w, \nu) = \int \int I(l, m, \nu) B(l, m, \nu) \frac{e^{-2\pi i [ul + vm + w(\sqrt{1-l^2-m^2}-1)]}}{\sqrt{1-l^2-m^2}} dldm \quad [\text{Jy}]. \quad (1.22)$$

Here,  $B(l, m, \nu)$  is the “primary beam” attenuation between a pair of antennas. For co-planar instruments with small Field-Of-View (FOV), the effects of sky

---

<sup>4</sup>These are complex numbers because the electric field is a wave, characterized by an amplitude and phase.

curvature are negligible and it is easily seen that  $\sqrt{1 - l^2 - m^2} \approx 1$  and  $w \approx 0$ , implying that the flat-sky approximation of the visibility ( $V_{\text{flat}}(u, v, \nu)$ ) is given by

$$V_{\text{flat}}(u, v, \nu) \approx \int \int I(l, m, \nu) B(l, m, \nu) e^{-2\pi i[ul+vm]} dl dm \quad [\text{Jy}]. \quad (1.23)$$

For interferometers that meet these requirements, the visibility thus can be simplified to a 2-Dimensional Fourier Transform of the beam-attenuated intensity of the sources.  $V(u, v, w, \nu)$  or  $V_{\text{flat}}(u, v, \nu)$  then undergoes a Fourier Transform in the spectral dimension, yielding  $V(u, v, w, \eta)$  or  $V_{\text{flat}}(u, v, \eta)$  respectively, which can then be cylindrically or spherically averaged to give the 2-D power spectrum<sup>5</sup>.

The angular and line-of-sight modes in cosmological unit,  $k_{\perp}$  and  $k_{\parallel}$ , can be respectively converted from the Fourier modes in observation unit,  $|\mathbf{u}|$  and  $\eta$ , following Morales & Wyithe (2010), where

$$k_{\perp} = \frac{2\pi|\mathbf{u}|}{D_M(z)} \quad [\text{Mpc}^{-1}\text{h}], \quad (1.24)$$

and

$$k_{\parallel} = \frac{2\pi H_0 f_{21} E(z)}{c(1+z)^2} \eta \quad [\text{Mpc}^{-1}\text{h}]. \quad (1.25)$$

Here,  $D_M(z)$  is the transverse comoving distance,  $H_0$  is the Hubble constant,  $f_{21}$  is the rest frequency of the 21 cm hydrogen hyperfine transition and  $E(z)$  is defined as

$$E(z) = \sqrt{\Omega_m(1+z)^3 + \Omega_k(1+z)^2 + \Omega_{\Lambda}}. \quad (1.26)$$

where  $\Omega_{\Lambda}$ , and  $\Omega_k$  are the dimensionless density parameters for dark energy and the curvature of space.

Another important aspect of radio synthesis is in calibrating the visibility data to set a reference. This step is usually done after removing contaminants from radio interference and also data from broken antennas that can affect the quality of data. The details of calibration are beyond the scope of this thesis but a brief summary of the two most-used methods are presented here.

---

<sup>5</sup>The exact steps taken to compute the power spectrum will be discussed in detail in §2.2.

In sky-based calibration, unresolved sources that have high Signal-to-Noise Ratio (SNR) are usually used as calibrators. Bright calibrators are used as reliable standard sources to compare high SNR measurements with a model so that a correction can be made in the gain when observing the target source (Thompson et al., 2017). Sky-based calibration is, however, very dependent on the sky model and at low frequency ( $\nu < 300$  MHz), the sky map is incomplete. In this case, redundant calibration, which makes use of equally-spaced and oriented antennas that probe the same Fourier mode, can be used to calibrate the gains. This is because baselines with equal spacing and orientation have visibilities that are equal, hence they contain information on the complex gains that include atmospheric and instrumental effects; information about the absolute flux scale and position, however, are not retained in the product of the visibility and gains (Wieringa, 1992). Redundant calibration is thus less dependent on the completeness of the sky model.

With interferometers, instrumental noise is less of a problem because it is uncorrelated between each antenna so it can be averaged down with time and bandwidth, unlike the signal, which is correlated. This helps the calibration process of interferometers. In addition, each antenna should have the same beam-width and should respond to the same effective intensity distribution that is the product of the intensity of the sky and the mean beam profile. In reality, however, antennas may have nonidentical shapes hence each pair does not necessarily respond to the same effective intensity distribution (Thompson et al., 2017).

Unsurprisingly, single element radio telescopes are relatively less complicated than interferometers. Their calibration process usually involves ensuring that the flux of a particular source is the same as the standard flux from catalogues. This involves accurate measurement of system noise,  $T_{\text{sys}}$ , which is given by

$$T_{\text{sys}} = T_{\text{A}} + T_{\text{LP}}[1/\epsilon - 1] + (1/\epsilon)T_{\text{R}}, \quad (1.27)$$

where  $T_{\text{A}}$  and  $T_{\text{R}}$  are the temperatures of the antenna and receiver respectively,  $T_{\text{LP}}$  is the physical temperature of the transmission line between the antenna and the receiver, and  $\epsilon$  is the efficiency of the transmission ( $0 \leq \epsilon \leq 1$ ). Because

there is only one element, single element radio telescopes usually have low SNR, although they can observe a large fraction of the sky and capture a lot of signal. In addition, although single element radio telescopes have higher sensitivity to extended structures, they have poor angular resolution because of their limited size. This is why they are mostly used to study the global signal from the cosmic dawn and EoR in the context of 21 cm cosmology.

The detection of signal from cosmic dawn and EoR is one of the key science goals of most current low-frequency telescopes. Here we present some relevant current and future 21 cm experiments instruments.

### 1.4.1 Murchison Widefield Array (MWA)



Figure 1.5: The MWA Phase II tiles at the MRO in Western Australia.

The MWA is a low-frequency radio aperture array telescope located at the radio-quiet zone, the Murchison Radio Astronomy Observatory (MRO) site, in Western Australia. The array operates in the 80 – 300 MHz frequency range. It comprises tiles with an effective area per tile ( $A_{\text{eff}}$ ) of 21 m<sup>2</sup> and a full-width

half-maximum FOV of  $26^\circ$  at  $\nu_0 = 150$  MHz, which is useful for large sky surveys. Each  $4.4 \text{ m} \times 4.4 \text{ m}$  tile consists of a  $4 \times 4$  grid of dual polarization “bow-tie” dipoles, as shown in Figure 1.5. The MWA reionisation observing scheme spans two 30 MHz bands, between 137 – 167 MHz and 167 – 197 MHz (Tingay et al., 2013; Jacobs et al., 2016).

There are two configurations of the MWA: compact and extended. The former consists of tiles that are mostly distributed within  $\sim 300$  m of the core, and is primarily used for EoR science; the latter comprises of pseudo-randomly distributed tiles up to a 6 km diameter from the core. The compact configuration also hosts many redundant baselines to aid calibration steps in EoR data analysis (Wayth et al., 2018). Although the MWA’s collecting area is small ( $\sim 2,800 \text{ m}^2$ ), its compact design makes up for this limitation in terms of the power spectrum sensitivity (Dillon et al., 2015). When the MWA was first commissioned, the MWA Phase I array consisted of 128 pseudo-randomly distributed tiles across the MRO (Lonsdale et al., 2009). In early 2017, the MWA Phase II upgrade was commissioned, whereby an additional 128 tiles were deployed at the MRO site, resulting in a total of 256 tiles; however, only 128 tiles are active during each observation time (Wayth et al., 2018).

### 1.4.2 Low Frequency Array (LOFAR)

LOFAR is a phased-array low-frequency interferometer that operates between 10 - 250 MHz, with a low band of 10 - 90 MHz and a high band of 110 - 250 MHz. It consists of 40 separate stations distributed over the northeastern part of the Netherlands and 14 additional international stations distributed all over Europe. The core station, which is located in Dwingeloo, Netherlands, comprises 24 tiles of dipole antennas distributed within a radius of 2 km; other stations, known as remote stations, consist of 48 tiles arranged over an area of  $\sim 40$  km east-west and 70 km north-south, although only the inner 24 tiles are used at the same time as the core station. Six of the core stations are located on a raised, 320 m diameter island known as the “Superterp” as shown in Figure 1.6. Similar to the MWA, each LOFAR tile consists of  $4 \times 4$  dual-polarization dipoles with a physical



Figure 1.6: The LOFAR Superterp stations in Dwingeloo, Netherlands from van Haarlem et al. (2013).

dimension of  $5 \text{ m} \times 5 \text{ m}$ . Its FOV can range from  $\sim 2 - 1200^\circ$ , depending on the observing frequency and the station configuration (van Haarlem et al., 2013). The LOFAR international stations are used for forming the sky model, and not for EoR science.

### 1.4.3 Giant Metrewave Radio Telescope (GMRT)

The GMRT is situated near Pune, India and is managed by the National Centre for Radio Astrophysics of India. Unlike other 21 cm experiments instruments, it comprises 30 fully-steerable stationary parabolic antennas, each with a diameter of 45 m, as shown in Figure 1.7. It has two distinct configurations: a compact configuration consisting of 14 antennas distributed within  $1 \text{ km}^2$ , and a Y-shaped configuration for the remaining antennas, yielding a maximum baseline of 25 km. GMRT operates from 150 to 1500 MHz, with six frequency bands centred around 50, 153, 233, 325, 610 and 1420 MHz. It has a total FOV at FWHM of  $\sim 3.8^\circ$  at 150 MHz. Although its unique features means that it can be used for a variety of experiments, the two main scientific goals of GMRT are to detect the EoR signal



Figure 1.7: A lit-up GMRT dish in Pune, India. Credit: SKA.

and to study pulsars (Swarup et al., 1991).

#### 1.4.4 Precision Array for Probing the Epoch of Reionization (PAPER)

PAPER was a low-frequency interferometer consisting of two distinct arrays located in United States of America (USA) and South Africa's Radio Quiet Zone, the Karoo region. The PAPER array in USA comprised 32 antenna-arrays distributed across the National Radio Astronomy Observatory site near Green Bank, West Virginia. The antennas were dual-polarization sleeved dipoles mounted on grounding structures to reduce gain variations arising from the ground conditions (Parsons et al., 2010). The array at this site was mainly used for engineering and field testing purposes. The South African array consisted of a 64 non-steerable antenna-array with dual linear polarization, with a FWHM primary beam of  $60^\circ$ . It operated between 110 - 190 MHz, which was divided into 2048 narrow frequency channels, each of width 48.83 kHz (Pober et al., 2012). The antennas were re-configurable and had operated in both fully-redundant and minimally-



Figure 1.8: A PAPER antenna element that is mounted on a grounding structure. Credit: SKA Africa.

redundant configurations. The latter configuration allowed PAPER to boost its power-spectrum sensitivity but sacrifices its ability to form a reasonable image from the data. PAPER was the precursor to another instrument, the Hydrogen Epoch of Reionization array, and has been decommissioned.

#### 1.4.5 Hydrogen Epoch of Reionization Array (HERA)

HERA is a radio interferometer designed to probe the EoR. It is located in the Karoo region, South Africa, alongside the PAPER and the future SKA-mid. HERA uses information, lessons, and results learnt from MWA and PAPER for its engineering design. The full HERA instrument will be made up of 350 elements operating between 50 to 250 MHz with 1024 frequency channels. Unlike other 21 cm experiments, HERA is made up of non-steerable parabolic dishes that are 14 m in diameter, with a FWHM FOV of  $10^\circ$ . The dishes are packed into a hexagonal grid 300 m across, leading to a total collecting area of  $\sim 54,000 \text{ m}^2$  (DeBoer et al., 2017). The elements are distributed in a highly-redundant configuration to make use of redundant calibration and increased SNR on cosmologically-relevant

modes. HERA also has a split-hexagon configuration, which gives it a boost in its  $uv$  coverage (Dillon & Parsons, 2016).

	<b>MWA</b>	<b>LOFAR</b>	<b>GMRT</b>	<b>PAPER</b>	<b>HERA</b>
<b>FOV at 150 MHz (<math>^{\circ}</math>)</b>	26	10	3.8	60	10
<b>Total collecting area (<math>\text{m}^2</math>)</b>	$\sim 2,800$	$\sim 8,500$	$\sim 48,000$	$\sim 18,000$	$\sim 54,000$
<b>Frequency Range (MHz)</b>	139 - 198	115 - 180	134 - 167	110 - 190	100-200
<b><math>k</math> modes</b>	0.1 - 1	0.4-1.2	0.01	0.5	-
<b>Redundant calibration</b>	Yes	Yes	No	Yes	Yes

Table 1.1: A summary of the specifications of the 21 cm interferometric experiments. Note that HERA has not published any limit so we do not have information on its  $k$  modes.

### 1.4.6 Next Generation Radio Interferometer

The GMRT, MWA, and LOFAR are precursor or pathfinder instruments for another next-generation radio instrument, the Square Kilometre Array (SKA). The SKA is an international collaboration aiming to build the largest radio telescope with an expected  $A_{\text{coll}}$  of a square kilometre. It will have two distinct arrays probing two different frequency ranges: the mid frequency part (SKA-Mid) will be located at the Karoo region alongside PAPER, while the low-frequency part of the future SKA (SKA-low) will be located at the MRO, Western Australia, alongside the MWA. SKA-Low, which is primarily used for EoR science, is expected to have a frequency resolution of 1 kHz with a frequency band of 50 to 200 MHz and a FOV of  $2.5^{\circ}$  -  $10^{\circ}$ . In addition, it will have 13, 000 dipoles in 512 stations with the size of each station being  $\sim 35$  m (Dewdney et al., 2009; Mellema et al., 2013), corresponding to an effective area of  $\sim 300 \text{ m}^2$ . The SKA is thus expected to be around 15 times more sensitive than the MWA, thus potentially allowing for a tomographic study of the EoR bubbles (Mellema et al., 2013).

### 1.4.7 Global 21 cm Experiments

Because the global 21 cm experiment is relatively less complicated than the interferometric 21 cm experiment, here we briefly discuss some of the instruments that are currently online. The Experiment to Detect the Global Epoch of Reionization

Signature (EDGES) experiment is one of the ongoing single-antenna instruments that aim to detect the global 21 cm signal from cosmic dawn and EoR. It operates a low-band (50 - 100 MHz), a mid-band ( $\sim 60 - 150$  MHz) a high-band (90 - 190 MHz) single-antenna instrument and is located at the MRO in Western Australia. The instruments each comprise a radio receiver and a single-polarisation dipole antenna pointed at zenith on top of a  $30 \text{ m} \times 30 \text{ m}$  ground shield. The two instruments are separated by a distance of 150 m and have been online since 2015 (Bowman et al., 2008; Monsalve et al., 2017).

The Broadband Instrument for Global HydrOgen ReioNization Signal (BIGHORNS) is another experiment that shares the same scientific goal. It consists of a broadband biconical antenna that is mounted 52 cm above a  $3 \text{ m} \times 3 \text{ m}$  wire mesh ground screen that operates between 10 to 480 MHz. BIGHORNS has been deployed at three different locations in Western Australia: Muresk, Eyre Bird Observatory (EBO) and Wondinong Station from late 2012 to mid 2014. The BIGHORNS system antenna is expected to be replaced with a conical log spiral antenna that has a FWHM of  $70 - 80^\circ$  at all frequencies and operates between 10 to 300 MHz (Sokolowski et al., 2015).

The Shaped Antenna measurement of the background RAdio Spectrum 2 (SARAS 2) is another instrument that shares the same scientific goal. It is located at the Timbaktu Collective in Southern India. It is a wide-band, wide-field monopole antenna made up of two elements: a circular aluminum disk with a radius of 0.435 m on the ground, and a sphere with a diameter of  $\sim 0.3$  m on top of an inverted cone. The exact size of the disk ensures that only sinusoids of period 350 MHz are produced from the internal reflection of currents. SARAS 2 operates between 40 to 230 MHz with 4096 frequency channels. The antenna has a FWHM beam width of  $45^\circ$  (Singh et al., 2017).

#### 1.4.8 Current Results and Limits

Currently, only one claimed detection has been published by a global 21 cm experiment, while none has been published by interferometric 21 cm experiments.

A claimed detection of signal from the cosmic dawn has been reported by

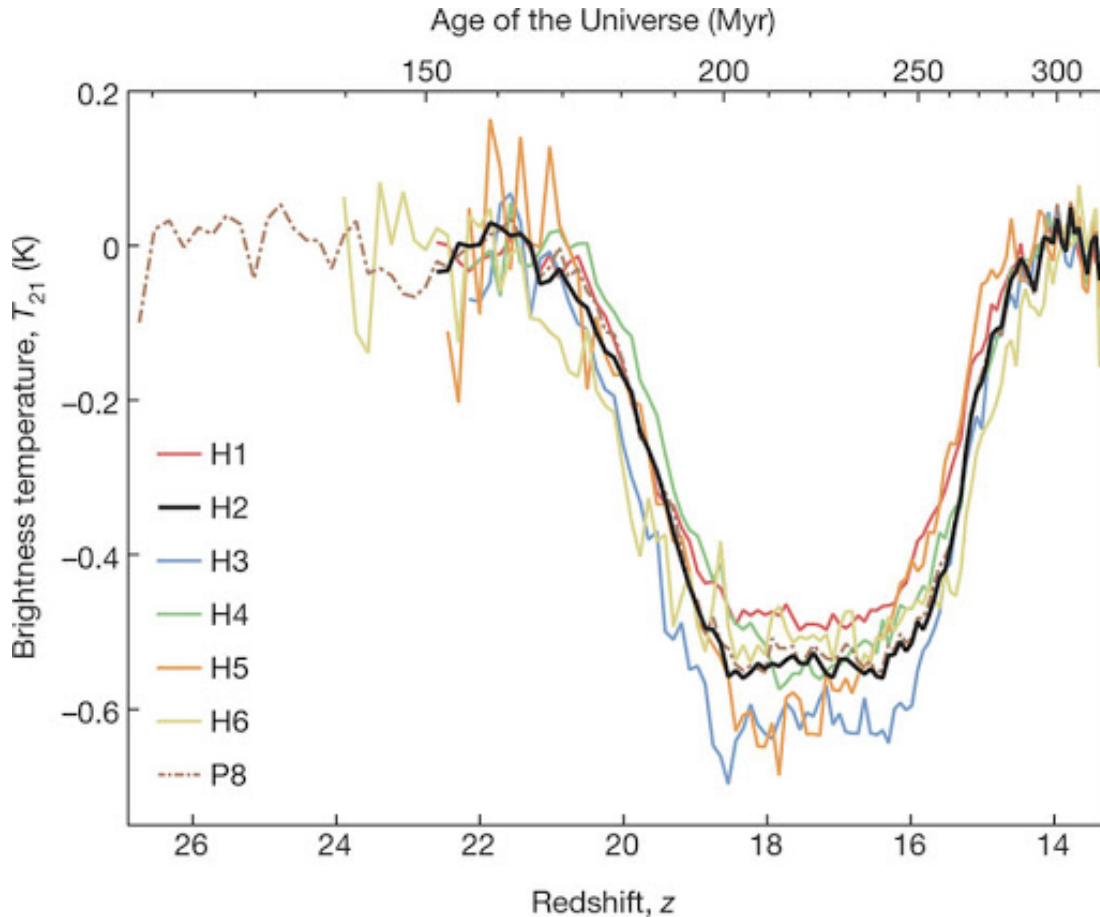


Figure 1.9: The flattened absorption lines from cosmic dawn as reported by Bowman et al. (2018). The different colors correspond to the different hardware configurations used to verify the finding.

Bowman et al. (2018) with the EDGES experiment. EDGES has reported a flattened absorption trough in the globally-averaged spectrum centred at 78 MHz. It has a best-fit FWHM of 19 MHz and an amplitude of 0.5 K, as shown in Figure 1.9. This result has also been tested with multiple hardware configurations. The timing of the profile is fairly consistent with expectations for the 21 cm signal from cosmic dawn, but the best-fit amplitude of the profile is at least a factor of two greater than the largest predictions presented by Cohen et al. (2017). Bowman et al. (2018) provides possible explanations for the absorption trough, which can be achieved if gas and background radiation temperatures decouple as early as  $z \sim 250$  or if dark matter particles have specific mass and cross-sections that can lower the gas temperature; the calculations for the latter are presented in Barkana (2018). The results from EDGES are still awaiting verification from

other independent global 21 cm and low-frequency interferometric experiments.

So far, there is still no reported detection of the EoR signal from any of the 21 cm interferometric experiments. There are, however, several published upper limits from the following experiments: MWA by Dillon et al. (2014), Dillon et al. (2015), Beardsley et al. (2016), Barry et al. (2019), Li et al. (2019a) and Trott et al. (2020); LOFAR by Patil et al. (2017) and Mertens et al. (2020); and GMRT by Paciga et al. (2013). PAPER has initially published a competitive upper limit of  $(22.4 \text{ mK})^2$  at  $z = 8.4$  and  $0.15 h \text{ Mpc}^{-1} \leq k \leq 0.5 h \text{ Mpc}^{-1}$ , but it has since been retracted (Ali et al., 2018) because of unaccounted signal loss (Cheng et al., 2018). A revised set of limits from PAPER have been published by Kolopanis et al. (2019). The current lowest upper limits are presented in Figure 1.10 whereby the blue squares represent the PAPER limit, the green circles, red pentagon, and purple triangle represent the MWA limit, the yellow diamond represent the LOFAR limit, and the black star represent the GMRT limit. The left panel shows the limit with respect to wavenumber, while the right panel is with respect to redshift. The various possible reionisation models from 21CMFAST (Mesinger et al., 2011) (grey lines) are also included to provide a baseline to show where we are now with the upper limits. Notice that we are still a factor of  $\sim 100$  away from observing the EoR, although current experiments are continuously pushing down the limits.

## 1.5 Challenges in 21 cm EoR Experiments

The faint nature of the signal from the early universe, coupled with the many difficulties faced by these experiments, makes 21 cm EoR experiments very challenging. This is why, so far, there is only one reported detection from the cosmic dawn and a null detection of the 21 cm signal from EoR by all the experiments. Here we briefly summarise the main difficulties faced by 21 cm experiments. There are, of course, other difficulties besides those presented below e.g. data processing/size, complexity of the statistical characterization and failure modes in the instrument, but they are considered as second-order effects,

---

<sup>7</sup>[https://github.com/ronniyjoseph/Thesis\\_Plotting](https://github.com/ronniyjoseph/Thesis_Plotting)

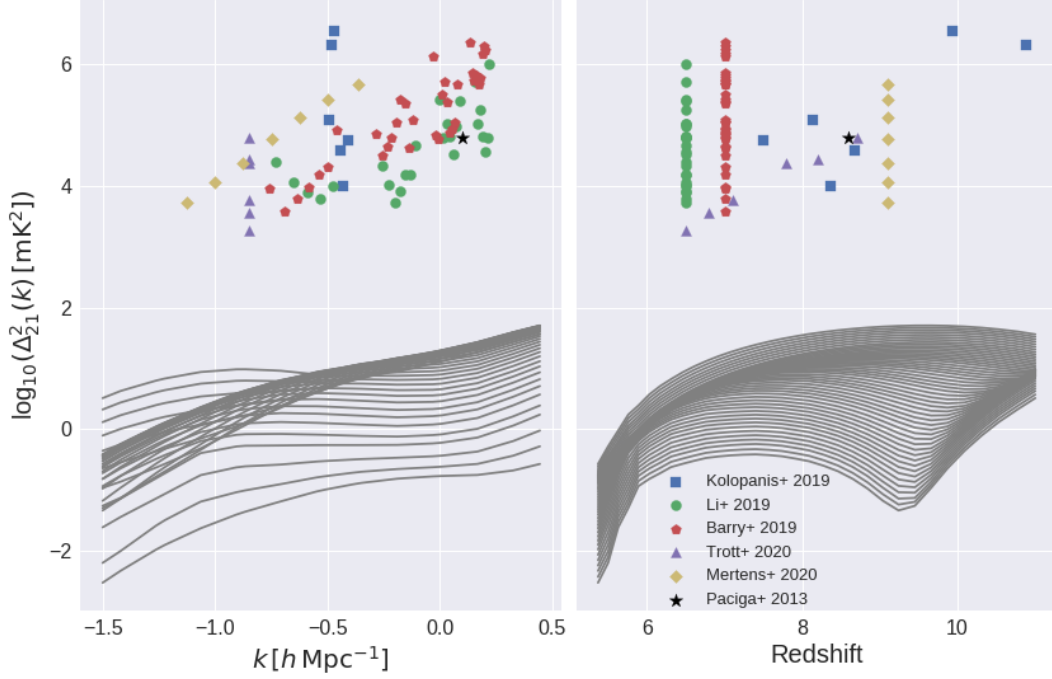


Figure 1.10: Current lowest EoR limits with respect to wavenumber (left panel) and redshift (right panel) from PAPER by Kolopanis et al. (2019) (blue square), MWA by Li et al. (2019a), Barry et al. (2019) and Trott et al. (2020) (green circles, red pentagon, and purple triangle respectively), LOFAR by Mertens et al. (2020) (yellow diamond), and GMRT by Paciga et al. (2013) (black star). The various possible reionisation models from 21CMFAST (Mesinger et al., 2011) (grey lines) are also included for comparison. Credit: R.C. Joseph<sup>7</sup>.

therefore are beyond the scope of this thesis.

### 1.5.1 Foregrounds

The EoR happened between 150 million to 1 billion years after the Big Bang, which means at least 12.8 billion years have lapsed between then and now. The first structures in the universe have since perished and have contributed to, or even evolved into, more complex forms that also produce radiation in the radio regime of the electromagnetic spectrum. Their emission thus contaminates the observation of the EoR signal. These ‘foregrounds’ of galactic and extra-galactic origins are expected to be up to 5 orders of magnitude brighter than the EoR signal (Shaver et al., 1999). They can be categorized into either discrete sources or extended sources.

Discrete foregrounds are generally extra-galactic objects that radiate both thermally and non-thermally. They are mainly made up of star forming galaxies and radio-loud AGN. At  $\nu = 1.4$  GHz, the AGN population dominates the source count for flux density  $S_\nu \geq 0.1$  Jy, while lower  $S_\nu$  range are dominated by star forming galaxies. An example of the Euclidean-normalized differential source count distribution of the two types of point source foregrounds from Mauch & Sadler (2007) are shown in Figure 1.11. Continuum point sources are considered to be one of the most challenging issues to tackle in the search for EoR signal. Because high-redshift radio astronomy is fairly recently established, a complete sky map at low frequency is not available. It is thus hard to completely peel the point sources from the data. Moreover, low brightness, unresolved point sources can contaminate modes in the power spectrum, which we will show later.

Extended foregrounds can originate from both galactic and extra-galactic sources. One important radiative process in extended sources is bremsstrahlung, which directly translates to “braking radiation” in German. In this process, electrons moving through the intergalactic medium suddenly decelerate because of deflection from a different set of charged particles; the loss of kinetic energy thus produces radiation. It is also known as free-free emission because electrons remain free before and after the deflection process instead of being captured. Bremsstrahlung can be classified into three categories: thermal emission, free-free absorption, and relativistic bremsstrahlung (Rybicki & Lightman, 2008). For extended foregrounds, thermal emission from ionised hydrogen clouds (HII regions) is the most relevant type of free-free emission process that can affect the search for the reionisation signal because of its strong emission.

Another source of diffuse foreground comes from synchrotron radiation originating from galactic sources. Synchrotron radiation has been extensively studied since the 1950’s. Also known as magnetobremsstrahlung, this radiation originates from relativistic electrons advancing through plasma (Ginzburg & Syrovatskii, 1965). Synchrotron emission is one of the main contributors of foregrounds in the sky at low radio frequency ( $\sim 70\%$ ), followed by extra-galactic continuum point sources ( $\sim 27\%$ ) (Shaver et al., 1999).

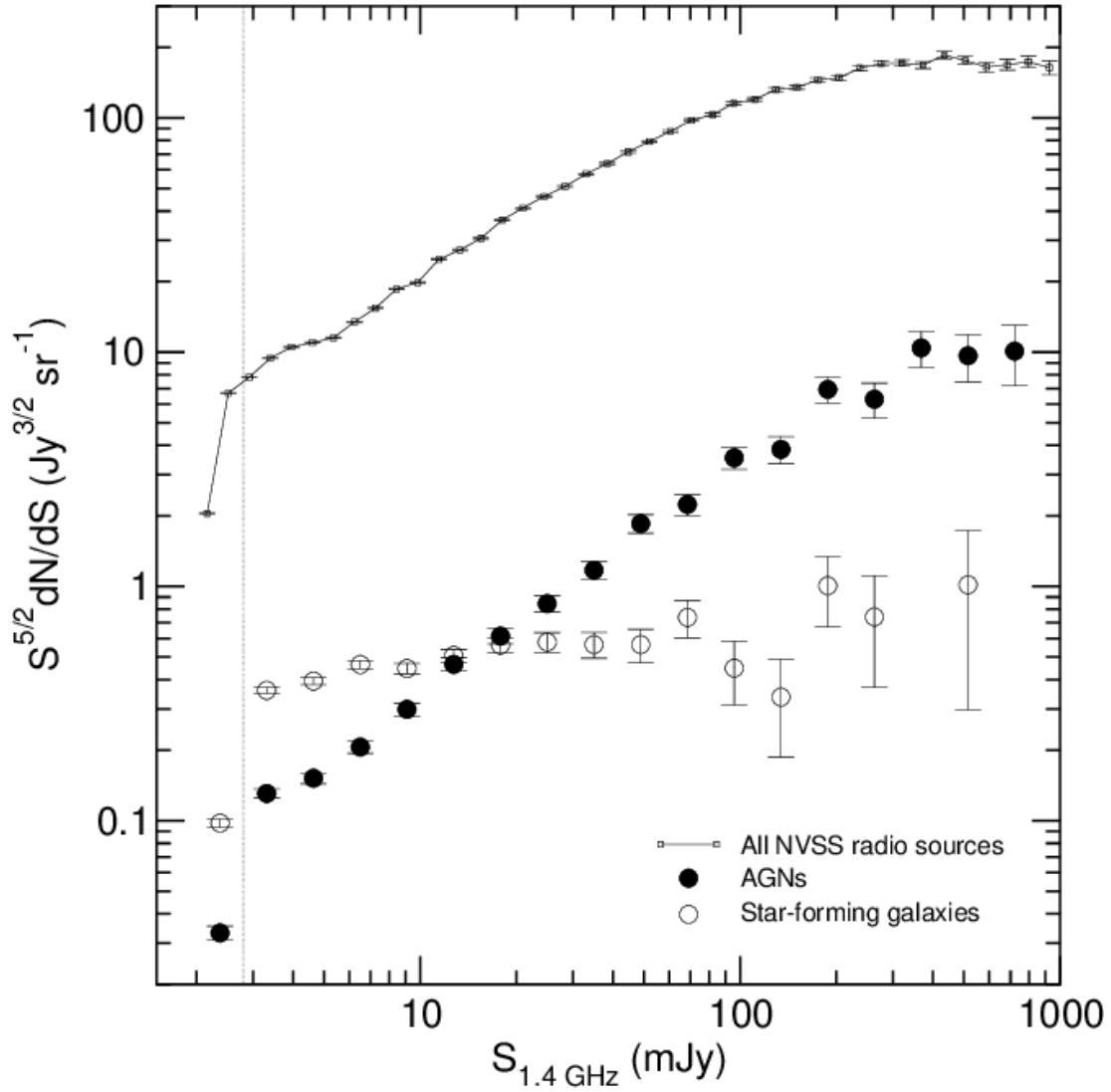


Figure 1.11: The Euclidean-normalized differential source count distribution of AGN (black circle) and star forming galaxies (white circle) from Mauch & Sadler (2007).

Finally, galactic radio recombination lines (RRLs) also contribute to diffuse foregrounds. They are produced by atoms cascading into the lower energy states, effectively emitting photons with the same energy level as the difference in the states. The first RRLs at low radio frequencies were discovered by Pedlar et al. (1978) and although multiple studies have discovered these lines within  $14 \leq \nu \leq 1420$  MHz, RRLs in the frequency range relevant to reionisation studies ( $100 \leq \nu \leq 200$  MHz) are not well studied. Currently, all known RRLs in the low frequency range are limited to carbon transitions. Because their optical depth is comparable to the EoR signal, RRL emissions can easily be mistaken for the 21 cm signal (Peters et al., 2011) and confound the search. To complicate matters, research suggests that the RRL emission transitions into absorption below 150 MHz (Payne et al., 1989).

Both diffuse and point-source foreground emission are a nuisance to the 21 cm reionisation studies because they dominate the sky at lower frequencies. This, coupled with the faint nature of the 21 cm signal and our incomplete sky model, makes the search very challenging. There is, however, one clear difference between the foregrounds and the EoR signal in frequency space that can aid the search; the former is expected to be spectrally smooth, whereas the latter is expected to be “decoherent.” Most research relies on this stark difference to characterize and manage foreground contamination in the data (Shaver et al., 1999; Jelić et al., 2008). When foregrounds are spectrally smooth, they are fully confined to low- $k_{\parallel}$  modes (assuming an appropriate spectral taper function is employed), while the spectrally structured EoR occupies a much larger region of  $k_{\parallel}$ -space, effectively providing a clear ‘window’ into the EoR signal.

However, this simplistic picture is complicated in actual 21 cm experiments, in which baselines sample different  $k_{\perp}$  scales at different frequencies (often dubbed ‘baseline migration’) and introduce extra spectral structure for long baselines. As shown in Figure 1.12, this causes foreground power to smear into the region in the power spectrum that is expected to be dominated by the EoR signal, known as the “EoR window.” This foreground contaminated area that arises from migrating baselines is referred to as the “foreground wedge.”

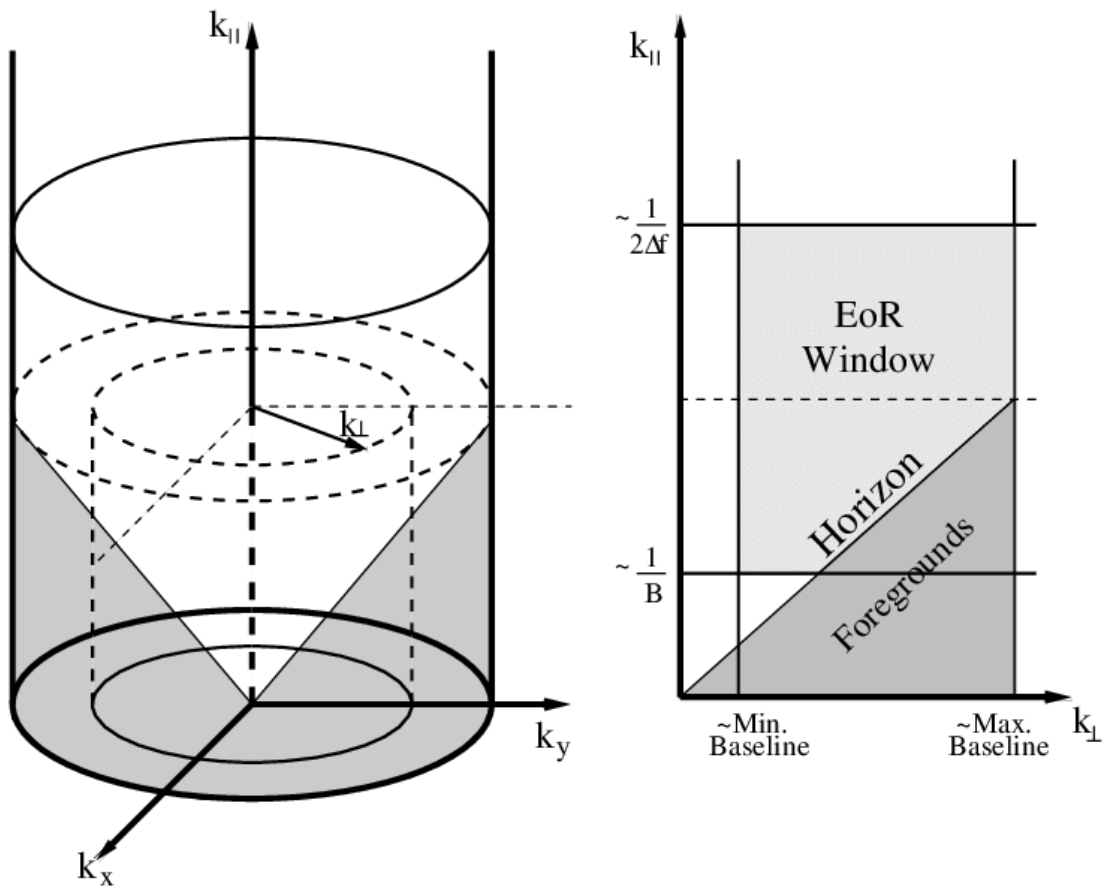


Figure 1.12: The left panel shows the foreground contamination (darker grey region) due to instrumental effects in 3-D and the right panel shows the same region after 2-D averaging from Thyagarajan et al. (2013).

Because foregrounds are a major challenge in the search for the EoR signal, several 21 cm studies have explored different ways to simulate this contaminant. Here, we briefly discuss two methods of simulating foregrounds by Jelić et al. (2008) and FG21CM (Li et al., 2019b).

Jelić et al. (2008) includes both extra-galactic and galactic foregrounds in their simulation intended for LOFAR-EoR experiments. The main component of the galactic foregrounds – the diffuse synchrotron emission – is assumed to have certain amplitude,  $A(x, y, z, \nu)$ , and spectral index,  $\beta$ , that are spatially modelled as 3-D Gaussian random fields.  $T_B$  is then found by integrating  $A(x, y, z, \nu)$  along  $z$  for each  $\nu$ . Moreover, linear polarization is also accounted for by assuming that the Stokes parameters  $Q$  and  $U$  are proportional to the unpolarised  $T_b$ . In addition to synchrotron emission, radiation from supernova remnants is modelled as a power-law in which the spectral index is based on the catalogue of Green (2006). Furthermore, based on the relation between free-free emission and the H $\alpha$  recombination line, the brightness temperature at 120 MHz is set to 2.2 K for a power-law spectrum with an index of -2.15. For extragalactic foregrounds, Jelić et al. (2008) uses the method of Jackson (2005) and simulates Fanaroff–Riley type I (FR I) and FR II radio sources (Fanaroff & Riley, 1974; Jackson & Wall, 1999), along with star-forming galaxies, as point-sources based on the number density and source distributions from Laing et al. (1983)<sup>8</sup> with their clustering drawn from the Rayleigh-Levy random walk by Mandelbrot (1975, 1977). Finally, a foreground contribution from radio galaxy clusters is also included in the simulation based on the publicly-available catalogue from The Hubble Volume Project<sup>9</sup> (Jelić et al., 2008).

Another foreground simulation code that has been more recently developed is FG21sim<sup>10</sup>. Instead of modelling a 3-D map of the synchrotron emission like Jelić et al. (2008), FG21SIM produces a 2-D map of this component based on observations by Giardino et al. (2002) and Haslam et al. (1982) at 408 MHz, with varying spectral index between -2.7 to -2.9. However, it does not include the polarized

---

<sup>8</sup>This catalogue used by Jackson (2005) only reports bright sources, hence an extrapolation of the flux densities are need to go down to sub-mJy range.

<sup>9</sup><http://www.mpa-garching.mpg.de/galform/virgo/hubble>.

<sup>10</sup><https://github.com/liweitianux/fg21sim>

component of Galactic synchrotron radiation. Also, similar to the approach of Jelić et al. (2008), the brightness temperature from free-free emission is simulated based on its relation with  $H\alpha$  found at 30 GHz. However, FG21sim sets its spectral index following a broken power-law with -2.10 for  $\nu \leq 10$  GHz and -2.15 for  $\nu > 10$  GHz (Wang et al., 2010). For extragalactic foregrounds, FG21SIM includes radio clusters by using the PS formalism (Press & Schechter, 1974) to generate dark matter haloes and sophisticated astrophysics that are beyond the scope of this thesis to generate a sky image of their brightness contribution (Li et al., 2019b). Lastly, four discrete extragalactic foreground components are also included based on the work by Wilman et al. (2008): star-forming galaxies (disk-like); radio-quiet AGNs (point-source); FRI and FRII sources (point-like core with extended lobe); and GHz peaked spectrum (GPS) and compact steep spectrum (CSS) AGNs (point-like).

### 1.5.2 Instrumental Systematics

As we have established earlier, radio interferometers are more complicated than single-element radio instruments and its systematics can affect the observation data for 21 cm experiments. Besides migrating baselines, other examples of these interferometric features include: the primary beam responses change between antennas, pointing and polarisation; the dipole array structure yields complex, frequency-dependent beam patterns; and signal transport over coaxial cable can lead to cable reflections which imprints frequency structure into the signal chain (Nasirudin et al., 2020). Furthermore, there are potential extra effects such as cross-talk i.e. artificial signal produced by an interferometer that contaminates the visibilities, thermal drift of receiver noise, and temporary non-redundancy caused by malfunctioning antennas.

In addition, the large FOV introduces wide-field effects that can introduce artefacts in the data if the visibilities or calibrations are not processed correctly (Thompson et al., 2017). Accurately calibrating low-frequency interferometer arrays also requires a full understanding of the elements involved, from the unknown antenna gains and phases to the unknown atmospheric and ionospheric

disturbances (Wijnholds et al., 2010), in addition to complete knowledge of the sky signal.

This list is non-exhaustive and is just meant to provide a brief overview of how complicated radio interferometers are and how instrumental effects can affect 21 cm experiments. The key feature of instrumental systematics is that they can be spectrally non-smooth. This spectral structure couples with the bright (but otherwise smooth) foregrounds and yields power outside the standard foreground wedge. Even very low-level instrumental spectral structure (on the order of 1 part in  $10^5$ ) can completely overwhelm the sought-after signal throughout the window, due to the overwhelming relative amplitude of the foregrounds. Instrumental effects are one of the main challenges in 21 cm experiments, hence it is extremely important that they are properly accounted for in the data analysis step.

### **1.5.3 Radio Frequency Interference (RFI)**

The use of radio waves in human activity has long preceded its use in astronomy. From communication to navigation, there are various applications of radio waves in modern technology. These waves can diffract and reflect depending on their wavelengths, causing interference between different transmitted signals. As such, they can also interfere with the EoR signal and end up in 21 cm experiment observations. Although most RFI comes from human activity, they can also originate from nature e.g. thunderstorms, solar activities (Hamidi et al., 2012), and meteors (Zhang et al., 2018) can produce powerful radio jets.

In interferometric data, the appearance of RFI is usually short-lived in time, and mostly narrow-band in frequency. It also usually occurs in a similar set of channels repeatedly but randomly. Its presence will contaminate the entire EoR window because narrow-band RFI appears like a delta function in frequency. It is thus imperative to get rid of RFI in the observation data and interpolate over the missing channels appropriately.

There are currently a few methods to mitigate and manage RFI in radio astronomy. One important step is to establish radio quiet zones in which strict regulations on radio transmitters and devices are imposed in the area to manage

the RFI level. The first radio quiet zone established for radio astronomy is the United States National Radio Quiet Zone which is located in an area in the borders of Virginia, West Virginia, and Maryland in the USA, and where the NRAO was built. Other global radio quiet zones include the MRAO in Western Australia and the Itapetinga Radio Observatory in Brazil (Cohen et al., 2003).

Despite these efforts, residual RFI can still end up in data because of signal reflection from airplanes (Wilensky et al., 2019), the moon (McKinley et al., 2012, 2018), and satellites (Zhang et al., 2018). To mitigate this issue, data contaminated with RFI are ignored from the data analysis step with help from RFI softwares which essentially search for sudden unnatural ‘jumps’ in time and frequency per antenna. This can be done applying a 2-D high-pass filter on the visibility amplitude, for example, as implemented by the AOFLAGGER software (Offringa, 2010), which is used by the MWA (Offringa et al., 2015) and LOFAR (Offringa et al., 2012). In addition, a filter can be used whereby the frequency ranges that are used commercially, especially those used by Frequency Modulating (FM) radio stations, are removed from the observation data. This method is currently employed by LOFAR to avoid saturating their receivers with RFI (Offringa et al., 2013), which can cause non-linearity in the gains due to saturation outside the RFI channel even though the affected channels have been excluded from the data analysis process.

#### 1.5.4 Ionosphere

The outermost part of the Earth’s atmosphere – the ionosphere– is susceptible to ionisation effects from the sun and cosmic rays. This ionised layer can affect the propagation of radio waves either by scattering radio signal into different directions or by absorbing the signal (Evans & Hagfors, 1968; Davies, 1990). The ionosphere can even emit radio thermal emission (Hsieh, 1966) that can complicate the search for the 21 cm EoR signal. The severity of these effects varies at different timescales and is dependent on a number of factors such as solar activity, solar cycle, and cosmic radiation flux. The phase fluctuations from ionospheric effects can cause scintillation noise that can be of the same order of

magnitude as thermal noise (Vedantham & Koopmans, 2016).

Currently, management of ionospheric effects in reionisation experiments make use of calibration algorithms to correct ionospheric phase errors. This method utilizes either a direction-dependent ionospheric phase calibration algorithm to measure and correct the phase shift of bright sources (Cotton et al., 2004) or source-peeling to model the ionospheric phase shift (Intema et al., 2009). Ionospheric calibration method is, however, computationally expensive and challenging. This gave rise to another method which aims to characterize the ionospheric effects in the data and utilize that information to decide whether to include or ignore the data in the data analysis (Jordan et al., 2017).

## 1.6 Thesis Motivation

The detection of HI signal from cosmic reionisation will revolutionise galaxy formation studies because of the intricate correlation between one and the other. This is because the birth to the first cosmic structures produces the radiation that reionised the IGM. In turn, the process of cosmic reionisation and galaxy formation are both dependent on the linear to non-linear transition of the universe gravitational growth, which sets the initial conditions of the density perturbations that gave formed the first structures in the universe. Because of these correlations, detection of the EoR signal will have a major impact on our understanding of the early universe and how it came to be.

Because of the extreme challenges that have to be overcome to detect the 21 cm signal, understanding the process of reionisation of the universe via simulation is of utmost importance to help narrow down the search. Exploration of the parameters affecting reionisation and quantification of the 21 cm signal are key to help supplement observation by constraining different reionisation models resulting from the different values of these parameters. As such, large-scale simulations that model the formation and evolution of galaxies in the early universe and their effects on the IGM have been extensively used to study the EoR and provide a set of baseline answers to these questions:

- What are the sources of reionisation?
- When did reionisation of the universe commence and conclude?
- What are the parameters that directly affect cosmic reionisation?

So far, simulations have provided us with a rough estimate on the start and end of cosmic reionisation and the global evolution of the signal, among other properties. These theoretical insights have indeed been useful in narrowing down the search for the signal, especially by providing a guideline on the range of frequencies to probe with our instruments.

In reionisation studies, semi-numerical models, which utilize prescriptions to describe astrophysical processes, are generally employed to ensure that the reionisation parameter space can be efficiently sampled in the evaluation process. The numerical approximations used by these models, however, need to align with the results from complete hydrodynamical and radiative transfer simulations. It is, therefore, imperative that the components in both types of simulations are as realistic as possible in order to provide accurate answers to the listed questions and aid 21 cm observations.

One main limitation of large-scale simulations is that they suffer from limited resolution due to the vast volume used, hence the role of small, low mass galaxies in the early stages of reionisation has often been neglected. In addition to this limitation, the effects of realistic foregrounds have not been well studied in works aiming to constrain the astrophysical parameters that influence cosmic reionisation. Moreover, current research has not considered the possibility that there is a correlation between the EoR signal and the foreground sources, even though the foregrounds are the evolutionary descendants of the sources that reionised the universe. The ultimate goal of this PhD thesis, thus, aims to explore and enhance these areas to help supplement future 21 cm observations, especially in the era of the SKA.

# Chapter 2

## Methodology

The main goal of this thesis is to address some first-order limitations of current reionisation studies. This is done via:

- the inclusion of stochasticity and temporal correlation of low-mass haloes in simulations (Chapter 3)
- the exploration of effects of including realistic foregrounds and instrument models in EoR parameter constraints (Chapter 4)
- the study of self-consistent foregrounds from reionisation simulations (Chapter 5)

In this chapter, we present the relevant simulation codes (CUBEP<sup>3</sup>M, GADGET-2, 21CMFAST, and MERAXES), the main statistical metric (the power spectrum), the Bayesian inference method (the Markov Chain Monte Carlo algorithm), and the EoR model discriminating tool (21CMMC) that are employed throughout this thesis to achieve the aforementioned goals, before briefly summarizing the chain that links them together.

### 2.1 Simulation Software

In general, there are two ways to model cosmic reionisation: 1) the output of a cosmological  $N$ -body simulation serves as the input of either a radiative transfer model (when baryons are present) or semi-analytic model (for dark matter only) to simulate the physics of reionisation; or 2) the cosmic-web structures and the astrophysics are both modelled using prescriptions in semi-numerical simulations.

Here, we describe the  $N$ -body simulation codes CUBEP<sup>3</sup>M and GADGET-2, which are used in Chapters 3 and 5 of this thesis respectively, the semi-numerical reionisation model 21CMFAST that is used in Chapter 4, and describe the relevant processes involved in these simulations.

### 2.1.1 CubeP<sup>3</sup>M

CUBEP<sup>3</sup>M is a publicly-available<sup>1</sup> high-performance  $N$ -body code designed to map the temporal evolution of a system of  $N$  particles that only interact gravitationally. It is written in FORTRAN90 and uses the Particle-Particle-Mesh (P<sup>2</sup>M) algorithm whereby clumps of particles are assigned into grids known as a “mesh” of a certain mean density. These density values are then used to solve Poisson’s equation:

$$\nabla^2\phi(\mathbf{x}) = 4\pi G\rho(\mathbf{x}), \quad (2.1)$$

with respect to the particle’s position in the mesh and which mesh it resides in,  $\mathbf{x}$ . Here,  $\phi$  and  $\rho$  are the gravitational potential and mass volume density in the mesh, respectively.

Solving Equation 2.1 in Fourier space yields

$$\tilde{\phi}(\mathbf{k}) = \frac{-4\pi G\tilde{\rho}(\mathbf{k})}{k^2} \equiv \tilde{\omega}_\phi(\mathbf{k})\tilde{\rho}(\mathbf{k}). \quad (2.2)$$

The potential,  $\phi$ , in real space can then be solved using the inverse Fourier Transform and convolution theorem, yielding

$$\phi(\mathbf{x}) = \int \omega_\phi(\mathbf{x}')\rho(\mathbf{x}' - \mathbf{x})d\mathbf{x}'. \quad (2.3)$$

The number of operations to solve ( $O$ ) scales with  $N$  as  $O(N\log N)$  because of the ability to use Fast Fourier Transform (FFT) with the PM method (Harnois-Déraps et al., 2013). In a traditional PM algorithm, because the particles interact with each other through the mean field instead of directly, the small-scale grav-

---

<sup>1</sup>Available on Github at <https://github.com/jharno/cubep3m>

itational interactions that are below the mesh size are suppressed (Hockney & Eastwood, 1988). The P<sup>2</sup>M algorithm resolves this issue by coupling the mean field description on large scales with a direct, suppressed treatment on small scales (Harnois-Déraps et al., 2013).

The CUBEP<sup>3</sup>M code imposes a Cloud-In-Cell (CIC) interpolation for the coarse grid and a Nearest-Grid-Point (NGP) interpolation for the fine grid. The former assumes that the particles are cubes of “clouds” of uniform density with size equal to the grid cell volume, while the latter assumes that the particles are point-like and the entire mass of the particle is assigned to the grid cell that hosts the particle (Hockney & Eastwood, 1988). The halo finder implemented in the code is based on the spherical overdensity algorithm whereby a spherical shell encapsulating the clumps of particles are evolved outwards until the mean density in the shell falls below the overdensity cut-off of 178 in units of mean density, corresponding to a top-hat collapse model (Lacey & Cole, 1994).

CUBEP<sup>3</sup>M also utilizes Message-Passing-Interface (MPI) parallelization in which small cubical sub-volumes are split from the global simulation volume and assigned to a distinct MPI node, where a second cubical division occurs as shown in Figure 2.1. The independent sub-volume tasks that can be done in parallel in the node are known as the tiles. To ensure that the long-range force from the coarse grid and the short-range force from the fine mesh grid can be matched, i.e interpolated, a buffer region is implemented surrounding each tile. This allows CUBEP<sup>3</sup>M to scale well up to 27 000 cores, making the code computationally efficient (Harnois-Déraps et al., 2013).

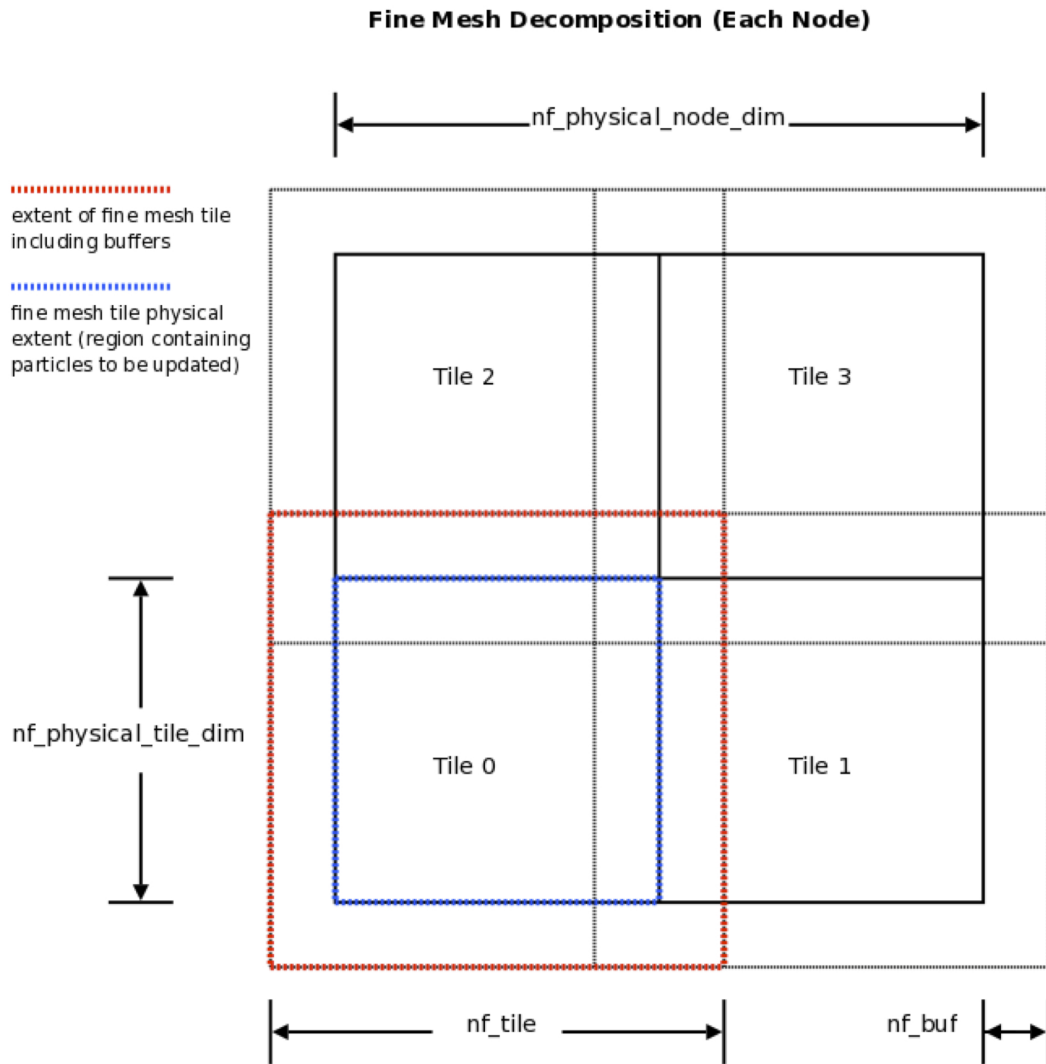


Figure 2.1: 2-D depiction of the CUBEP<sup>3</sup>M code sub-volume decomposition process in each MPI node from Harnois-Déraps et al. (2013). Here,  $nf\_physical\_node\_dim$ ,  $nf\_physical\_tile\_dim$ , and  $nf\_buff$  are the fine-mesh cells in the entire node, fine-mesh cells in the tile, and the buffer region corresponding to 24 fine cells respectively.

### 2.1.2 GADGET-2

GADGET-2 is a cosmological hydrodynamic simulation software that is massively-parallel and publicly-available<sup>2</sup> (Springel, 2005). Although GADGET-2 can simulate both dark matter and gas particles, we limit the discussion to processes that are related to dark matter only because we are only interested in this component in our research.

GADGET-2 uses a hybrid method called TreePM, which combines the PM algorithm with a particle-based approach called the hierarchical tree code algorithm. In the tree method, gravitational interactions are approximated using multipole moments whereby distant particles are grouped into expanding cells known as the “root” nodes. These cells are then recursively divided into smaller daughter cells until only single particles are left in the cells known as leaf nodes. Starting from the root to the leaf, the cells are repeatedly evaluated based on the multipole expansion of the node moments until a suitable partial force is obtained from the tree. Because the particles are not dealt with separately, similar to the PM approach,  $O$  scales with  $N$  as  $O(N\log N)$  for the tree code method. GADGET-2 uses the PM approach on large scale gravitational interactions, and the direct tree approach for short range forces, thus resolving the suppression of small scales issue that PM algorithm has (Springel, 2005).

The particle dynamics can be described by the Hamiltonian,  $H$ , given by

$$H = \sum_i \frac{\mathbf{p}_i^2}{2m_i a(t)} + \frac{1}{2} \sum_{ij} \frac{m_i m_j \varphi(\mathbf{x}_i - \mathbf{x}_j)}{a(t)}. \quad (2.4)$$

Here,  $\mathbf{p}_i$ ,  $m_i$ , and  $\mathbf{x}_i$  are the momentum, mass, and the comoving coordinate vectors of particle  $i$  respectively;  $\varphi$  is the interaction potential between two particles  $i$  and  $j$ , and  $a(t)$  is the universe scale factor from the Friedman-Lemaître model (Springel, 2005). Because GADGET-2 assumes a periodic boundary condition in the simulation cube of a discretized particle system, the mean density is

---

<sup>2</sup>Available at <https://wwwmpa.mpa-garching.mpg.de/gadget/>

subtracted from Equation 2.1, yielding the peculiar potential,  $\phi$ , of

$$\phi(\mathbf{x}) = \sum_i m_i \varphi(\mathbf{x}) \rho(\mathbf{x} - \mathbf{x}_i). \quad (2.5)$$

This is split into two components in the Fourier space,  $\phi(\mathbf{k}) = \phi_{\text{short}}(\mathbf{k}) + \phi_{\text{long}}(\mathbf{k})$ , where,

$$\phi_{\text{long}}(\mathbf{k}) = \phi(\mathbf{k}) e^{-\mathbf{k}^2 r_s^2}, \quad (2.6)$$

whereby  $r_s$  describes the spatial scale of the force split. The short-range component is then solved in real space by noting that for a simulation cube with length,  $L$ , when  $r_s \ll L$ ,

$$\phi_{\text{short}}(\mathbf{x}) = -G \sum_i \phi \frac{m_i}{r_i} \operatorname{erfc} \left( \frac{r_i}{2r_s} \right). \quad (2.7)$$

Here,  $r_i$  is the minimum distance from particle  $i$  to coordinate  $\mathbf{x}$  (Springel, 2005).

### 2.1.3 21cmFAST

21CMFAST is a fast, highly-efficient semi-numerical reionisation simulation code that is publicly-available on Github<sup>3</sup> (Mesinger et al., 2011). It is written in C but has a fully-featured Python wrapper and is based on an existing reionisation code called DEXM (Mesinger & Furlanetto, 2007).

Based on Mesinger & Furlanetto (2007), the initial condition of matter particles, set at  $z = 300$  in 21CMFAST, is assumed to be a linear density field whereby the density field of the universe is described by the *overdensity*,  $\delta(\mathbf{x}) \equiv \rho(\mathbf{x})/\bar{\rho} - 1$ , at coordinate,  $\mathbf{x}$  and mean density in the volume,  $\bar{\rho}$ . In Fourier space, this yields

$$\delta(\mathbf{k}) = \frac{V}{N} \sum \delta(\mathbf{x}) e^{i\mathbf{k} \cdot \mathbf{x}}, \quad (2.8)$$

where  $V$ ,  $N$ , and  $\mathbf{k}$  are the volume of the box, the number of cells in the box, and the Fourier wavevector respectively. The linear density field can be fully represented as a Gaussian field, whose statistical properties are completely described by the power spectrum,  $P(\mathbf{k}) \equiv \langle |\delta(\mathbf{k})|^2 \rangle / V$ . For each independent wavevector,

---

<sup>3</sup>Available at <https://github.com/21cmFAST/21cmFAST>

21CMFAST thus sets

$$\delta(\mathbf{k}) = \sqrt{\frac{VP(k)}{2}}(a_k + ib_k) \quad (2.9)$$

with  $a_k$  and  $b_k$  drawn from a zero-mean Gaussian distribution. It then uses first-order perturbation theory – also known as the Zel’dovich approximation – to move the particle and simulate gravitational collapse, following  $\mathbf{x}_1 = \mathbf{x} + \psi(\mathbf{x})$ , where  $\mathbf{x}$ ,  $\mathbf{x}_1$ , and  $\psi(\mathbf{x})$  are the initial Lagrangian coordinates, updated Eulerian coordinates, and the displacement vector respectively. Because  $\delta(\mathbf{x}) \ll 1$  due to the linearity of the field,

$$\begin{aligned} \delta(\mathbf{x}) &= -\nabla \cdot \{[1 + \delta(\mathbf{x})]\psi(\mathbf{x})\} \\ &\approx -\nabla \cdot \psi(\mathbf{x}); \end{aligned} \quad (2.10)$$

the linear velocity and density fields are thus related by

$$\mathbf{v}(\mathbf{k}, z) = \frac{i\mathbf{k}}{k^2} \dot{D}(z) \delta(\mathbf{k}), \quad (2.11)$$

where  $D(z)$  is the first moment of the linear growth factor that has been normalized such that  $D(0) = 1$ , whereby the differentiation is performed in  $k$ -space. With the first-order Zel’dovich approximation, the velocity field can be separated into a space and time component, therefore the spatial part of the calculation only needs to be performed once for each simulation (Mesinger & Furlanetto, 2007; Mesinger et al., 2011).

The main difference between 21CMFAST and DEXM is in the algorithm to generate the ionisation fields. 21CMFAST bypasses the need to identify halos by using the evolved density field and the conditional Press-Schechter mass function generated by the semi-numeric algorithm FFRT (Zahn et al., 2011), based on the excursion-set formalism (Furlanetto et al., 2004). In this method, ionised cells, whether fully or partially ionised, with collapse fraction,  $f_{\text{coll}}(\mathbf{x}, z, R)$  that is smoothed on decreasing scales from a maximum radius ( $R_{\text{max}}$ ) down to the cell size, are evaluated based on the criterion

$$f_{\text{coll}}(\mathbf{x}, z, R) \leq \zeta^{-1}, \quad (2.12)$$

for some efficiency parameter,  $\zeta$ . If the requirement in Equation 2.12 is satisfied, only the central cells are flagged as ionised (fully or partially), as opposed to the entire spherical region as implemented by DEXM. By skipping the halo-finding and consequently, tree-building procedures, 21CMFAST is able to save some computational time and resources, making the code highly-efficient and extremely fast (Mesinger et al., 2011).

In the remainder of this section, we discuss the computation of relevant astrophysical parameters adopted in 21CMFAST. The brightness temperature calculation employed in 21CMFAST is identical to Equation 4.2. The redshift space distortion effects brought by the term  $dv_r/dr$  are included in this calculation whereby taking the derivative of Equation 2.11 yields

$$\frac{dv_r}{dr}(\mathbf{k}, z) = ik_r v_r(\mathbf{k}, z) \quad (2.13)$$

$$\approx -\frac{k_r^2}{k^2} \dot{D}(z) \delta_{\text{nl}}(\mathbf{k}). \quad (2.14)$$

Additionally,  $T_S$  which is used to compute  $\delta T_B$  is described as

$$T_S = \frac{T_{\text{CMB}}^{-1} + x_\alpha T_\alpha^{-1} + x_c T_K^{-1}}{1 + x_\alpha + x_c}, \quad (2.15)$$

where  $T_\alpha$  is the colour temperature of the gas assumed to be closely coupled to  $T_K$  (i.e.  $T_\alpha \approx T_K$  (Field, 1959)),  $x_\alpha$  is the Wouthuysen-Field coupling coefficient (Wouthuysen, 1952; Field, 1958) from the Lyman- $\alpha$  background of first generation stars, and  $x_c$  is the collisional coupling coefficient. The complete calculation of the Lyman- $\alpha$  background, which affects the calculation of  $T_S$ , is beyond the scope of this thesis. It is however, dependent on the angle-averaged specific intensity,  $J_X(\mathbf{x}, E, z)$ , for photon energy,  $E$ , which is solved by integrating the X-ray specific intensity,  $\epsilon_X(\mathbf{x}, E_e, z')$ , over the lightcone following Greig & Mesinger (2017)

$$J_X(\mathbf{x}, E, z) = \frac{(1+z)^3}{4\pi} \int_z^\infty dz' \frac{c dt}{dz'} \epsilon_X(\mathbf{x}, E_e, z') e^{-\tau} [\text{erg s}^{-1} \text{keV}^{-1} \text{cm}^{-2} \text{sr}^{-1}], \quad (2.16)$$

where  $e^{-\tau}$  is the probability that a photon emitted at an earlier redshift,  $z'$ ,

remains un-absorbed until  $z$  due to IGM attenuation,  $E_e$  is the energy in the emitted time-frame where  $E_e = E(1 + z')/(1 + z)$ , and

$$\epsilon_X(\mathbf{x}, E_e, z') = \frac{L_X}{\text{SFR}}(\mathbf{x}, E_e, z') \rho_{\text{crit},0} \Omega_b f_* (1 + \delta_{\text{nl}}) \frac{df_{\text{coll}}(z')}{dt} [\text{erg s}^{-1} \text{keV}^{-1} \text{cm}^{-3}]. \quad (2.17)$$

Here,  $L_X/\text{SFR}(\mathbf{x}, E_e, z')$  [ $\text{erg s}^{-1} \text{keV}^{-1} M_{\odot}^{-1} \text{yr}$ ] is the specific X-ray luminosity per unit star formation escaping the galaxies,  $\rho_{\text{crit},0}$  is the current critical density, and the terms in the square brackets represent the SFR density along the lightcone.

Based on these calculations, 21CMFAST uses the properties of each cell in the simulation volume to compute the 3-D 21 cm background from  $\delta T_B$ , which is given by Furlanetto et al. (2006b) in Equation 4.2. The full evolution of the 21 cm signal is available either as a complete lightcone or separate volumes at each redshift. The results from 21CMFAST matches well with hydrodynamical simulation from Trac et al. (2008) down to scales which are relevant for current and upcoming 21 cm experiments ( $\gtrsim 1$  Mpc) (Mesinger et al., 2011). This agreement, along with 21CMFAST's ability to generate the full reionisation history of large simulation volumes in a fast and efficient manner, makes the code extremely valuable for reionisation studies.

### 2.1.4 MERAXES

The semi-analytic model MERAXES from the Dark-ages Reionization And Galaxy Observables from Numerical Simulation (DRAGONS) project<sup>4</sup> is designed to study the formation of galaxies and their effects during the EoR (Mutch et al., 2016). It uses the output from an  $N$ -body simulation to populate the centre of the dark matter haloes with galaxies. The properties of the haloes are then used to model astrophysical processes related to galaxy formation and evolution, which include gas infall and cooling, star formation, AGN and supernova feedback, metal enrichment, reionisation feedback and black hole growth. In this work, we use the latest version of MERAXES with updates in the black hole growth and supernova

---

<sup>4</sup><http://dragons.ph.unimelb.edu.au/>

feedback introduced by Qin et al. (2017b) and Qiu et al. (2019) respectively. We discuss the astrophysical processes that are most relevant to our work below.

MERAXES embeds each newly-formed galaxy with a central black hole of mass  $10^3 M_\odot h^{-1}$  (Qin et al., 2017b). Black hole growth is dependent on the reservoirs of hot gas in the halo component and cold gas in the disk component of the galaxy, whereby black holes grow via radio mode for the former and quasar mode for the latter (Croton et al., 2016).

Hot gas from the galaxy reservoir is accreted at the Bondi-Hoyle accretion rate ( $\dot{M}_{\text{Bondi}}$ ) of

$$\dot{M}_{\text{Bondi}} = \left( \frac{2.5\pi G^2}{c_s^3} \right) M_\bullet^2 \rho_{\text{hot}}, \quad (2.18)$$

where  $G$  is the gravitational constant,  $c_s$  is the speed of sound,  $M_\bullet$  is the black hole mass and  $\rho_{\text{hot}}$  is the density of the hot gas reservoir.

The growth of black hole, however, is limited by the Eddington limit,  $M_{\text{Edd}}$ . This value is found by integrating the Eddington accretion rate,  $\dot{M}_{\text{Edd}}$ , over a time interval,  $\Delta t$ .  $\dot{M}_{\text{Edd}}$  is related to the Eddington luminosity limit,  $L_{\text{Edd}}$ , by  $\dot{M}_{\text{Edd}} = L_{\text{Edd}}/(0.1c^2)$  whereby

$$L_{\text{Edd}} \equiv M_\bullet \left( \frac{4\pi G m_p c}{\sigma_T} \right). \quad (2.19)$$

Here,  $m_p$ ,  $c$ , and  $\sigma_T$  are the mass of a proton, the speed of light, and the Thomson scattering cross-section of the electron. The integration thus leaves us with

$$M_{\text{Edd}} = M_\bullet \left[ \exp \left( \frac{\epsilon \Delta t}{\eta t_{\text{Edd}}} - 1 \right) \right], \quad (2.20)$$

where  $\epsilon$ ,  $\eta$ , and  $t_{\text{Edd}}$  are the Eddington ratio (assumed to be 1), fraction of accreted mass that is radiated, and the Eddington accretion time-scale ( $t_{\text{Edd}} \equiv \frac{\sigma_T c}{4\pi G m_p}$ ) respectively. Note that in Equation 2.20,  $\Delta t$  is the time interval between two snapshots and that  $M_\bullet$  is the mass of black hole at the start of the time

interval. The growth in mass in radio mode is given by

$$\Delta M_{\bullet}^{\text{radio}} = (1 - \eta) \min \left( M_{\text{hot}}, M_{\text{Edd}}, k_h \dot{M}_{\text{Bondi}} c^2 \right), \quad (2.21)$$

where  $k_h$  is a free parameter that modifies the efficiency of the growth because not all black holes accrete at the full Bondi-Hoyle rate.

The accretion of cold gas from the galaxy reservoir is triggered by a galaxy-galaxy merger or disk instability. The growth in mass in quasar mode is assumed to be accreted at  $\dot{M}_{\text{Edd}}$  and is given by (Qin et al., 2017b)

$$\Delta M_{\bullet}^{\text{quasar}} = \min \left[ M_{\text{cold}}, M_{\text{Edd}}, \frac{k M_{\text{cold}}}{\left( 1 + \frac{280 \text{ km s}^{-1}}{V_{\text{vir}}} \right)^2} \right], \quad (2.22)$$

where  $V_{\text{vir}}$  is the virial velocity of the dark matter halo in the galaxy and  $k$  is a free parameter that modifies the growth in quasar mode<sup>5</sup>.

Moreover, MERAXES assumes that stars are only formed if  $M_{\text{cold}}$  is greater than the critical mass,  $M_{\text{crit}}$ , which is given by

$$M_{\text{crit}} = \Sigma_{\text{SF}} \left( \frac{V_{\text{max}}}{100 \text{ km/s}} \right) \left( \frac{r_{\text{disk}}}{10 \text{ kpc}} \right) 10^{10} M_{\odot}. \quad (2.23)$$

Here,  $\Sigma_{\text{SF}}$  is a free parameter,  $V_{\text{max}}$  is the maximum circular velocity of the host halo, and  $r_{\text{disk}}$  is the disk scale radius, which is defined as  $r_{\text{disk}} = 3R_{\text{vir}} \frac{a}{\sqrt{2}}$ , where  $R_{\text{vir}}$  is the virial radius of the host halo and  $a$  is the spin parameter. The mass of newly-formed stars,  $\Delta M_{\star}$ , is then given by

$$\Delta M_{\star} = \alpha_{\text{SF}} \left( \frac{M_{\text{cold}} - M_{\text{crit}}}{t_{\text{dyn,disk}}} \right) \Delta t \quad (2.24)$$

where  $\alpha_{\text{SF}}$  is a free parameter that sets the star formation efficiency, and  $t_{\text{dyn,disk}}$  is the dynamical time of the disk that is defined by  $t_{\text{dyn,disk}} = r_{\text{disk}}/V_{\text{max}}$ .

---

<sup>5</sup> $k$  is proportional to the merger ratio for merger-triggered growth.

In addition, the reionisation model adopted by MERAXES is based on 21CM-FAST (Mesinger et al., 2011; Mesinger et al., 2014). In this model, reionisation processes and galaxy evolution are self-consistently evolved from the start of the halo merger history. It uses the excursion set formalism to find ionised regions when the resulting number of ionising photons is greater than the number of absorbed and recombined photons following

$$N_{b\star}(r)N_{\gamma}f_{\text{esc}} \geq (1 + \bar{N}_{\text{rec}})N_{\text{atom}}(r). \quad (2.25)$$

Here,  $N_{b\star}(r)$ ,  $N_{\gamma}$ ,  $\bar{N}_{\text{rec}}$  and  $N_{\text{atom}}$  are the respectively the numbers of stellar baryon in a sphere of radius  $r$ , ionising photons emitted per stellar baryon, mean recombination per baryon, and atoms being ionised within the same volume, and  $f_{\text{esc}}$  is the escape fraction of the emitted photons.

Helium is assumed to be singly ionised at the same rate as hydrogen, hence Equation 2.25 can be re-written in terms of the integrated stellar mass ( $M_{\star}(r)$ ) and total mass ( $M_{\text{tot}}(r)$ ) within the volume, yielding (Mutch et al., 2016)

$$\frac{M_{\star}(r)}{m_p}N_{\gamma}f_{\text{esc}} \geq (1 + \bar{N}_{\text{rec}})\frac{f_b(1 - \frac{3}{4}Y_{\text{He}})M_{\text{tot}}(r)}{m_p}, \quad (2.26)$$

where  $Y_{\text{He}}$  is the helium mass fraction, and  $f_b$  is cosmic baryon fraction,  $f_b = \Omega_b/\Omega_m$ . The term  $(1 - \frac{3}{4}Y_{\text{He}})$  corresponds to the combined number of hydrogen and helium atoms per baryon.

The calculation of  $\delta T_B$  in MERAXES follows the calculation from Furlanetto et al. (2006b) but assumes it to be saturated i.e the kinetic temperature of the gas is much larger than the temperature of the CMB. MERAXES outputs the 3-D tomography of the 21 cm signal, along with a comprehensive dataset detailing the galaxy properties, over the entire history of the simulation. The self-consistent treatment of processes governing reionisation and galaxy formation in MERAXES allows for a realistic study of the correlation between them.

## 2.2 Power Spectrum

The power spectrum is the primary metric used to quantify the cosmic reionisation signal because of the signal’s partially<sup>6</sup> Gaussian property and faint nature. As briefly mentioned in §1.3.4, it measures the variance of a signal over a volume. For a simulation cube with periodic boundary conditions, the power spectrum can be simply computed by taking a FFT over the 3-D volume of the simulation box, and then spherically averaging the resulting Fourier-space cube.

In practice, however, we do not observe noiseless periodic cubic regions of the sky sampled at regular intervals. Real observations are made in volumes that have complex window functions – due to the primary beam and bandpass of the instrument – and are sampled differently in angular and line-of-sight dimensions, dependent on the physical layout of the array and its frequency sampling characteristics. If the simple power spectrum gained from Fourier-transforming a periodic simulation can be considered the ‘true’ power spectrum, then real observations are ‘estimates’ of this true spectrum, and many analysis techniques have been finely honed to improve the robustness of this estimate (Liu et al., 2014). It is therefore crucial, when analysing the ability of an instrument to obtain estimates of astrophysical parameters via their influence on this power spectrum estimate, to forward-model this ‘estimated’ power spectrum with all of its realistic instrumental effects. Such a procedure can be divided into two separate parts: forward-modelling and data-reduction.

### Forward-modelling steps

1. Convolution of instrumental beam with the simulation
2. 2-D FFT over the ‘angular’ or ‘perpendicular’ modes of the (mock) observation volume to obtain a grid of visibilities (critical)

---

<sup>6</sup>Being spherically-averaged, the power-spectrum is able to produce higher signal-to-noise on the inherently faint signal than metrics which do not integrate over phase information. While this comes with a trade-off in that the power spectrum is insensitive to non-Gaussianity in the spatial fluctuations, a significant fraction of the information in the field is captured by the Gaussian approximation.

3. Evaluation/interpolation of uniform grid of visibilities onto discrete baseline locations of the actual instrument per frequency
4. Addition of all instrumental systematics, including thermal noise, to the visibilities

The forward-modelling part involve steps that are taken to simulate data that looks like the expected observed visibilities. The first and second steps are represented by Equations 1.22 and 1.23 in §1.4. Note that steps 2 and 3 can be combined by using a direct Fourier Transform at each baseline location instead of a FFT. However, it requires that the observation be treated as discrete point sources and, thus, can be quite slow because discrete FT has  $O \sim N^2$  rather than  $N \log N$ . On the other hand, sampling the visibilities onto the baseline locations can also be memory-intensive and time-consuming due to the need for 2-D interpolation.

### **Data-reduction steps**

1. Re-gridding i.e. arranging and averaging the visibilities on a regular 2-D grid of  $\mathbf{k}_\perp$ , at each frequency slice
2. Application of a frequency taper (optional)
3. 1-D FFT over the frequency dimension of the gridded visibilities
4. Spherical or cylindrical averaging of the volume

The steps listed in the data-reduction part are generally the same ones that are used on real observation data. Step 1 can be non-trivial depending on the treatment of the visibilities. One simple gridding method that can be applied is by incoherently summing the visibilities whereby all baselines that fall in a particular  $k$ -cell are assumed to be located at the centre of the cell. However, depending on how large the cells are and how well-sampled the  $k$  modes are, the baselines may contribute to a different cell because they ‘migrate’ with frequency following  $\mathbf{k}_{\perp,i} = (\nu/\nu_0)\mathbf{k}_{\perp,i,0}$  for spatial Fourier mode  $\mathbf{k}_{\perp,i,0}$  at previous frequency,

$\nu_0$ .

As a result, *sharp steps* in frequency may be induced in the resulting averaged visibilities because the transition of a baseline out of a cell is instantaneous. As we have mentioned in §1.5.1, 21 cm experiments rely on the spectral smoothness of the foregrounds in frequency space to distinguish between foregrounds and the “lumpy” EoR signal. This is the motivation behind doing the forward-modelling and data-reduction steps with utmost care so that no artificial structure is introduced.

To mitigate the issue arising from the sharp spectral structure of foregrounds, a smooth gridding kernel can be applied. This means that each baseline contributes some of its visibility to each cell in the grid, with the actual percentage being dependent on the position of the cell relative to the baseline, and the visibilities at each cell centre can be added coherently.

Mathematically, the optimal gridding kernel to apply is the Fourier-transform of the primary beam<sup>7</sup> (Hazelton et al., 2013),  $\tilde{B}(x_{\parallel}, \mathbf{k}_{\perp})$ , where the weight at cell  $j$  for baseline  $i$ ,  $w_{ij}(\nu) = \tilde{B}(x_{\parallel}, \mathbf{k}_{\perp,j} - (\nu/\nu_0)\mathbf{k}_{i,0})$ . The gridded visibility at cell  $j$ ,  $V_{\text{grid}}(\mathbf{k}_{\perp,j}, x_{\parallel})$ , for comoving distance,  $x_{\parallel}$ <sup>8</sup>, is given by

$$V_{\text{grid}}(\mathbf{k}_{\perp,j}, x_{\parallel}) = \frac{\sum_{i=0}^{N_{\text{bl}}} w_{ij} V(\mathbf{k}_{\perp,i}, x_{\parallel})}{\sum_{i=0}^{N_{\text{bl}}} w_{ij}}, \quad (2.27)$$

where  $N_{\text{bl}}$  is the number of all included baselines. For convenience, we let  $W_j = \sum_{i=0}^{N_{\text{bl}}} w_{ij}$ .

To further aid readers in understanding this step, we visualize it in Figure 2.2 for a simplified 2-D grid with  $4^2$  cells, 2 baselines, and a Fourier Gaussian

<sup>7</sup>It can be seen via the convolution theorem and Equation 1.23 that each baseline “sees” a windowed patch of the Fourier-transformed sky, with the window corresponding to the FT of the primary beam (Tegmark, 1997)

<sup>8</sup>This is inversely proportional to  $\nu$  and proportional to  $z$ .

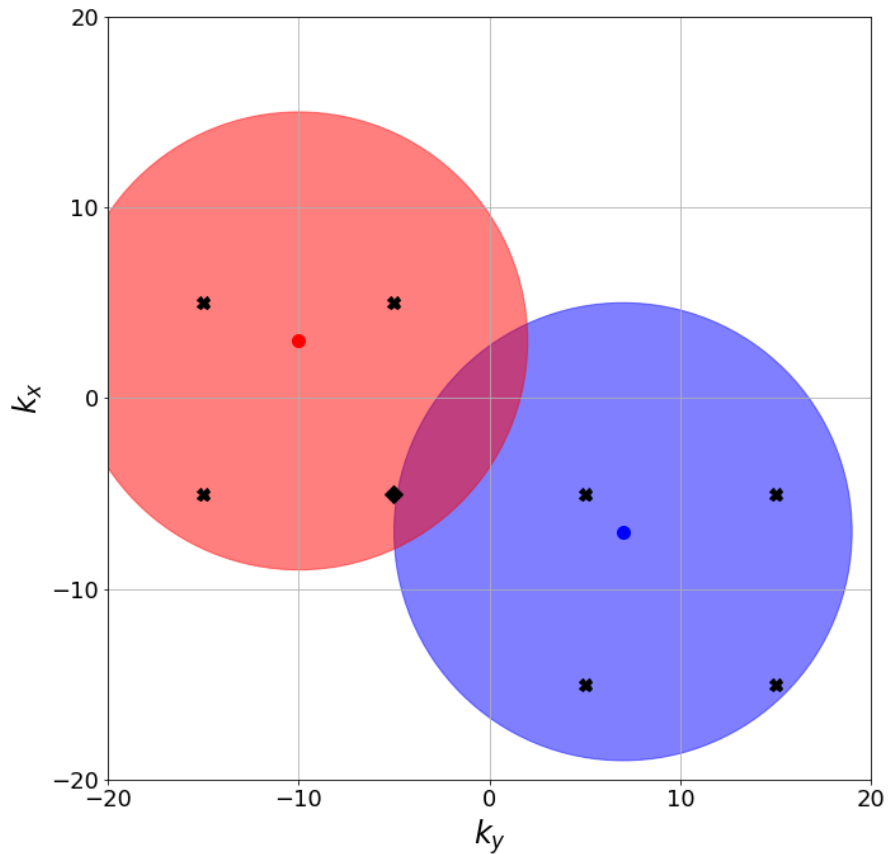


Figure 2.2: 2-D depiction of the gridding process involving a Gaussian gridding kernel for  $4^2$  grid cells with 2 baselines. The different coloured regions correspond to the visibilities convolved with the normalized gridding kernel, with the actual position of the baseline represented by the coloured circles. The centre of cells that receive contributions from the convolved visibility are shown by the black crosses. At the centre of the cell in which both baselines contribute to the visibility (diamond marker), the convolved values are coherently averaged to give the final visibility of that cell, based on Equation 2.27.

beam gridding kernel. The different coloured regions correspond to the visibilities convolved with the normalized gridding kernel, with the actual position of the baseline represented by the coloured circles. The centre of cells that receive contributions from the convolved visibility are shown by the black crosses. At the centre of the cell in which both baselines contribute to the visibility (diamond marker), the convolved values are coherently averaged to give the final visibility of that cell.

Next, a frequency taper can be applied before performing a 1-D FFT along the frequency axis. The taper is necessary to reduce spectral leakage in the side lobes due to the limited bandwidth (Thyagarajan et al., 2013) which can contaminate the EoR window (Morales & Hewitt, 2004), which is shown in Figure 1.12. In this research, we use the Blackman-Harris taper which has a correlation length of 4 cells.

Finally, the visibility cube is cylindrically or spherically averaged to give the 2-D or 1-D power spectrum respectively. For the 2-D power spectrum,  $P(k_{\perp}, k_{\parallel})$ , this involves binning the gridded cell,  $\mathbf{k}_{\perp,j}$ , based on the radial bin,  $k_{\perp}$ , and finding the average following

$$P(k_{\perp}, k_{\parallel}) \equiv \frac{\sum_{j=0}^{\mathbf{k}_{\perp,j} \in k_{\perp}} W_j^2 V_{\text{grid}}^{\dagger}(\mathbf{k}_{\perp,j}, x_{\parallel}) V_{\text{grid}}(\mathbf{k}_{\perp,j}, x_{\parallel})}{\sum_{j=0}^{\mathbf{k}_{\perp,j} \in k_{\perp}} W_j^2}, \quad (2.28)$$

where  $\dagger$  denotes the conjugate, and

$$V_{\text{grid}}(\mathbf{k}_{\perp}, k_{\parallel}) = \int V_{\text{grid}}(\mathbf{k}_{\perp}, x_{\parallel}) \phi(x_{\parallel}) \exp(-2\pi i k_{\parallel} \cdot x_{\parallel}) dx_{\parallel}, \quad (2.29)$$

with frequency taper,  $\phi(x_{\parallel})$ , and Fourier dual of the  $x_{\parallel}$ ,  $k_{\parallel}$ .

The convolution of  $V_{\text{grid}}(\mathbf{k}_{\perp,j}, k_{\parallel})$  with  $V_{\text{grid}}^{\dagger}(\mathbf{k}_{\perp,j}, k_{\parallel})$  in Equation 2.28 is not limited to a conjugate of itself; in fact, 21 cm experiments often use  $V_{\text{grid}}(\mathbf{k}, k_{\parallel})$  from different observations that are statistically identical (i.e. same pointing) to cancel the contribution of instrumental noise in the power spectrum because while

the signal remains unchanged from multiple observations at the same epoch, the noise is uncorrelated. In Chapter 4, however, we use the  $V_{\text{grid}}(\mathbf{k}_{\perp}, k_{\parallel})$  from the same observation to calculate the power spectrum.

## 2.3 Parameter Estimation

Estimating cosmic reionisation parameters is a non-trivial pursuit because of the relatively unknown nature of the early universe. In this section, we summarize the well-known statistical method, the Markov Chain Monte Carlo, and its application in constraining the parameters of reionisation via the tool, 21CMMC.

### 2.3.1 Markov Chain Monte Carlo

The Markov Chain Monte Carlo (MCMC) method was first introduced by Metropolis et al. (1953) and was later made general by Hastings (1970) with the method known as the Metropolis-Hastings algorithm. It combines repeated sampling of random realizations (Monte Carlo) with the ansatz that the probabilities of these realizations are only dependent on the probability at the previous state (Markov Chain) to obtain numerical results on the expectation and variance of functions under this distribution. This method involves a proper sampling of the posterior Probability Density Function (PDF) of the models generated via a random walk, and using the PDF or some likelihood function to analyse the distribution data.

Suppose that the target PDF,  $P(x)$ , for which we would like to sample is related to another function,  $P^*(x)$ , such that

$$P(x) = \frac{P^*(x)}{Y}, \quad (2.30)$$

for multiplicative variable,  $Y$ , and state or position  $x$ . The original MCMC method, the Metropolis-Hastings algorithm, attempts to solve  $P(\mathbf{x})$  by proposing a density  $Q$  which is dependent on current state  $x(t)$  and proposed state  $x'$ . Note that  $Q$  is not required to be similar to  $P$ , and can be modelled for example, by a simple Gaussian distribution around  $x(t)$ . The samples are evaluated based on

the quantity,  $q$ , which is the multiplied ratios of the densities given by

$$q = \frac{P^*(x')}{P^*(x(t))} \frac{Q(x(t)|x')}{Q(x'|x(t))}. \quad (2.31)$$

Notice that we do not have to solve for  $Y$  because it is cancelled out in Equation 2.31 (MacKay, 2003).

The sample is accepted if  $q \geq a_f \in (0, 1]$ , whereby at the next step,  $x(t+1)$  is set to  $x'$ ; otherwise, the previous value is kept i.e.  $x(t+1) = x(t)$ . The accepted sample of states are thus *not* independent. The minimum number of iterations that give a sample which is independent of the initial sample is known as the auto-correlation time,  $\tau$ , and is generally given by  $\tau \simeq (L/\epsilon)^2$ , where  $L$  is the largest length scale of the accepted states, and  $\epsilon$  is the step size (MacKay, 2003). The first and second moment of  $P(x)$  can therefore be computed from the set of accepted, independent samples. The Metropolis-Hastings algorithm forms the basis of MCMC method but some minor adjustments may be added to simplify the process, giving rise to other specialized MCMC algorithms.

One such modification was introduced by Goodman & Weare (2010) which made use of a set of sampling algorithm that are linearly invariant. This method involves an ensemble of  $K$  walkers,  $S = \{x_k\}$ , that are simultaneously evolved whereby  $Q$  of one walker  $k$  is chosen based on the current position of the  $K - 1$  walkers in the complementary ensemble,  $S_{[k]} = \{x_j; \forall j \neq k\}$ .  $x_k(t)$  is updated by drawing a walker,  $x_j$ , randomly from  $S_{[k]}$  using the “stretch move”, where

$$x' = x_j + Z[x_k(t) - x_j]. \quad (2.32)$$

Here, the scaling variable,  $Z$ , is drawn from a density distribution,  $g(Z = z)$ , which is symmetric if  $g(\frac{1}{z}) = zg(z)$ , therefore the chain satisfies the detailed balance  $P(x_k(t) \rightarrow x') = P(x' \rightarrow x_k(t))$ . Goodman & Weare (2010) sets  $a = 2$  for

$$g(z) \propto \begin{cases} \frac{1}{\sqrt{z}} & \text{if } z \in [\frac{1}{a}, a], \\ 0 & \text{otherwise,} \end{cases} \quad (2.33)$$

and the evaluation quantity is given by

$$q = Z^{N-1} \frac{P^*(x')}{P^*(x_k(t))}, \quad (2.34)$$

for  $N$ -dimensional parameter space. Because the proposed states are *not* random as in the traditional MCMC method, with this algorithm, less iterations are needed to yield an independent set of samples, resulting in a lower  $\tau$ .

### 2.3.2 21cmMC

21cMMC is a publicly-available<sup>9</sup> MCMC reionisation analysis tool that is designed to statistically compare a mock observation to the 3-D tomographic maps generated by 21cmFAST. 21cMMC makes use of a PYTHON wrapper to enable the use of the highly-efficient, parallelized MCMC module EMCEE (Foreman-Mackey et al., 2013), which implements the basic Metropolis-Hastings algorithm and the affine invariant sampling method discussed in the previous section within a parallelized environment.

The likelihood statistic used in 21cMMC is the 1-D 21 cm power spectrum and the uncertainty in 21cMMC’s quantitative evaluation is based on the noise profiles of the low-frequency interferometers which are computed by 21cmSENSE (Pober et al., 2013; Pober et al., 2014), whereby

$$\Delta_{21}^2(k) \approx X^2 Y \frac{k^3}{2\pi} \frac{\Omega'}{2t} T_{\text{sys}}^2 [\text{mK}^2]. \quad (2.35)$$

Here,  $X^2 Y$ ,  $\Omega'$ , and  $t$  are the cosmological normalization that depends on the observing bandwidth and redshift, the beam-dependent normalization based on Parsons et al. (2014), and the cumulative time spent by all baselines within a certain  $k$  mode, respectively. A fiducial value of 20% modelling uncertainty is added in quadrature with the total noise power spectrum in Equation 2.35. 21cMMC uses 21cmFAST to model the astrophysics and cosmology, which has been explained in §2.1.3.

Recall from Chapter 1 that  $T_{\text{vir}}$  is proportional to  $M_{\text{min}}$  and in the literature,

---

<sup>9</sup><https://github.com/21cmFAST/21cMMC>

$M_{\min}$  is commonly assumed to be  $\sim 10^8 M_{\odot}$ , yielding  $T_{\text{vir}} \sim 10^4$  K. In 21CMFAST,  $T_{\text{vir}}$  and  $M_{\min}$  are, in fact, related via

$$M_{\min} = 10^8 h^{-1} \left( \frac{\mu}{0.6} \right)^{-3/2} \left( \frac{\Omega_m \Delta_c}{18\pi^2 \Omega_m^z} \right)^{-1/2} \left( \frac{T_{\text{vir}}}{1.98 \times 10^4} \right)^{3/2} \left( \frac{1+z}{10} \right)^{-3/2} M_{\odot}, \quad (2.36)$$

where  $\mu$  is the mean molecular weight,  $\Omega_m^z = \Omega_m(1+z)^3 / [\Omega_m(1+z)^3 + \Omega_{\Lambda}]$ , and  $\Delta_c = 18\pi^2 + 82(\Omega_m^z) - 39(\Omega_m^z)^2$ . The 21CMFAST component in 21CMMC allows the critical temperature threshold,  $T_{\text{vir}}$ , to vary within a user-specified range which can be larger than  $10^4$  K.

The implementation of 21CMFAST used by 21CMMC describes the ionising threshold,  $\zeta$ , from Equation 2.12 as

$$\zeta = \left( \frac{f_{\text{esc}}}{0.3} \right) \left( \frac{f_{\star}}{0.05} \right) \left( \frac{N_{\gamma}}{4000} \right) \left( \frac{2}{1+n_{\text{rec}}} \right). \quad (2.37)$$

Here,  $n_{\text{rec}}$  is the typical number of times a hydrogen atom recombines and  $\zeta$  is essentially the UV ionising efficiency of high-redshift galaxies.

In the implementation of 21CMFAST used by 21CMMC, the quantity  $L_X$  from Equation 2.17 is assumed to be a power-law,  $L_X \propto E^{\alpha_X}$ , for X-ray spectral index,  $\alpha_X$ . In addition, photons with energy below the threshold,  $E_0$ , are assumed to be absorbed by the host galaxy InterStellar Medium (ISM), and the rate integrals have an arbitrary upper limit of 10 keV to avoid divergent behaviour for  $\alpha_X \leq 0$ . Furthermore, the X-ray efficiency is normalized based on an integrated soft-band luminosity of  $< 2$  keV per unit SFR, whereby

$$L_{X<2\text{keV}}/\text{SFR} = \int_{E_0}^{2\text{keV}} dE_e L_X/\text{SFR} [\text{ergs}^{-1}\text{keV}^{-1}M_{\odot}^{-1}\text{yr}]. \quad (2.38)$$

The quantities  $\alpha_X$ ,  $E_0$ , and  $\log_{10}(L_{X<2\text{keV}}/\text{SFR})$  are available to be constrained by 21CMMC. The default range of these parameters are presented in Table 2.3.2. Note that there are, of course, other parameters that can be constrained by 21CMMC but we limit the discussion to those that are most relevant to our research.

Parameter	Unit	Default range
$\log_{10}(T_{\text{vir}})$	K	[4, 6]
$\zeta$	-	[10, 250]
$\alpha_X$	-	[-0.5, 2.5]
$E_0$	keV	[0.1, 0.5]
$\log_{10}(L_{X<2\text{keV}}/\text{SFR})$	$\text{erg s}^{-1} \text{ keV}^{-1} \text{ M}_{\odot}^{-1} \text{ yr}$	[38.0, 42.0]

Table 2.1: The default range of some 21CMC astrophysical parameters which are most influential during cosmic reionisation.

## 2.4 Summary of Methods

The various tools we have discussed in this chapter are extensively used in the following chapters to include realistic components in reionisation studies. We summarize the use of each tool in helping to constrain reionisation parameters in Figure 2.3. Recall that we can either 1) use the result of an  $N$ -body simulation as an input to a semi-analytical model to simulate the physics of reionisation (enclosed in orange dotted line); or 2) use a semi-numerical model such as 21CMFAST to generate both the cosmic-web structures and the astrophysics; for simplicity, we chose the latter. Note that not all of these tools are actually used to constrain reionisation parameters in this thesis; only those that are within the dashed blue line are used in Chapter 4. The other tools are used in Chapter 3 and 5 to address the resolution issues affecting low-mass haloes in  $N$ -body simulations (enclosed in green dash line) and the relationship between foregrounds and cosmic reionisation (enclosed in orange dash line), respectively.

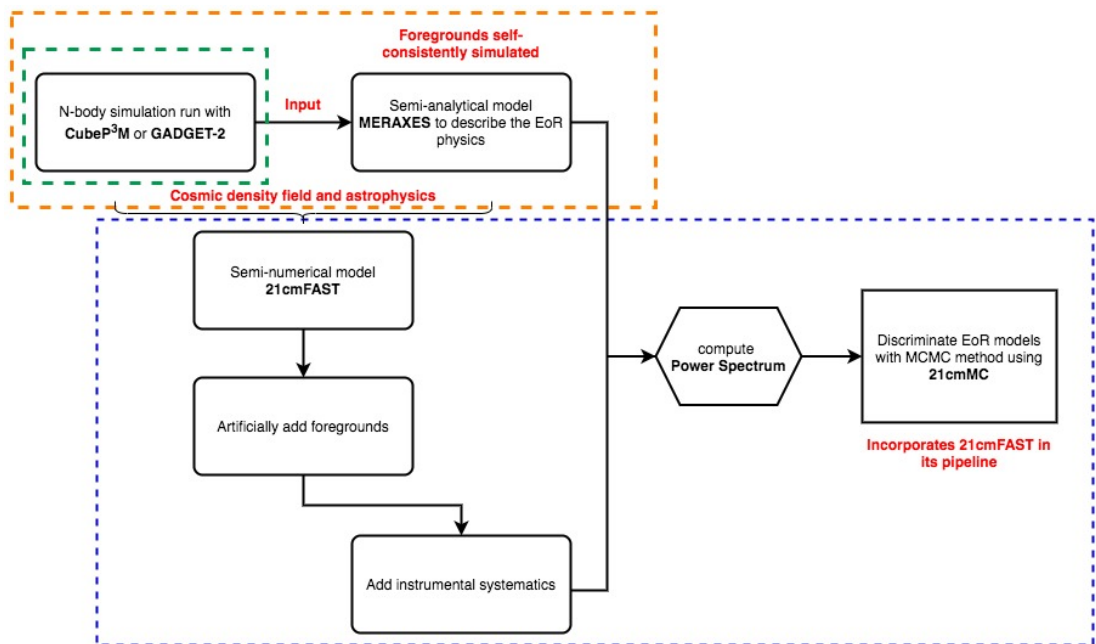


Figure 2.3: A summary of the relationship between the tools we have presented that are used to achieve the final goal of reionisation studies: parameter estimation. Note that not all of these tools are actually used to constrain reionisation parameters in this thesis; only those that are within the dashed blue lines are used in Chapter 4. The other tools are used in Chapter 3 and 5 to address the resolution issues affecting low-mass haloes in  $N$ -body simulations (enclosed in green dash line) and the relationship between foregrounds and cosmic reionisation (enclosed in orange dash line), respectively.



# Chapter 3

## Modelling the stochasticity of high-redshift halo bias

This work was published by Nasirudin, A., Iliev, I. T., and Ahn K. in the *Monthly Notices of the Royal Astronomical Society*, Volume 494, Issue 3, pp.3294-3309. DOI: 10.1093/mnras/staa853

### 3.1 Abstract

As explained in 1.2.3, a very large dynamic range with simultaneous capture of both large- and small-scales in the simulations of cosmic structures is required for correct modelling of many cosmological phenomena, particularly at high redshift. This is not always available, or when it is, it makes such simulations very expensive. We present a novel sub-grid method for modelling low-mass ( $10^5 M_{\odot} \leq M_{\text{halo}} \leq 10^9 M_{\odot}$ ) haloes, which are otherwise unresolved in large-volume cosmological simulations limited in numerical resolution. In addition to the deterministic halo bias that captures the average property, we model its stochasticity that is correlated in time. We find that the instantaneous binned distribution of the number of haloes is well approximated by a log-normal distribution, with overall amplitude modulated by this “temporal correlation bias”. This is the first time that such bias has been included in sub-grid modelling of haloes. The robustness of our new scheme is tested against various statistical measures, and we find that temporally correlated stochasticity generates mock halo data that is significantly more reliable than that from temporally uncor-

related stochasticity. Our method can be applied for simulating processes that depend on both the small- and large-scale structures, especially for those that are sensitive to the evolution history of structure formation such as the process of cosmic reionisation. As a sample application, we generate a mock distribution of medium-mass ( $10^8 \leq M/M_\odot \leq 10^9$ ) haloes inside a  $500 \text{ Mpc } h^{-1}$ ,  $300^3$  grid simulation box. This mock halo catalogue bears a reasonable statistical agreement with a halo catalogue from numerically-resolved haloes in a smaller box, and therefore will allow a very self-consistent sets of cosmic reionisation simulations in a box large enough to generate statistically reliable data.

## 3.2 Introduction

Cosmological haloes are the sites where most active astrophysical processes occur. Understanding the formation, evolution and spatial distribution of cosmological haloes thus allows theoretical access to many astrophysical phenomena and links to observational cosmology. The halo information is typically summarised in the form of a halo catalogue. Modelling galaxy surveys in observational cosmology and studies of the process of cosmic reionisation, which generates observational features at cosmological scales, are both examples that can benefit from reliable, realistic halo catalogues.

For cosmic reionisation modelling in particular, properly understanding the nature of the ionising sources responsible for the Epoch of Reionization (EoR) is an important problem that can aid in interpreting current and future detection experiments. Minihaloes, small haloes in which gas cannot cool through atomic line cooling, are generally conceived to be the site of the first, Pop. III, stars responsible for the early stages of EoR (Barkana & Loeb, 2001; Dayal & Ferrara, 2018). At the same time, both the stellar-mass binaries and the progenitors of super-massive black holes are believed to be among the main sources of X-ray radiation, which heats the neutral inter-galactic medium (IGM) unreachable by UV radiation from stars (Ricotti & Ostriker, 2004; Madau et al., 2004; Knevitt et al., 2014). The later stages of reionisation are thought to be dominated by

emission from more massive galaxies, with halo masses above about  $10^8 M_\odot$ , which we refer to as atomically cooling haloes (ACHs) based on their dominant gas cooling mechanism. These can in turn be split into low-mass ACH (LMACHs), with masses less than about  $10^9 M_\odot$ , for which the gas accretion onto them can be suppressed by radiative feedback, and the larger, high-mass ACH (HMACHs) which are largely unaffected by such feedback (Iliev et al., 2007; Dixon et al., 2016; Ahn et al., 2015). The process of reionisation is believed to be inhomogeneous and anisotropic on large scales (Iliev et al., 2014), hence a large-volume simulation box is needed to capture the extent of the processes involved. However, this also means that cosmic reionisation simulations often have a relatively low resolution, resulting in the need for sub-grid modelling of the low-mass haloes in which the majority of reionisation sources reside.

One perspective towards modelling the sub-grid halo population is the peak-background split scheme (Bardeen et al., 1986) which provides a framework for understanding how haloes form in a way biased toward high-density environment. In this approach, a halo is associated with the linear overdensity  $\delta_{\text{lin}}$  that satisfies the halo formation criterion,  $\delta_{\text{lin}} > \delta_c$ , where  $\delta_c \approx 1.686$  is the critical overdensity. This put theoretical foundations under the well-known Press-Schechter (PS) formalism (Press & Schechter, 1974), whose fudge multiplicity factor 2 was later explained rigorously by Bond et al. (1991) through their extended Press-Schechter formalism (or the excursion set formalism). The halo bias due to a large-scale density environment specified by its linear overdensity  $\Delta_{\text{linear}}$  can also be naturally accounted for in this framework, because the small-scale density fluctuation now only needs to satisfy the modified criterion  $\delta_{\text{lin}} > \delta_c - \Delta_{\text{linear}}$  (Cole & Kaiser, 1989). Mo & White (1996) calculated a fully nonlinear bias prescription, by combining this peak-background split scheme with the spherical top-hat collapse model.

A notable shortcoming of both the average PS halo mass function and the nonlinear halo bias model by Mo & White (1996) is that the number of haloes predicted this way does not match the numerically simulated haloes well, especially massive, rare haloes at any given epoch. The discrepancy in the average

halo mass function stimulated a set of fitting functions based either on a more detailed theory in the halo formation, supported by simulation data (e.g. Sheth & Tormen 1999, ST hereafter) or empirical fits to numerical simulations (Jenkins et al. 2001; Warren et al. 2006; Reed et al. 2007; Lukić et al. 2007; Lim & Lee 2013; Watson et al. 2014). The discrepancy in the biased halo mass function seems to be resolved by a simple yet attractive solution by Barkana & Loeb (2004, BL hereafter), which is a hybrid scheme of combining the ST mass function and the bias prescription from the extended PS formalism. Ahn et al. (2015) extended this idea to combine the average mass function of simulated haloes, instead of the ST mass function, and the bias prescription from the extended PS formalism, and have found that this scheme has an excellent predictive power on the nonlinear bias of haloes in the high-redshift regime.

In order to add more naturalness to the sub-grid modelling, however, the “deterministic” prescription described so far is not sufficient, and the stochasticity of halo bias also needs to be implemented. This stochasticity does not follow the pure Poisson distribution, because the correlation of haloes at the sub-grid level produces a variance in the number of haloes, in addition to the usual shot noise (Peebles, 1993; Dekel & Lahav, 1999). In the presence of the sub-grid correlation, this additive variance extends the tails of the distribution function of the halo number, or “super-Poissonian” distribution, which is well fitted by functional forms by Saslaw & Hamilton (1984) and Sheth (1995).

The sub-grid modelling of haloes is naturally connected to the effort to generate mock halo catalogues under the knowledge of large-scale density field. This idea is implemented in PINOCCHIO (Monaco et al., 2002, 2013) and PTHALOES (Scoccimarro & Sheth, 2002; Manera et al., 2013), which generate mock halo catalogues based on the quasi-linear density field. With an adaptive high-order perturbation theory, mock catalogues can be generated even more precisely (e.g. Patchy by Kitaura et al. 2014 in which they used the 2nd-order Lagrangian perturbation theory but at the same time improved on mitigating the problems caused by the unwanted free-streaming of particles in small scales). The feasibility to use such a prescription to study e.g. the Baryon Acoustic Oscillation (BAO) feature

in density power spectrum has been presented (Kitaura et al., 2014). In addition, the bias assignment method (BAM) is another way to generate mock halo catalogues whereby the halo distribution is mapped onto a target dark matter density field according to the field’s properties (Balaguera-Antolínez et al., 2019, 2020).

We find that one key ingredient is still missing in sub-grid modelling efforts described above. This is the *temporally correlated stochasticity*: stochasticities in the halo distribution at mutually nearby epochs should be correlated. This would not be crucial if one is interested only in a limited range of redshifts. For example, the study of BAO through galaxy surveys at low redshift may need to focus only on the fields of halo population that is instantaneous or mildly changing in time. However, in cases where continuous evolution is important, correlation of stochasticity in time is also crucial. For example, in the study of cosmic reionisation, how haloes are generated in time and space are cumulatively imprinted in the late phase of the process in terms of the morphology of H II regions. Therefore, in this paper, we present our quantitative study on the temporally correlated stochasticity and the feasibility to use this prescription to self-consistently generating mock halo catalogues both in time and space. Previously we have implemented the deterministic bias only, without stochasticity, as sub-grid treatment. Nevertheless, through this method, we have found that small-mass haloes impact the physics of reionisation quite substantially: minihaloes yield extended and self-regulated reionisation epoch (Ahn et al. 2012; even found favoured by the CMB polarization data by Planck: Heinrich et al. 2017), the observed 3-dimensional (3D) imaging and 21-cm power spectrum depends on the minimum halo mass (Dixon et al., 2016; Giri et al., 2018), and statistics of neutral gas islands in the late phase of islands will be affected by LMACHs (Giri et al., 2019), to give a few examples. Application of a self-consistently calculated stochasticity is therefore expected to provide a more reliable picture on the physics of cosmic reionisation. We note that this is the first time that a temporal bias has been included in sub-grid modelling of haloes.

The simulations presented in this work use the following set of cosmological

parameters  $\Omega_\Lambda = 0.73$ ,  $\Omega_M = 0.27$ ,  $\Omega_b = 0.044$ ,  $h = 0.7$ ,  $\sigma_8 = 0.8$ ,  $n_s = 0.96$  where  $H_0 = 100h \text{ km s}^{-1} \text{ Mpc}^{-1}$ , broadly consistent with the *WMAP* 5-year data (Komatsu et al., 2009) and latest Planck results (Planck Collaboration et al., 2020). However, our method is generic and do not depend on the specific cosmology used because it is purely based on the statistics of the data.

This paper is organized as follows. We describe our method to generate halo bias that can assimilate the  $N$ -body simulation data in § 3.3. We present mock realizations of haloes in those boxes that resolve haloes of given mass range, and compare the resulting statistical measures of the actual  $N$ -body data and the mock data in § 3.4.1. An application of our method to a large,  $500 h^{-1} \text{ Mpc}$  box with a test on its validity is described in § 3.4.2. We summarise our results and discuss relevant issues in § 3.5.

## 3.3 Methodology

### 3.3.1 $N$ -body simulation data

Halo bias is composed of the deterministic bias and the stochastic bias. The former represents the average conditional probability that cells with given overdensity  $\delta$  will host haloes of given mass range. The latter represents the unavoidable stochasticity, due to dependencies beyond local density, in the number (or collapsed fraction) of haloes across cells with given  $\delta$ . These two components can be expressed in a single probability distribution function in terms of the average quantity  $\mu$  and at the least the standard deviation  $\sigma$  (that of the approximately log-normal distribution in our case as in Equation 3.3), respectively.

Motivated by the physics of the radiation sources during the Cosmic Dawn and EoR, we split the dark matter haloes into three physically-motivated mass ranges (see e.g. Iliev et al., 2007): high-mass atomically-cooling haloes (HMACHs), defined by  $M_{\text{halo}} > 10^9 M_\odot$ ; low-mass atomically-cooling haloes (LMACHs), with  $10^8 M_\odot < M_{\text{halo}} < 10^9 M_\odot$ , and minihaloes (MHs), with  $M_{\text{halo}} < 10^8 M_\odot$ . We focus on implementing the stochasticity of the latter two types in large-scale simulations, since HMACHs are relatively more easily resolved (Iliev et al., 2007)

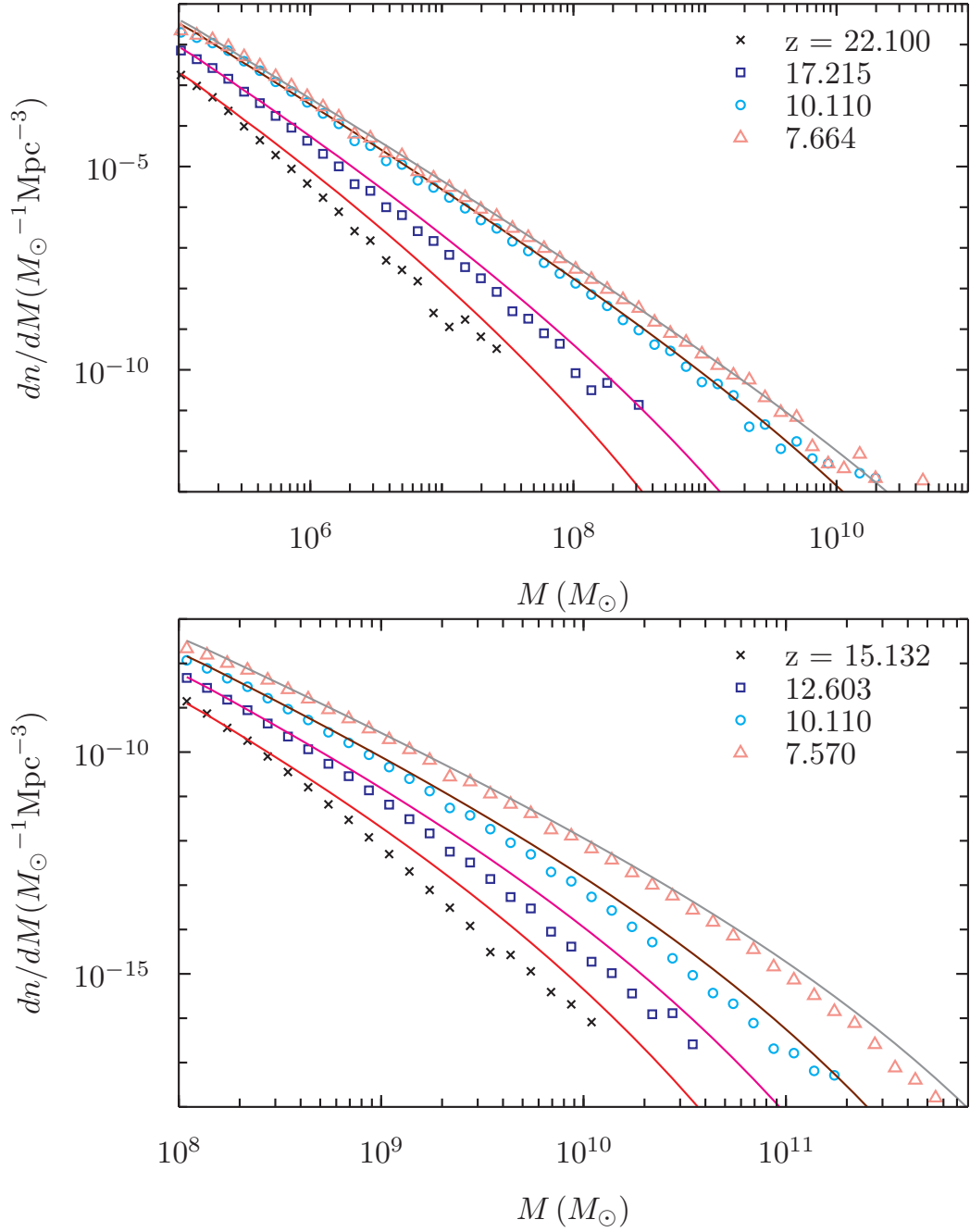


Figure 3.1: Halo mass functions in  $N$ -body simulations, with the box size of  $6.3 h^{-1}$  Mpc (top) and  $114 h^{-1}$  Mpc (bottom). The  $N$ -body halo data is plotted as points and compared to the Sheth-Tormen mass function (solid lines) at different redshifts (decreasing from top to bottom).

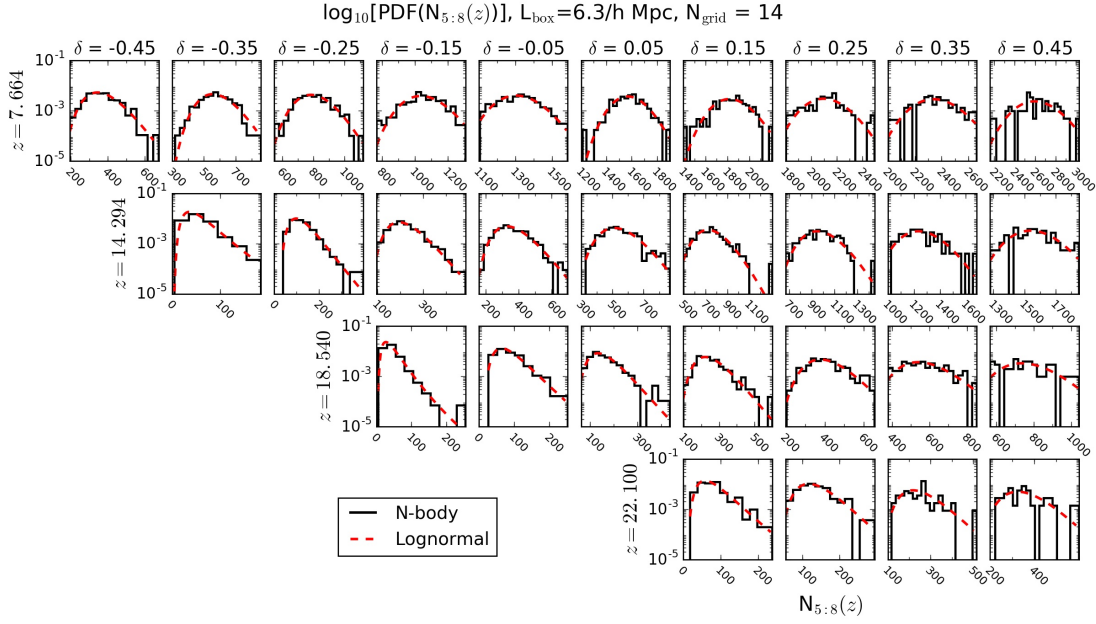


Figure 3.2: PDF of the number of MHs,  $N_{5:8}$ , contained within cells of given overdensity  $\delta$  on our  $14^3$ -grid  $6.3 h^{-1}$  Mpc-box.  $\delta$  is shown on top of each subplot while redshifts are shown on the left. The PDF of the  $N$ -body halo data (black solid) is fit by a log-normal distribution (red dashed).

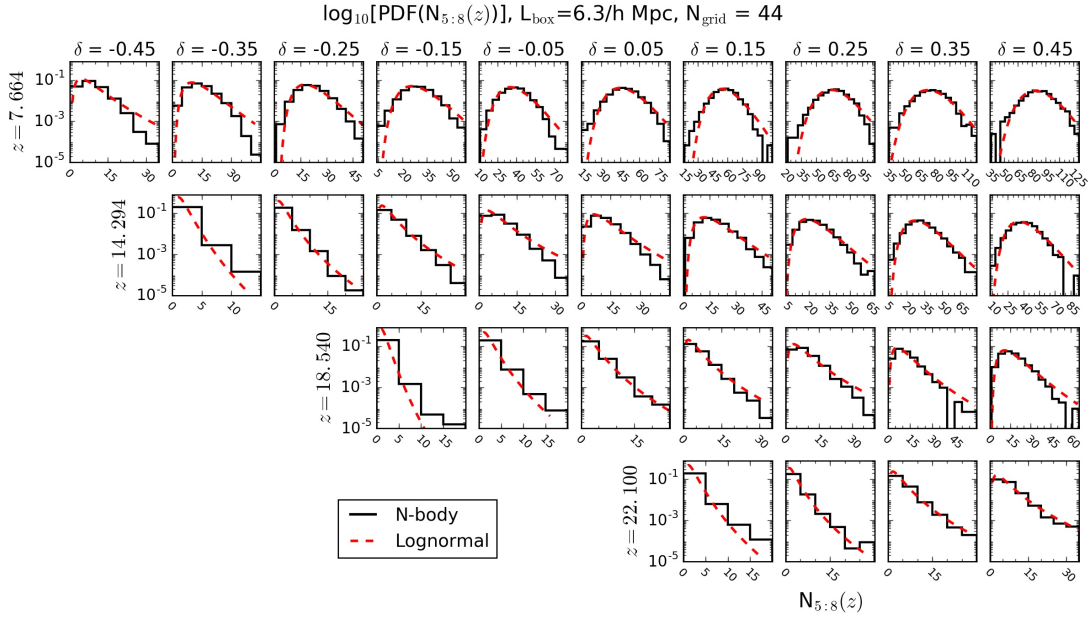


Figure 3.3: Same as in Fig. 3.2, but with the number of haloes sampled on a  $44^3$  grid.

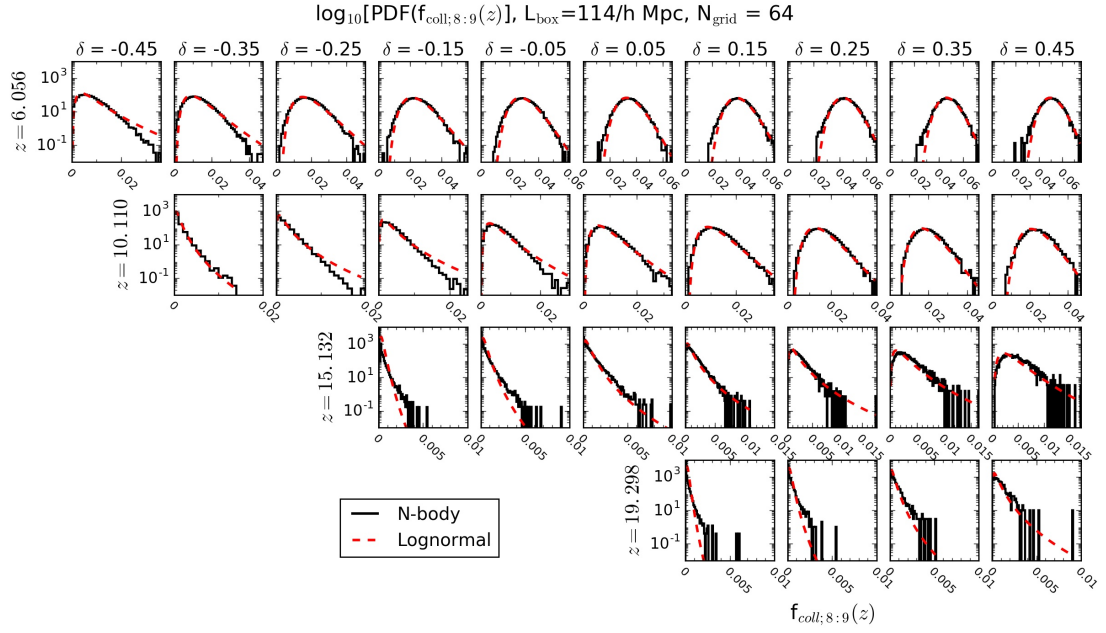


Figure 3.4: PDF of the LMACH collapsed fraction,  $f_{\text{coll};8:9}$ , contained within cells of given overdensity  $\delta$  on our  $64^3$ -grid  $114 h^{-1}$  Mpc-box. Plotting convention is the same as in Figure 3.2.

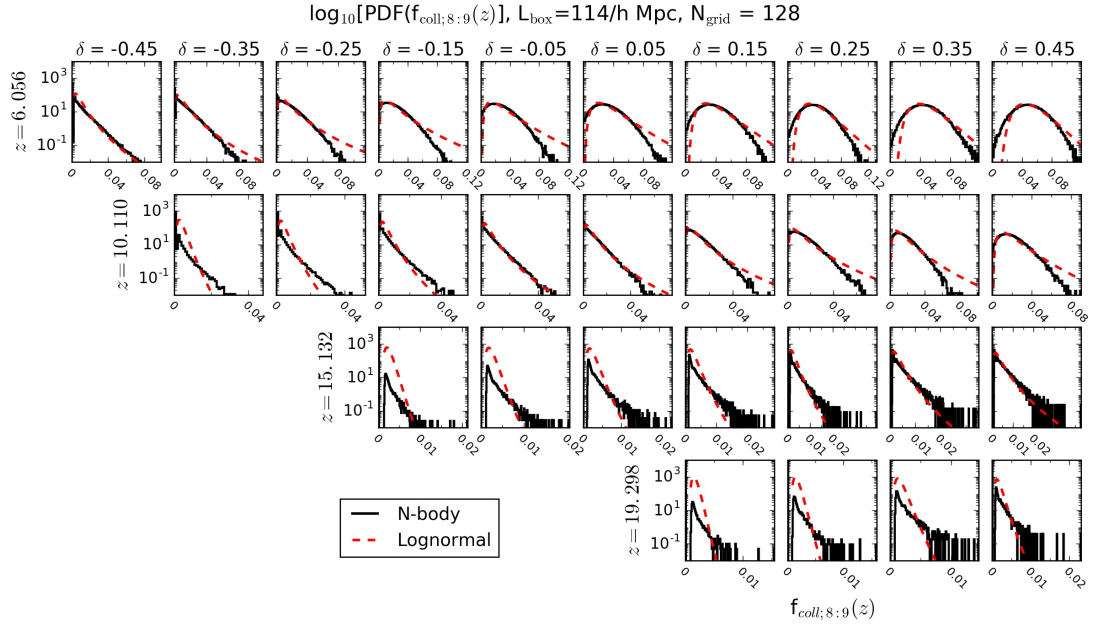


Figure 3.5: Same as in Fig. 3.4, but with the collapsed fraction sampled on a  $128^3$  grid.

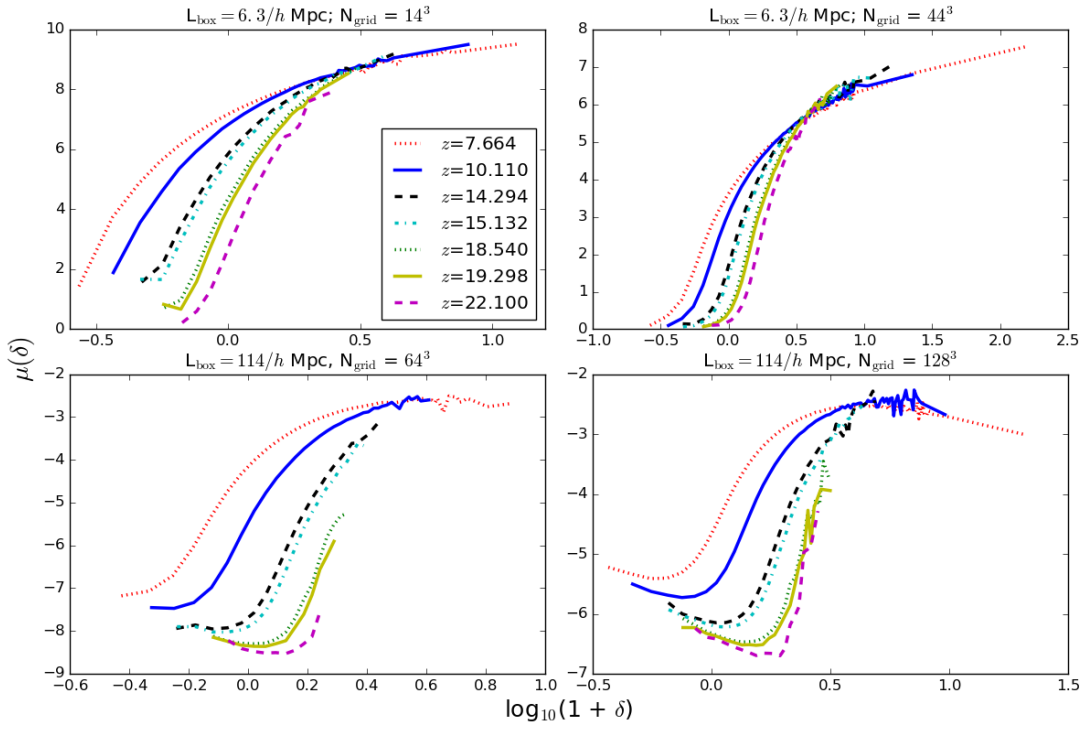


Figure 3.6: The evolution of  $\mu$  with respect to overdensity for the  $6.3 \text{ Mpc } h^{-1}$  (top panels) and  $114 \text{ Mpc } h^{-1}$  box (bottom panels)  $14^3$ ,  $44^3$ ,  $128^3$  and  $64^3$  grid for several representative redshifts, all as labelled.

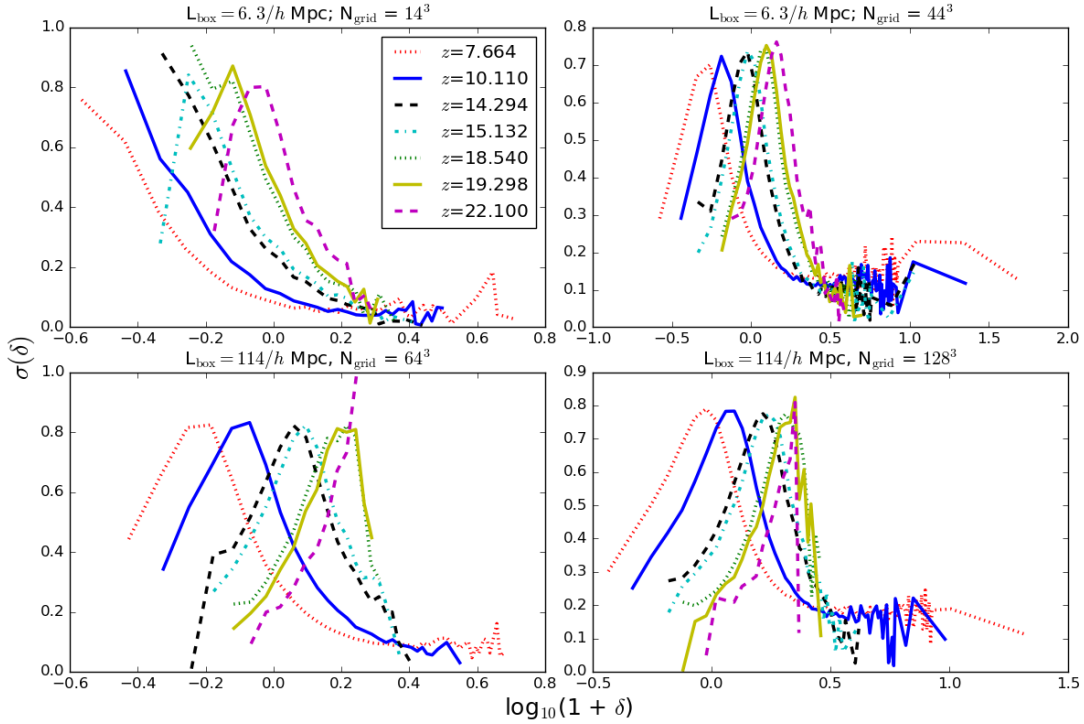


Figure 3.7: The evolution of  $\sigma$  with respect to overdensity for the  $6.3 \text{ Mpc } h^{-1}$  (top panels) and  $114 \text{ Mpc } h^{-1}$  box (bottom panels) with  $14^3$ ,  $44^3$ ,  $128^3$  and  $64^3$  grid for several representative redshifts, all as labelled.

and thus sub-grid modelling is usually unnecessary, although our model is easily extensible to such haloes as well. By definition, ACHs form stars efficiently by cooling the gas through atomic line radiation, and the star formation therefore is expected to be roughly proportional to the total amount of gas available, which in turn is proportional to the collapsed fraction in such haloes. In contrast, gas in MHs is easily disrupted and photo-evaporated by the first star(s) to form within each halo, or in nearby haloes, thus we expect that each MH forms just one, or at most a few stars, irrespective to its actual total gas mass. Therefore, in our modelling for LMACHs we consider the local collapsed fraction, while for MHs we consider the local number of haloes. Our model is applicable to either quantity.

The simulation data used throughout this work is based on a suite of  $N$ -body simulations using the CubeP<sup>3</sup>M code (Harnois-Déraps et al., 2013). The halos are identified on-the-fly using a spherical overdensity halo finder with overdensity parameter of 180. The MH data is based on a high-resolution simulation in a box of  $6.3 h^{-1}$  Mpc per side, with  $1728^3$  particles, force resolution of  $182 h^{-1}$  pc and minimum halo mass resolved (with 20 particles or more) of  $\sim 10^5 M_{\odot}$ . This roughly corresponds to the halo ‘filtering mass’ (Gnedin, 2000) below which haloes struggle to keep their gas content even before reionisation. The LMACHs data is based on a simulation in a box of  $114 h^{-1}$  Mpc per side, with  $3072^3$  particles, force resolution of  $1.8 h^{-1}$  kpc and minimum resolved halo mass of  $\sim 10^8 M_{\odot}$ . To illustrate the halo-mass resolution of each  $N$ -body simulation, we plot halo mass functions ( $dn/dM$ ) in Figure 3.1. The empirical mass function has a reasonable agreement with a reference semi-analytical prediction, the Sheth-Tormen (ST) mass function (Sheth & Tormen, 1999). The discrepancy observed in the high-mass end is also reasonable, considering the usual over-estimation of the ST mass function of rare haloes.

The density field is smoothed (using particle-in-cell, PiC, method) onto a uniform grid<sup>1</sup> of  $14^3$  and  $44^3$  cells when sampling MHs (hereafter  $N_{5,8}$ ), and into  $64^3$  and  $128^3$  cells when sampling the *local* collapsed fraction of LMACHs ( $f_{\text{coll},8,9}$ ),

---

<sup>1</sup>In general, sub-grid modeling treats unresolved low-mass haloes as a single statistic per cell – either the total halo count or the collapse fraction. These values are then used to assign the number of ionizing stars per cell. Because their masses are small, they do not contribute to the merger trees, so the specific mass and position distribution within the cell is not needed.

given by

$$f_{\text{coll},8:9} = \frac{M_{8:9}}{M}, \quad (3.1)$$

where  $M_{8:9}$  is the mass of haloes between  $10^8$  and  $10^9 M_\odot$  and  $M$  is the mass of a cell. The local overdensity,  $\delta$ , of each cell is defined by

$$\delta = \frac{\rho}{\bar{\rho}} - 1, \quad (3.2)$$

where  $\rho$  is the average density of a cell and  $\bar{\rho}$  is the mean density of the universe.

### 3.3.2 Instantaneous halo bias in $N$ -body simulation

We empirically quantify the instantaneous halo bias (“instantaneous bias” hereafter) from  $N$ -body simulation data. For now we ignore any possible temporal correlation but just consider the local cell overdensity  $\delta$  and redshift  $z$ . First, we sample  $\delta$ ’s of cells with the bin width  $\Delta\delta = 0.1$ . This guarantees a reasonable amount of sampling of grid cells for any  $\delta < 10$ . Only for the highest- $\delta$  cells which are rare, we enlarge the bin size substantially: cells of  $\delta > 10$  are grouped into two coarse bins –  $10 \leq \delta \leq 15$  and  $\delta > 15$ . Second, for each  $\delta$  bin, we measure the empirical probability distribution function (PDF) of  $N_{5:8}$  or  $f_{\text{coll},8:9}$  by visiting all cells of the given  $\delta$ .

Any conditional parameters hereafter denote parameters measured in appropriate bins; e.g.  $\mu(z|\delta = 0.5)$  is the average value of all  $\mu(z|\delta)$ ’s when  $\delta \in [0.5 - \Delta\delta/2, 0.5 + \Delta\delta/2] = [0.45, 0.55]$ . The following terminology and parameters are useful in describing the empirical, instantaneous stochasticity:

- $x$ : the value of either  $N_{5:8}$  or  $f_{\text{coll},8:9}$ .
- $x_{\min}(z|\delta)$ ,  $x_{\max}(z|\delta)$ : the minimum and maximum, respectively, of  $x$  found in cells of overdensity  $\delta$  at redshift  $z$ .
- $\mu(z|\delta)$ : the average of  $\ln(x)$ , given cells of  $\delta$  at  $z$ .
- $\sigma(z|\delta)$ : the standard deviation of  $\ln(x)$ , given cells of  $\delta$  at  $z$ .

- $N_+(z)$ : the total number of non-empty cells at  $z$ .
- $N_0(z)$ : the total number of empty cells at  $z$ .
- $N_+(z|\delta)$ : the number of cells of  $\delta$  which are non-empty at redshift  $z$ .
- $N_0(z|\delta)$ : the number of cells of  $\delta$  which are empty at  $z$ .

The empirical results for PDFs of  $N_{5,8}$  are shown in Figures 3.2 and 3.3, and those for PDFs of  $f_{\text{coll},8,9}$  are shown in Figures 3.4 and 3.5. The PDFs are roughly Gaussian close to its peak, but have considerable skewness away from it, and are thus overall not well represented by a Gaussian. This “super-Poissonian” distribution is caused by the non-zero auto-correlation of halo population in the sub-cell scale (Peebles, 1980; Ahn et al., 2015), which can be well-fit by distribution functions suggested by Saslaw & Hamilton (1984) and Sheth (1995). Instead, we employ a lognormal distribution, with which the skewness is easily realized with just two parameters – the average and the standard deviation of the logarithmic – to fit the  $N$ -body simulation data:

$$f(x, z|\delta) = \frac{1}{x} \frac{1}{\sigma \sqrt{2\pi}} \exp^{-\frac{(\ln x - \mu)^2}{2\sigma^2}}, \quad (3.3)$$

where  $\mu = \mu(z|\delta)$  and  $\sigma = \sigma(z|\delta)$ . We use this lognormal PDF to represent the PDF of non-empty cells only, since empty cells are not of interest here and including them would distort distribution. Note that we do not take  $\{\mu, \sigma\}$  as free parameters to find the best fit to the  $N$ -body data, but instead use the empirical values of  $\{\mu(z|\delta), \sigma(z|\delta)\}$  taken from the  $N$ -body simulation data and check the goodness of the fit afterwards by comparing the lognormal fit with the empirical parameter values to the PDF of the  $N$ -body data. The evolution of empirical  $\mu$  and  $\sigma$  with respect to overdensity for some representative redshifts are shown in Figure 3.6 and 3.7 respectively.

The lognormal fits (red dashed lines in Figs. 3.2 - 3.5) largely match the empirical distributions well. In both cases of MHs and LMACHs, the lognormal fit works better for the larger cell size:  $N_{\text{grid}} = 14$  case (Fig. 3.2) is better than  $N_{\text{grid}} = 44$  case (Fig. 3.3) for MHs, and  $N_{\text{grid}} = 64$  case (Fig. 3.4) is better than

$N_{\text{grid}} = 128$  case (Fig. 3.5) for LMACHs. The mismatch occurs in many cases, but only in the tails of PDFs where the fractional contribution becomes relatively unimportant. Only at high-redshift ( $z \gtrsim 15$ ), small cell-size cases for LMACHs show the biggest mismatch (Fig. 3.5), even in its amplitude. Overall, we expect that any resulting statistical measures from this lognormal fitting will be only slightly different from those of the  $N$ -body data.

### 3.3.3 Implementing instantaneous halo bias

We now describe our scheme to realize instantaneous bias for generating mock halo catalogues using the empirical parameters, described in section 3.3.2, as the basis. A fluctuating 3D density field should be provided at a target redshift, ideally by numerical simulations that resolve the nonlinear density environment for given filtering scale (Eulerian cell size).

Our algorithm is described by the sequence below. Any quantity with a prime symbol denotes a value related to the mock data.

1. Once the  $N$ -body particle density field is interpolated onto a uniform grid, group the grid cells according to discrete bins of  $\delta$ .
2. Among the cells of given  $\delta$ , randomly choose a fraction  $P_+(z|\delta)$  of these cells that will host haloes, with the ‘‘conditional occupation probability’’

$$P_+(z|\delta) = \frac{N_+(z|\delta)}{N_+(z|\delta) + N_0(z|\delta)}, \quad (3.4)$$

and leave the remaining cells devoid of any haloes. The number of non-empty cells of  $\delta$  in the given density field found this way,  $N'_+(z|\delta)$ , may differ from  $N_+(z|\delta)$  in general, because  $N'_+(z|\delta) = P_+(z|\delta) N'(z|\delta)$  where  $N'(z|\delta)$  is the number of grid cells of  $\delta$  in the given density field. Similarly, the total of  $N'_+(z|\delta)$ , ( $N'_+(z)$ ) should follow

$$N'_+(z) = \frac{N_+(z)}{N_{\text{grid}}} N'_{\text{grid}}. \quad (3.5)$$

3. Use Monte Carlo sampling of  $x$  based on Equation (3.3) to populate these

non-empty cells with haloes. Sample  $x$  from the bounded range  $x = [x_{\min}(z|\delta), x_{\max}(z|\delta)]$ .

4. When  $N'_+(z|\delta) \lesssim 10$  it is inappropriate to use the Monte Carlo sampling due to rarity of such cells; in such cases the empirical data shows convergence of  $x$  to  $\mu(z|\delta)$ . If this happens, only use the deterministic bias, by setting  $x = e^{\mu(z|\delta)}$  in those cells.

This scheme only considers the instantaneous information, and thus can be easily applied once the empirical parameters described in § 3.3.2 are available. Note that when the range of  $\delta$  in the given density field exceeds the range of the empirical values due to e.g. the increased size of a simulation box, one needs to extrapolate the empirical parameters for those outliers of  $\delta$ .

### 3.3.4 Temporal halo bias in $N$ -body simulation

Just as in the case of the instantaneous bias, we first find an empirical model for the temporal stochastic halo bias (“temporal bias” hereafter) from  $N$ -body halo data, and then develop a method to generate mock halo catalogues based on this model. Ideally, it would be best to find e.g. a universal relation between the redshift  $z$  and the degree of stochasticity for any given Eulerian or Lagrangian cell. Unfortunately we could not find such a clean relation yet, but instead found a model that reflects temporal stochasticity of  $N$ -body halo catalogues to a significant extent. We will show how well this method mimics the actual  $N$ -body halo catalogues in § 3.4 through various statistical measures.

Our empirical model for temporal stochasticity can be described by the following parameters, where appropriate binning is assumed for conditional values:

- $\Delta z_{+,i}$ : the redshift interval during which an Eulerian cell  $i$  is not empty.
- $\Delta z$ : the full duration of our  $N$ -body simulation, under the assumption that haloes of interest start to emerge in the simulation volume from the starting redshift.
- $\bar{\delta}_i$ : the average overdensity of the cell  $i$  over  $\Delta z$ .

- $f_{+,i} \equiv \Delta z_{+,i}/\Delta z$ : the fraction of time during which the cell  $i$  is not empty.
- $f_+(\bar{\delta})$ : the time fraction that an Eulerian cell with mean overdensity  $\bar{\delta}$  is not empty. Here,  $\bar{\delta}$  is the average of  $\bar{\delta}_i$  of cells having  $f_{+,i} = f_+$ , and thus this function relates  $f_+$  and  $\bar{\delta}$  in averaged, deterministic way.
- $N_+(z|x_{\text{prev}}, +)$ : the total number of non-empty cells at  $z$ , among those cells which had  $x = x_{\text{prev}} \equiv x(z_{\text{prev}}) > 0$ . Here,  $z_{\text{prev}}$  is the redshift of the  $N$ -body data recorded just before the redshift  $z$ .
- $N_0(z|x_{\text{prev}}, +)$ : the total number of empty cells at  $z$ , among those cells which had  $x = x_{\text{prev}} > 0$ .

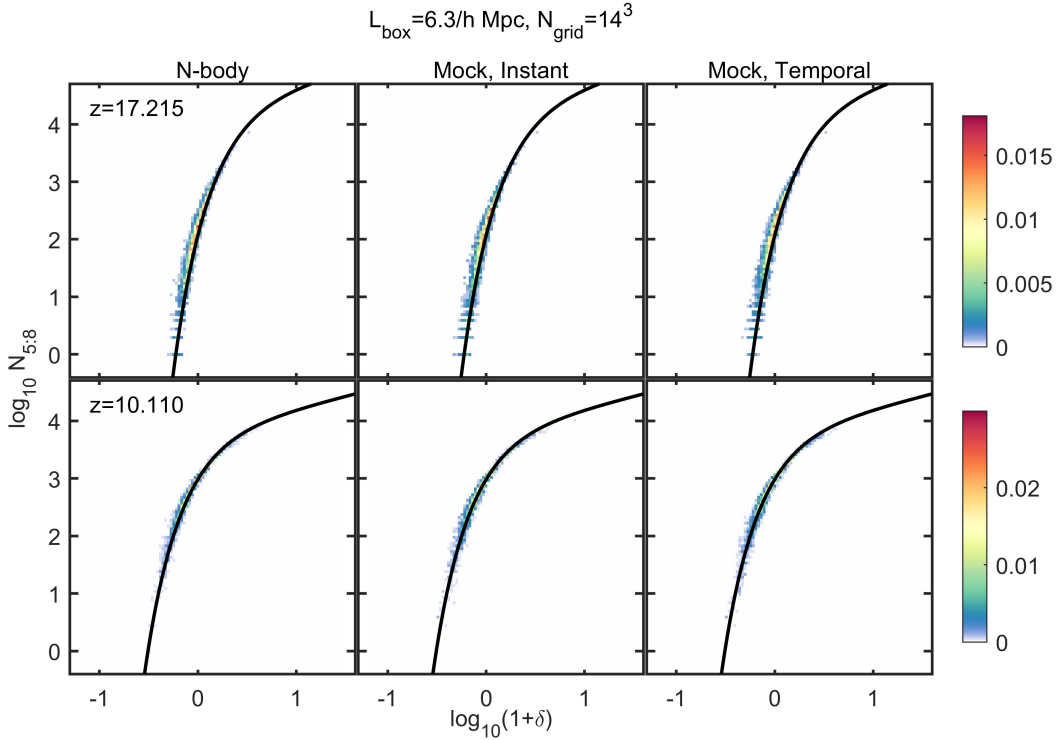


Figure 3.8: Number of MHs,  $N_{5:8}$ , per cell vs cell overdensity  $\delta$  at  $z = 17.215$  (upper panel) and  $z = 10.110$  (lower panel) for 6.3 Mpc/h box and  $14^3$  grid (cell size  $450 h^{-1} \text{kpc}$ ). Shown are the  $N$ -body halo data (left panels), the instantaneous mock halo (middle panels), and temporal mock halo (right panels). Data points are projected onto a 2-dimensional uniform grid of  $\log_{10}(1 + \delta)$  and  $\log_{10}(N_{5:8})$ , and are then shown collectively as the ratio of the number of data points on each grid cell (color map) to the total number of data points. The data is compared to the mean deterministic bias (solid line) by Ahn et al. (2015).

The halo catalogues from the  $N$ -body simulations cover the redshift range  $6 < z < 25$  and are equally spaced in time, every 11.5 Myr. There are 65 redshifts data for the  $6.3 h^{-1}$  ( $6.483 \leq z \leq 24.597$ ) and 73 redshifts data for the  $114 h^{-1}$  Mpc data ( $6.000 \leq z \leq 24.597$ ).

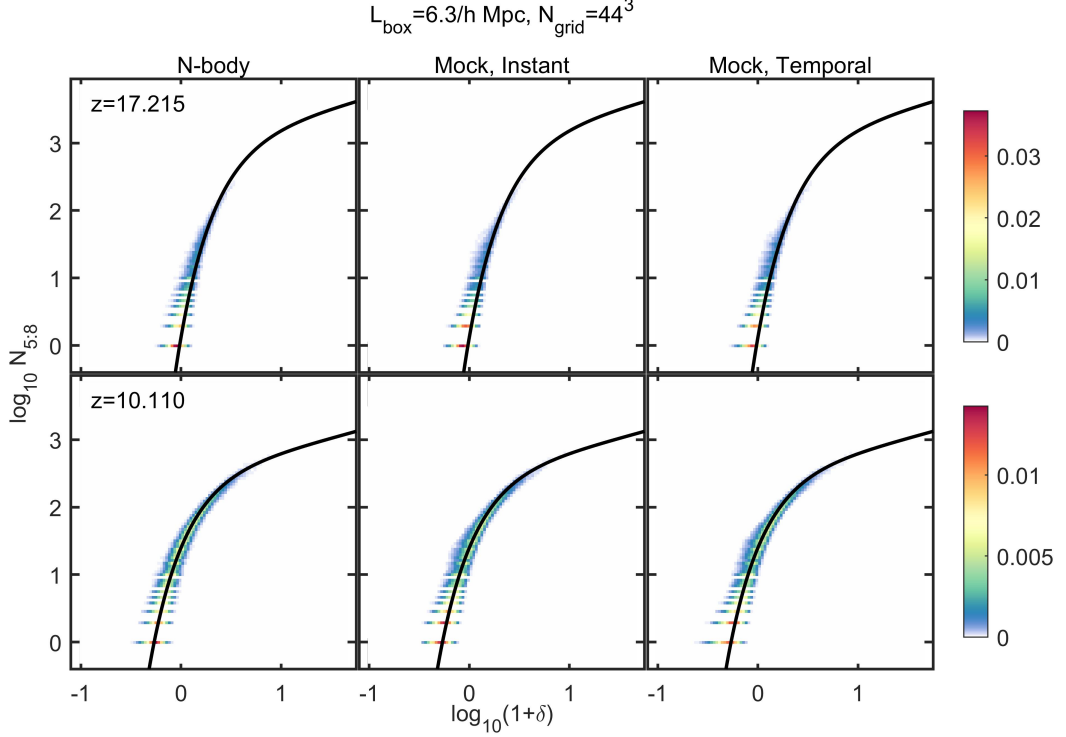


Figure 3.9: Same as Fig. 3.8, but for  $44^3$  grid (cell size  $143 h^{-1} \text{kpc}$ ).

### 3.3.5 Implementing temporal halo bias

We now describe our method to generate mock halo catalogues with temporal bias, based on the empirical parameters described in Sections 3.3.2 and 3.3.4. Again, a fluctuating 3D density field should be provided at target redshifts and the uniform Eulerian grid is used, while any quantity with a prime symbol denotes a value related to the mock data.

1. Set  $\Delta z$  of the density field identical to  $\Delta z$  of the  $N$ -body simulation that were used to set parameters in § 3.3.4.
2. At starting redshift ( $z_{\text{start}}$ ), which should also be identical to that of the

$N$ -body simulation, apply the scheme for instantaneous bias (§ 3.3.3) using  $P_+(z_{\text{start}}|\delta)$  to choose the cells.

3. Presume that mock haloes were generated at  $z_{\text{prev}}$ . Among the cells of given  $x' = x_{\text{prev}} > 0$  at  $z_{\text{prev}}$ , randomly choose a fraction  $P_0(z|x_{\text{prev}}, +)$  of these cells that will become empty at  $z$ , with the “conditional de-occupation probability”

$$P_0(z|x_{\text{prev}}, +) = \frac{N_0(z|x_{\text{prev}}, +)}{N_0(z|x_{\text{prev}}, +) + N_+(z|x_{\text{prev}}, +)}, \quad (3.6)$$

and let the remaining cells host haloes again at  $z$ . The number of these empty cells at  $z$  given they were non-empty at  $z_{\text{prev}}$  chosen this way,  $N'_0(z|x_{\text{prev}}, +)$ , may differ from  $N_0(z|x_{\text{prev}}, +)$  in general, so similarly,  $N'_+(z|x_{\text{prev}}, +)$ , may also differ from  $N_+(z|x_{\text{prev}}, +)$ . Let “Group (+|+)” denote the group of these cells which will still host haloes.

4. Get the total number of cells in Group (+|+) from step (iii),  $N'_+(z|+) = \sum_{\text{bin of } x_{\text{prev}}} N'_+(z|x_{\text{prev}}, +)$ .
5. Exclude Group (+|+) from the whole set of grid cells at  $z$ . Let “Group (0)” denote this group of cells. Note that Group (0) also includes cells that have been de-occupied of halos at this redshift.
6. Obtain  $N'_+(z)$  using Equation 3.5 of § 3.3.3.
7. Inside Group (0), try selecting  $N'_+(z) - N'_+(z|+)$  cells through the following procedure. For each and every cell inside Group (0), identify  $f_+(\bar{\delta}) * P_+(z|\delta)$  as the probability for the cell to host haloes, where  $\bar{\delta}$  is the average overdensity of the cell over  $\Delta z$ . Perform Monte Carlo sampling cell by cell to mark non-empty cells, and count their number  $N'_+(A|0)$ . Check if  $N'_+(A|0)$  is within pre-set tolerance of the target number  $N'_+(z) - N'_+(z|+)$ . If not, then iterate the Monte Carlo procedure until convergence. Let “Group (+|0)” denote the resulting group of non-empty cells.
8. Finally, apply steps (iii) and (iv) in § 3.3.3 on all cells of both Group (+|+)

and Group (+|0).

9. Steps (iii) – (viii) are done over all redshifts, taking the results from step (ii) as the first case of  $z_{\text{prev}}$ .

We note that the target number of non-empty cells at  $z$  is  $N'_+(z)$  (step vi) is also the number of non-empty cells in the case of instantaneous bias following Equation 3.5. This is because the temporal bias prescription should of course satisfy the instantaneous statistics at the least. We also note that the smaller  $x_{\text{prev}}$  is, the larger  $P_0(z|x_{\text{prev}}, +)$  becomes, implying that cells containing a small number or mass of haloes are relatively likely to become devoid of haloes in the near future.

Moreover, the main reason we use  $f_+(\bar{\delta})$  instead of  $P_+(z|\delta)$  for the starting redshift is because we want to assign the halo-hosting probability based on the cell-density evolution. For the temporal stochasticity, the choice of cells at starting redshift is extremely important because it could affect where halos are at later redshifts, whereas for the instantaneous stochasticity, the halos are essentially reset at each redshift so the starting choice matters less. The density evolution is a good tracer of this relationship instead of the instantaneous density alone.

## 3.4 Results

Based on the methodology presented in § 3.3, we can create mock realizations of spatial halo distributions based on an input cosmological density field for a given spatial resolution (cell size) and simulation volume. Our immediate aim and first application for this method is to create such mocks as input for large-volume radiative transfer simulations of cosmic reionisation for cases where low-mass galaxies driving reionisation cannot be resolved numerically. This is discussed in § 3.4.2 below.

However, before discussing the large-scale mocks in § 3.4.2, we first demonstrate in § 3.4.1 our methodology on the density fields derived from the same high-resolution  $N$ -body simulations that provided the fitting parameters in the

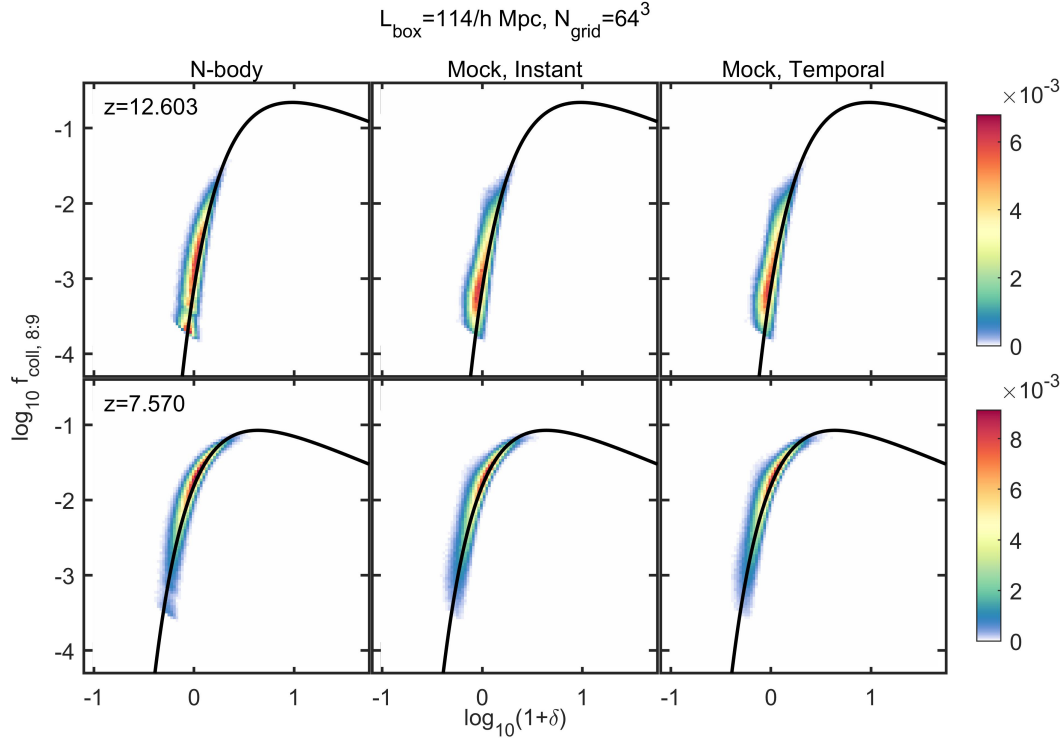


Figure 3.10: LMACHs collapsed fraction,  $f_{\text{coll},8:9}$ , per cell vs cell overdensity  $\delta$  at  $z = 12.603$  (upper panel) and  $z = 7.570$  (lower panel) for  $114 \text{ Mpc } h^{-1}$  box and  $64^3$  grid (cell size  $1.781 \text{ h}^{-1} \text{ Mpc}$ ). Shown are the  $N$ -body halo data (left panels), the instantaneous mock haloes (middle), and the temporal mock haloes (right). Data points are projected onto a 2-dimensional uniform grid of  $\log_{10}(1 + \delta)$  and  $\log_{10}(f_{\text{coll},5:8})$ , and are shown collectively as the ratio of the number of data points on each grid cell (color map) to the total number of data points. The data is compared to the mean deterministic bias (solid line) by Ahn et al. (2015).

first place, both with and without the temporal bias. Since in this case we directly resolve the low-mass haloes of interest, we can evaluate the fidelity of our mocks against the actual known halo numbers and spatial distribution.

Furthermore, the direct comparison of the cases with and without temporal bias helps us understand the importance of its inclusion in modelling the stochasticity. We start sampling the data from  $z = 30$ , but only start implementing the stochasticity from  $z \leq 25$  to ensure that there is sufficient data to determine the parameters that are truly reflective of the distribution.

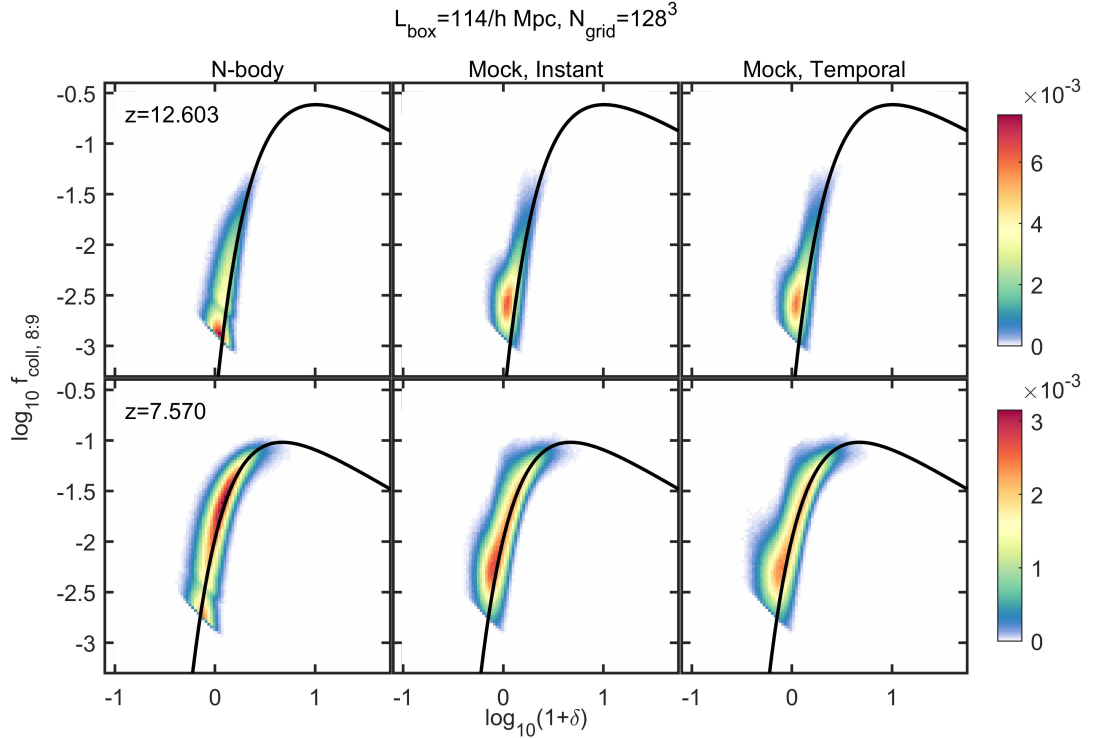


Figure 3.11: Same as in Fig. 3.10, but for  $128^3$  grid (cell size  $0.891 \text{ Mpc } h^{-1}$ ).

### 3.4.1 Testing the method

In Figures 3.8 and 3.9, we show the relation between the number of MHs per cell,  $N_{5,8}$ , and the density of a cell,  $\delta$ , at  $z = 17.215$  (upper panels) and  $z = 10.110$  (lower panels) based on data from our  $6.3 \text{ Mpc } h^{-1}$  box simulation with cell sizes  $450 \text{ } h^{-1} \text{ kpc}$  and  $143 \text{ } h^{-1} \text{ kpc}$ , respectively. Shown are the  $N$ -body simulation data (left panels), the instantaneous mock haloes (middle panels), and temporal mock haloes (right panels). The colours indicate the density of haloes and the solid black lines correspond to the mean (deterministic) bias relation based on Ahn et al. (2015). The particular redshifts shown are chosen as representative of the early and late stages of the epoch during which the MHs are expected to be an important component of and a regulating factor to early star formation (Ahn et al., 2012). For consistency, we will use the same colour scheme throughout this paper to represent the different types of data.

Similarly, Figures 3.10 and 3.11 show plots of the LMACH collapsed fraction,  $f_{\text{coll},8:9}$  vs.  $\delta$  at redshifts  $z = 12.603$  (upper panels) and  $z = 7.570$  (lower panels).

Data is based on the 114 Mpc  $h^{-1}$  volume with  $64^3$  and  $128^3$  grid cells per each dimension (cell sizes of 1.781 Mpc  $h^{-1}$  and 0.891 Mpc  $h^{-1}$ ), respectively. We again show the  $N$ -body simulation data (left panels), the instantaneous mock haloes (middle panels), and temporal mock haloes (right panels). The illustrative redshifts shown roughly correspond to the beginning and the peak of the reionisation process in certain classes of EoR models.

Figures 3.8 and 3.9 show that the relation between  $N_{5:8}$  and  $\delta$ , including stochasticity, closely replicates that of  $N$ -body MHs once the bias is sampled from the lognormal distribution described in the previous section. This is true for both the instantaneous and the temporal case with only minor differences. In all cases the agreement with the mean bias trend (black curve) is excellent.

The stochasticities in the mock halo data have a good agreement with those of the  $N$ -body halo data, but with some modest difference in the low- $\delta$  regime as seen in Figures 3.10 and 3.11. A few “indentations” (or dips) in the distribution of the  $N$ -body halo data (color map) on the  $\delta - f_{\text{coll},8:9}$  plane are visible, which are not apparent in the mock data (Figs. 3.10 and 3.11). These indentations are the obvious result of the discreteness in the number of haloes per cell,  $N_{8:9}$ , which is simply integer numbers. The first “island” of the empirical distribution seen at the lowest- $f_{\text{coll},8:9}$  end in these figures correspond to a single halo per cell, or  $N_{8:9} = 1$ . Due to the natural variance in the mass of these haloes, the actual distribution is seen not as a line but as an island. The same applies to  $N_{8:9} > 1$ , which quickly smears out the indentation feature as  $N_{8:9}$  increases. The mock data of  $f_{\text{coll},8:9}$ , however, is devoid of this indentation feature because  $f_{\text{coll},8:9}$  is realized not from the mock halo but instead directly from applying a smooth PDF of  $f_{\text{coll},8:9}$ . Even though one can generate mock haloes first and then calculate  $f_{\text{coll},8:9}$  later, to recover this indentation feature, we ignore this detail because this feature appears in the very low- $f_{\text{coll},8:9}$  end which takes only a minor fraction of the whole data. Overall, the agreement between the empirical data and the mock data seems reasonable.

Credibility of the generated mock halo catalogues can be tested in terms of statistical measures, and we investigate (1) overall normalisations (either number

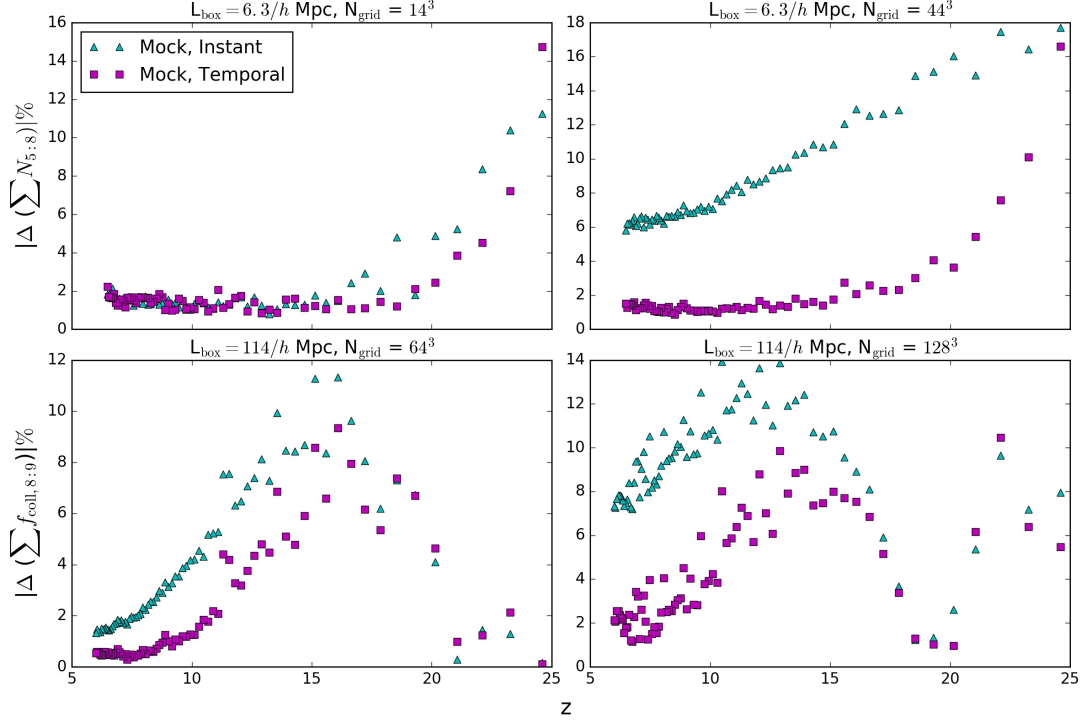


Figure 3.12: Evolution of the absolute value of the percentage difference between the  $N$ -body data and the total number of MHs,  $N_{5:8}$ , (upper panels) and the LMACH collapsed fraction,  $f_{\text{coll},8:9}$ , summed over the grid (lower panels) vs. redshift,  $z$ , for the  $6.3 \text{ Mpc } h^{-1}$  and  $114 \text{ Mpc } h^{-1}$  box respectively. Plotted are the difference between the  $N$ -body data and the instantaneous mock haloes (triangles) and the temporal mock haloes (squares) for the  $14^3$ ,  $44^3$ ,  $128^3$  and  $64^3$  grid, as labelled.

of haloes or total collapsed fraction) for the deterministic bias, (2) the temporal correlation coefficient for the cell-wise evolution, and (3) the power spectrum for the spatial clustering of haloes.

We show the overall normalisations and their evolution with redshift in Figure 3.12. In all cases, difference between the mock data and the  $N$ -body halo data are modest, within  $\sim 15\%$ , and often substantially better, particularly at lower redshifts. The mocks with temporal bias consistently match the simulations more closely than those with instantaneous bias, within  $\sim 2\%$  below  $z = 10$  and otherwise within  $5\%$  or less except for the highest redshifts, where the rarity of haloes make the correlation with the underlying density field weak. The mocks follow the  $N$ -body halo data better for the lower-resolution grids for each volume, and the temporal bias yields little difference for the number of MHs in that case. The instantaneous bias is considerably worse than the temporal bias in

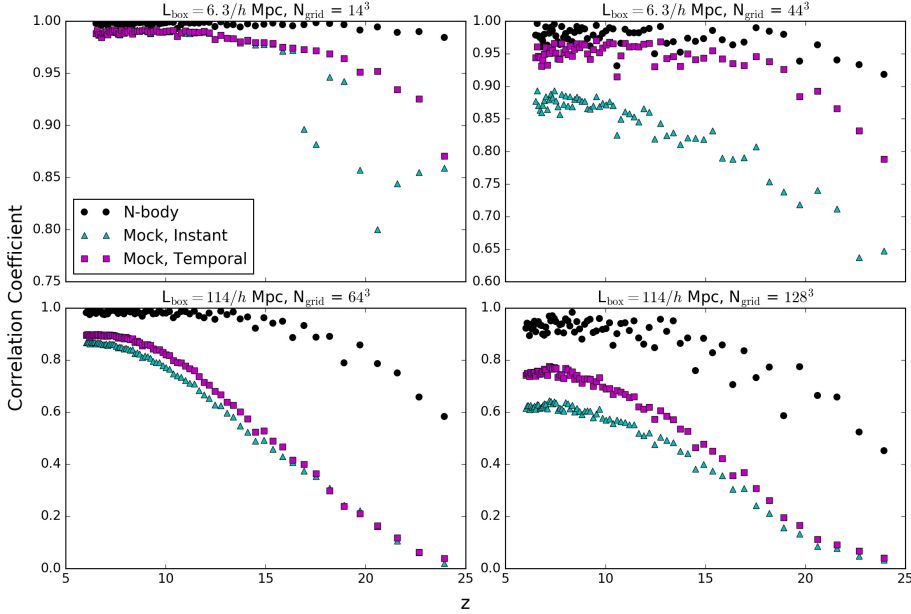


Figure 3.13: Pearson correlation coefficient between consecutive time slices vs redshift  $z$  for: (top)  $6.3 \text{ Mpc } h^{-1}$  box with (left) grids of  $14^3$ , and (right)  $44^3$ , for the simulation data, and realisations of instantaneous mock and temporal mock haloes as labelled; (bottom) same as the top panels, but for  $114 \text{ Mpc } h^{-1}$  box with (left) grids of  $64^3$  and (right)  $128^3$ .

normalisations by up to a factor of 2-4, especially for higher grid resolutions.

Next we compare the Pearson correlation coefficient between consecutive time-slices of the simulation data and the respective generated stochastic realisations.

The correlation coefficient is as usual defined as

$$r_{X,Y} = \frac{\text{cov}(X,Y)}{\sigma_X \sigma_Y}$$

where  $X$  and  $Y$  are the fields being correlated,  $\text{cov}$  is the covariance matrix, and  $\sigma_{X,Y}$  are the standard deviations of  $X$  and  $Y$ , respectively. The value of  $r_{X,Y}$  is 1 if  $X$  and  $Y$  are completely correlated, 0 if they are uncorrelated and  $-1$  if they are completely anti-correlated. We use the values of either  $N_{5:8}$  or  $f_{\text{coll},8:9}$  in each cell at current redshift and the closest previous redshift for  $X$  and  $Y$  respectively. Results are shown in Fig. 3.13. For the simulation data, the late-time correlation is fairly tight in all cases. At early times the correlation coefficient is considerably lower than unity due to the increasing rarity of haloes, and the related significant Poisson noise. At that epoch, the halo population, which form

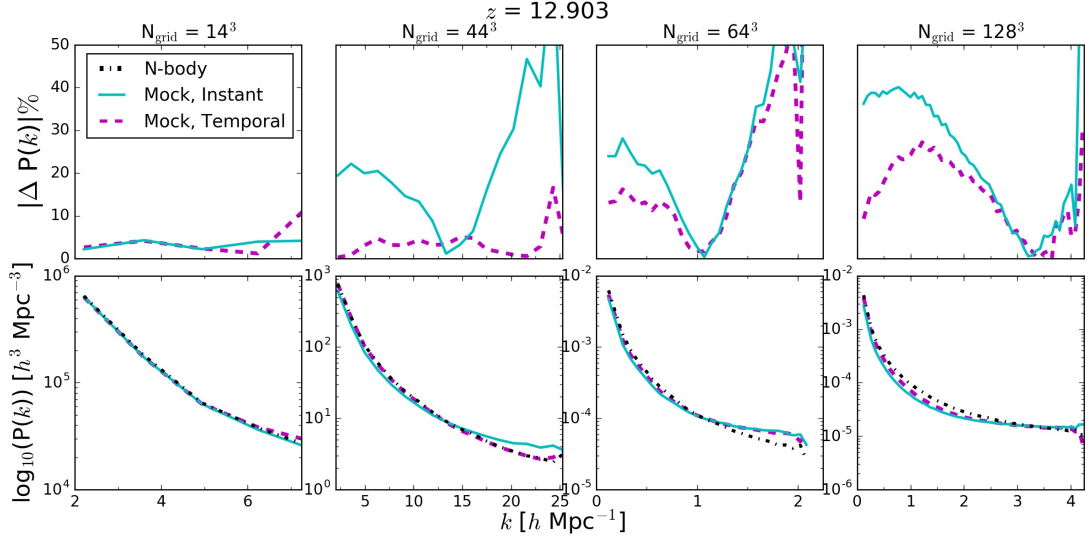


Figure 3.14: The lower panels show the  $P(k)$  and the upper panels show the percentage of absolute difference of the  $P(k)$  between the  $N$ -body data and the mock realisations for the respective grids at  $z = 12.903$ . The black dash-dot line corresponds to the  $N$ -body data, the cyan solid line corresponds to the generated instantaneous mock haloes and the magenta dash line corresponds to the generated temporal mock haloes. The percentage in the upper panel is capped at 50%.

stochastically in high-density regions, grows exponentially, thereby resulting in the lower correlation with the previous time-slice. This effect is larger for more massive haloes, as could be expected, as they are more strongly biased.

Randomly-sampled mocks without the temporal correlation bias significantly underestimate the correlations compared to the simulation data, and yield almost no correlation for LMACHs at high redshift (independent of the grid resolution). As could be expected, in all cases the agreement is improved substantially by including the temporal bias, although the correlation remains somewhat lower than the simulated one. This agreement could potentially be improved further by modifying our model to take into account the tight empirical time correlation found in the simulation data, but at the expense of a more complex model.

Finally, we consider the spatial halo clustering in each case, as represented by the spherically-averaged power spectrum  $P(k)$  whereby the grid sizes are 0.45, 0.14, 1.78 and 0.89  $\text{Mpc}/h$  for the 14, 44, 64, and  $128^3$  grids data;  $P(k)$ 's are shown in Figures 3.14 (for  $z = 12.903$ ) and 3.15 ( $z = 8.283$ ). In these figures, the lower panels show  $P(k)$ , and upper panels show the percentage differences between the mocks and the  $N$ -body halo data, for all cases as labelled. The

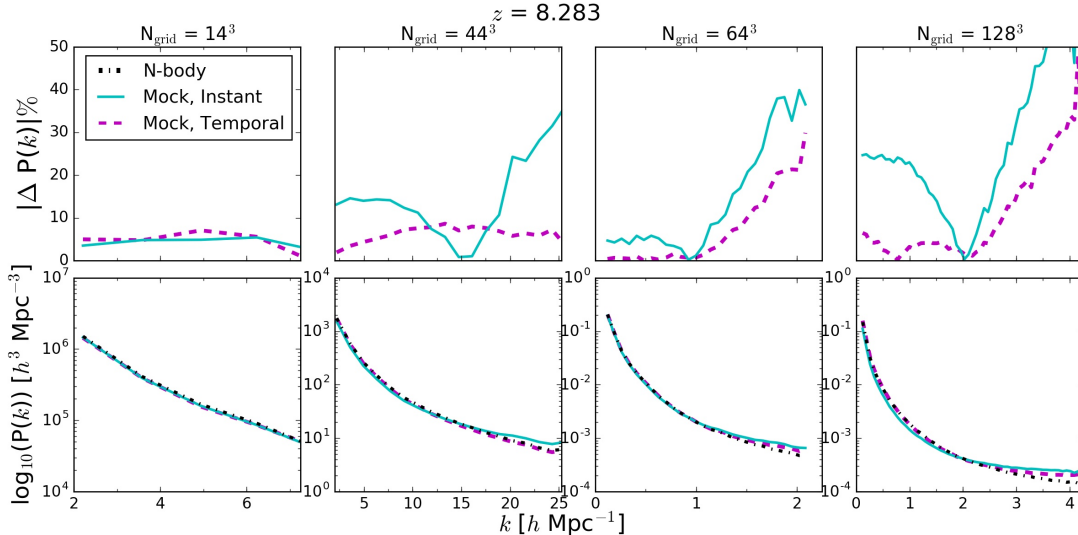


Figure 3.15: Same as Figure 3.14 but for  $z = 8.283$ .

halo clustering of the mock realizations with temporal bias generally matches the simulated one very well, within a few to 10 per cent. The only exceptions are at small scales ( $k \gtrsim 10 h\text{Mpc}^{-1}$ ) and at very high redshift ( $z > 20$  for MHs and  $z > 15$  for LMACHs), due to the aforementioned rarity of haloes at high redshift and the consequent Poisson noise, in which cases the discrepancy can reach  $\sim 50\%$ . The agreement is considerably worse in general when the temporal bias is not included, with typical differences of  $\sim 20\text{-}50\%$ . The only exception is the MH numbers in the low-resolution grid, where the agreement becomes better, indicating that the halo clustering is insensitive to the temporal bias in this limited case.

### 3.4.2 Sub-grid Modelling of Temporal Stochasticity in Multi-Scale Reionisation

We implement our fiducial method, namely assigning stochasticity sampled from a log-normal distribution with temporal correlations (§ 3.3.5) in generating mock halo catalogues on a  $300^3$ -grid density field in a large volume of  $500 \text{ Mpc } h^{-1}$  per side simulated with the CubeP<sup>3</sup>M code (Harnois-Déraps et al., 2013), in which the mass resolution is  $10^9 M_\odot$ . We have previously shown that  $500 \text{ Mpc } h^{-1}$  box is large enough to obtain very reliable statistics in various physical properties of

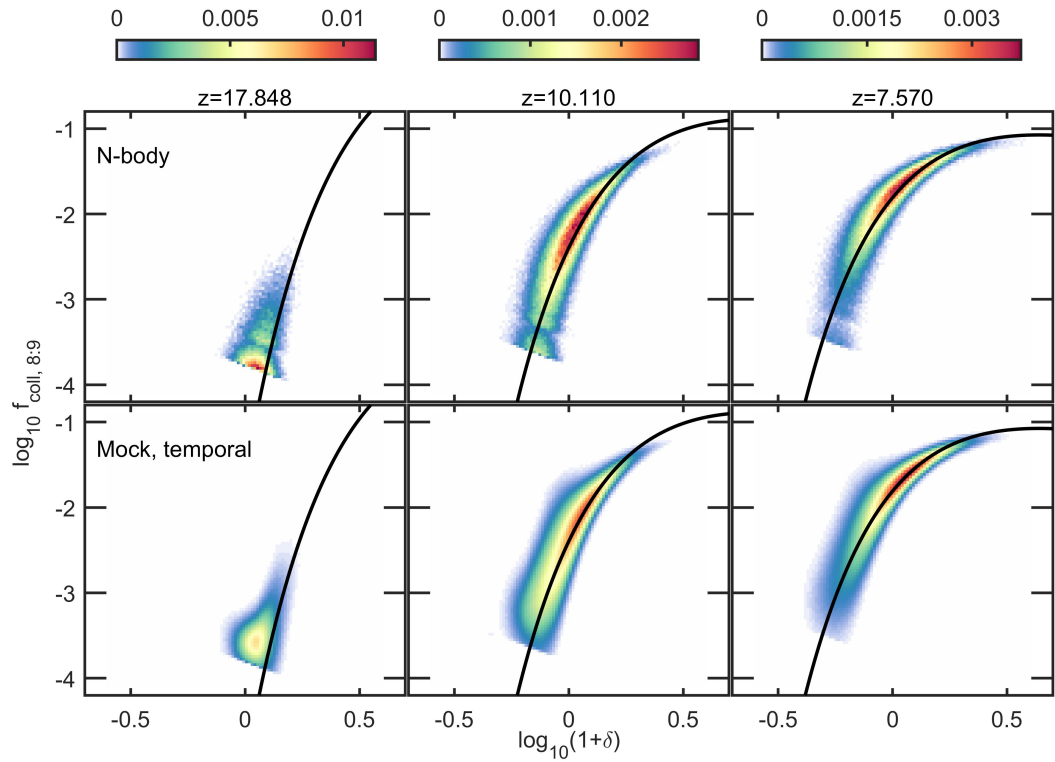


Figure 3.16: The figure shows the LMACH collapsed fraction  $f_{\text{coll},8.9}$  per cell with respect to  $\delta$  at  $z = 17.848, 10.110$  and  $7.570$  (left to right). The top panels correspond to the actual  $N$ -body simulation data from our  $114 h^{-1}$  Mpc box on a  $64^3$  grid, while the bottom panels show the generated mock haloes with temporal bias for  $500 h^{-1}$  Mpc box on a  $300^3$  grid. The plotting convention is the same as in Figure 3.10.

EoR (Iliev et al., 2014), and  $300^3$ -grid is optimal for simulating patchy reionisation with reasonable computational resources. The size of the grid cell is also chosen to match the cell size of the  $64^3$ -grid in  $114 \text{ Mpc } h^{-1}$ -box we used above for the LMACHs collapsed fraction. This approach enables populating such a large volume, which is usually limited in realizing small-mass haloes due to numerical resolution limit, with LMACHs very reliably as shown in the previous sections.

In Figure 3.16 we show the modelled stochasticity with temporal correlations of the  $f_{\text{coll};8;9}$  over a range of redshifts, representative of the early, middle and late phases of reionisation, respectively. The overall characteristics of the mock data are in good agreement with those of the  $N$ -body data, as intended. While not clearly shown in Figure 3.16, the large volume contains cells with  $\delta$ 's in the more extended tail ends of the PDF than the small box. We note that it is again difficult to simulate the apparent dip (dubbed as “indentation” in § 3.4.1) shown in the  $N$ -body data with this prescription.

We compare the power spectra generated from the mock vs.  $N$ -body data (Figure 3.17) to check the reliability of our approach for future reionisation simulations. For the range of redshifts shown and wavenumbers  $k \lesssim 1 h^{-1} \text{ Mpc}$ , the error is no larger than  $\sim 10 - 30\%$ . At the same wavenumber range,  $P(k)$  of the mock data has a trend to be larger at high  $z$  but gradually shifting to be smaller at low  $z$  than that of the  $N$ -body data. Disagreement always exists for  $k$ 's around the Nyquist value, whose impact on reionisation requires further investigation. However, we expect that the influence of this will be minor if one is only interested in relatively large-scale ( $k \lesssim 1 h^{-1} \text{ Mpc}$ ) phenomena.

## 3.5 Summary and Discussion

In this work we present a novel scheme developed for creating realistic sub-resolution low-mass halo populations in large-scale  $N$ -body simulation volumes. The mock haloes produced by our method reproduce the correct average local numbers or collapsed fraction of the unresolved haloes very well, down to the smallest halo masses, as well as their spatial clustering and local population evo-

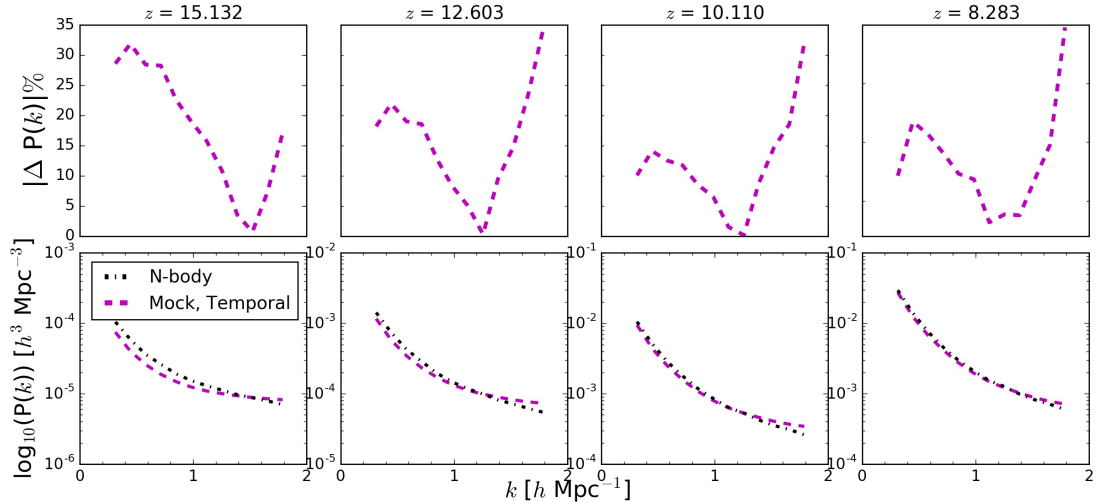


Figure 3.17: The lower panels show the  $P(k)$  and the upper panels show the percentage of absolute difference of the  $P(k)$  of  $f_{\text{coll};8:9}$  at the indicated redshift between the  $N$ -body ( $114 \text{ Mpc } h^{-1}$ ,  $64^3$  grid, black dotted in lower panel) and mock data ( $500 \text{ Mpc } h^{-1}$ ,  $300^3$  grid; magenta dashed).

lution. This new halo bias prescription can be used as a sub-grid model for studies of structure formation for a range of applications that would otherwise be limited in dynamic range, thereby enabling studies of the small-scale structures and their impact within large, cosmological volumes.

We achieve this by including not only the deterministic bias as a function of the local density environment (Ahn et al., 2015), but also an additional stochastic bias, which accounts for its other dependencies, which yields a more natural representation of the universe. Using very high-resolution  $N$ -body data, we have compared two distinct methods for realising this stochastic bias: (1) stochasticity reconstruction based on the current cell overdensity  $\delta$  only and (2) one based on both  $\delta$  and the past history of the halo population in that locality. We found the latter method, which we dubbed “temporal bias”, is superior to the former. Including the temporal bias yields mock halo catalogues with significantly better statistical properties than without it in terms of the local halo population evolution as well as the power spectrum  $P(k)$  of the 3D halo-number field, both compared to the high-resolution  $N$ -body data where the relevant halo range is resolved.

There are a number of possible applications for our method. A direct ap-

plication of this temporal bias is in simulations of cosmic reionization. They require very large dynamic range, since the H II region expansion is driven by low-mass galaxies, while proper statistics of the patchiness demands very large volumes to be followed (Iliev et al., 2014). Importantly, in this case, the evolution is cumulative and depends on the temporal evolution of structure formation. This is in contrast to e.g. cosmology studies with galaxy surveys, where only an instantaneous halo bias is necessary at any observed redshift. In the future, we will use these results to perform very large-box simulations of cosmic reionization with minimum halo mass of  $10^5 - 10^8 M_\odot$  and  $500 h^{-1} \text{Mpc}$  volume, which requires applying our scheme to model the haloes with masses below  $10^9 M_\odot$  and thus to overcome the numerical resolution limit. The mock halo catalogue of LMACHs we generated for this volume, presented in § 3.4.2 is promising, in a reasonable agreement in terms of its statistical properties, especially  $P(k)$  of the 3D collapsed fraction field, compared to  $N$ -body halo data from a smaller volume ( $114 h^{-1} \text{Mpc}$ ), where LMACHs haloes are directly resolved.

This study shows that the temporal correlation in stochasticity plays an important role in shaping the statistical properties of cosmological haloes. This is proven by the fact that the temporal bias (method 2 above) generates halo catalogues in much better agreement with the  $N$ -body halo data than method (1) in terms of  $P(k)$  and cross-correlations. This also implies that even when one is to generate halo catalogues for the study of galaxy surveys, which seemingly requires an instantaneous halo bias, this temporal bias scheme can work as a very reliable solution. Further study along this line is warranted.

There are some caveats and room for improvement in our methodology. In our current approach, the temporal bias is based on the complete history of a given Eulerian cell, while in reality the stochasticity should only depend on the past history. Furthermore, advection of matter to and from neighbouring cells means that the Eulerian cell density does not contain the full information on the matter field evolution. For a better temporal bias prescription, one may instead adopt a scheme that takes a limited lookback-time history of an Eulerian cell to mitigate these two problems. This requires further investigation, which we

will address in the near future. While our approach and results are general, the specific parameterisation of the temporal bias is based on empirical fits based on a specific structure-formation simulation. Therefore, if one were to apply this to a universe described by a different set of cosmological parameters, our approach would require a new small-box, high-resolution simulation resolving haloes of our interest. It would be preferable to find a more analytical scheme that allows *deterministic temporal stochasticity* in halo bias that could be easily re-calculated.

Regardless of this, our enhanced scheme, which accounts for the temporal bias, provides significant improvement over the same scheme without temporal bias, yielding a more accurate mock halo catalogues at high redshift, which will be very helpful in improved descriptions of the cosmic reionization process and interpretation of high-redshift observations. Using this approach will yield better answers on how much impact low-mass haloes, which have usually been neglected or treated with crude approximations, have on structure formation at high redshift and the history of cosmic reionization.

### 3.6 Acknowledgment

AN is supported by the Australian Research Council Centre of Excellence for All Sky Astrophysics in 3 Dimensions (ASTRO 3D), through project number CE170100013. KA was supported by NRF-2016R1D1A1B04935414 and NRF-2016R1A5A1013277. This work was supported by the Science and Technology Facilities Council [grant number ST/I000976/1] and the Southeast Physics Network (SEPNet). We acknowledge that the results in this paper have been achieved using the PRACE Research Infrastructure resource Marenostrom based in the Barcelona Supercomputing Center, Spain. Time on this resource was awarded by PRACE under PRACE4LOFAR grants 2012061089 and 2014102339 as well as under the Multi-scale Reionization grants 2014102281 and 2015122822. The authors gratefully acknowledge the Gauss Centre for Supercomputing e.V. ([www.gauss-centre.eu](http://www.gauss-centre.eu)) for funding this project by providing computing time through the John von Neumann Institute for Computing (NIC) on the GCS Supercomputer

JUWELS at Jülich Supercomputing Centre (JSC). Some of the numerical computations were done on the Apollo cluster at The University of Sussex. KA also appreciates APCTP for its hospitality during completion of this work.

# Chapter 4

## The Impact of Realistic Foreground and Instrument Models on 21 cm Epoch of Reionisation Experiments

This work was published by Nasirudin, A., Murray, S. G., Trott, C. M., Greig, B., Joseph, R. C., and Power, C. in the *Astrophysical Journal*, Volume 893, Issue 2, id.118. DOI:10.3847/1538-4357/ab8003

### 4.1 Abstract

Predictions for the ability of 21-cm interferometric experiments to discriminate Epoch of Reionisation (EoR) signal models are typically limited by the simplicity of data models, whereby foreground signals and characteristics of the instrument are often simplified or neglected. To move towards more realistic scenarios, we explore the effects of applying more realistic foreground and instrument models to the 21 cm signal, and the ability to estimate astrophysical parameters with these additional complexities. We use a highly-optimized version of 21CMFAST, integrated into 21CMMC, to generate lightcones of the brightness temperature fluctuation for Bayesian parameter estimation. We include a statistical point-source foreground model and an instrument model based on the Murchison Widefield Array (MWA) scaled in observation time to have an effective sensitivity similar to the future Square Kilometre Array (SKA). We also extend the current likelihood prescription to account for the presence of beam convolution and foregrounds, the

2-Dimensional Power Spectrum (PS), and the correlation of PS modes. We use frequency bands between 150 and 180 MHz to constrain the ionising efficiency ( $\zeta$ ), the minimum virial temperature of halos ( $T_{\text{vir}}$ ), the soft X-ray emissivity per unit Star Formation Rate (SFR) ( $L_X/\text{SFR}$ ), and the X-ray energy threshold ( $E_0$ ). We find that the inclusion of realistic foregrounds and instrumental components biases the parameter constraints due to unaccounted for cross-power between the EoR signal, foregrounds and thermal noise. This causes estimates of  $\zeta$  to be biased by up to  $5\sigma$  but the estimates of  $T_{\text{vir}}$ ,  $L_X/\text{SFR}$  and  $E_0$  remain unaffected and are all within  $1\sigma$ .

## 4.2 Introduction

The Cosmic Dawn (CD) and the subsequent Epoch of Reionisation (EoR) mark the end of the cosmic dark ages, during which time the baryonic content of the dark, early universe existed in a warm, neutral state. The intergalactic medium (IGM), predominantly comprised of hydrogen, was illuminated by photons from the first ionising sources, forming regions of reionised hydrogen with temperatures contrasting with the neutral IGM and background CMB (Barkana & Loeb 2001; Furlanetto et al. 2006b). The significance of these periods is prevalent in almost all areas of astrophysics, particularly in understanding the transition between the current and early universe as well as the formation of primordial structures in the universe.

A key probe into these epochs is the imprint of the 21 cm spin-flip transition of neutral hydrogen (HI) that is redshifted into the low-frequency radio regime. Recently, the Experiment to Detect the Global Epoch of Reionization Signature (EDGES) published a measurement of a flattened absorption profile with timing that somewhat coincides with the expected HI signal from the CD (Bowman et al., 2018), although it needs further verification from independent experiments. Detection of the EoR, however, has not been reported and remains one of the key science goals of most current low-frequency interferometric telescopes (e.g., the Murchison Widefield Array (MWA) (Tingay et al., 2013; Wayth et al., 2018),

the Hydrogen Epoch of Reionization Experiment (HERA) (DeBoer et al., 2017), and the Low Frequency Array (LOFAR) (van Haarlem et al., 2013)).

Since direct imaging of the EoR remains beyond the sensitivity capabilities of current experiments, these instruments aim to detect the spatial fluctuations of the averaged power spectrum. In the near future, however, upcoming low-frequency interferometers such as the Square Kilometre Array (SKA) (Dewdney et al., 2009) and the final phase of HERA are expected to have the sensitivity to directly detect the tomographic imprints of the EoR.

Even with experiments focused on the detection of the variance instead of direct imaging of the EoR signal, its detection is still challenging due to astrophysical foregrounds and other contaminants. These include foregrounds from Galactic and extragalactic origins (Jelić et al. 2010; Gleser et al. 2008), ionospheric distortion (Jordan et al., 2017), instrument noise and radio frequency interference (Offringa et al., 2015). The foregrounds prove to be the primary contaminant as they are expected to be up to 5 orders of magnitude brighter than the 21 cm signal (Pritchard & Loeb, 2012). Various foreground mitigation and removal methods have been extensively studied (e.g. see Liu & Shaw (2020) for details); however, for foreground removal method such as source peeling, residual power is still left in the power spectrum due to our incomplete knowledge of the extra-galactic foregrounds. This is due to imperfect peeling and fainter sources existing below the peeling threshold (Datta et al., 2010; Trott et al., 2012; Morales et al., 2012; Vedantham et al., 2012)<sup>1</sup>.

Exploration of a physical understanding of the EoR is performed through theoretical simulations of the sources and signal to help supplement observations and constrain the signal. In particular, most simulation work has focused on establishing the roles of the first ionising sources and finding the impact of astrophysical parameters on the signal (see eg. Barkana & Loeb 2001; Ricotti & Ostriker 2004; Madau et al. 2004; Knevitt et al. 2014). Although countless parameters may affect the EoR signal whose estimates vary across the literature, some of the most influential EoR parameters (and their generally-accepted esti-

---

<sup>1</sup>In this work, we assume that the former is negligible and focus on the latter.

mates) are: the number of ionising photons per baryon ( $N_\gamma \sim 4000$ ) (Barkana & Loeb, 2005); the power-law scale of the baryonic gas fraction in stars with source halo mass ( $\alpha_* \approx 0.5$ ) (Behroozi & Silk, 2015; Ocvirk et al., 2016); and the number of times a hydrogen atom recombines ( $n_{rec} \approx 1$ ) (Sobacchi & Mesinger, 2014).

The ultimate goal of understanding the EoR from 21 cm observations will require constraining these parameters using theoretical models. It involves quantitatively evaluating the cosmic EoR signal by making use of one of the many existing EoR simulations, usually semi-numerical, to extract information on the astrophysics. Aside from comparing the results of fiducial reionisation simulations with experimental data (Choudhury & Ferrara, 2005), other methods used to achieve this goal include using the maximum likelihood ( $\chi^2$ ) fitting (Barkana, 2009), and Bayesian analyses via model selection (Binnie & Pritchard, 2019) or Monte Carlo Markov Chain (MCMC) methods (see eg. Harker et al., 2011; Patil et al., 2014; Greig & Mesinger, 2015; Hassan et al., 2017)<sup>2</sup>. Alternative methods to on-the-fly MCMC sampling include emulating simulations using the power spectrum (Kern et al., 2017) and using artificial neural networks (Shimabukuro et al., 2017; Schmit & Pritchard, 2018) or convolutional neural network (Gillet et al., 2019).

A particularly powerful existing code that uses the MCMC approach is 21cmMC (Greig & Mesinger, 2015; Greig & Mesinger, 2017, 2018). 21cmMC is a parallelized, efficient EoR analysis code that wraps the publicly-available EoR semi-numerical simulator 21cmFAST (Mesinger et al., 2011) into its Bayesian MCMC framework to produce an EoR lightcone per-iteration<sup>3</sup>. It uses the differential brightness temperature field, constructed as a lightcone, to compute the spherically averaged power spectrum that is, in turn, used in the likelihood prescription.

Previous applications of 21cmMC have used 21cmSENSE<sup>4</sup> to gauge the uncertainties in the 1-Dimensional (1-D) power spectrum arising from the instrumental

---

<sup>2</sup>The recent work of Sims & Pober (2019) also uses an MCMC framework, but focuses on estimating the power spectrum band-powers rather than astrophysical parameters, though it mentions a simple extension to do so.

<sup>3</sup>In this work, we use the most recent version available at <https://github.com/BradGreig/Hybrid21cm>. As of writing, the most up-to-date version of 21cmMC has moved permanently to <https://github.com/21cmFAST/21cmMC>, and the underlying optimized 21cmFAST code has been modularized and exists at <https://github.com/21cmFAST/21cmFAST>.

<sup>4</sup><https://github.com/jpober/21cmSense>

noise and smooth foregrounds, completely excising spherical  $k$ -modes dominated by the latter (Poher et al., 2013; Poher et al., 2014). While this approach is a good first-order approximation, it does not account for potential residual foreground contamination in  $k$ -modes that it uses due to more complicated instrumental systematics. This can cause difficulties in disentangling contamination and signal power, thus possibly leading to a biased estimate of reionisation parameters. Moreover, it does not account for the induced chromaticity from the instrument on the 21 cm signal.

This work provides an extension to 21cMMC in the publicly-available plugin PY21cMMC-FG. Using this framework, we aim to explore the impact of foreground and instrumental components on the ability to constrain the astrophysical parameters of the EoR. We apply a statistical point-source foreground model and an MWA-based instrument model to the 21cmMC lightcone outputs before averaging to a power spectrum. It is these “corrupted” lightcones that we use to estimate observed power spectra within the MCMC framework, thereby investigating more realistic constraints on astrophysical parameters.

The paper is structured as follows. We first setup the mathematical framework, which includes describing the foreground and instrumental effects we employ in our analysis, in §4.3. In §4.4, we analyze the observational effects on the EoR lightcones and in §4.5, we present the MCMC analysis using 21cmMC with our pipeline. We then discuss the results in §4.6 and conclude in §4.7.

## 4.3 Mathematical Framework

### 4.3.1 Interferometric Visibilities

The baseline displacement,  $\mathbf{u}$ , is defined as  $\mathbf{u} = \mathbf{x}/\lambda$ , where  $\mathbf{x}$  is the physical displacement between the baseline tiles and  $\lambda$  is the wavelength. We define the sky coordinate as  $\mathbf{l} = (l, m) = (\sin \theta \cos \phi, \sin \theta \sin \phi)$ , where  $\theta$  is the zenith angle, and  $\phi$  the angle around the zenith pole.

Based on these definitions, the measured correlation of the electric fields between two sensors for an interferometric observation, the visibility  $V(\mathbf{u}, \nu)$  at

frequency  $\nu$ , in the flat-sky approximation is defined as

$$V(\mathbf{u}, \nu) = \int I(\mathbf{l}, \nu) B(\mathbf{l}, \nu) \exp(-2\pi i \mathbf{u} \cdot \mathbf{l}) d\mathbf{l} \quad [\text{Jy}], \quad (4.1)$$

with  $I(\mathbf{l}, \nu)$  and  $B(\mathbf{l}, \nu)$  being the intensity of each point-source and beam attenuation at sky coordinate  $\mathbf{l}$  and frequency  $\nu$ , respectively. Using the flat-sky approximation whereby the effects of curvature are neglected, we assume that the observed interferometric visibility is identical to the Fourier Transform of the product of signal and the beam model. We will address the second-order effects of spatial curvature on the visibility in future work.

### 4.3.2 Brightness Temperature and Power Spectrum

The EoR differential brightness temperature,  $\delta T_b$ , can be quantified by (Furlanetto et al., 2006b)

$$\begin{aligned} \delta T_b(z) \approx & 27 x_{\text{HI}} (1 + \delta_{\text{nl}}) \left( \frac{H(z)}{dv/dr + H(z)} \right) \left( 1 - \frac{T_\gamma}{T_s} \right) \\ & \times \left( \frac{1+z}{10} \frac{0.15}{\Omega_m h^2} \right)^{\frac{1}{2}} \left( \frac{\Omega_b h^2}{0.023} \right) [\text{mK}]. \end{aligned} \quad (4.2)$$

Here,  $x_{\text{HI}}$  is the neutral fraction,  $\delta_{\text{nl}}$  is the evolved Eulerian overdensity,  $H$  is the evolving Hubble constant,  $dv/dr$  is the gradient of the line-of-sight velocity component,  $T_\gamma$  is the temperature of the CMB,  $T_s$  is the spin temperature of ,  $z$  is the redshift,  $\Omega_m$  is the dimensionless matter density parameter,  $\Omega_b$  is the dimensionless baryonic density parameter and  $h$  is the normalized Hubble constant.

For interferometric observations, the power spectrum (hereafter PS), is the primary metric used to characterise the EoR signal. It measures the spatial variance of a signal over a spatial volume  $V$  and is defined as

$$P(k) \equiv \frac{|\langle \delta T_b^\dagger(\vec{k}) \delta T_b(\vec{k}) \rangle_{|\vec{k}|=k}|}{V} \quad [\text{mK}^2 \text{ Mpc}^{-3} h^3], \quad (4.3)$$

where  $k$  is the spatial scale in Fourier space. The PS can be computed either

directly from the image cube or from the observed interferometric visibilities, whereby the signal is spherically-averaged over the 3-D spatial scales and is normalised by the volume of the observed area of the sky. The dimensionless 1-D PS is given by

$$\Delta^2(k) = \frac{k^3}{2\pi^2} P(k) \quad [\text{mK}^2], \quad (4.4)$$

and is routinely used in current experiments.

It is useful, however, to first compute the cylindrically-averaged 2-D PS,  $P(k_\perp, k_\parallel)$ . The angular and line-of-sight modes of the 2-D PS,  $k_\perp$  and  $k_\parallel$ , are converted from the Fourier dimensions following (Morales & Wyithe, 2010)

$$k_\perp = \frac{2\pi|\mathbf{u}|}{D_M(z)} \quad [\text{Mpc}^{-1}\text{h}], \quad (4.5)$$

and

$$k_\parallel = \frac{2\pi H_0 f_{21} E(z)}{c(1+z)^2} \eta \quad [\text{Mpc}^{-1}\text{h}]. \quad (4.6)$$

Here,  $z$  is the observation redshift,  $D_M(z)$  is the transverse comoving distance,  $H_0$  is the Hubble constant,  $f_{21}$  is the rest frequency of the 21 cm hydrogen hyperfine transition and  $E(z)$  is defined as

$$E(z) = \sqrt{\Omega_m(1+z)^3 + \Omega_k(1+z)^2 + \Omega_\Lambda}, \quad (4.7)$$

where  $\Omega_\Lambda$ , and  $\Omega_k$  are the dimensionless density parameters for dark energy and the curvature of space. Because the 2-D PS bins the signal into separable perpendicular and line-of-sight modes, it effectively allows for the management of systematic effects arising from the different modes, and hence is commonly used as an initial step to decontaminate the cosmological EoR signal from the foregrounds. Colloquially termed the “wedge”, the broad region of cylindrical  $k$ -space dominated by the foregrounds can be understood as the signature of smooth-spectrum foregrounds when being sampled by an imperfect instrument (Vedantham et al., 2012; Trott et al., 2012; Parsons et al., 2012; Datta et al., 2010). The key imperfections are the band-limiting attenuation due to the primary beam, and the discrete sampling of an interferometer, where the sampled wavemodes change

with frequency (“chromaticity”).

### 4.3.3 Components of Observable Signal

In this subsection, we present the mathematical framework of the different components of the observable signal, which is made of the EoR signal and foregrounds as observed by our instrument model.

#### 4.3.3.1 EoR Lightcones and Parameters

We use a model  $\delta T_b$  field generated by 21CMFAST wrapped in 21CMMC. 21CMFAST is a semi-numerical EoR modelling tool designed to efficiently simulate the 21-cm signal using approximate methods combining the excursion-set formalism (Bond et al., 1991; Furlanetto et al., 2004) and perturbation theory. The code generates realizations of  $\delta_{nl}$ , ionisation, peculiar velocity, and  $T_s$  in 3D which are then combined to compute  $\delta T_b$  during the EoR. The astrophysical parameters involved in the code are customizable, allowing for the exploration of models and parameter space affecting the EoR (Mesinger et al., 2011; Mesinger et al., 2014).

The key parameters that we are primarily interested in are:

- the ionising efficiency i.e., the number of ionising photons escaping into the IGM per baryon ( $\zeta$  [dimensionless])
- the minimum virial temperature of halos required to form stars in galaxies ( $T_{\text{vir}}$  [K])
- the soft X-ray emissivity per unit Star Formation Rate (SFR) escaping galaxies ( $L_X/SFR$  [ $\text{erg s}^{-1} \text{keV}^{-1} \text{M}_{\odot}^{-1} \text{yr}$ ])
- the X-ray energy threshold for self-absorption by galaxies ( $E_0$  [keV]).

These four parameters are chosen due to their relatively high influence on the  $\delta T_b$  field, as they directly affect the parameters governing  $T_b$  given by Eq. 4.2, particularly  $x_{\text{HI}}$ <sup>5</sup>. The fiducial values (and ranges) we adopt are based on Greig

---

<sup>5</sup>21cmMC now includes an updated parameterization that uses >6 parameters, but we chose this “legacy” set for ease of comparison to previous work.

Parameter	Fiducial Value	Range
$\zeta$	20.0	[10, 250]
$\log_{10}(T_{\text{vir}})$	4.48	[4, 6]
$\log_{10}(L_X/\text{SFR})$	40.5	[38, 42]
$E_0$	0.5	[0.1, 1.5]

Table 4.1: Fiducial astrophysical parameters and their ranges adopted in this work.

& Mesinger (2017), Park et al. (2019) and Gillet et al. (2019) and summarised in Table 4.1. We note that we only use these values in our final analysis in §4.6. For exploration and validation purposes presented in §4.4 and 4.5, we use the default parameters of  $\zeta = 30$  and  $\log_{10}(T_{\text{vir}}/\text{K}) = 4.7$ . We also use the same random seed to generate the signal throughout this research.

We assume a  $\Lambda$  Cold Dark Matter ( $\Lambda$ CDM) universe using the default cosmological parameters values of 21CMFAST ( $h = 0.68$ ,  $\Omega_b=0.048$ ,  $\Omega_m= 0.31$ ,  $\Omega_k=0$ , and  $\Omega_\Lambda= 0.69$ ), consistent with results from Adam et al. (2016).

The conversion from  $T_b$  to flux density  $S(\nu)$  is given by the beam-modified Rayleigh-Jeans law,

$$S(\nu) = \left( \frac{2k_B T_b}{A_{\text{eff}}} \right) \Omega \times 10^{26} \quad [\text{Jy}], \quad (4.8)$$

where  $k_B$  is the Boltzmann constant,  $A_{\text{eff}}$  is the effective area of the tile (units of  $\text{m}^2$ ) and  $\Omega$  is the angular size of the beam (units sr).

#### 4.3.3.2 Point-Source Foreground Model

We use a simple point-source foreground model to simulate the effects of extragalactic foreground sources based on the power-law relation,

$$\frac{dN}{dS}(S, \nu) = \alpha S_\nu^{-\beta} \left( \frac{\nu}{\nu_0} \right)^{-\gamma\beta} [\text{Jy}^{-1}\text{sr}^{-1}]. \quad (4.9)$$

Here,  $dN/dS$  is the source spatial density per unit flux density,  $S_\nu$  is the flux at a specific frequency  $\nu$ ,  $\beta$  is the slope of the source-count function, and  $\gamma$  is the mean spectral-index of point sources. We fiducially use  $\alpha = 4100 \text{ Jy}^{-1} \text{ sr}^{-1}$ ,  $\beta = 1.59$ , and  $\gamma = 0.8$  at  $\nu_0 = 150 \text{ MHz}$  based on an observational result from Intema

et al. (2011).

Our adopted statistical foreground model, while an improvement over previous modeling in the context of parameter estimation, is by no means complete. It ignores potential point-source clustering (Murray et al., 2017), ionospheric effects (Jordan et al., 2017; Mevius et al., 2016; Trott et al., 2018), and more subtly, any potential correlations of the foregrounds with their antecedent EoR counterparts. More importantly, we have not included a galactic diffuse foreground model in this work. These effects are expected to be second-order, except for the diffuse emission, which is bright and spatially-structured. These components are left as extensions to this work.

#### 4.3.3.3 MWA and SKA-based Instrument Model

Our instrument components are based on the MWA (Tingay et al., 2013; Wayth et al., 2018) and the future SKA (Dewdney et al., 2009). The MWA is a low-frequency radio aperture array telescope located at the Murchison Radio Astronomy Observatory (MRO) site in Western Australia. The array consists of 128 connected tiles with an effective area per tile ( $A_{\text{eff}}$ ) of  $21 \text{ m}^2$  at 150 MHz. Each tile consists of a 4x4 grid of dual polarization dipoles with a full-width half-maximum field of view of  $26^\circ$  at  $\nu_0 = 150 \text{ MHz}$ . It operates in the 80 – 300 MHz frequency range, making it an excellent probe of the redshifted EoR signal. As one of its primary scientific goals, the MWA reionisation observing scheme spans two 30 MHz bands, between 137 – 167 MHz and 167 – 197 MHz (Jacobs et al., 2016).

The low-frequency part of the future SKA (SKA-low) will be located at the MRO alongside the MWA (Dewdney et al., 2009; Mellema et al., 2013). It is expected to have a frequency resolution of 1 kHz with a frequency band of 50 to 200 MHz, and a Field-Of-View (FOV) of  $2.5^\circ - 10^\circ$ .

The instruments themselves are hugely complicated; e.g., primary beam responses change between antennas, pointing and polarisation (Sutinjo et al., 2015b); the dipole array structure yields complex, frequency-dependent beam patterns (Sutinjo et al., 2015b); and signal transport over coaxial cable can lead to cable re-

flections (imprinting frequency structure into the signal chain) (Kern et al., 2020); and the large FOV introduces wide-field effects (Thyagarajan et al., 2015a,b). We restrict ourselves to the primary instrumental response, including baseline sampling, FOV, and frequency-dependent primary beams, because these are the leading-order effects, and leave other instrumental effects to future work. We also neglect the fact that the earth is rotating and assume a fixed zenith pointing at the same patch of the sky. Neglecting the rotation of the Earth changes the  $uv$  coverage of the visibilities, hence the sample variance is different, and, due to the wide FOV of the MWA, amounts to a reduction of the overall thermal noise by (only) a factor of up to three on long baselines for the same total integration time. While this should be kept in mind, it is tangential to the point of our present work, and will be explored in more detail in future work.

We approximate the beam attenuation,  $B(\mathbf{l}, \nu)$ , to be Gaussian-shaped with

$$B(\mathbf{l}, \nu) = \exp\left(\frac{-|\mathbf{l}|^2}{\sigma_{\text{beam}}^2(\nu)}\right), \quad (4.10)$$

where

$$\sigma_{\text{beam}}(\nu) \simeq \frac{\epsilon c}{\nu D}. \quad (4.11)$$

Here,  $\epsilon \simeq 0.42$  is the scaling from the more natural Airy disk to a Gaussian width,  $c$  is the speed of light and  $D$  is the tile diameter (4 m for the MWA). Although the wide field-of-view of the MWA renders the flat sky-approximation (and hence Eq. 4.1) inaccurate (Thyagarajan et al., 2015a,b), we will still use it as a reasonable first approximation as the curved-sky treatment will be much more important when using a more realistic beam with side-lobes, which enhances the “pitchfork” effect. We assume a fixed zenith pointing of the instrument over  $\mathbf{l} \in (-1, 1)$  and pad the sky with zeros over 3 times the size of the sky to increase the resolution of the discrete Fourier Transform.

We add thermal noise to our framework corresponding to both measurement and radiometric noise. This is the uncertainty of the visibility arising from the

finite number of samples, given by

$$\sigma_N = 10^{26} \frac{2k_B T_{\text{sys}}}{A_{\text{eff}}} \frac{1}{\sqrt{\Delta\nu \Delta t}} \quad [\text{Jy}], \quad (4.12)$$

where  $T_{\text{sys}}$  is the system temperature,  $\Delta\nu$  is the bandwidth of one frequency channel, and  $\Delta t$  is the integration time of the observation in seconds.  $\sigma_N$  is essentially an estimation of the global sky signal (or temperature) for a given set of information that is dependent on the sky temperature, bandwidth and sampling time for each visibility.

In addition, we use the unnormalized<sup>6</sup> Fourier Gaussian beam kernel in re-gridding the visibilities after baseline sampling where the weight in cell  $i$ ,  $w_i$  is given by

$$w_i = \exp(-[\pi\sigma_{\text{beam}}(\nu)|\mathbf{u}_i - \mathbf{u}_j|^2]), \quad (4.13)$$

for baseline  $j$ . The gridded visibility  $V_{\text{grid}}(\mathbf{u}, \nu)$  is, hence, given by

$$V_{\text{grid}}(\mathbf{u}, \nu) = \frac{\sum_{i=0}^{N_{\text{bl}}} w_i V(\mathbf{u}_i, \nu)}{\sum_{i=0}^{N_{\text{bl}}} w_i}, \quad (4.14)$$

where  $N_{\text{bl}}$  is the number of all included baselines. A Blackman-Harris frequency taper ( $H(\nu)$ ) has also been applied to reduce spectral leakage in the side lobes due to the limited bandwidth. Note that we do not normalize the beam and taper, but the steps we have taken are consistent with those taken by current 21 cm experiments.

#### 4.3.3.4 2-D Power Spectrum

In this work, we mostly use observational units hence  $k_{\perp}$  and  $k_{\parallel}$  are known as  $u$  [unitless] and  $\eta$  [1 / MHz] respectively and the 2-D PS ( $P(\mathbf{u}, \eta)$ ) is in unit of  $\text{Jy}^2 \text{Hz}^2$ . We compute  $P(\mathbf{u}, \eta)$  by cylindrically averaging the power of the visibilities

---

<sup>6</sup>The normalization cancels out in Equation 4.14.

within radial bin  $\mathbf{u}$ ,

$$P(\mathbf{u}, \eta) \equiv \frac{\sum_{\mathbf{u}_i < \mathbf{u}} \left( \sum_{i=0}^{N_{\text{bl}}} w_i \right)^2 V_{\text{grid}}^\dagger(\mathbf{u}_i, \eta) V_{\text{grid}}(\mathbf{u}_i, \eta)}{\sum_{\mathbf{u}_i < \mathbf{u}} \left( \sum_{i=0}^{N_{\text{bl}}} w_i \right)^2} \quad [\text{Jy}^2 \text{Hz}^2], \quad (4.15)$$

where

$$V_{\text{grid}}(\mathbf{u}, \eta) = \int V_{\text{grid}}(\mathbf{u}, \nu) H(\nu) \exp(-2\pi i \eta \cdot \nu) d\nu \quad [\text{Jy Hz}]. \quad (4.16)$$

The full algorithm from §4.3.3.3 and 4.3.3.4 is summarized in Figure 4.1.

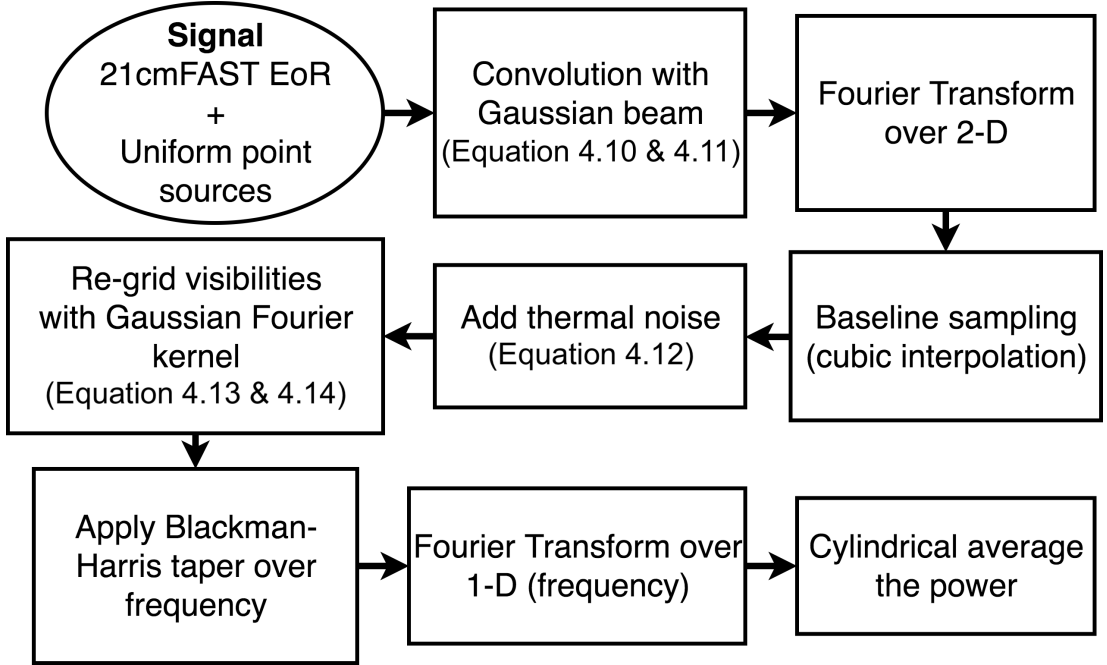


Figure 4.1: A summary of our instrumental algorithm.

#### 4.3.4 Bayesian Parameter Estimation

Bayesian parameter estimation through Monte Carlo Markov Chain (MCMC) is a powerful algorithm that is widely used in a variety of scientific fields to constrain parameters of interest by determining their full posterior distribution. We have chosen to use 21cMMC, an MCMC analysis tool designed to estimate astrophysical parameter constraints from the EoR. It incorporates EoR simulation

data produced on-the-fly by an optimized version of 21CMFAST to statistically compare the models to either mock or observed data (Greig & Mesinger, 2015).

The existing log-likelihood prescription used by 21cmMC uses the 1-D PS and is given by:

$$\ln \mathcal{L} = -\frac{1}{2} \sum_j \frac{(P_D(k_j) - P_M(\theta, k_j))^2}{\sigma_D^2(k_j) + (\alpha P_M(\theta, k_j))^2}, \quad (4.17)$$

where  $P_D$  is the 1-D PS of the experiment or mock data,  $P_M$  is the model 1-D PS,  $\theta$  is the set of EoR parameters for the model,  $\sigma_D^2$  is the uncertainty of the experiment computed using 21CMSENSE (Pober et al., 2014), and  $\alpha$  is a variable corresponding to the uncertainty of the model, often set to 10–20% by inspecting how close 21CMFAST is to radiative transfer models, with 15% being the default value. All estimates are a function of wavenumber,  $k$ . In the presence of foregrounds and the instrumental beam, this prescription is only optimal<sup>7</sup> if the following set of conditions is satisfied:

1. The brightness temperature fluctuations are truly Gaussian
2. The EoR signal is 3-D isotropic
3. The sources of uncertainty have 3-D isotropic signal
4. The PS modes for both the EoR and foregrounds are Gaussian
5. The PS modes are independent for both the EoR and foregrounds
6. The foreground noise is independent of the EoR parameters.

We postulate that the first and second conditions are valid first-order assumptions and we leave the last one for future work. We discuss and address the others, along with a summary of our improvements to 21cMMC, in the following subsections.

---

<sup>7</sup>It uses all available information to generate the likelihood and therefore posterior, rather than losing some information by improper assumptions

#### 4.3.4.1 3-D Isotropic Uncertainties

The 1-D PS is employed because it provides complete information about the isotropic EoR signal. However, it confounds the impact of foregrounds because they naturally reside in a larger cylindrical Fourier space (i.e., smooth-spectrum versus angular clustering). In a 1-D PS, the wedge-mode contaminates the entire annulus because the foregrounds show a non-isotropic signature, corrupting some otherwise good modes. Although some sort of avoidance method is typically used to minimize the corruption of 1-D PS modes, it does not account for the full information.

We extend the likelihood formalism by using the 2-D PS instead of the 1-D PS as it allows for the management of systematic effects arising from  $k_{\perp}$  and  $k_{\parallel}$  modes respectively. The 2-D PS is commonly used as an initial step to decontaminate the cosmological EoR signal from the foregrounds in the forms of the “wedge” and the “EoR window”. Foreground power dominates the lower  $k_{\parallel}$  modes, yielding higher variance in the wedge as compared to the EoR window. Using the 2-D PS means that modes in the same  $|\vec{k}|$ -annulus that may come from different  $k_{\parallel}$  modes (from within and without the wedge) can be treated independently, and therefore the full information extracted.

#### 4.3.4.2 Gaussianity and Independence of Instrument-Convolved Foregrounds

In Eq. 4.17, the use of  $\sigma_D^2$  follows the assumption that the input data are Gaussian and independent. While this will hold true for the EoR signal since the cosmological signal is close to Gaussian, in the presence of foregrounds and instrumental effects, this assumption might break. We will focus on investigating the Gaussianity and independence of the instrument-convolved foregrounds because the variance of the data is dominated by the variance of the foregrounds in most bins. This can then dictate the appropriate formalism to adopt, without adding unnecessary complexity. Since we have established in the previous sub-section that we will be using the 2-D PS to accommodate the presence of foregrounds, we will continue this discussion using the 2-D PS of instrument-convolved fore-

grounds that were simulated based on our models; the ensemble is then used to compute the skewness and correlation in each 2-D mode.

We investigate the Gaussianity of the 2-D PS by finding the skewness in bins of  $k_{\perp}$  and  $k_{\parallel}$ . The skewness measures the asymmetry of the probability distribution about its mean, with a skewness of 0 being perfectly symmetric and increasing skewness showing increasing asymmetry. Figure 4.2 shows the skewness of the 2-D PS of the instrument-convolved point source foregrounds. Over the primary range of interest (0.1 to 1  $h$   $\text{Mpc}^{-1}$ ), the bins are predominantly close to Gaussian. Regions of higher skewness are found only at either high  $k_{\parallel}$ , where the signal is low, or low  $k_{\parallel}$ , where the foregrounds are strong so the mode is therefore heavily down-weighted in the likelihood, and thus in our fits for the underlying parameters  $\theta$ . We are thus content to maintain the assumption of a Gaussian likelihood.

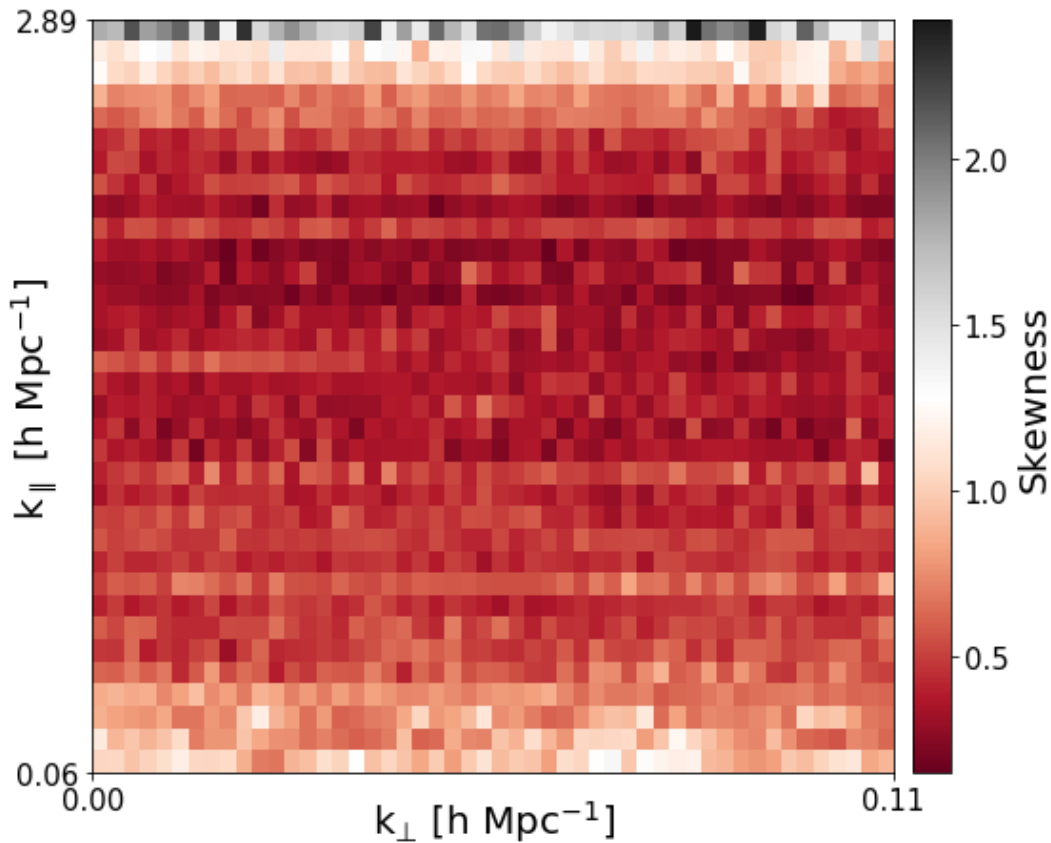


Figure 4.2: The skewness of the 2-D PS of the instrument-convolved point source foregrounds. The bins are predominantly close to Gaussian over the primary range of interest (0.1 to 1  $h$   $\text{Mpc}^{-1}$ ).

We investigate the assumption of independence of the instrument-convolved

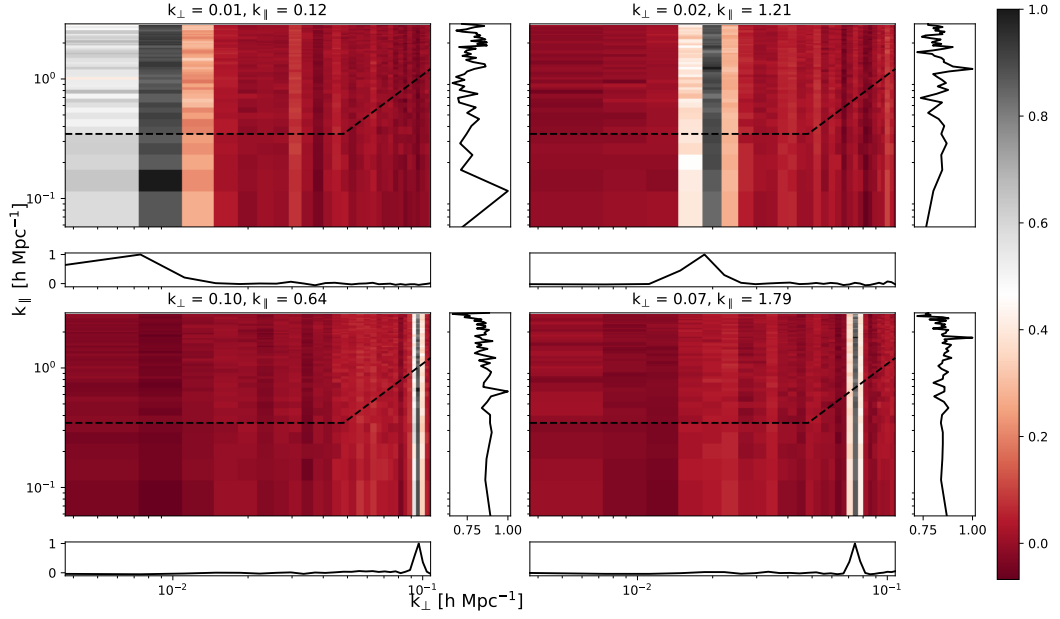


Figure 4.3: The correlation coefficient of the 2-D PS of the instrument-convolved foregrounds between a single cell with all other cells. The horizontal and vertical plots show cuts through the 2-D space at the chosen single cell locations, demonstrating the degree of correlation in the angular and line-of-sight modes. Each chosen  $(k_{\perp}, k_{\parallel})$  bin is completely correlated with itself (black cell in main panels corresponding to highest point in the smaller side panels). However, also note that the bin is highly correlated over  $k_{\parallel}$  and the correlation spills over to the two  $k_{\perp}$  bins adjacent to the chosen bin.

foreground model by finding the correlation coefficient between  $k_{\perp}$ - and  $k_{\parallel}$ -bins in the 2-D PS. The correlation measures the strength of the joint variability of two random variables, in this case the bins of  $k_{\perp}$  and  $k_{\parallel}$ , with possible values ranging from -1 being completely anti-correlated to +1 being completely correlated. As with Gaussianity (cf. §4.3.4.2), we focus on the foregrounds rather than the 21 cm signal.

Figure 4.3 shows the correlation coefficient of the 2-D PS of the instrument-convolved foregrounds of four individual  $(k_{\perp}, k_{\parallel})$  bins with all other bins. The right- and bottom- sub-panels of each major panel show the correlation coefficient along a 1-D slice (in the displayed dimension) through the selected 2-D bin of each main panel. The dotted black line divides the area between the wedge and the EoR window. As expected, each chosen  $(k_{\perp}, k_{\parallel})$  bin is completely correlated with itself (black cell in main panels corresponding to highest point in the smaller side

panels). However, we can also see that the bin is highly correlated over  $k_{\parallel}$  and the correlation spills over to the two  $k_{\perp}$  bins adjacent to the chosen bin. This is due to the frequency-dependence of the instrument, resulting in chromatic mode-mixing of foregrounds (Morales et al., 2012; Datta et al., 2010; Vedantham et al., 2012; Trott et al., 2012). As such, we can conclude that the 2-D PS of the instrument-convolved foregrounds is not independent between modes and that we must use the covariance, instead of the variance, in the likelihood prescription. Neglecting the dependence of the modes may result in over-constraining of parameters, regardless of whether the PS is 1-D or 2-D.

We thus extend the likelihood prescription to use the multivariate normal likelihood,  $\ln \mathcal{L}$ , following the use of the 2-D PS and the presence of foregrounds.  $\ln \mathcal{L}$  is given by

$$\ln \mathcal{L} = -\frac{1}{2} \left[ \left( P_D - P_M(\vec{\theta}) \right)^T \Sigma^{-1} \left( P_D - P_M(\vec{\theta}) \right) \right], \quad (4.18)$$

where  $\Sigma$  is the covariance<sup>8</sup> of our *fiducial* noise and foreground ( $N + FG$ ) model with the addition of sample variance (second term of following equation), so that the total variance,  $\sigma_T^2$ , is given by

$$\sigma_T^2 = \sigma^2(P_{N+FG;M}) + \frac{P_{21;M}^2}{\sum_j \left( \sum_{i=0}^{N_{\text{bl}}} w_i \right)^2}; \quad (4.19)$$

$$P_D = P_D(k_{\perp}, k_{\parallel}) = P_{21+N+FG;D} \quad (4.20)$$

is the (mock) data PS, assumed to be comprised of a 21 cm component, and a noise and foreground component; and

$$P_M(k_{\perp}, k_{\parallel} | \vec{\theta}) = P_{21}(k_{\perp}, k_{\parallel} | \vec{\theta}_{21}) + P_{N+FG}(k_{\perp}, k_{\parallel} | \vec{\theta}_{N+FG}) \quad (4.21)$$

---

<sup>8</sup> $\Sigma$  is computed numerically using the Monte Carlo method to simulate the noise and foreground over 1000 random realizations at the fiducial parameters. The ensemble of realizations is passed through the algorithm summarized in Figure 4.1 to produce the 2-D PS and calculate  $\Sigma$ . This is pre-computed prior to the MCMC. We note that the covariance may not have converged (see e.g Dodelson & Schneider (2013) and Taylor & Joachimi (2014)) hence further investigation is necessary, but we have left this for future work.

is a parameter-dependent *model* of the data. Note that we use the *expected* power of noise and foregrounds instead of just one specific realization for the model. Because it is computationally-expensive and difficult to calculate the expected power of all components at each iteration, we have modelled the 21 cm signal separately and use the same expected foregrounds and noise power each time, which is possible because we do not have  $\theta_{N+FG}$  parameter in the likelihood. This also assumes that the cross-power<sup>9</sup> terms are negligible and is a reasonable first-order approximation consistent with other works; however, we will see in §4.6 that this assumption is not true.

Note that  $P_D$  and  $P_M$  are *not* the true power spectrum computed from the simulation box. They are related to the true power spectrum,  $P^*$ , by  $P = \hat{W}P^*$  where  $\hat{W}$  is all the window functions that encompasses the instrumental and analysis effects such as the beam and frequency taper used in this research. The fact that we compute  $P_D$ ,  $P_M$ , and  $\Sigma$  using exactly the same pipeline means that they are self-consistent hence the effects of  $\hat{W}$  should cancel out in the likelihood. Also note that the form of Eq. 4.18 explicitly assumes that the covariance does not depend strongly on the astrophysical parameters. Otherwise, it would require an extra term of  $-\ln \det(\Sigma^{-1})$ . This is a reasonable assumption for most cylindrical  $k$ -modes which are dominated by foregrounds whose parameters we are not directly interested in.

### 4.3.5 Extensions to 21cmMC

The foregrounds and instrumental components, along with other improvements developed in this work and described in the previous sections, are combined in a publicly-available plug-in to the new 21CMMC, called PY21CMMC-FG<sup>10</sup>. It makes use of 21CMMC’s new ability to allow the user to arbitrarily insert code to modify the lightcone before producing a likelihood. This creates realizations of the EoR signal obscured by the foregrounds which are measured by an instrument model and then used as input to the log-likelihood.

---

<sup>9</sup>An explicit derivation of its variance is shown later in §4.6 (Equation 4.23)

<sup>10</sup>Found at <https://github.com/BellaNasirudin/py21cmmc-fg>

To summarise, the extensions to 21cmMC that are available in PY21CMMC-FG include:

- **a foreground model:** includes both diffuse and point-source foregrounds (although only the latter is used in this work for simplicity)
- **an instrument model:** includes a Gaussian beam model, the array baseline sampling and thermal noise
- **calculation of the 2-D PS:** to separate the cosmological EoR signal from the foregrounds
- **the covariance of the PS:** to account for the correlated instrument-convolved foregrounds
- **the likelihood prescriptions for the MCMC:** expand to multivariate normal distribution
- **stitching of the lightcones:** to account for the wide FOV of the instrumental beam model
- **padding of the sky:** to increase the image resolution for Fourier Transform
- **Fourier beam gridding kernel:** to properly interpolate, average and weight visibilities onto a grid

All of these have been discussed in detail in this section, except for the stitching of the lightcones. We will discuss this in the next section (§4.4) when we explore the observational effects on the EoR lightcones.

### 4.3.6 Comparison to Existing Framework

The final focus of this section is to compare the uncertainty level from our framework, PY21CMMC-FG, to that from the publicly-available existing framework, 21CMSENSE (Pober et al., 2013; Pober et al., 2014). In general, 21CMSENSE performs a separate calculation of the instrument sensitivity arising from thermal

noise and cosmic variance while avoiding the foreground-dominated region; the uncertainty file is then used as input into 21cmMC. For more details, we refer readers to Pober et al. (2013) and Pober et al. (2014).

For 21CMSENSE, we adopt the drift scan mode and “moderate” foreground removal with the MWA Phase II baselines,  $A_{\text{eff}} = 21 \text{ m}^2$  and  $T_{\text{sys}} = 240 \text{ K}$ . We also use  $\Delta t = 2 \times 10^5$  hours in both frameworks. The reasoning behind this value is explained in detail in §4.5, but in general, we use this value so that we can approximate the noise level for 1000 hours observation of the future SKA\_LOW1.

Note that the uncertainty with sample variance is calculated differently in the two frameworks. Our framework calculates  $\sigma_T^2$  based on Equation 4.19, while 21CMSENSE defines  $\sigma_T^2$  as

$$\sigma_T^2(k) = \left( \sum_i \frac{1}{(P_{21}(k) + P_{N,i}(k))^2} \right)^{-\frac{1}{2}}, \quad (4.22)$$

whereby an inverse-weighted summation is performed over the  $uv$  cell  $i$  for each  $k$  mode bin (Pober et al., 2013). The main difference between the two frameworks is the presence of the cross-terms between the EoR PS and the noise variance for 21CMSENSE.

In addition to the calculation of sample variance, 21CMSENSE and PY21CMMC-FG have a few key differences that can affect the total uncertainty level. We have summarized these differences in Table 4.2. The resulting total uncertainty from the two frameworks are presented in Figure 4.4. The total uncertainties loosely match at the relevant modes where the signal dominates, with a difference of less than half an order of magnitude. At high  $k$ , however, the difference is as high as one order of magnitude. We attribute the difference in total uncertainty to the missing Earth rotation synthesis which essentially fills up more  $uv$  space hence increasing the overall noise level (i.e., less modes can combine coherently). Even though the Fourier beam gridding kernel we employ partly takes this into account, it does not restore the noise to the full level that it would be with a proper rotation synthesis. We note that this is a shortcoming of our framework, and is left for future work.

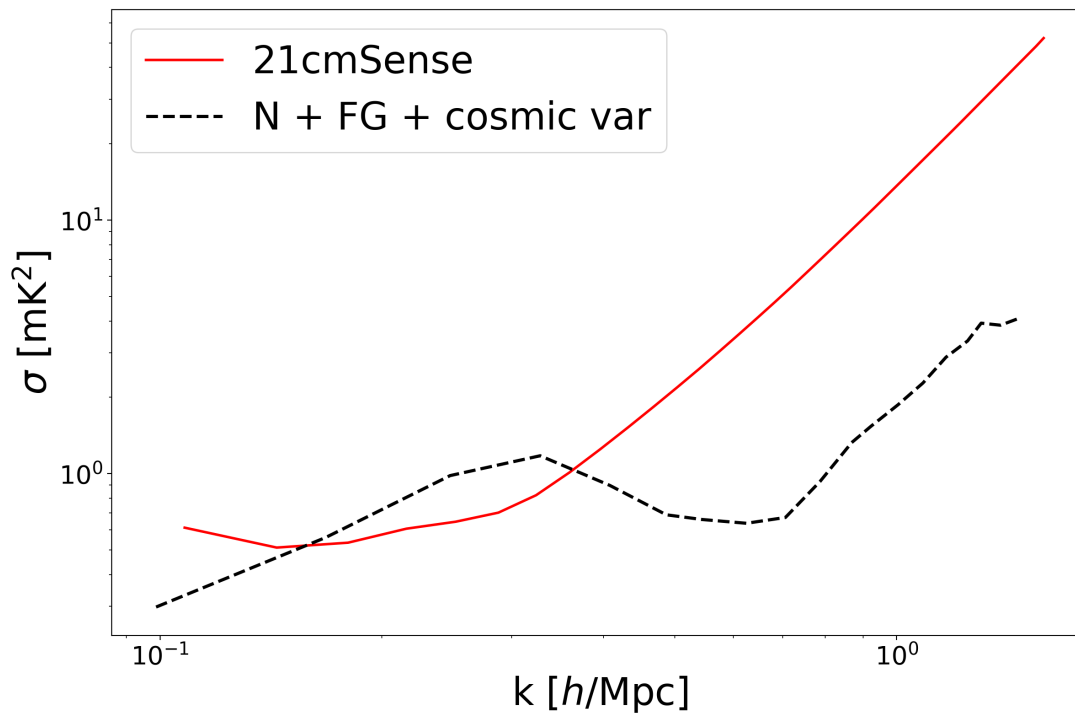


Figure 4.4: The total uncertainty from 21CMSENSE (red solid line) compared to the total uncertainty from our framework (black dash line) with  $T_{sys} = 240$  K and  $\Delta t = 2 \times 10^5$  hours.

	<b>21cmSense</b>	<b>py21cmmc-fg</b>
PS	1-D	2-D
Frequency-dependent baselines	No	Yes
Cross-power in variance	Yes	No
Foregrounds	Avoidance	Suppression
Earth rotation synthesis	Yes	No
Baseline sampling on EoR PS	No	Yes
Frequency taper	No	Yes
Gridding kernel	No	Yes

Table 4.2: The differences between 21CMSENSE and PY21CMMC-FG.

## 4.4 Observational Effects on EoR Lightcones

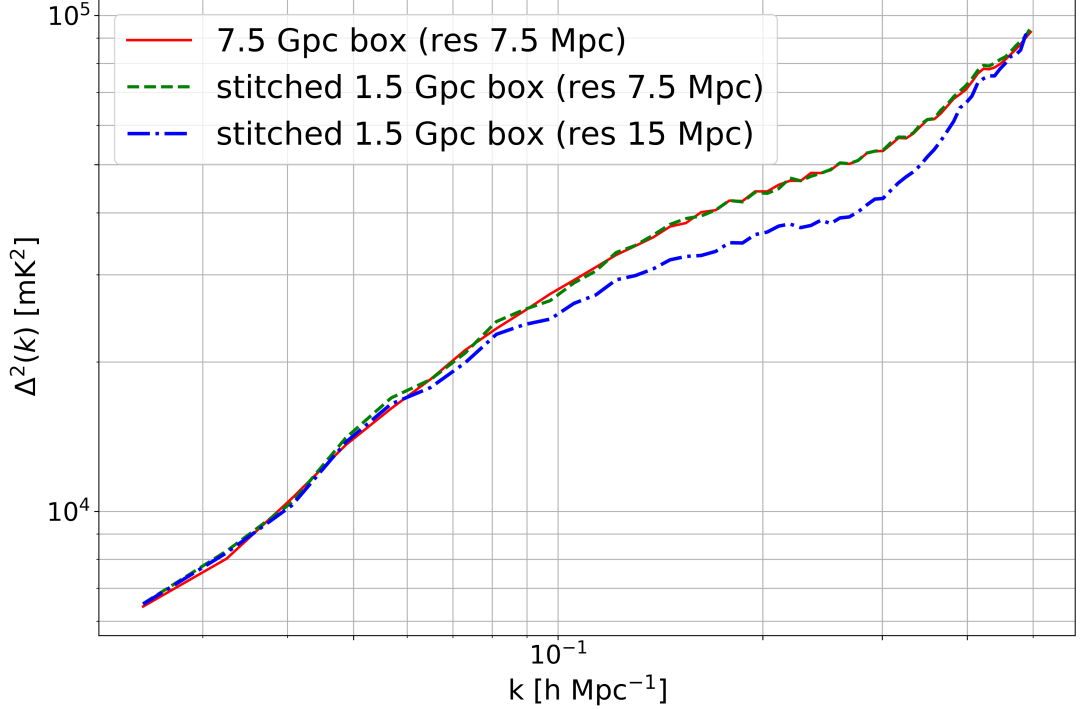


Figure 4.5: Comparison of the 1-D PS of the 7.5 Gpc box (red), the stitched 1.5 Gpc box (green dotted), and the stitched 1.5 Gpc coarsened to a resolution of 15 Mpc (blue dash-dot). The 7.5 Gpc box and the stitched 1.5 Gpc box agree very well on most scales, but the 1-D PS of the stitched and coarsened box differs from the 1.5 Gpc box at high  $k$  due to finite resolution.

In this section, we explore the observational effects of adding foregrounds to the EoR signal. This is first done by explaining the steps we have taken to ensure that both the EoR signal and foregrounds can be added together. We then analyse the effects on the 1-D and 2-D power spectra and compare the differences in image space.

In order to add the foreground and EoR lightcones, they need to cover the same angular size and have the same angular resolution. At  $z = 6$ , the resulting angular sky size of a 1 Gpc/ $h$  simulation box, which is considered to be large in theoretical studies, is merely  $\sim 0.12$  radian. On the other hand, the FOV of the MWA is  $\sim 1$  radian. Running a massive box that covers the MWA FOV is unrealistic and computationally expensive, so instead, we have made a realization of the lightcone across the mock sky by assuming that the same structure is

periodically repeated. To preserve the wavenumber, we have ensured that the full box is used in the stitching i.e., we use an integer number of boxes. We also limit ourselves to using scales smaller than the box size in the parameter estimation to avoid systematics due to this repetition.

Furthermore, due to memory-limitation, we have opted to coarsen the EoR signal using interpolation. Of course, the coarsening process can be avoided by setting the EoR lightcone from 21CMFAST to be of the same angular size. This, however, will affect the small-scale processes involved in determining  $\delta T_b$ , so we prefer to perform the coarsening post-stitching.

To study the effects of tiling and coarsening of the lightcone, we use simulation boxes of size 1.5 and 7.5 Gpc, both with a resolution of 7.5 Mpc. While we will typically work with the 2-D PS, we use the 1-D PS when comparing data quantitatively in this section. We compare the 1-D PS of the 7.5 Gpc box, the stitched 1.5 Gpc box, and the stitched 1.5 Gpc coarsened to a resolution of 15 Mpc in Figure 4.5. The  $y$ -axis shows the dimensionless 1-D PS while the  $x$ -axis shows the  $k$  scales.

The 7.5 Gpc box and the stitched 1.5 Gpc box agree very well on most scales, suggesting that stitching the box does not negatively affect the PS. However, the 1-D PS of the stitched and coarsened box differs from the 1.5 Gpc box at high  $k$ <sup>11</sup>. This is, of course, expected as the coarsening of the box results in a different resolution, hence affecting the small scale structure of the  $\delta T_b$ . The stitching of boxes and coarsening of the resolution may potentially affect the statistics of the PS due to lack of cosmic variance.

Herein, we have been presenting plots in cosmological units. In the code and hereafter in the paper, we have opted for observation units of Jy, Hz and radians to minimise inconsistencies and errors in converting between the two units. Note that the choice of units is inconsequential for the likelihood, as long as the same units are used in numerator and denominator.

---

<sup>11</sup>The curves converge again at high  $k$  because modes  $\geq 0.2 h/\text{Mpc}$  (corresponding to the Nyquist value) is not reliable.

## 4.5 MCMC Analysis

For parameter estimation, we use an EoR lightcone of size  $750 h^{-1}\text{Mpc}$  with 250 cells. The lightcone is stitched together to cover 1 steradian of the sky and coarsened to 800 cells (resolution of  $\approx 24 h^{-1}\text{Mpc}$ ) before being padded by zeros to 3 times the sky size to increase the resolution for the Fourier Transform. The bandwidth of the observation is 10 MHz from 150 to 160 MHz with 100 frequency channels. We assume that  $T_{sys} = 240\text{ K}$ , corresponding to the average sky temperature at 150 MHz.

To ensure that our MCMC framework is consistent, we first perform simpler tests in which we attempt to loosely constrain only two parameters,  $\zeta$  and  $T_{vir}$  (with fiducial values of  $\zeta=30.0$  and  $T_{vir} = 4.7 \log_{10}\text{K}$ ). These systematic tests include:

1. Uniform – regular and filled –  $uv$  sampling with no thermal noise or foregrounds
2. Uniform  $uv$  sampling with point-source foregrounds but no thermal noise
3. Uniform  $uv$  sampling with thermal noise but no foregrounds
4. MWA baseline sampling with thermal noise but no foregrounds
5. MWA baseline sampling with thermal noise and point-source foregrounds

Step 5 constitutes the end-goal of this work (but with all four parameters from Table 4.1). Note that with these tests, we are not interested in properly estimating the values of the parameters; we only want to gauge whether the MCMC walkers would assemble around the right values, thereby the burn-in phase of the walkers are still included in this section. We initially set the observation time to 1000 hours consistent with other research, but the observation time is later increased to  $2 \times 10^5$  hours (the motivation of which is explained later in this section). To clarify, only steps 1 - 3 are done with 1000 hours of observation time. The final two steps, along with everything else after, are done with  $2 \times 10^5$  hours.

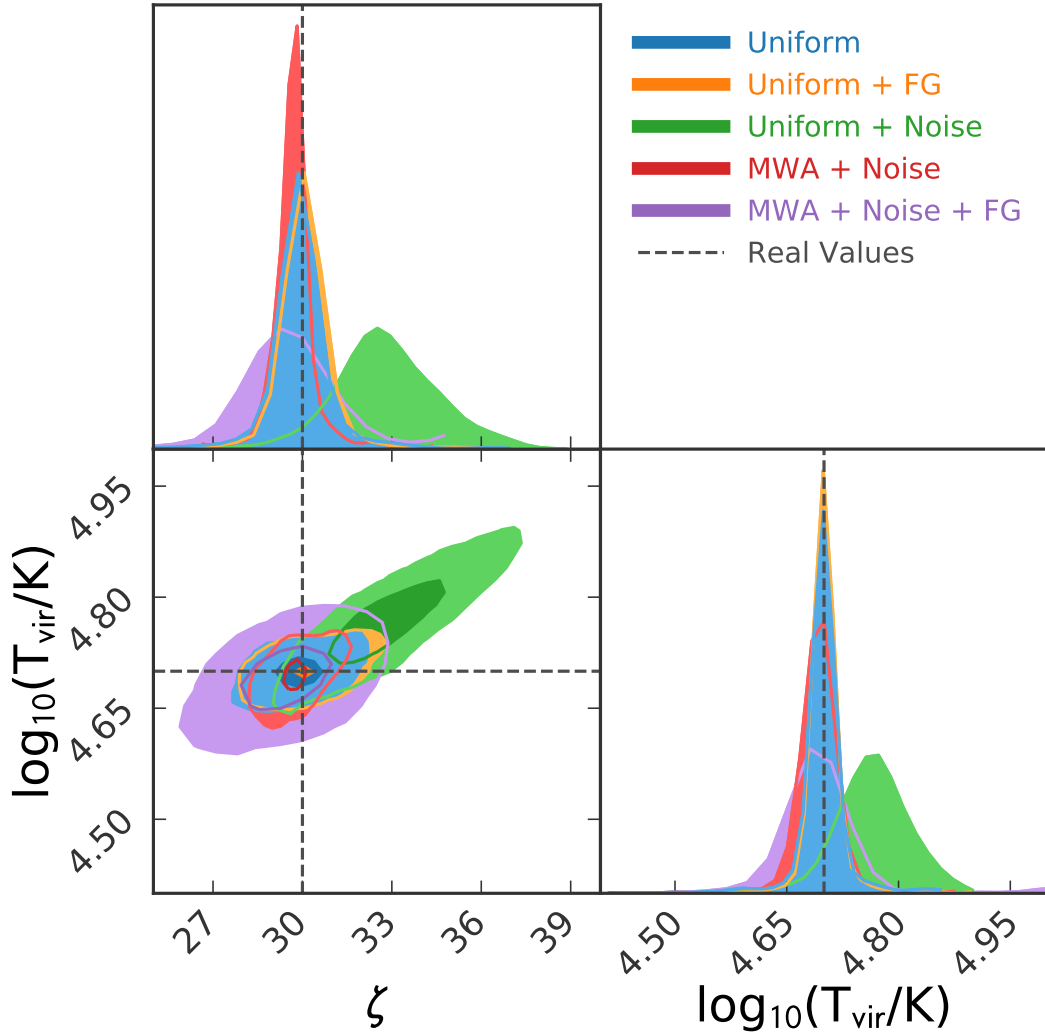


Figure 4.6: A corner plot comparing the constraints our systematic tests: uniform  $uv$  sampling with no thermal noise or foregrounds (blue); uniform  $uv$  sampling with point-source foregrounds but no thermal noise (orange); uniform  $uv$  sampling with 1000 hours of thermal noise with the MWA but no foregrounds (green); MWA baseline sampling with  $2 \times 10^5$  hours of thermal noise with the MWA but no foregrounds (red); MWA baseline sampling with  $2 \times 10^5$  hours of thermal noise with the MWA and point-source foregrounds (purple). The use of  $2 \times 10^5$  hours of thermal noise with the MWA is comparable to the noise level of 1000 hours with the SKA. The artificial “uniform”  $uv$  sampling unnecessarily inflates the impact of thermal noise (green) as it restricts the number of baselines per  $uv$  cell to one and the small collecting area of the MWA gives a signal-to-noise ratio of order unity; both of these factors results in a biased estimate. With the addition of baselines sampling and the use of SKA sensitivity, the constraints are remain unbiased (purple and red) although the final test (red) gives a really inflated constraint compared to the other tests. Note that these constraints still have the burn-in phase included.

We present a corner plot of our checks in Figure 4.6, which shows the projection of the values of the parameters over 1-D and 2-D space density. The black dash lines show the actual value of the parameter while the colored, shaded regions show the values of the estimated parameter that have been projected over the density space in 1-D (diagonal plots) and 2-D (non-diagonal plots).

It is clear that convolving the stitched and coarsened EoR signal with the Gaussian beam and implementing the 2-D PS and the multivariate normal distribution in the likelihood prescription do not negatively impact the parameter estimation, as apparent from the constraints from Step 1 (blue region). The addition of point source foregrounds in Step 2 (orange) does not significantly expand the constraints. This can be attributed to the fact that the foreground contamination is fully contained at smaller  $\eta$  due to the uniform  $uv$  sampling.

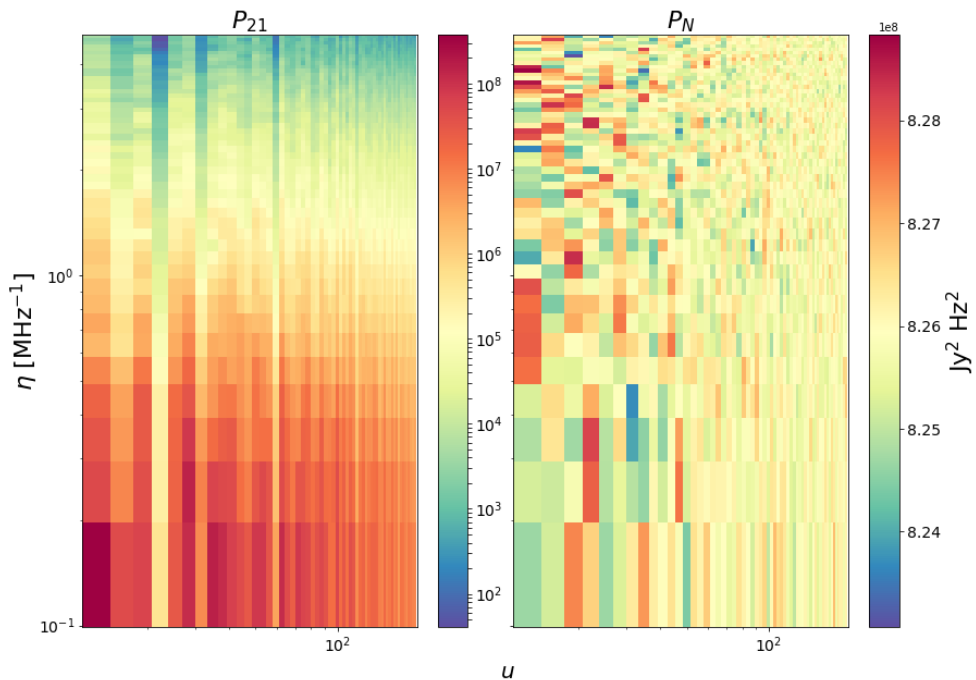


Figure 4.7: The power spectra of the EoR signal (left) and the thermal noise with the MWA sensitivity (right) in unit of  $\text{Jy}^2\text{Hz}^2$ . With the uniform  $uv$  sampling, the signal to noise ratio is of order unity for 1000 hours of observation time due to the small collecting area of the MWA. While this is enough for an EoR signal detection over the slope of the 1-D PS, it is not sensitive enough for EoR parameter estimation with the MWA.

However, with the addition of thermal noise in Step 3 (green region), the peak

of the distribution is significantly shifted with respect to the true value, indicating that the results are biased. We note also that the artificial “uniform”  $uv$  sampling unnecessarily inflates the impact of thermal noise, as it restricts the number of baselines per  $uv$  cell to one. To investigate the cause of the bias, we plot the 2-D PS of the EoR signal and the thermal noise, presented in Figure 4.7. With the uniform  $uv$  sampling, the signal-to-noise ratio is of order unity for 1000 hours of observation time due to the small collecting area of the MWA, either with the MWA baselines sampling or the uniform  $uv$  sampling. While this is enough for an EoR signal detection over the slope of the 1-D PS, it is not sensitive enough for EoR parameter estimation with the MWA.

To enable parameter constraints for the remainder of the work, we henceforth increase  $\Delta t$  in Equation 4.12 to  $2 \times 10^5$  hours for the MWA-based instrument model that we have. This  $\Delta t$  is equivalent to adopting an SKA-like sensitivity for which  $A_{\text{eff}} = 300 \text{ m}^2$  but is achievable with only 1000 hours. As seen in Step 4 (red region), both the use of the larger collecting area and the presence of  $uv$  sampling reduces the noise, resulting in the MCMC converging to the model values.

In Step 5 (purple region), the presence of point source foregrounds expands the posteriors by 100% compared to thermal noise alone without bias. The reason the purple contour is larger than the red, while the orange is not larger than the blue, is that non-uniform sampling implies chromaticity which creates the wedge, and therefore removes a lot of otherwise useful modes.

## 4.6 Parameter Estimation Results

Now that we have established the robustness of our additional model complexities, we can use the MWA baseline sampling with thermal noise and point-source foregrounds to constrain the four reionisation parameters in Table 4.1. We use three different frequency bands: 150–160, 160–170, and 170–180 MHz to observe the EoR signal, which is obscured by point-source foregrounds in the presence of instrumental effects and thermal noise.

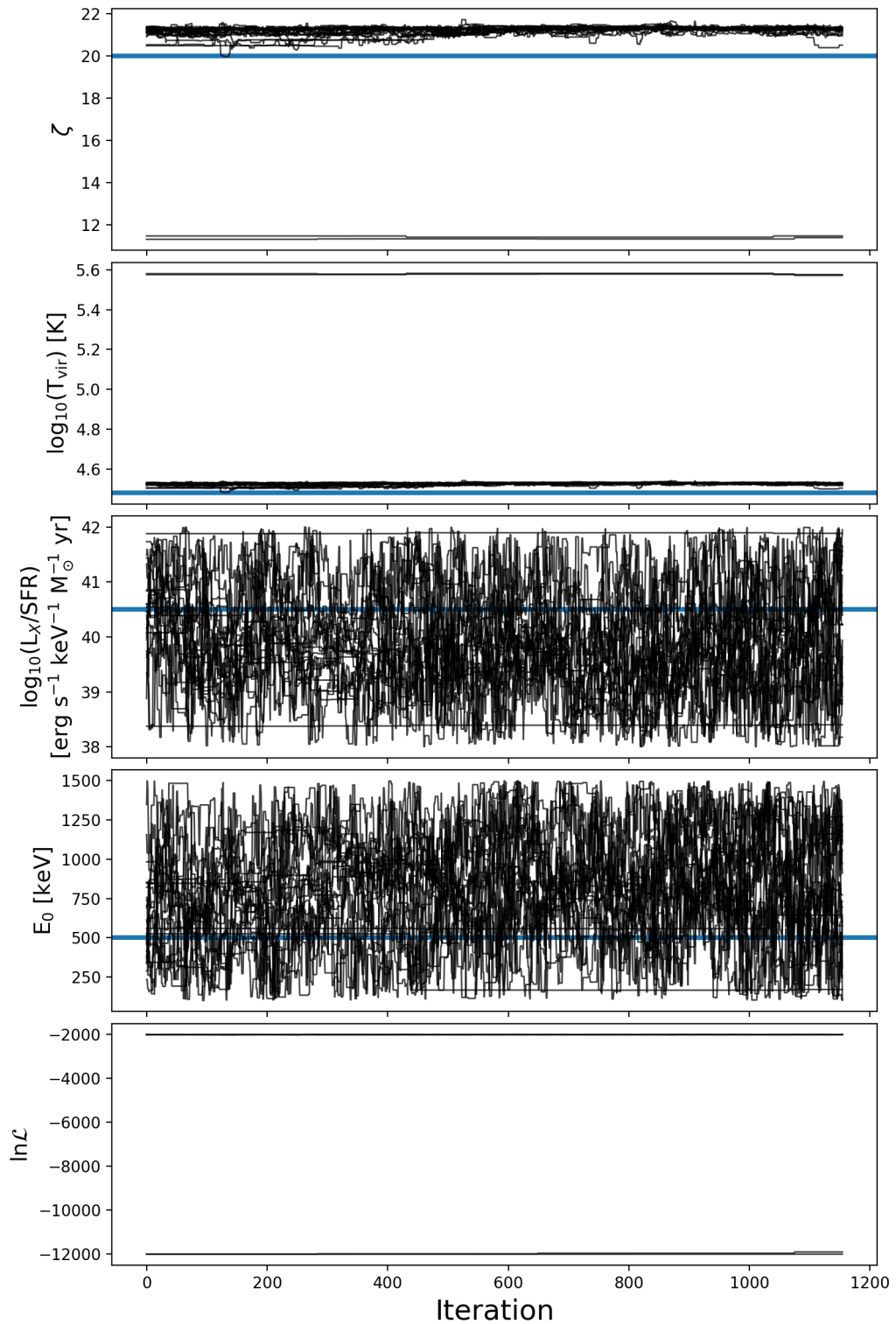


Figure 4.8: An example trace plot from the 160–170 MHz band with thermal noise and foregrounds. The blue lines show the true value of the parameter while the black lines show the progression of the parameter estimation at each iteration. In this particular case, we have ignored the walkers with  $\ln \mathcal{L} < -4000$ .

Before we proceed with our results, we would like to emphasize that our pipeline is computationally intensive and time-consuming. With 5 chains run for each parameter, we have 20 walkers in total. One iteration per walker uses 10 GB of memory per node and takes roughly 20 minutes to completely simulate the EoR brightness temperature field, tile and coarsen it to cover the whole sky, add a Gaussian beam, Fourier Transform the beam-convolved sky and sample the  $uv$  sample, re-grid the visibilities and cylindrically average them to find the 2-D PS before finding the log-likelihood. The bottleneck of our pipeline is in re-gridding the visibilities using a Gaussian beam kernel after baseline sampling, which takes around 15 minutes to complete.

To test the performance, we use a Gaussian Process model to fit for the maximum likelihood autocorrelation function which is used to estimate the autocorrelation time,  $\tau$ . We found that  $\tau \approx 200$  iterations irrespective of which frequency band is being used, with the recommended total iteration being  $50\tau$ . However, because of the memory and time limitations we have mentioned above, we have only run our chains up to around  $5\tau$ . This is not enough to definitively claim that our chains have properly converged, but the results we currently have are useful to give an initial estimate of how well we can constrain the EoR parameters in the presence of foregrounds and thermal noise with our pipeline and gauge the plausibility of our assumptions.

Furthermore, in calculating our constraints, we have ignored walkers that are stuck in local minima. An example of this is shown in Figure 4.8, where we have plotted the trace plots which show the values of the four EoR parameters at every iteration and the corresponding  $\ln \mathcal{L}$  after burn-in for the 160–170 MHz band with thermal noise and foregrounds. In this particular case, we have ignored the walkers with  $\ln \mathcal{L} < -4000$ .

We present a corner plot of the different observation bands in Figure 4.9 in which the orange, green, and blue shaded regions represent the 150–160, 160–170, and 170–180 MHz bands respectively. The black dashed lines show the true values of the parameters ( $\zeta = 20$ ,  $\log_{10}(T_{\text{vir}}) = 4.48$ ,  $L_X/\text{SFR} = 40.5$ , and  $E_0=0.5$  keV). The darker/lighter shaded regions represent  $1\sigma/2\sigma$  confidence regions cor-

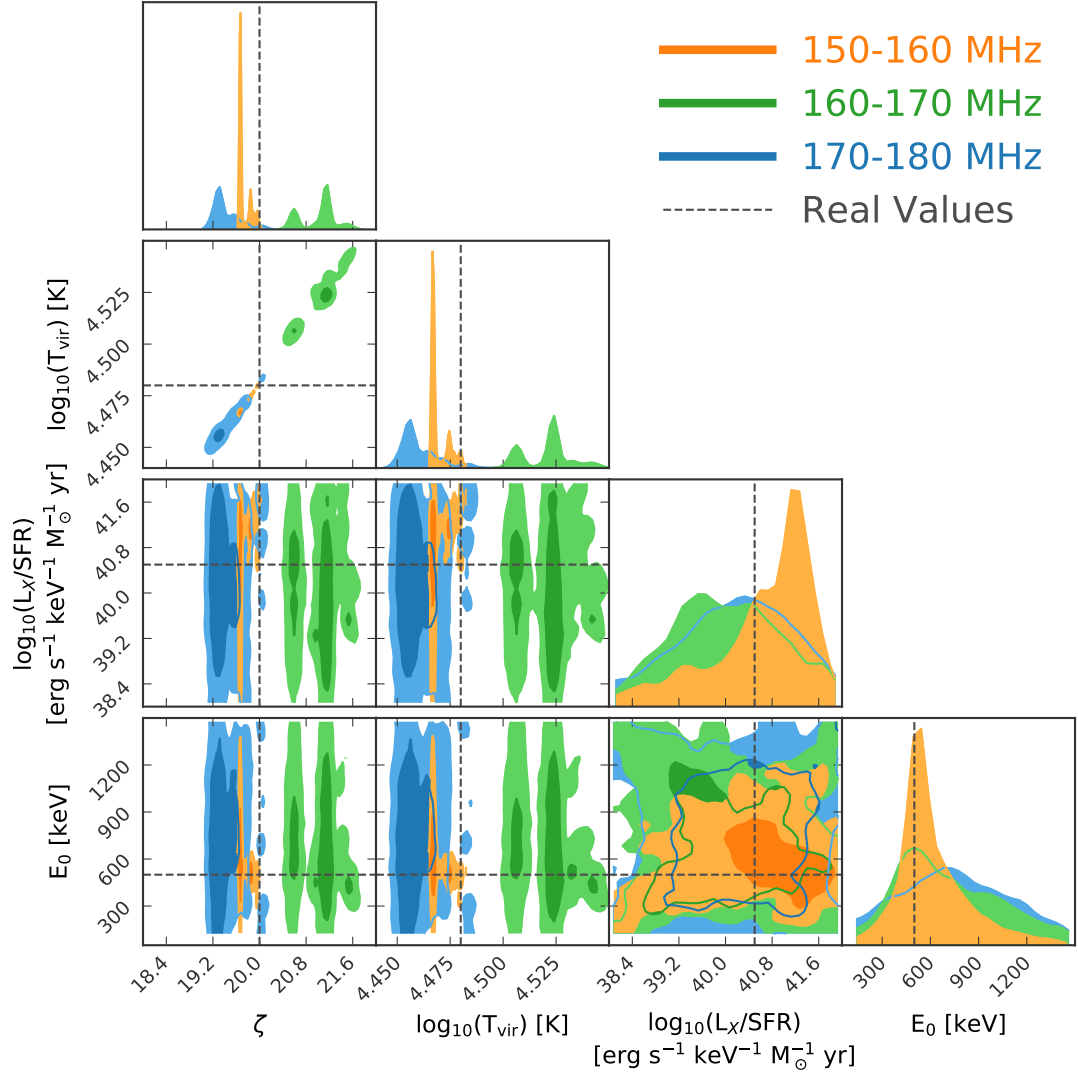


Figure 4.9: A corner plot comparing the constraints of EoR parameters in the presence of instrumental noise and foregrounds in the different frequency bands: 150–160 (orange), 160–170 (green), and 170–180 (blue) MHz.

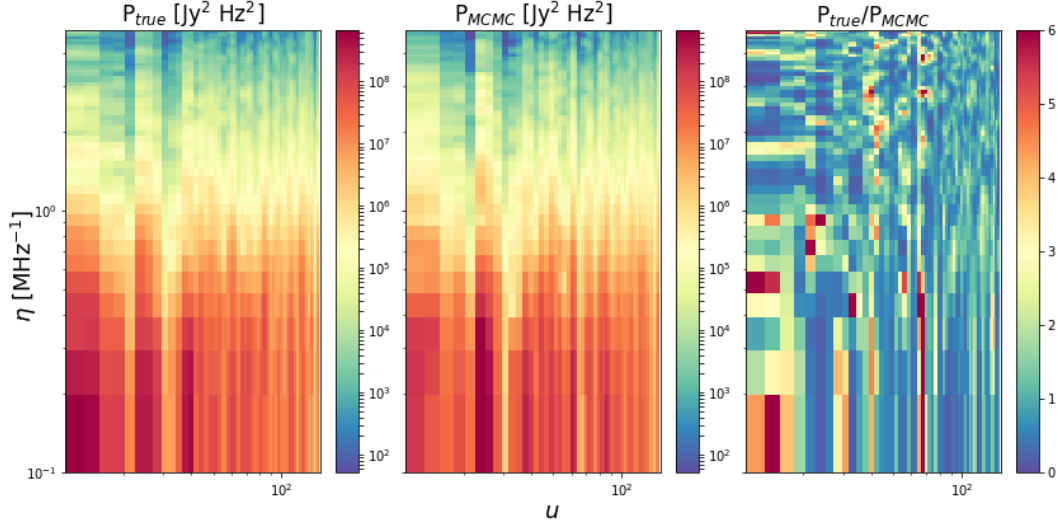


Figure 4.10: The 2-D power spectra of the EoR signal (i.e. without foregrounds or thermal noise) in the 160–170 MHz band for the true values (left) and the MCMC values (middle) – the median values of  $\zeta = 21.13$ ,  $\log_{10}(T_{vir}) = 4.52$ ,  $L_X/\text{SFR} = 40.00$ , and  $E_0=0.656$  keV– along with their ratio. The true parameters give a maximum power that is up to 6 times higher than the MCMC parameters in the EoR window, suggesting that it is deceptively easy to discriminate between the two models.

responding to the 84<sup>th</sup> and 16<sup>th</sup> percentiles. From the figure, it is clear that  $L_X/\text{SFR}$  and  $E_0$  are relatively unconstrained in all frequency bands and that  $T_{vir}$  is tightly constrained. Note that  $\zeta$  and  $T_{vir}$  are quite correlated and biased in all bands. This is especially true for the 160–170 MHz band in which the green region is further from the truth values. The bias suggests that the primary effects of  $\zeta$  and  $T_{vir}$  are on regions which are most affected by foregrounds on the larger scales. A bias indicates either a very anomalous noise realization (more than 2 sigma over the whole 2D parameter space), or an incorrect model.

To investigate the reason for the bias in the presence of foregrounds, we present the 2-D power spectra of the EoR signal (i.e. without foregrounds or thermal noise) in the 160–170 MHz band for the true values and the MCMC values – the median values of  $\zeta = 21.13$ ,  $\log_{10}(T_{vir}) = 4.52$ ,  $L_X/\text{SFR} = 40.00$ , and  $E_0=0.656$  keV– along with their ratio in Figure 4.10. The true parameters give a maximum power that is up to 6 times higher than the MCMC parameters in the EoR window, suggesting that it is deceptively easy to discriminate between the models.

In reality, however, it should be considered that the presence of foregrounds

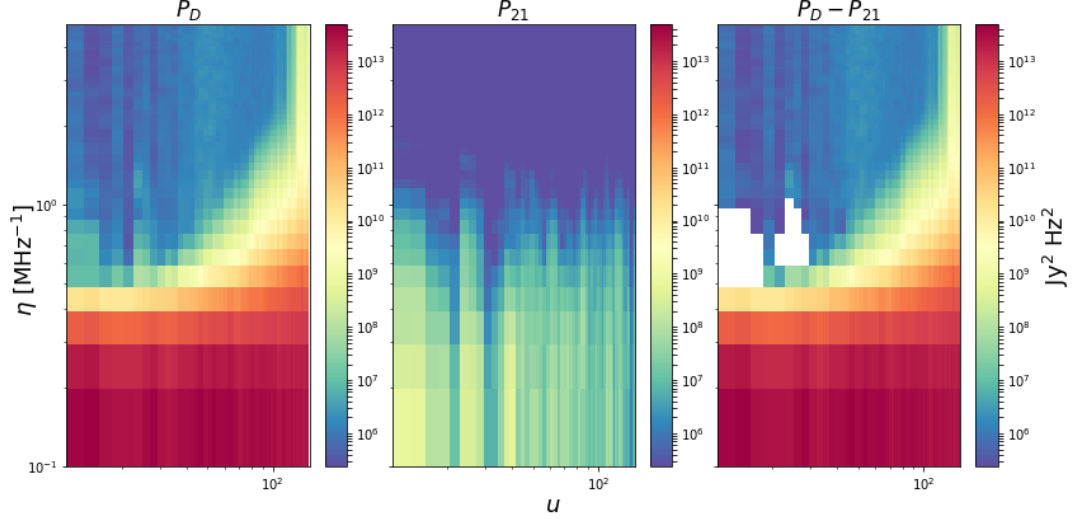


Figure 4.11: The 2-D power spectra of the data i.e. EoR signal, foregrounds and thermal noise (left) and the EoR signal (middle) in the 160–170 MHz band along with their difference (right). The negative power (white region) in the right panel is caused by the unaccounted contribution of the cross-power terms between the EoR signal and the foregrounds and thermal noise.

and noise may obscure modes that are vital for differentiation of these models. Figure 4.11 shows from left to right: the 2-D PS of the data i.e. the EoR signal, thermal noise and point source foregrounds, the 2-D PS of the true EoR signal and the difference between these two. The negative power in the right panel is caused by the unaccounted contribution of the cross-power terms between the EoR signal and the foregrounds and thermal noise. This is because the EoR signal and the expected thermal noise and foregrounds are modelled separately as mentioned in §4.3.4.

We can estimate cross-power by looking at the variance of the difference between the 2-D power spectra of the data ( $P_D$ ) and the model ( $P_M$ ) for a single realization of 21 cm power spectrum but with an ensemble of foregrounds and noise realizations following

$$\begin{aligned}
 \text{Var}(P_D - P_M) &= \text{Var}[\langle |(\mathbf{V}_{21} + \mathbf{V}_{FG} + \mathbf{V}_N)|^2 \rangle_{\mathbf{u}} \\
 &\quad - \langle |(\mathbf{V}_{FG} + \mathbf{V}_N)|^2 + |(\mathbf{V}_{21})|^2 \rangle_{\mathbf{u}}] \\
 &= \langle 2P_{21}[\text{Var}(\mathbf{V}_{FG}) + \text{Var}(\mathbf{V}_N)] \rangle_{\mathbf{u}}^*, \tag{4.23}
 \end{aligned}$$

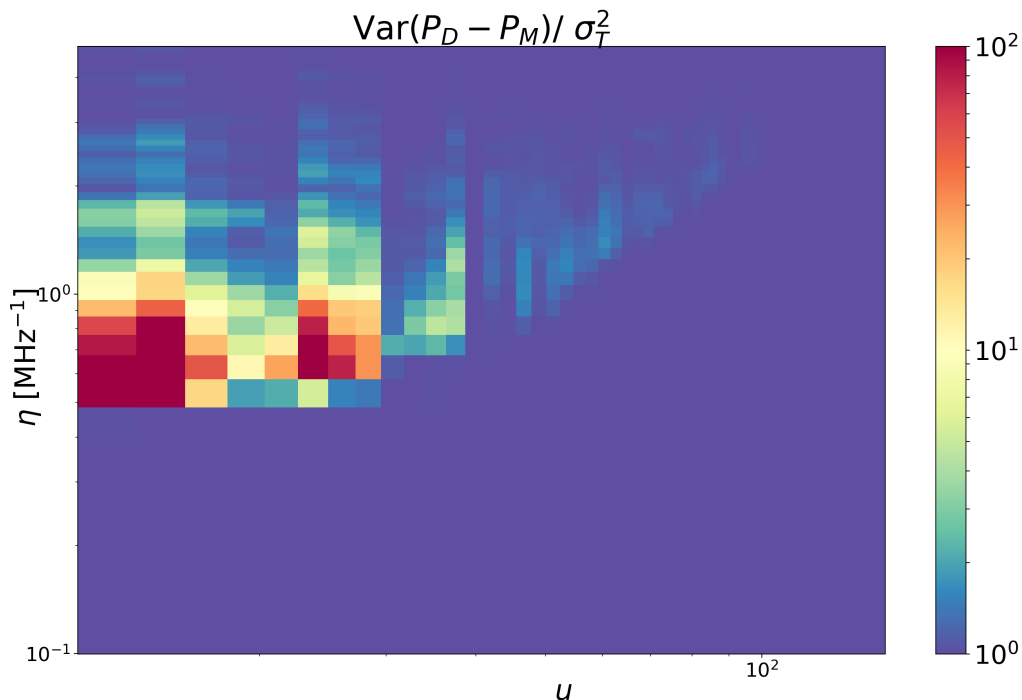


Figure 4.12: The ratio of the variance of the  $P_D - P_M$  to the actual total variance,  $\sigma_T$ .

where  $V_{21}$ ,  $V_{FG}$ , and  $V_N$  are the visibilities of the EoR signal, foregrounds and noise respectively. For simplification,  $\langle \rangle_{\mathbf{u}}$  denotes the cylindrical average in  $\mathbf{u}$  bin with weighting as described in §4.3.3 and  $\langle \rangle_{\mathbf{u}}^*$  is the same as  $\langle \rangle_{\mathbf{u}}$  except the weighting is squared; see the appendix for the complete derivation. From the equation, we can see that the variance is largest when  $P_{21}$  is larger than the noise and foregrounds. To investigate this further, we present the ratio of the variance of  $P_D - P_M$  and the true total variance  $\sigma_T^2$  in Figure 4.12. The region that is more correlated than the other modes is at  $\mathbf{u} \leq 30$ , whereby the size of the correlated bins are dictated by the correlation lengths of the window functions. This is evident from the red regions in the figure which extend over  $2\mathbf{u}$  by  $4\eta$  bins, corresponding to the correlation length of the MWA following  $D/\lambda$  and the Blackman-Harris taper respectively.

To further explore the region where most of the biasing takes place and gauge the net effect of the cross-power on the likelihood, we calculate the pseudo-

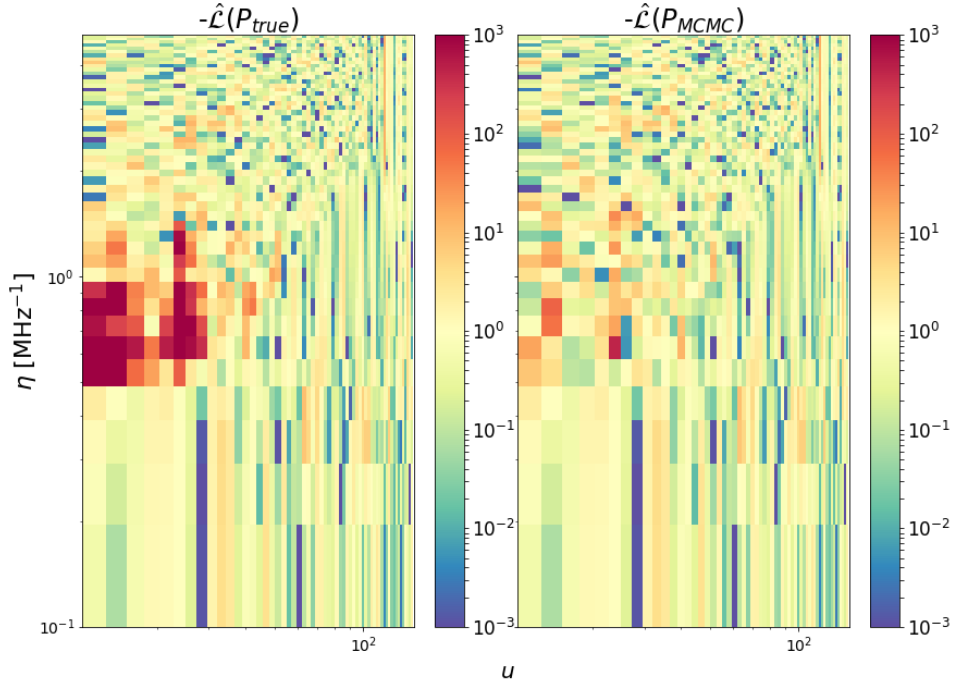


Figure 4.13:  $-\hat{\mathcal{L}}$  for the true (left) and MCMC (right) parameters.  $-\hat{\mathcal{L}}$  is overall greater for the true parameters, as apparent from the overwhelming red region in the left panel coinciding with low  $u$ .

likelihood ( $\hat{\mathcal{L}}$ ) given by

$$\hat{\mathcal{L}} = -\frac{(P_D - P_M)^2}{\sigma_T^2}. \quad (4.24)$$

This is a variation of Equation 4.18 but with  $\sigma_T^2$  instead of  $\Sigma$ . Figure 4.13 show  $-\hat{\mathcal{L}}$  for the true (left) and MCMC (right) parameters.  $-\hat{\mathcal{L}}$  is overall greater for the true parameters, as apparent from the overwhelming red region in the left panel. This region coincides with low  $u$ , thus supporting our argument that this region is more correlated. With realistic datasets whereby the visibilities from the different components are summed before the PS is calculated, the likelihood has biased signal discrimination power when the same steps are not taken for the model. The likelihood favours whichever EoR model that accounts for the cross-power term thus resulting in biased constraints.

In principle, the signal to noise ratio is greater than one in every PS cell outside the wedge because of our low level of thermal noise. This results in the

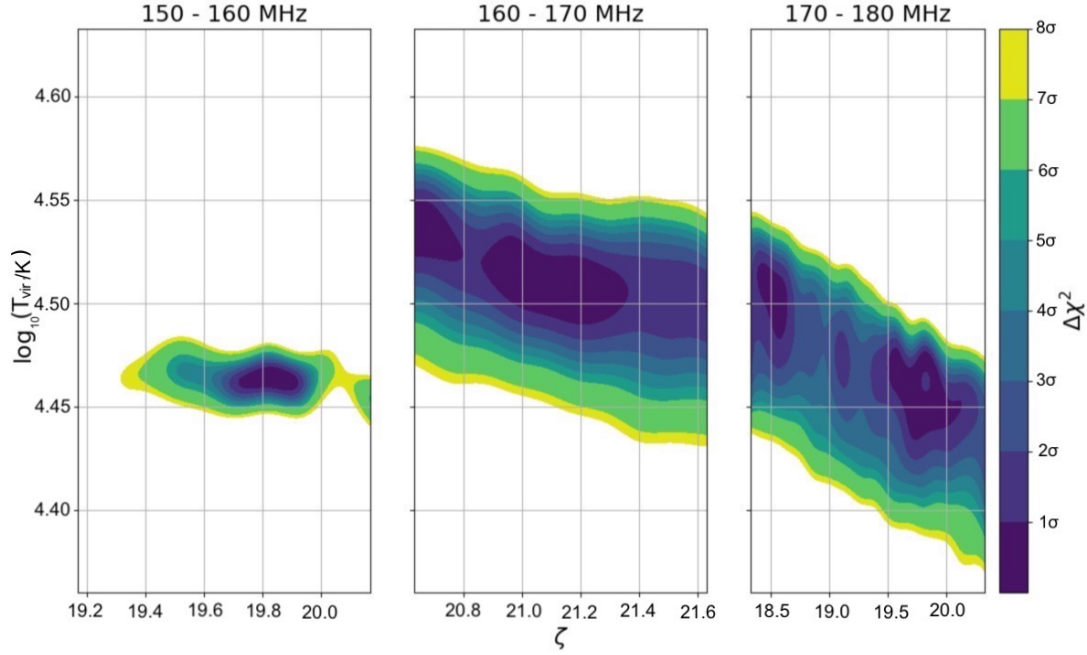


Figure 4.14: The  $\Delta\chi^2$  contours for the three bands using the best fitting parameters from our framework which are presented in Table 4.3. With  $df = 2996$ , the  $1\sigma$  level is  $\sim 77$ . Because the constraints for  $L_X/\text{SFR}$  and  $E_0$  from the MCMC look reasonably inflated, we only focus on examining the  $\Delta\chi^2$  contours for  $\zeta$  and  $T_{\text{vir}}$ .

use of all modes of the PS in calculating the likelihood, including the ones that do not have any real constraining power, i.e. less signal. In addition, because the signal is stronger at modes with  $\mathbf{u} \leq 30$ , these modes are more affected by the subtle cross-correlation effects from noise and foregrounds. The deficits in the modelling can thus lead to biased answers as the likelihood tries to compensate for the missing power.

Because our MCMC runs are shorter and may have not properly converged, the constraints from the MCMC may be invalid. To sample the “true”  $1\sigma$  contours for a Gaussian posterior, we explore the  $\Delta\chi^2$  contours by assuming that the true  $\chi^2$  value is identical to the degree of freedom ( $df$ ) (hence the  $1\sigma$  level is  $\sqrt{2df}$ ).

In Figure 4.14, we present the  $\Delta\chi^2$  contours for the three bands using the best fitting parameters from the MCMC results shown in Figure 4.9. With  $df = 2996$ , the  $1\sigma$  level is  $\sim 77$ . Because the constraints for  $L_X/\text{SFR}$  and  $E_0$  from the MCMC look reasonably inflated and unbiased, we focus on examining the  $\Delta\chi^2$  contours for  $\zeta$  and  $T_{\text{vir}}$ .

		150 - 160 MHz	160 - 170 MHz	170 - 180 MHz
$\zeta$	<b>20</b>	$19.67^{+0.23}_{-0.00}$	$21.13^{+0.18}_{-0.23}$	$19.33^{+0.77}_{-0.00}$
$\log_{10}(T_{vir})$	<b>4.48</b>	$4.47^{+0.01}_{-0.00}$	$4.52^{+0.01}_{-0.04}$	$4.46^{+0.04}_{-0.03}$
$\log_{10}(L_X/\text{SFR})$	<b>40.5</b>	$40.09^{+0.48}_{-1.19}$	$40.00^{+0.99}_{-0.92}$	$40.22^{+0.94}_{-1.06}$
$E_0$	<b>500</b>	$531.51^{+209.64}_{-34.39}$	$656.50^{+409.39}_{-242.44}$	$739.60^{+385.11}_{-348.29}$

Table 4.3: Results of astrophysical parameter constraints from the MCMC for the different frequency bands and with different components. The upper and lower limit show the  $1\sigma$  level from the  $\Delta\chi^2$  grid.

We see that there are multiple regions in the parameter space that satisfy the  $1\sigma$  condition in the middle and last frequency bands. This can confound the parameter estimation via MCMC. Additionally, we can see that the constraints for  $T_{vir}$  are not as tight as shown in Figure 4.9 but the constraints for the other parameters match the results from the MCMC.

We present the estimated median values of the parameters from each of the MCMC runs in Table 4.3, with the upper and lower limit being the  $1\sigma$  level from the  $\Delta\chi^2$  grid. In the presence of both foregrounds and thermal noise,  $T_{vir}$ ,  $L_X/\text{SFR}$  and  $E_0$  are all within  $1\sigma$  from the truth for the three frequency bands. For  $\zeta$ , however, the best fitting parameter values are off by as much as  $5\sigma$  due to the unaccounted cross-power terms. This suggests that the effects of  $\zeta$  on the PS space are primarily at low  $u$  region, since these modes are significantly impacted by the missing power.

## 4.7 Discussion and Conclusion

Our 21cmMC plug-in, PY21CMMC-FG, simulates statistical point-source foregrounds and instrumental components that include a Gaussian beam,  $uv$ -sampling and thermal noise. It uses a Gaussian Fourier beam to re-grid the data before spherically averaging it to compute the 2-D PS. The 2-D PS allows for the use of the entire parameter space in the likelihood computation, effectively ensuring that the effects of foregrounds are accounted for, even in the EoR window.

We show that the implementation of a multivariate normal likelihood and the covariance of the noise and foregrounds appropriately down-weights modes

that are contaminated by foregrounds, thus optimally accounting for all Gaussian information. Additionally, the low level of noise ensures that all modes in the EoR window are used in calculating the likelihood, even though not all modes actually have constraining power. Due to incomplete sampling of the posteriors and insufficient convergence of the chains, a cross-check with a Gaussian posterior distribution is needed to properly constrain the parameters.

Furthermore, in order to accurately constrain the parameters, it is imperative that future experiments take into account the cross-power terms between the EoR signal and the foregrounds and noise. This can be done by either properly modelling all the components together, or by quantifying the cross-power terms separately and adding it to the framework we have developed. Nevertheless, both of these approaches may be computationally expensive and require a lot of memory because the gridded visibilities from all the foregrounds and thermal noise runs need to be stored and added to the EoR signal on each iteration.

Though our research does not address the full complexity of 21 cm parameter estimation experiments, it is the first step towards a more realistic one. In the future, however, it would be useful to include:

- Earth rotation synthesis;
- the full curved-sky visibility equation, including the  $w$ -term particularly for the MWA;
- more realistic, non-Gaussian beams, including non-analytic ones such as the MWA beam (Sutinjo et al., 2015a);
- multi-redshift parameter estimation;
- other systematics such as RFI, ionosphere, gain errors and cable reflections;
- diffuse Galactic foregrounds;
- clustered extragalactic point-source foregrounds; and

- uncertain foreground parameters.

Out of all these effects, the inclusion of Earth rotation synthesis and Galactic foregrounds are the most important because they can lead to a higher noise level up to  $3\times$  for longer baselines, as shown by 21CMSENSE, and contain spatially-structured signal, for the latter. Moreover, a further optimization of the code is necessary for more accurate constraints and absolute convergence of the MCMC.

## Acknowledgements

AN would like to thank R. J. J. Poulton and A. Bahramian for their contribution to this research. This work is supported by the Australian Research Council Centre of Excellence for All Sky Astrophysics in 3 Dimensions (ASTRO 3D), through project number CE170100013. CMT is supported by an ARC Future Fellowship through project number FT180100321. The International Centre for Radio Astronomy Research (ICRAR) is a Joint Venture of Curtin University and The University of Western Australia, funded by the Western Australian State government. We acknowledge that the results in this paper have been achieved by using resources provided by the Pawsey Supercomputing Centre with funding from the Australian Government and the Government of Western Australia, and OzSTAR, funded by Swinburne and the Australian Governments Education Investment Fund.

## 4.8 Appendix

### 4.8.1 Fourier Conventions

The Fourier Transform (hereafter FT) conventions used in this paper are as follows. The continuous  $n$ -dimensional FT,  $F(\mathbf{k})_\infty$ , can be written as

$$F(\mathbf{k})_\infty = \sqrt[n]{\frac{|b|}{(2\pi)^{1-a}}} \int f(\mathbf{r}) \exp(-ib\mathbf{k} \cdot \mathbf{r}) d^n \mathbf{r}, \quad (4.25)$$

where  $\mathbf{r}$  is the comoving coordinate in real space,  $\mathbf{k}$  is the Fourier dual of  $\mathbf{r}$ , and  $a$  and  $b$  are arbitrary constants (Murray, 2018). Conventionally, radio interferometry uses  $(a, b) = (0, 2\pi)$ , while cosmology uses  $(a, b) = (1, 1)$ . To approximate a continuous FT, a discrete FT normalises by the physical length of the data set ( $L$ ) per number of data available for each dimension ( $N$ ). The resulting modes,  $k$ , measured from the transform are

$$k = \frac{2\pi}{b} \frac{m}{L}, m \in (-N/2, \dots, N/2). \quad (4.26)$$

### 4.8.2 Variance of Residual

Let  $w_i$  be the weights used in averaging from 3D  $(u, v, \eta)$ -space down to 2D  $(u, \eta)$ -space, and  $N_{uv}^u$  is the number of UV cells in a given  $|u|$  bin; the variance of  $P_D$  is thus

$$\begin{aligned} \text{Var}(P_D) &= \frac{\sum_{i \in uv} N_{uv}^u w_i^2 \text{Var}(\mathcal{Q})}{\left(\sum_{i \in uv} N_{uv}^u w_i\right)^2} \\ &\equiv \langle \text{Var}(\mathcal{Q}) \rangle_{\mathbf{u}}^*, \end{aligned}$$

where

$$\mathcal{Q} = V_{21} V_{21}^\dagger + V_{FG} V_{FG}^\dagger + V_N V_N^{i\dagger} + 2\mathcal{R}e(V_{21} V_{FG}^\dagger + V_{21} V_N^\dagger + V_{FG} V_N^\dagger). \quad (4.27)$$

In our case, while both  $V_{FG}$  and  $V_N$  are complex random variables,  $V_{21}$  is *not* random. We use the same random seed to create the signal that comprises the mock data and all the model realizations throughout the MCMC (though these have different input astrophysics). Essentially, we treat the signal field as deterministic given the input parameters, and thus ignore cosmic variance. When taking the variance of  $\mathcal{Q}$ , this leads to all cross-terms involving  $\text{Var}(V_{21})$  or  $\text{Var}(P_{21})$  to be

zero, leaving

$$\begin{aligned}
\text{Var}(\mathcal{Q}) = & \text{Var}[P_{FG}] + \text{Var}[P_N] \\
& + 4\text{Var}[\mathcal{R}e(V_{21}V_{FG}^\dagger)] + 4\text{Var}[\mathcal{R}e(V_{21}V_N^\dagger)] + 4\text{Var}[\mathcal{R}e(V_NV_{FG}^\dagger)] \\
& + 4\text{Cov}[V_{FG}V_{FG}^\dagger, \mathcal{R}e(V_{21}^\dagger V_{FG})] + 4\text{Cov}[V_NV_N^\dagger, \mathcal{R}e(V_{21}^\dagger V_{FG})] \\
& + 4\text{Cov}[V_NV_N^\dagger, \mathcal{R}e(V_{21}^\dagger V_N)] + 4\text{Cov}[V_NV_N^\dagger, \mathcal{R}e(V_N^\dagger V_{FG})] \\
& + 8\text{Cov}[\mathcal{R}e(V_{21}V_N^\dagger), \mathcal{R}e(V_{FG}^\dagger V_N)], \tag{4.28}
\end{aligned}$$

and the difference between the data and model variance is

$$\begin{aligned}
\Delta\text{Var}(\mathcal{Q}) = & 4\text{Var}[\mathcal{R}e(V_{21}V_{FG}^\dagger)] + 4\text{Var}[\mathcal{R}e(V_{21}V_N^\dagger)] \\
& + 4\text{Cov}[V_{FG}V_{FG}^\dagger, \mathcal{R}e(V_{21}^\dagger V_{FG})] + 4\text{Cov}[V_NV_N^\dagger, \mathcal{R}e(V_{21}^\dagger V_{FG})] \\
& + 4\text{Cov}[V_NV_N^\dagger, \mathcal{R}e(V_{21}^\dagger V_N)] + 8\text{Cov}[\mathcal{R}e(V_{21}V_N^\dagger), \mathcal{R}e(V_{FG}^\dagger V_N)]. \tag{4.29}
\end{aligned}$$

Assuming both  $V_{FG}$  and  $V_N$  to be proper complex random variables with a uniform phase distribution, we can simplify to

$$\begin{aligned}
\Delta\text{Var}(\mathcal{Q}) = & 4P_{21}\text{Var}(V_{FG}^{\mathcal{R}}) + 4P_{21}\text{Var}(V_N^{\mathcal{R}}) \\
& + 4(V_{21}^{\mathcal{R}} + V_{21}^{\mathcal{I}})[\langle V_{FG}^{3,\mathcal{R}} \rangle - \langle V_{FG}^{2,\mathcal{R}} \rangle \langle V_{FG}^{\mathcal{R}} \rangle] + 4(V_{21}^{\mathcal{R}} + V_{21}^{\mathcal{I}})[\langle V_N^{3,\mathcal{R}} \rangle - \langle V_N^{2,\mathcal{R}} \rangle \langle V_N^{\mathcal{R}} \rangle] \\
& + 8(V_{21}^{\mathcal{R}} + V_{21}^{\mathcal{I}}) \langle V_{FG}^{\mathcal{R}} \rangle \text{Var}(V_N^{\mathcal{R}}), \tag{4.30}
\end{aligned}$$

where a superscript  $\mathcal{R}$  indicates taking just the real component (which is statistically equivalent to the imaginary component). Here the 3-point term in the noise disappears because it is symmetric about zero. Without explicitly modelling the 3-point term of the foregrounds, we also assume that it is very much sub-dominant – there is nothing to favour a negative over a positive foreground visibility component. Recognising that  $\text{Var}(V^{\mathcal{R}}) = \text{Var}(V)/2$ , we finally obtain

$$\Delta\text{Var}(\mathcal{Q}) = 2P_{21} [\text{Var}(V_{FG}) + \text{Var}(V_N)]. \tag{4.31}$$



# Chapter 5

## The Correlation between Self-Consistent Foregrounds and Cosmic Reionisation

### 5.1 Introduction

As we have already established, the search for the 21 cm signal from cosmic dawn and the EoR is challenging due to the presence of foreground contaminants. They originate from celestial objects and are expected to be up to 5 orders of magnitude brighter than the prized signal itself (Pritchard & Loeb, 2012). In the radio regime, extra-galactic foregrounds are dominated by Active Galactic Nuclei (AGN) and star-forming galaxies. Much work has been done to statistically model the foregrounds at low frequency (e.g. Shaver et al. 1999, Jackson 2005, and Intema et al. 2011), whereby the sources are predicted to cover the sky following a certain distribution. Typically, studies assume a complete decoupling of the high-redshift EoR signal from the statistical extragalactic foreground model designed to match low-redshift observations (e.g. Jelić et al. (2008) and Gleser et al. (2008)) and do not take into account that the foreground contaminants are the evolutionary descendants of the same sources that reionised the universe during the EoR, which are assumed to be second-order effects.

This assumption of foreground independence from EoR signal is motivated by a few factors. Although cosmic reionisation has completed around  $z \sim 6$  based on existing observational constraints of the Gunn-Peterson trough from

the spectra of high-redshift quasars (Fan et al., 2006), the number density of AGN and the star formation rate do not peak until  $z \sim 2$  (Wolf et al., 2003; Richards et al., 2006; Madau & Dickinson, 2014). The merger rate of galaxies is also considerably constant before  $z \sim 1$  e.g. Fakhouri et al. (2010). These, along with the separation of at least 300 Mpc between the two epochs, suggest that the state of galaxies at the end of reionisation does not have a strong influence on their evolution below  $z \sim 6$  as they are dominated by merger events, which are highly stochastic and therefore, act to de-correlate the input reionisation from the output foreground galaxies. The correlation between realizations of the Universe at these different epochs given the same astrophysical parameters is thus expected to be close to zero.

However, it is still possible that for the same Universe, there exists a correlation between the inferred parameters of the 21 cm EoR signal and the extragalactic foreground contaminants in power spectrum space. To study this in the context of the EoR, we need a simulation that covers the entire history of structure formation down to the local universe. We utilize the halo merger trees from the ASTRO 3D GENESIS  $N$ -body simulation as input to MERAXES, which provides the analytical prescriptions for the astrophysical processes involved in reionisation and galaxy formation and evolution. The GENESIS simulation box we use contains  $2048^3$  dark matter particles in a  $105 \text{ Mpc}/h$  comoving box with  $128^3$  grid (Poulton et al., 2020), run with a memory-lean version of the GADGET-2 code (Springel, 2005). It extends from  $z = 20$  down to  $z = 0$  with 132 snapshots corresponding to an evenly-spaced logarithmic interval in the growth factor. In addition, to ensure that we can efficiently sample the parameter space, a semi-analytic model that studies both reionisation and galaxy formation is needed. We utilize the code MERAXES (Mutch et al., 2016) to explore the effects of self-consistent foregrounds and EoR signal in the power spectrum space. From this, we can gauge whether the astrophysical parameters we use for the EoR simulations have any statistically-significant impact on the foreground statistics. Moreover, the study of self-consistent reionisation and foreground signals also allows for a comparison between its statistical variation and the natural variation of the

foreground observed from multiple sky pointings i.e., cosmic variance.

Furthermore, the correlation between foregrounds and reionisation may be able to help with the EoR parameter estimation studies. The framework of 21CMMC (Greig & Mesinger, 2015; Greig & Mesinger, 2018) uses a prescription to quantify the statistical likelihood of a set of data given an input model and parameters. Explicit definition of this model is non-trivial thus some assumptions are implemented with a Gaussian likelihood, whereby separate reionisation signal and foreground covariances are employed and the foreground covariance term is assumed to be independent of EoR parameters (Greig & Mesinger, 2015; Greig & Mesinger, 2018; Nasirudin et al., 2020). Our research will thus help either reaffirm or reject the assumptions made and explore the possibility to use foregrounds to understand cosmic reionisation.

In this work, we consider the standard paradigm of a flat  $\Lambda$  cold dark matter universe with the most up-to-date parameters from Planck Collaboration et al. (2016) whereby the reduced Hubble, matter density, baryon density, dark energy density, average matter fluctuation, and spectral index parameters ( $h, \Omega_m, \Omega_b, \Omega_\Lambda, \sigma_8, n_s$ ) are 0.678, 0.308, 0.0484, 0.692, 0.815, and 0.968 respectively. We use the default MERAXES parameters that have been calibrated in Qin et al. (2017a) with the TIAMAT N-body simulation. Note that a further calibration of MERAXES parameters is needed in the future because of the higher simulation resolution that we use, which subsequently affects the observable properties of foregrounds, as we will show in this work.

## 5.2 Methodology

In this section, we explain the scaling relations used to convert the black hole mass and star forming rate of galaxies to radio luminosity at 1.4 GHz, and the calculation of the power spectrum.

## 5.2.1 Luminosity Scaling Relation

The luminosity,  $L_\nu$ , arising from accretion of matter onto black holes can be categorized into either radio-mode or quasar-mode based on the accretion of hot or cold gas. Following previous works e.g. Meier (2002), Fanidakis et al. (2011), and Amarantidis et al. (2019),  $L_\nu$  at  $\nu = 1.4$  GHz for the two accretion modes are given by

$$\nu L_\nu^{\text{radio}} = A_{\text{radio}} \left( \frac{M_\bullet}{10^9 M_\odot} \times \frac{\dot{M}_{\text{hot}}}{0.01} \right)^{0.42} L_{\text{jet}}^{\text{radio}} [\text{W}], \quad (5.1)$$

$$\nu L_\nu^{\text{quasar}} = A_{\text{quasar}} \left( \frac{M_\bullet}{10^9 M_\odot} \right)^{0.32} \left( \frac{\dot{M}_{\text{cold}}}{0.01} \right)^{-1.2} L_{\text{jet}}^{\text{quasar}} [\text{W}], \quad (5.2)$$

where  $\dot{M}_{\text{hot}}$  and  $\dot{M}_{\text{cold}}$  are the accretion rates of hot and cold gas respectively with respect to  $\dot{M}_{\text{Edd}}$  and

$$L_{\text{jet}}^{\text{radio}} = 2 \times 10^{45} \left( \frac{M_\bullet}{10^9 M_\odot} \times \frac{\dot{M}_{\text{hot}}}{0.01} \right) a^2 [\text{W Hz}^{-1}], \quad (5.3)$$

$$L_{\text{jet}}^{\text{quasar}} = 2.5 \times 10^{43} \left( \frac{M_\bullet}{10^9 M_\odot} \right)^{1.1} \left( \frac{\dot{M}_{\text{cold}}}{0.01} \right)^{1.2} a^2 [\text{W Hz}^{-1}]. \quad (5.4)$$

$a$  is the spin parameter and the values of MERAXES normalization parameters are from Amarantidis et al. (2019) whereby  $A_{\text{radio}} = 8.0 \times 10^{-5}$  and  $A_{\text{quasar}} = 5.0 \times 10^{-2}$ .

For star-forming galaxies, the relations between  $L_\nu$  from free-free electrons (Thermal; T) and synchrotron radiation (Non-Thermal; NT) origins and the Star-Forming Rate (SFR) of stars with masses  $M > 5M_\odot$  are given by

$$\frac{L_\nu^{\text{T}}}{\text{WHz}^{-1}} = 5.5 \times 10^{20} \left( \frac{\nu}{\text{GHz}} \right)^{-0.1} \frac{\text{SFR}}{M_\odot \text{yr}^{-1}}, \quad (5.5)$$

$$\frac{L_\nu^{\text{NT}}}{\text{WHz}^{-1}} = 5.3 \times 10^{21} \left( \frac{\nu}{\text{GHz}} \right)^{-0.8} \frac{\text{SFR}}{M_\odot \text{yr}^{-1}}, \quad (5.6)$$

based on results of Condon (1992).

The conversion from  $L_\nu$  to the flux density,  $S_\nu$ , follows

$$S_\nu = \frac{L_\nu}{4\pi d_L^2} (1+z)^{1+\alpha} \quad [\text{W m}^{-2} \text{ Hz}^{-1}], \quad (5.7)$$

where  $d_L$  is the luminosity distance and  $\alpha$  is the spectral index of the Spectral Energy Distribution (SED). We artificially set the value of  $\alpha$  by randomizing its value for each foreground source following a normal distribution with  $\mu = 0.8$  and  $\sigma = 0.05$  to calculate  $S_\nu$  at low frequency. For clarity, the stochasticity of the spectral index is one of the sources of our *uncertainty* in this research, the other being the lightcone generation. Finally,  $S_\nu$  is converted to  $T_B$  following the Rayleigh-Jeans law and is given by

$$T_B = \left( \frac{c^2}{2\nu^2 k_B} \right) S_\nu \quad [\text{W m}^{-2} \text{ Hz}^{-1}], \quad (5.8)$$

where  $k_B$  is the Boltzmann constant.

## 5.2.2 Source Count Distribution

To compare the self-consistently evolved foregrounds from MERAXES with a simple, commonly-used model that simulates the effects of extra-galactic point-source foregrounds (e.g. in Murray et al. (2017) and Nasirudin et al. (2020)), we use the source spatial density per unit flux density,  $dN/dS$ , given by

$$\frac{dN}{dS}(S, \nu) = \alpha S_\nu^{-\beta} \left( \frac{\nu}{\nu_0} \right)^{-\gamma-\beta} \quad [\text{Jy}^{-1} \text{ sr}^{-1}]. \quad (5.9)$$

Here,  $S_\nu$  is the flux at a specific frequency  $\nu$ ,  $\beta$  is the slope of the source-count function, and  $\gamma$  is the mean spectral-index of point sources, with  $\alpha = 4100 \text{ Jy}^{-1} \text{ sr}^{-1}$ ,  $\beta = 1.59$ , and  $\gamma = 0.8$  at  $\nu_0 = 150 \text{ MHz}$  based on an observational result from Intema et al. (2011). This is different from the foreground simulation employed by Jelić et al. (2008), which uses the method by Jackson (2005) to simulate a sky that is extrapolated down to sub-mJy flux densities and includes an angular correlation in populating their extra-galactic foreground in the mock sky, and by Li et al. (2019b), which extrapolates the sky map from higher frequency down

to low frequencies (refer to §1.5.1). We assume that foregrounds brighter than 10 mJy have been peeled from the observation and set  $S_{\min}$  and  $S_{\max}$  to be 10 nJy and 10 mJy respectively. We also assume that the sources are uniformly randomly distributed in the sky.

### 5.2.3 Power Spectrum

In our research, we employ the Blackman-Harris window function in the spectral dimension and smooth the visibilities over frequency via interpolation to contain the foreground contamination in the 2-D power spectrum. For clarity, hereafter, we refer to the estimated 2-D power spectrum with the frequency taper as  $P(k_{\perp}, k_{\parallel})$ , where  $k_{\perp}$  and  $k_{\parallel}$  are the angular and line-of-sight modes. All  $P(k_{\perp}, k_{\parallel})$  in this work are computed between 150 to 160 MHz with 150 equally-spaced frequency channels.

Given that the foreground model we use is purely based on Equation 5.9 and that the foregrounds are uniformly distributed in the sky, the foreground power,  $P(u, \eta)$ , for spatial scale  $u$  and frequency scale  $\eta$ , can be derived analytically. In the presence of a Gaussian beam model, Murray et al. (2017) describes this as

$$P(u, \eta) \approx K \sigma^2 \mu_1^2 P(u) e^{-\eta^2 (\frac{W^2 u^2}{\sigma^2} + \sigma_f^2)}, \quad (5.10)$$

where  $K$  and  $W$  are the normalization constants,  $\sigma$  is the width of the Gaussian beam, and  $\mu_1$  is the first moment of the source count distribution

$$\mu_n = \int S^n \frac{dN}{dS} dS [\text{Jy}^n \text{sr}^{-1}]. \quad (5.11)$$

$P(u)$  is the angular power spectrum of the point-source foregrounds, assumed to be a power law  $P(u) = \left(\frac{u}{u_0}\right)^{-\kappa}$  with spectral index  $\kappa$ , and  $\sigma_f$  is the width of the frequency taper. Note that in Equation 5.10, the only terms that are dependent on the sky model are  $\mu_1$  and  $P(u)$ . Given the assumption of a smooth power-law SED for each source that we artificially enforce in this work, the foreground power spectrum can really be factored into two parameters: 1) an overall amplitude given by the integral of the source counts ( $\mu_1$ ), and 2) a shape given by the

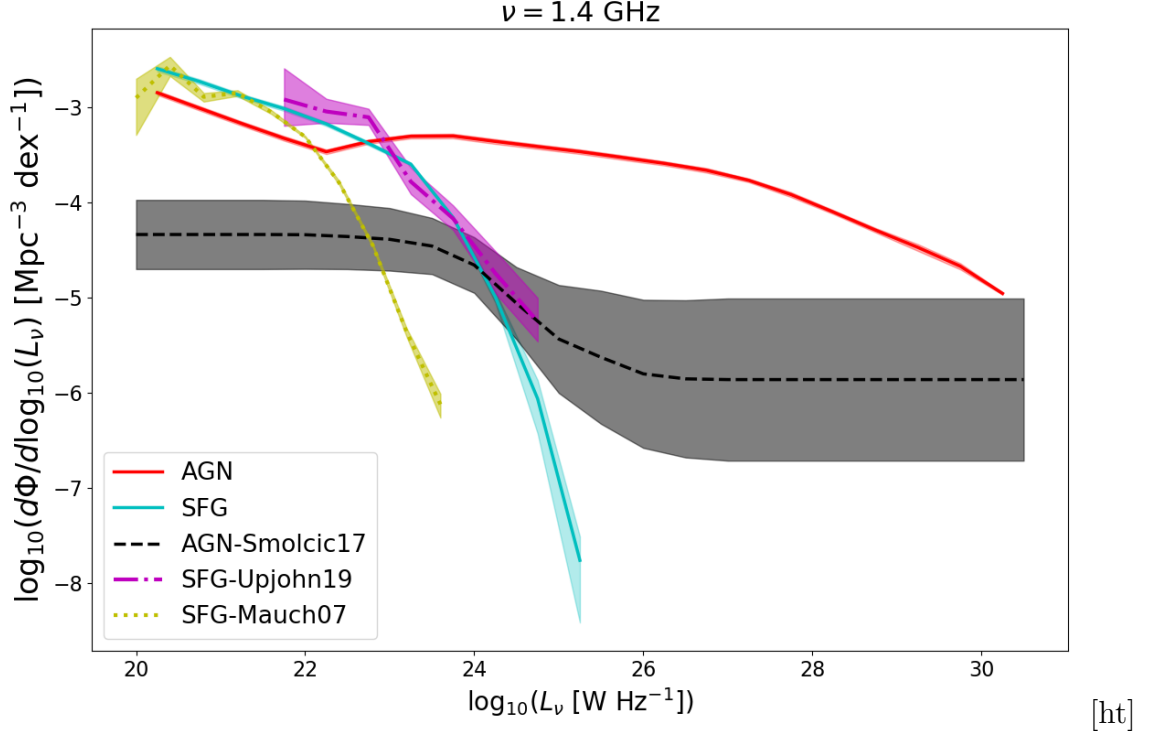


Figure 5.1: The luminosity function of the foregrounds at 1.4 GHz, in which the AGN and SFG from MERAXES are given by the solid red and cyan lines respectively, the AGN observations by Smolčić et al. (2017) is given by the black dash line, and the SFG observations by Mauch & Sadler (2007) and Upjohn et al. (2019) are given by the yellow dotted and magenta dash dot lines respectively. Note that AGN observations from Smolčić et al. (2017) are within  $0 < z < 5.5$ , but the SFG observations from Mauch & Sadler (2007) and Upjohn et al. (2019) are between  $0 < z < 0.3$  and  $0 < z < 1.3$  respectively; as such, the AGN and SFG from MERAXES are presented over the same  $z$  ranges as the observations ( $0 < z < 1.3$  for the SFG). The overall magnitude and shape of the SFG luminosity function from our framework is consistent with both SFG observations at  $\log_{10}(L_\nu) < 25$ . For the AGN, however, there is a discrepancy in both the magnitude and shape of the luminosity function across  $\log_{10}(L_\nu)$ . There is no flattening in the AGN luminosity function from MERAXES at  $\log_{10}(L_\nu) > 25$  and the discrepancy is as high as 2 orders of magnitude.

angular power spectrum of the sources ( $P(u)$ ). These two parameters are, in turn, dependent on the  $dN/dS$  and  $\kappa$  respectively.

### 5.3 Results

We first compare the luminosity function of the AGN and Star Forming Galaxies (SFG) foregrounds from one realization of a lightcone from MERAXES, to the results with observations of AGN and SFG from Smolčić et al. (2017), Mauch & Sadler (2007) and Upjohn et al. (2019) respectively at 1.4 GHz in Figure 5.1.

Note that AGN observations from Smolčić et al. (2017) are for  $0 < z < 5.5$ , but the SFG observations from Mauch & Sadler (2007) and Upjohn et al. (2019) are for  $0 < z < 0.3$  and  $0 < z < 1.3$  respectively; as such, the AGN and SFG from MERAXES are presented over the same  $z$  ranges as the observations ( $0 < z < 1.3$  for the SFG). The overall magnitude and shape of the SFG luminosity function from our framework is consistent with both SFG observations at  $\log_{10}(L_\nu) < 25$ . For the AGN, however, there is a discrepancy in both the magnitude and shape of the luminosity function across  $\log_{10}(L_\nu)$ . There is no flattening in the AGN luminosity function from MERAXES at  $\log_{10}(L_\nu) > 25$  and the discrepancy is as high as 2 orders of magnitude. This shows that with its current calibrated parameters, MERAXES over-predicts the number of AGNs observed at 1.4 GHz, especially those that are more luminous.

Next, we compare  $P(k_\perp, k_\parallel)$  of the EoR and self-consistent MERAXES foregrounds run with the default parameters with the foregrounds from the Intema et al. (2011) empirical model described in §5.2.2. We show  $P(k_\perp, k_\parallel)$  with respect to  $k_\parallel$  for some values of  $k_\perp$  in Figure 5.2. The red region shows the foreground-contaminated region because most of the foreground power is contained in the first four  $k_\parallel$  cells, which is the width of the Blackman-Harris taper<sup>1</sup>. The EoR signal (black line) dominates in the EoR window compared to the observed Intema foregrounds (cyan line) because most of the foreground power is contained in the first four  $k_\parallel$  cells. However, the self-consistent MERAXES foreground power (orange line) dominates all area in the power spectrum space and is up to  $\sim 8$  orders of magnitude brighter than the empirically observed foregrounds from Intema et al. (2011). This is consistent with our earlier observation that MERAXES over-predicts the overall number of foreground sources, thus resulting in an overall increase in foreground power throughout the power spectrum space. Even though MERAXES over-predicts the number of foregrounds, Figure 5.2 suggests that this does not affect the EoR physics because the level of EoR power is similar to the magnitude prediction from other studies at  $z \sim 6$  e.g. (Mesinger et al., 2011).

To study the effects of changing the reionisation astrophysical parameters on

---

<sup>1</sup>Note that in this work we do not apply observational systematics such as baseline migration, hence the ‘wedge’ is not present.

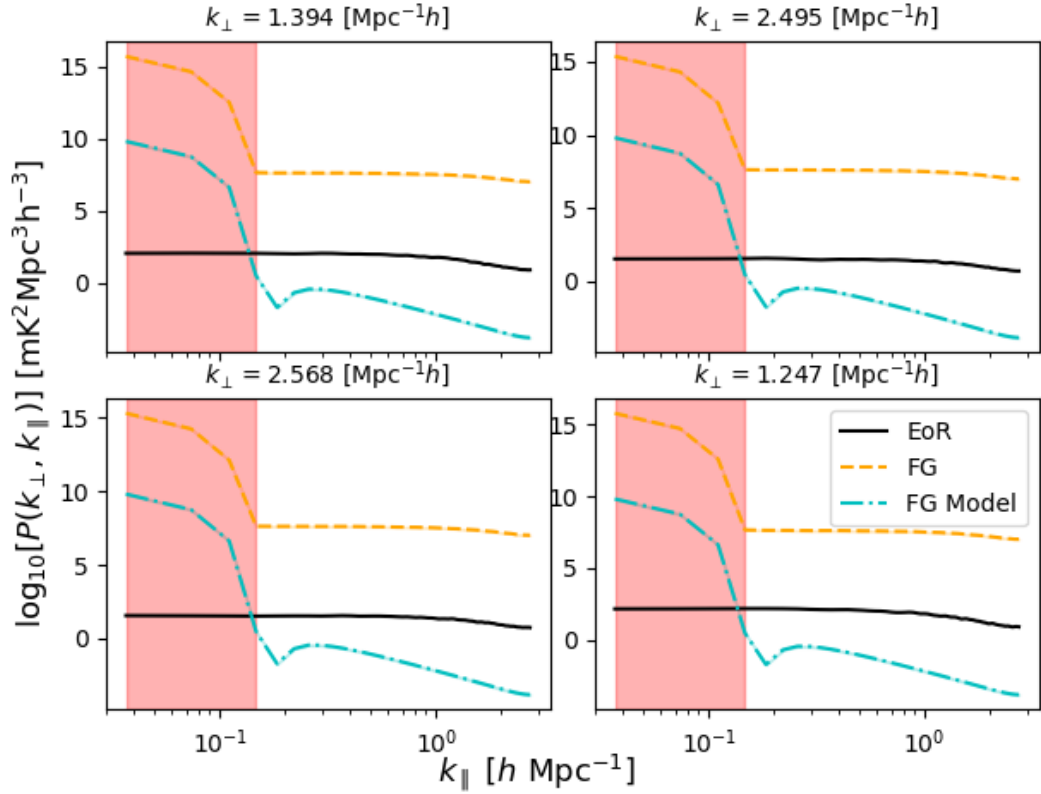


Figure 5.2:  $P(k_{\perp}, k_{\parallel})$  of the EoR, self-consistent foregrounds and the foreground model with respect to  $k_{\parallel}$  for some  $k_{\perp}$ . The red region shows the foreground-contaminated region because most of the foreground power is contained in the first four  $k_{\parallel}$  cells, which is the width of the Blackman-Harris taper. The EoR signal (black line) dominates in the EoR window compared to the observed Intema foregrounds (cyan line). However, the self-consistent MERAXES foreground power (orange line) dominates all regions of the 2D power spectrum space and is up to  $\sim 8$  orders of magnitude brighter than the empirically observed foregrounds from (Intema et al., 2011) across all  $k_{\parallel}$ .

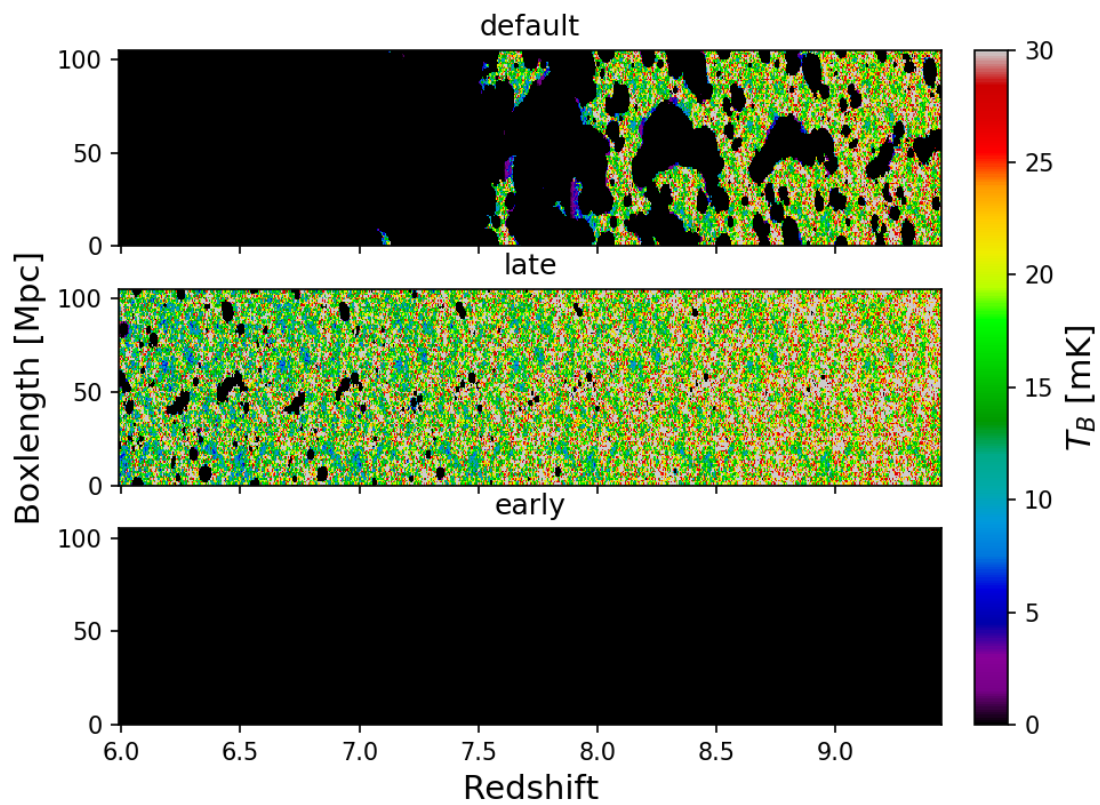


Figure 5.3: From top to bottom, the  $T_B$  field lightcone from the implementation of extreme reionisation models with  $f_{\text{esc}|z=5} \in [0.06, 1e^{-4}, 1.0]$ , dubbed as default, late, and early respectively. The use of a lower/higher  $f_{\text{esc}|z=5}$  value (middle/bottom panel) results in a(an) later/earlier completion of reionisation, as expected.

the self-consistent foregrounds, we employ three different reionisation models by fiducially increasing and decreasing the value of the escape fraction normalisation,  $f_{\text{esc}|z=5}$ , where, for a  $z$ -varying  $f_{\text{esc}}$  model,

$$f_{\text{esc}} = \min \left[ f_{\text{esc}|z=5} \left( \frac{1+z}{6} \right)^\kappa, 1 \right] \quad (5.12)$$

and  $\kappa = 2.5$  (Mutch et al., 2016). We refer to the use of  $f_{\text{esc}|z=5} \in [0.06, 1e^{-4}, 1.0]$  as default, late, and early models respectively; as the names suggest, they correspond to extreme model of reionisation which radically affects the timing of reionisation. The resulting  $T_B$  field lightcones are shown in Figure 5.3. The use of a lower/higher  $f_{\text{esc}|z=5}$  value (middle/bottom panel) results in a(an) later/earlier completion of reionisation, as expected.

We then run 50 different realizations of lightcone and spectral index for the three reionisation models that we have employed to look at their variance. Hereafter, the MERAXES uncertainties presented in this work arise from random generation of 1) the spectral indices, and 2) the lightcone in which different orientations and chunks of comoving volumes are chosen each time. For clarity, we use the same density field as input to MERAXES hence the variance that we have is *not* the true cosmic variance. Random generation of the lightcone, however, somewhat represents cosmic variance. In addition, we have not taken into account the uncertainty arising from the luminosity scalings that we have presented in §5.2.1.

We then compare the ratio of the  $P(k_\perp, k_\parallel)$  from the late and early models to the  $P(k_\perp, k_\parallel)$  of the default model in Figure 5.4. The top panels show the ratio of  $P(k_\perp, k_\parallel)$  for the EoR signal and the bottom panels show the ratio of  $P(k_\perp, k_\parallel)$  for the foregrounds, with the left and right panels representing the late and early models respectively. Note that the top right panel is completely empty because for the early model, based on Figure 5.3, reionisation has ended in the frequency range that we are interested in ( $150 \leq \nu \leq 160$  MHz corresponds to  $\sim 7.9 \leq z \leq 8.5$ ). In the top left panel, the ratio of the EoR signal for the late model is as high as  $\sim 90\%$  greater than the default, which is expected because reionisation of HI is still ongoing. Furthermore, the lower panels show that the ratios of foreground power of the two models to the default also differ by as high

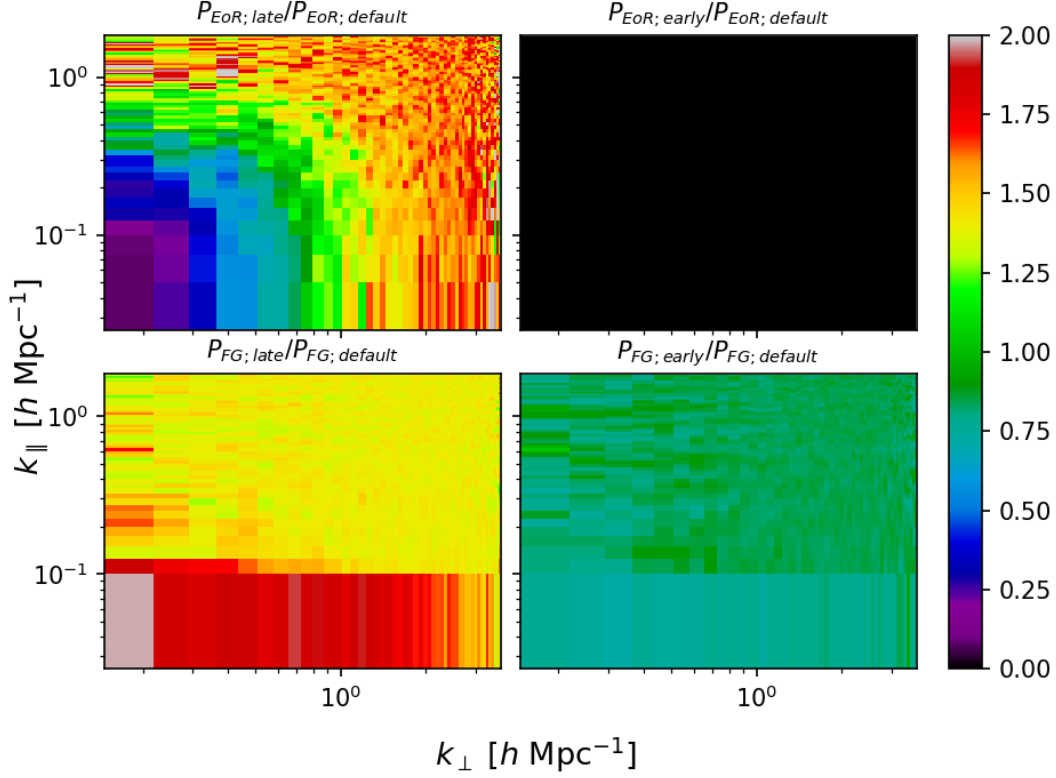
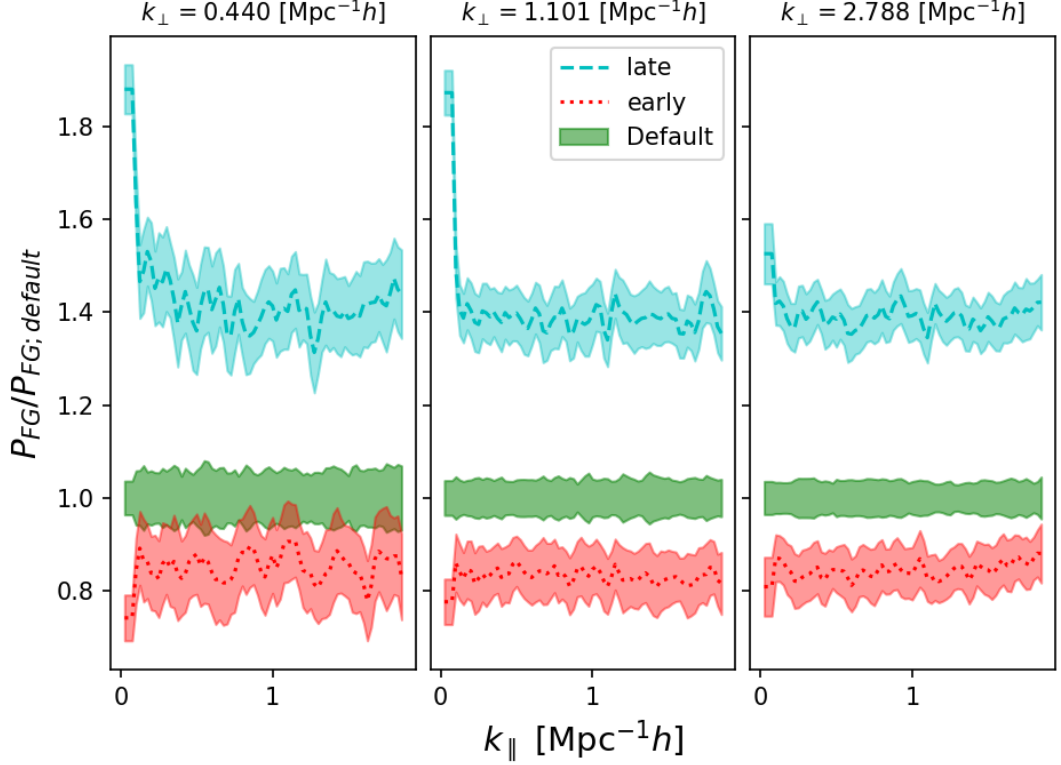


Figure 5.4: The ratio of the  $P(k_{\perp}, k_{\parallel})$  of EoR signal (top panels) and foregrounds (bottom panels) of the late model (left panels) and early model (right panels) to the default model. Note that the top right panel is completely empty because for the early model as shown in Figure 5.3, reionisation has ended in the frequency range that we are interested in ( $150 \leq \nu \leq 160$  MHz corresponds to  $\sim 7.8 \leq z \leq 8.5$ ). In the top left panel, the ratio of the EoR signal for the late model is as high as  $\sim 90\%$  greater than the default, which is expected because reionisation of HI is still ongoing. Furthermore, the lower panels show that the ratios of foreground power of the two models to the default also differ by as high as  $\sim 90\%$  and  $\sim 25\%$  in the foreground-dominated region of the power spectrum, and as low as  $\sim 50\%$  and  $\sim 10\%$  in the rest of the power spectrum space.



[ht]

Figure 5.5: The evolution of the ratio of the foregrounds  $P(k_{\perp}, k_{\parallel})$  with the different EoR models to the default model in some  $k_{\perp}$  cells with respect to  $k_{\parallel}$ . The cyan, red, and green regions represent the ratio of uncertainties of  $P(k_{\perp}, k_{\parallel})$  for the late, early, and default MERAXES runs respectively, in which the uncertainty arises from the lightcone generation and spectral index variance. The dashed cyan line and dotted red line represent the mean  $P(k_{\perp}, k_{\parallel})$  ratio of the late and early model to the default model.

as  $\sim 90\%$  and  $\sim 25\%$  in the foreground-dominated region of the power spectrum.

To explore the correlation between reionisation physics and foregrounds, we present the foreground  $P(k_{\perp}, k_{\parallel})$  ratio in some  $k_{\perp}$  cells with respect to  $k_{\parallel}$  for two models to the default model in Figure 5.5. The cyan, red, and green regions represent the ratio of uncertainties of  $P(k_{\perp}, k_{\parallel})$  for the late, early, and default MERAXES runs respectively, in which the uncertainty arises from the lightcone generation and spectral index variance. The dashed cyan line and dotted red line represent the mean  $P(k_{\perp}, k_{\parallel})$  ratio of the late and early model to the default model. The mean and uncertainty of the two extreme EoR models are distinct from the default, deviating by at least  $4\sigma$  and  $2\sigma$  for the late and early model respectively. Interestingly, the ratios are in increasing order based on the values

of  $f_{\text{esc}|z=5}$ , with the early model having the lowest ratio and the late model having the highest ratio. This suggests that there may be a weak correlation between reionisation and the foreground contaminants, although it is hard to ascertain given that the AGN model is not accurate with respect to current observation.

Nevertheless, to further investigate this potential correlation, we plot the mean Euclidean-normalized differential source count and the uncertainty arising from the lightcone and spectral index variance for the different EoR models at 150 MHz in Figure 5.6. Note that the uncertainty is calculated by running each reionisation model 50 times with random spectral indices and lightcone generation, whereby different directions and chunks of comoving volume are chosen each time. The square, circle and triangle markers represent the values from the default, late, and early runs respectively, the orange solid line shows the values from the foreground model based on Intema et al. (2011), and the black dash line and grey region show the mean value and uncertainty from multiple AGN simulations based on Amarantidis et al. (2019), which is what we use for our AGN scaling relation as described in §5.2.1.

The AGN produced by MERAXES are consistently higher than other AGN simulations (black dash line), deviating by more than  $1\sigma$  at  $S_\nu \geq 0.5$  mJy. On the other hand, the shape and magnitude of the source count distribution of SFG from MERAXES is comparable to the total observed foregrounds in the same  $S_\nu$  range, with minimal difference of less than 0.5 order of magnitude. At low  $S_\nu$ , the source count from both the AGN and SFG from MERAXES are lower than the Intema et al. (2011) observation. The fact that the foreground observation is not deep enough, as is apparent from the lack of a spectral flattening caused by the SFG in the orange solid line, may explain why the discrepancy between simulation and observation is larger than that of the luminosity function at 1.4 GHz shown in Figure 5.1. Notice that for both the AGN and the SFG, the mean differential source counts are relatively similar for the three extreme reionisation scenarios that we have employed.

Although the fractional difference of the source counts from the different reionisation scenarios, as shown in Figure 5.5, is more than the cosmic variance of

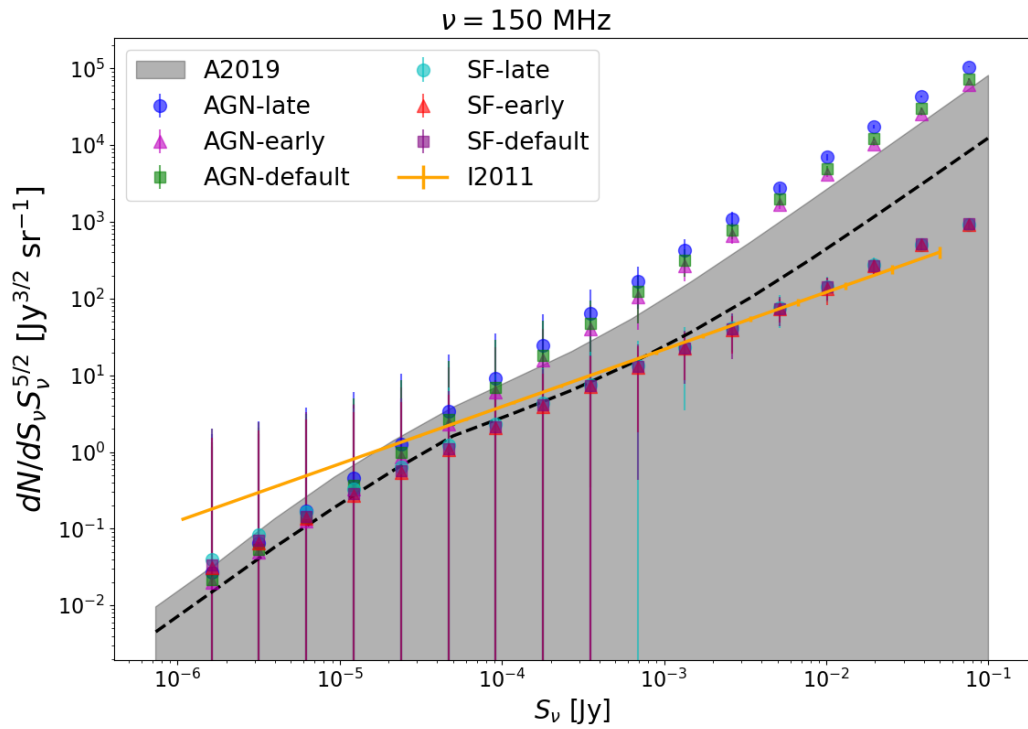


Figure 5.6: The mean Euclidean-normalized differential source count and uncertainty from the default, early, and late runs (square, triangle and circle markers respectively with colours as labelled), the foregrounds model based on Intema et al. (2011) (orange solid line), and the mean value (black dash line) and uncertainty (grey region) from multiple AGN simulations based on Amantidis et al. (2019), which is what we use for our AGN scaling relation as described in §5.2.1.

$\sim 7\%$ , Figure 5.1 demonstrates that the uncertainty from the AGN simulation and scaling relation outweighs the uncertainty from the correlation between the extra-galactic foregrounds and the EoR. This is because the only sky-dependent terms of the foreground power described in Equation 5.10 are the source count distribution and the power-law index, and the fact that these two terms are comparable suggests that the change in foreground power resulting from the change in EoR model is small.

## 5.4 Discussion and Conclusion

From the results presented in §5.3, we have demonstrated that the physics of reionisation has little effect on foregrounds and consequently, its power spectrum. Even with the relevant extreme reionisation scenarios employed, the resulting source count distributions are all relatively similar, signifying that there is no correlation between cosmic reionisation and foregrounds within the uncertainties of this work because the uncertainty from the scaling relation outweighs the uncertainty from the correlation. Although the MERAXES needs to be calibrated to match with AGN observation, we do not expect the correlation to change by much; the calibration will only cause the AGN foregrounds from MERAXES to match with observations.

The question now is whether our fiducial uncertainty from the spectral index that we have employed is larger than *other* sources of uncertainty? The scaling relations used to translate the physical properties of the foregrounds to  $L_\nu$  and  $S_\nu$  is a dominant source of uncertainty because they directly affect the observable properties of these sources. This is evident from the large uncertainty arising from the astrophysical model of multiple AGN simulations as reported by Amarantidis et al. (2019) that is shown in Figure 5.6, suggesting that the variance of the scaling relation – which is derived based on the results of these simulations – will dominate over systematic dependence on EoR. Furthermore, a more robust implementation of cosmic variance will also add more observational uncertainty because the different realizations of the density field of the universe will have a

large effect on the clustering of foreground sources.

Another related question is whether applying higher-order statistics (or different statistics) to the foregrounds do have discriminating power on reionisation models. The power spectrum, or variance, is used because it captures the majority of information on the EoR signal but a different metric can be applied to the foreground, which may be able to distinguish the different reionisation scenarios that precede our current epoch.

The result of our research shows that we cannot directly constrain the EoR parameters by a better understanding of the foregrounds, hence we can only use our knowledge of foregrounds to reduce the degrees of freedom for the EoR parameter constraints. However, this consequently means that the covariance matrices of EoR and foregrounds can be properly separated and that the foreground covariance matrix does not depend strongly on the EoR parameters. A constant covariance which is only dependent on the foreground parameters can therefore be used in Bayesian analyses to map the EoR parameter space e.g. 21CMMC (Greig & Mesinger, 2015; Greig & Mesinger, 2018), thus simplifying reionisation parameter estimation studies.



# Chapter 6

## Conclusion

In this thesis, we have addressed some first-order limitations in cosmic reionisation studies that can potentially have severe effects in understanding the physics of the EoR. Our implementation of the stochasticity and temporal correlation of low-mass haloes based on the distribution from  $N$ -body simulations in Chapter 3 allows us to extend the resolution of dark matter simulations. We can thus self-consistently study the impact low-mass galaxies have on their surroundings, especially during the early stages of reionisation. This is important for 21 cm studies because 1) the cosmic structures forming inside these low-mass haloes set the initial conditions of the EoR, and 2) the imprint on the IGM that these cosmic structures leave behind will reveal the tomography of the early universe with respect to time.

In the future, one further research avenue that needs to be explored in detail is the effect of including traditionally-unresolved haloes that are generated from our method in radiative transfer simulations. While dark matter haloes form the gravitational scaffolding of the universe, baryons and their physics govern the astrophysical processes that trigger cosmic reionisation. Therefore, to understand how our implementation affects the 21 cm signal from the EoR, it is imperative that such a follow-up study is conducted.

In terms of our actual method to implement the stochasticity of temporally-correlated, low-mass haloes, there are several main caveats that can be improved. Our current method uses the entire history of the haloes from  $z \sim 25$  down to  $z \sim 6$  in administering the temporal bias of these haloes; this means that we have generalized the bias to encompass different epochs, e.g cosmic dawn and X-

ray heating, whereas the contribution of ionising photons from low-mass haloes during the EoR is supposed to be different. Therefore, instead of the entire history, smaller sets of temporal evolution should be considered in the future.

Moreover, in reality, the temporal bias should only be based on the *past* conditions of the haloes because the future should not have an effect on the present conditions of the haloes. The reason we have implemented this method is to somewhat take into account the spatial bias of these haloes with respect to the overdensity field. By looking at the entire halo-hosting history of each cell in the density field, we can see that some cells are more likely to host haloes e.g. due to close proximity to other haloes. To enable the implementation of a more “realistic” method whereby only the past is considered for the temporal correlation, the spatial bias i.e. the clustering of the haloes needs to be implemented as well.

Nonetheless, we find our improved model accurately reproduces the average local number or collapsed fraction of the low-mass haloes. Additionally, the clustering and evolution of the halo population are generally in agreement with the actual  $N$ -body simulation, as shown by the comparison of correlation coefficients and power spectra from the two sets of data. The method that we have developed to resolve low-mass haloes in  $N$ -body simulation is useful not only for reionisation studies, but also for other studies that rely on a more complete and realistic halo catalogue to explore the effects of small-scale structures on large, cosmological volumes.

In Chapter 4, we have explored the effects of including realistic extra-galactic foregrounds and instrumental components in EoR parameter estimation experiments by developing a framework that complements 21CMMC. We find that the results are biased because foreground power is separately added in the likelihood function, whereby the cross-power terms between the 21 cm signal and the foregrounds in the EoR window are unaccounted for. This finding is important for future 21 cm parameter estimation experiments whereby the observational data has both foregrounds and 21 cm signal, along with other instrumental factors.

Consequently, the first improvement that should be implemented in our pipeline is including the cross-power terms. Unfortunately, it can be computationally ex-

pensive because at each MCMC iteration, it will require that the gridded visibilities of foregrounds and thermal noise be stored and added to the gridded visibilities of the EoR signal. Given that our pipeline takes 20 minutes per iteration to go from simulating the reionisation model to finding the log-likelihood, a further optimization of the software is critical to ensure that the MCMC can sufficiently converge.

In addition, our pipeline does not incorporate a few complex components that can influence the observational data. These include: Earth rotation synthesis which directly impacts the visibility sampling and noise level; the curvature effects of a wide-field array; realistic beams with sidelobes; diffuse Galactic foregrounds; clustering of point-source foregrounds; and other systematics such as RFI and ionospheric effects. The presence of these components in the data can potentially skew the results of 21 cm parameter estimation because they directly affect the resulting power spectrum, hence the effects of each component need to be properly quantified and included in future work.

Despite these caveats, with the framework we have developed in Chapter 4, for the first time, we have coherently combined realistic foregrounds with realistic instruments in 21 cm parameter estimation experiments and explored their importance in this area of research. We have demonstrated that their presence affects not only the wedge area of the power spectrum, which is what has always been assumed in previous works, but also the EoR window hence skewing the MCMC constraints of the reionisation parameters. Thus, realistic foregrounds and instrument systematics must be included in future work to enable a more robust constraint. The pipeline we have developed is publicly available, allowing researchers to coherently apply instrumental effects on the signal as well as the foreground contaminants.

Finally, in Chapter 5, we have explored the correlation between self-consistent extra-galactic foregrounds and cosmic reionisation. In the EoR studies, an assumption that these two components are uncorrelated has always been made, although its validity has never been tested before. If it is found to be wrong, this assumption could potentially affect the results from parameter estimation

experiments. The results of our research, however, demonstrates that this assumption is valid and that there is no statistical correlation between the cosmic reionisation and foregrounds, hence the foreground power is insensitive to the EoR parameters.

One caveat of our research on self-consistent foregrounds is the need to recalibrate the semi-analytic model MERAXES based on current observational constraints for the cosmological simulation that we use. This is because the current parameters used in MERAXES overestimate the number of AGNs when used with the slightly less resolved GENESIS simulation. While the recalibrated parameters are expected to cause the results of AGN from MERAXES to match with observations, we do not expect any further changes caused by this minor improvement in terms of the correlation between the foreground galaxies and cosmic reionisation.

Moreover, instead of the calibration of MERAXES to account for the lower resolution of cosmological simulation, we can in fact use our method of sub-grid modelling low mass haloes from Chapter 3 to *increase* the resolution of the GENESIS  $N$ -body simulation. This will alleviate the need for recalibrating the MERAXES parameters and will provide the most accurate model of galaxy formation and evolution, along with cosmic reionisation.

Nevertheless, this is the first time that the correlation between self-consistent foregrounds and the EoR has been explored in large-scale reionisation simulations. Our discovery has confirmed the previously untested assumption that these two components are uncorrelated within the limitations of current experiments and models. Although this means that we cannot directly constrain the EoR parameters by their effect on observed foregrounds, our finding simplifies the EoR parameter estimation studies via Bayesian analyses, such as the one we have performed in Chapter 4. Since the foreground covariance does not depend on the EoR parameters, it may be cleanly separated from the cosmic covariance of the EoR.

Even though we have not included the uncertainties from the scaling relations used to translate the physical properties of the foregrounds, the fact that our version of “cosmic variance” shows a larger uncertainty than the correlation be-

tween the EoR and foregrounds is indeed promising. This is because the scaling relations directly affect the observable properties of the foregrounds sources. As reported by Amaratidis et al. (2019), there is a large uncertainty arising from the astrophysical model of multiple AGN simulations that are used to derive the scaling relations. As such, the variance of the scaling relation will dominate over systematic dependence on the EoR. This further demonstrates that the correlation between the EoR and foregrounds is negligible compared to other sources of uncertainty.

The work we have presented in this thesis supplements different aspects of reionisation studies, encompassing the entire timeline from when the first structures were formed and eventually evolved into their bright foreground descendants, down to our current time in which low-frequency radio interferometers are observing the emission from these epochs. We have introduced new methods to resolve temporally-correlation low mass haloes and implemented their stochasticities, explored the effects of including realistic foregrounds and instrumental systematics in the EoR parameter estimation experiment, and gauged the correlation between self-consistent foregrounds and cosmic reionisation. These projects are particularly useful in ensuring that EoR studies via simulation are as realistic as possible so that we can have a better understanding of the astrophysics of reionisation through a realistic lens. This information can, in turn, be used to help narrow down the search for the EoR signal. With the upcoming deployment of the next-generation low-frequency interferometers such as the SKA, in a few years time, we can expect to have a 3-D tomography of the 21 cm signal that contains more information than we currently have. Hopefully, with the assistance from our various findings, we can perform more accurate EoR parameter estimation experiments and consequently, have more accurate answers about the early universe.



# Appendices



# Appendix A

## Co-author Agreements

This section is provided to comply with the university requirement that the co-authors outline their contribution in the published works included in this thesis. All co-authors have read and agreed to the following statements. Their responses, if there is any, can be found below.

### A.1 Statement of Originality

In Chapter 3, we modelled the stochasticity of low-mass dark matter haloes that are temporally-biased from  $N$ -body simulations. I carried out the data analysis part of this work with input from I. T. Iliev and K. Ahn. The pipeline used to fit the lognormal distribution to model the number or mass of haloes in each cell and the modelling of the correlation of these attributes was developed by myself. I also ran the pipeline and produced most plots for the paper. The data used in this work is obtained from the suite of  $N$ -body simulations run using the CubeP<sup>3</sup>M code (Harnois-Déraps et al., 2013), which was obtained by I. T. Iliev. K. Ahn wrote a minor part of the introduction and discussion; the rest were written by myself, with edits by I. T. Iliev and K. Ahn where necessary, before and after the referee comments were received.

The pipeline used to coherently include foregrounds and instrumental effects in Chapter 4 was developed by myself with input from S. G. Murray, C. M. Trott and B. Greig. I ran the pipeline, produced all the plots and wrote the resulting paper, which incorporated minor comments from all co-authors. S. G. Murray and B. Greig made major adjustments in the existing version of 21CMMC to accommodate for the inclusion of my pipeline. C. M. Trott and C. Power

provided necessary computing time on supercomputers for this work and R. C. Joseph made useful suggestions that aided in the interpretation of the results. S. G. Murray derived the variance of the cross-power in Appendix B.

## A.2 Co-Author Responses

**Kyungjin Ahn** <kjahn@chosun.ac.kr>

Mon 7/27/2020 4:53 PM

Sounds fair, it's OK with the current form for me. Hope you have a successful wrap up of your thesis!

Kyungjin

**Ilian T. Iliev** <iti20@sussex.ac.uk>

Mon 7/27/2020 7:13 PM

Hi Bella,

this is fine with me, good luck with your thesis and defense! I am sure all will go well.

Please send me a copy of your thesis when it is finished.

Cheers,

Ilian

**Cathryn Trott** <Cathryn.Trott@curtin.edu.au>

Tue 8/4/2020 12:22 PM

Hi Bella,

That is fine with me.

Thanks,

Cath

**Ronniy Joseph** <ronniy.joseph@postgrad.curtin.edu.au>

Tue 8/4/2020 12:25 PM

Dear Bella,

I agree that your statement correctly reflects my contribution.

Kind regards,

Ronniy

**Bradley Greig** <greigb@unimelb.edu.au>

Tue 8/4/2020 12:26 PM

Hi Bella,

This text all looks fine to me. Congrats on the pending thesis submission!

Thanks,

Brad

**Chris Power** <chris.power@uwa.edu.au>

Tue 8/4/2020 1:35 PM

Looks fine to me, too.

Good luck!

c.

**Steven Murray** <steven.g.murray@asu.edu>

Tue 8/4/2020 9:25 PM

And me!



# Appendix B

## Copyright Information

### B.1 Copyright for Chapter 3

The Monthly Notices of Royal Astronomical Society (MNRAS) allows the use of publication in thesis or dissertation as long as the editor is informed, as written here: <https://global.oup.com/academic/rights/permissions/autperm/?lang=en&cc=gb>. An email has been sent to the MNRAS editor as shown below.

05/08/2020

Mail - Bella Nasirudin - Outlook

**Re: Contact Us Form**

LEWIS, Jeremy <Jeremy.Lewis@oup.com>

Tue 8/4/2020 9:18 PM

To: Bella Nasirudin <a.nasirudin@postgrad.curtin.edu.au>

Dear Bella,

You can find information about requesting permission for journal articles at this page:

<https://global.oup.com/academic/rights/permissions/?lang=en&cc=gb>

Sincerely,

Jeremy

---

**From:** a.nasirudin@postgrad.curtin.edu.au <a.nasirudin@postgrad.curtin.edu.au>

**Sent:** Tuesday, August 4, 2020 2:23 AM

**To:** LEWIS, Jeremy <Jeremy.Lewis@oup.com>

**Subject:** Contact Us Form

Name: Bella Nasirudin

Email: a.nasirudin@postgrad.curtin.edu.au

Message: Dear Editor,

I would like to request the re-publication of my article "Modelling the stochasticity of high-redshift halo bias" (doi:10.1093/mnras/staa853) as a chapter in my Doctoral thesis.

I understand that as first author I retain the right to reproduce the material how I see fit; however, my University requires that I retrieve formal permission from the journal. Is it possible to get a letter or other official document allowing me to publish the material as part of my thesis?

Regards,  
Bella Nasirudin

## B.2 Copyright for Chapter 4

05/08/2020

Mail - Bella Nasirudin - Outlook

Re: Request to re-publish article as a thesis chapter

Permissions <permissions@iopublishing.org>

Tue 8/4/2020 5:06 PM

To: Bella Nasirudin <a.nasirudin@postgrad.curtin.edu.au>

Dear Bella Nasirudin,

Thank you for your email.

AAS authors may reuse their own work in a thesis without needing permission, providing it is not then published commercially. You are also allowed to use figures from the article. Therefore, please go ahead with the inclusion of this material in your new work – no permission is required from AAS.

Please include the following alongside the material:

- the source of the material, including author, article title, title of journal, volume number, issue number (if relevant), page range (or first page if this is the only information available) and date of first publication. This material can be contained in a footnote or reference.
- for material being published electronically, a link back to the article (via DOI)
- if practical and IN ALL CASES for works published under any of the Creative Commons licences the words "© AAS. Reproduced with permission".

This permission does not apply to any material/figure which is credited to another source in the AAS publication or has been obtained from a third party. Express permission for such materials/figures must be obtained from the copyright owner.

Kind regards,

Cameron Wood

### Copyright & Permissions Team

Sophie Brittain - Rights & Permissions Assistant

Cameron Wood - Legal & Rights Adviser

Contact Details

E-mail: [permissions@iopublishing.org](mailto:permissions@iopublishing.org)

For further information about copyright and how to request permission:

<https://publishingsupport.iopscience.iop.org/copyright-journals/>

See also: <https://publishingsupport.iopscience.iop.org/>

Please see our Author Rights Policy <https://publishingsupport.iopscience.iop.org/author-rights-policies/>

**Please note:** We do not provide signed permission forms as a separate attachment. Please print this email and provide it to your publisher as proof of permission. **Please note:** Any statements made by IOP Publishing to the effect that authors do not need to get permission to use any content where IOP Publishing is not the publisher is not intended to constitute any sort of legal advice. Authors must make their own decisions as to the suitability of the content they are using and whether they require permission for it to be published within their article.

<https://outlook.office.com/mail/inbox/id/AAQkADkxZWJmRjLWY5MGEiNDUwOS1hYTZlLTFkY2UyNGEyZDQzNwAQAPGonK9%2BhO9lothgGfKY...> 1/2

# Bibliography

- R. Adam, et al. (2016). ‘Planck intermediate results-XLVII. Planck constraints on reionization history’. *Astronomy & Astrophysics* **596**:A108.
- K. Ahn, et al. (2012). ‘Detecting the Rise and Fall of the First Stars by Their Impact on Cosmic Reionization’. *The Astrophysical Journal Letters* **756**:L16.
- K. Ahn, et al. (2015). ‘Non-linear bias of cosmological halo formation in the early universe’. *Monthly Notices of the Royal Astronomical Society* **450**(2):1486–1502.
- Z. S. Ali, et al. (2018). ‘Erratum: “PAPER-64 Constraints on Reionization: The 21 cm Power Spectrum at  $z=8.4$ ” (2015, ApJ, 809, 61)’. *The Astrophysical Journal* **863**(2):201.
- S. Amarantidis, et al. (2019). ‘The first supermassive black holes: indications from models for future observations’. *Monthly Notices of the Royal Astronomical Society* **485**(2):2694–2709.
- W. Baade & R. Minkowski (1954). ‘Identification of the radio sources in Cassiopeia, Cygnus A, and Puppis A’. In *Classics in Radio Astronomy*, pp. 251–272. Springer.
- A. Balaguera-Antolínez, et al. (2020). ‘One simulation to have them all: performance of the Bias Assignment Method against N-body simulations’. *Monthly Notices of the Royal Astronomical Society* **491**(2):2565–2575.
- A. Balaguera-Antolínez, et al. (2019). ‘BAM: bias assignment method to generate mock catalogues’. *Monthly Notices of the Royal Astronomical Society* **483**(1):L58–L63.

- J. M. Bardeen, et al. (1986). ‘The Statistics of Peaks of Gaussian Random Fields’. *The Astrophysical Journal* **304**:15.
- R. Barkana (2009). ‘Studying the sources of cosmic reionization with 21-cm fluctuations’. *Monthly Notices of the Royal Astronomical Society* **397**(3):1454–1463.
- R. Barkana (2018). ‘Possible interaction between baryons and dark-matter particles revealed by the first stars’. *Nature* **555**(7694):71–74.
- R. Barkana & A. Loeb (2001). ‘In the beginning: the first sources of light and the reionization of the universe’. *Physics Reports* **349**(2):125–238.
- R. Barkana & A. Loeb (2004). ‘Unusually Large Fluctuations in the Statistics of Galaxy Formation at High Redshift’. *The Astrophysical Journal* **609**:474–481.
- R. Barkana & A. Loeb (2005). ‘A Method for Separating the Physics from the Astrophysics of High-Redshift 21 Centimeter Fluctuations’. *The Astrophysical Journal Letters* **624**(2):L65–L68.
- J. Barnes & P. Hut (1986). ‘A hierarchical O (N log N) force-calculation algorithm’. *nature* **324**(6096):446.
- N. Barry, et al. (2019). ‘Improving the Epoch of Reionization Power Spectrum Results from Murchison Widefield Array Season 1 Observations’. *The Astrophysical Journal* **884**(1):1.
- A. P. Beardsley, et al. (2016). ‘First Season MWA EoR Power spectrum Results at Redshift 7’. *The Astrophysical Journal* **833**(1):102.
- P. S. Behroozi & J. Silk (2015). ‘A Simple Technique for Predicting High-redshift Galaxy Evolution’. *The Astrophysical Journal* **799**(1):32.
- T. Binnie & J. R. Pritchard (2019). ‘Bayesian model selection with future 21cm observations of the epoch of reionization’. *Monthly Notices of the Royal Astronomical Society* **487**(1):1160–1177.

- J. R. Bond, et al. (1991). ‘Excursion set mass functions for hierarchical Gaussian fluctuations’. *The Astrophysical Journal* **379**:440–460.
- J. D. Bowman, et al. (2008). ‘Toward empirical constraints on the global redshifted 21 cm brightness temperature during the epoch of reionization’. *The Astrophysical Journal* **676**(1):1.
- J. D. Bowman, et al. (2018). ‘An absorption profile centred at 78 megahertz in the sky-averaged spectrum’. *Nature* **555**:67–70.
- A. H. Bridle, et al. (1989). *Synthesis Imaging in Radio Astronomy: A Collection of Lectures from the Third NRAO Synthesis Imaging Summer School Held at Socorro, New Mexico, June 1988*. Astronomical Society of the Pacific.
- V. Bromm, et al. (2009). ‘The formation of the first stars and galaxies’. *Nature* **459**(7243):49–54.
- C. Cheng, et al. (2018). ‘Characterizing Signal Loss in the 21 cm Reionization Power Spectrum: A Revised Study of PAPER-64’. *The Astrophysical Journal* **868**(1):26.
- T. R. Choudhury & A. Ferrara (2005). ‘Experimental constraints on self-consistent reionization models’. *Monthly Notices of the Royal Astronomical Society* **361**(2):577–594.
- A. Cohen, et al. (2017). ‘Charting the parameter space of the global 21-cm signal’. *Monthly Notices of the Royal Astronomical Society* **472**(2):1915–1931.
- R. Cohen, et al. (2003). ‘Radio-Quiet Zones’. In *Light Pollution: The Global View*, pp. 225–259. Springer.
- S. Cole & N. Kaiser (1989). ‘Biased clustering in the cold dark matter cosmogony’. *Monthly Notices of the Royal Astronomical Society* **237**:1127–1146.
- J. Condon (1992). ‘Radio emission from normal galaxies’. *Annual review of astronomy and astrophysics* **30**(1):575–611.

- W. D. Cotton, et al. (2004). ‘Beyond the isoplanatic patch in the VLA Low-frequency Sky Survey’. In *Ground-based Telescopes*, vol. 5489, pp. 180–189. International Society for Optics and Photonics.
- D. J. Croton, et al. (2016). ‘Semi-analytic galaxy evolution (sage): Model calibration and basic results’. *The Astrophysical Journal Supplement Series* **222**(2):22.
- A. Datta, et al. (2010). ‘Bright Source Subtraction Requirements for Redshifted 21 cm Measurements’. *ApJ* **724**:526–538.
- K. Davies (1990). *Ionospheric radio*. No. 31. IET.
- P. Dayal & A. Ferrara (2018). ‘Early galaxy formation and its large-scale effects’. *Physics Reports* **780**:1–64.
- D. R. DeBoer, et al. (2017). ‘Hydrogen Epoch of Reionization Array (HERA)’. *Publications of the Astronomical Society of the Pacific* **129**(974):045001.
- A. Dekel & O. Lahav (1999). ‘Stochastic Nonlinear Galaxy Biasing’. *The Astrophysical Journal* **520**:24–34.
- P. E. Dewdney, et al. (2009). ‘The square kilometre array’. *Proceedings of the IEEE* **97**(8):1482–1496.
- M. Dijkstra (2014). ‘Ly $\alpha$  emitting galaxies as a probe of reionisation’. *Publications of the Astronomical Society of Australia* **31**.
- M. Dijkstra (2016). ‘Constraining Reionization with Ly $\alpha$  Emitting Galaxies’. In *Understanding the Epoch of Cosmic Reionization*, pp. 145–161. Springer.
- M. Dijkstra, et al. (2011). ‘The detectability of Ly  $\alpha$  emission from galaxies during the epoch of reionization’. *Monthly Notices of the Royal Astronomical Society* **414**(3):2139–2147.
- J. S. Dillon, et al. (2014). ‘Overcoming real-world obstacles in 21 cm power spectrum estimation: A method demonstration and results from early Murchison Widefield Array data’. *Physical Review D* **89**(2):023002.

- J. S. Dillon, et al. (2015). ‘Empirical covariance modeling for 21 cm power spectrum estimation: A method demonstration and new limits from early Murchison Widefield Array 128-tile data’. *Physical Review D* **91**(12):123011.
- J. S. Dillon & A. R. Parsons (2016). ‘Redundant array configurations for 21 cm cosmology’. *The Astrophysical Journal* **826**(2):181.
- K. L. Dixon, et al. (2016). ‘The large-scale observational signatures of low-mass galaxies during reionization’. *Monthly Notices of the Royal Astronomical Society* **456**(3):3011–3029.
- S. Dodelson & M. D. Schneider (2013). ‘The effect of covariance estimator error on cosmological parameter constraints’. *Physical Review D* **88**(6):063537.
- C. Doppler (1842). ‘Über das farbige Licht der Doppelsterne und einiger anderer Gestirne des Himmels (On the colored light of the double stars and certain other stars of the heavens)’. *Abh. Kniglich Bhmischen Ges. Wiss* **2**:467–482.
- A. Einstein (1917). ‘Cosmological considerations in the general theory of relativity’. *Sitzungsber. Preuss. Akad. Wiss. Berlin (Math. Phys.)* **1917**:142–152.
- J. V. Evans & T. Hagfors (1968). ‘Radar astronomy’. *New York: McGraw-Hill, 1968, edited by Evans, John V.; Hagfors, Tor*.
- O. Fakhouri, et al. (2010). ‘The merger rates and mass assembly histories of dark matter haloes in the two Millennium simulations’. *Monthly Notices of the Royal Astronomical Society* **406**(4):2267–2278.
- X. Fan, et al. (2006). ‘Constraining the Evolution of the Ionizing Background and the Epoch of Reionization with  $z \sim 6$  Quasars. II. A Sample of 19 Quasars’. *The Astronomical Journal* **132**:117–136.
- B. L. Fanaroff & J. M. Riley (1974). ‘The morphology of extragalactic radio sources of high and low luminosity’. *Monthly Notices of the Royal Astronomical Society* **167**(1):31P–36P.
- N. Fanidakis, et al. (2011). ‘Grand unification of AGN activity in the  $\Lambda$ CDM cosmology’. *Monthly Notices of the Royal Astronomical Society* **410**(1):53–74.

- G. B. Field (1958). ‘Excitation of the hydrogen 21-cm line’. *Proceedings of the IRE* **46**(1):240–250.
- G. B. Field (1959). ‘The Spin Temperature of Intergalactic Neutral Hydrogen.’. *The Astrophysical Journal* **129**:536.
- A. Fontana, et al. (2010). ‘The Lack of Intense Ly $\alpha$  in Ultradeep Spectra of  $z=7$  Candidates in GOODS-S: Imprint of Reionization?’. *The Astrophysical Journal Letters* **725**(2):L205.
- D. Foreman-Mackey, et al. (2013). ‘emcee: the MCMC hammer’. *Publications of the Astronomical Society of the Pacific* **125**(925):306.
- S. R. Furlanetto (2016). ‘The 21-cm Line as a Probe of Reionization’. In *Understanding the Epoch of Cosmic Reionization*, pp. 247–280. Springer.
- S. R. Furlanetto, et al. (2006a). ‘Characteristic scales during reionization’. *Monthly Notices of the Royal Astronomical Society* **365**(1):115–126.
- S. R. Furlanetto, et al. (2006b). ‘Cosmology at low frequencies: The 21cm transition and the high-redshift Universe’. *Physics Reports* **433**(4):181–301.
- S. R. Furlanetto, et al. (2004). ‘The growth of H II regions during reionization’. *The Astrophysical Journal* **613**(1):1.
- E. George, et al. (2015). ‘A measurement of secondary cosmic microwave background anisotropies from the 2500 square-degree SPT-SZ survey’. *The Astrophysical Journal* **799**(2):177.
- G. Giardino, et al. (2002). ‘Towards a model of full-sky Galactic synchrotron intensity and linear polarisation: A re-analysis of the Parkes data’. *Astronomy & Astrophysics* **387**(1):82–97.
- N. Gillet, et al. (2019). ‘Deep learning from 21-cm tomography of the cosmic dawn and reionization’. *Monthly Notices of the Royal Astronomical Society* **484**(1):282–293.

- V. Ginzburg & S. Syrovatskii (1965). ‘Cosmic magnetobremstrahlung (synchrotron radiation)’. *Annual Review of Astronomy and Astrophysics* **3**(1):297–350.
- S. K. Giri, et al. (2019). ‘Neutral island statistics during reionization from 21-cm tomography’. *Monthly Notices of the Royal Astronomical Society* **489**(2):1590–1605.
- S. K. Giri, et al. (2018). ‘Bubble size statistics during reionization from 21-cm tomography’. *Monthly Notices of the Royal Astronomical Society* **473**:2949–2964.
- L. Gleser, et al. (2008). ‘Decontamination of cosmological 21-cm maps’. *Monthly Notices of the Royal Astronomical Society* **391**(1):383–398.
- N. Y. Gnedin (2000). ‘Effect of Reionization on Structure Formation in the Universe’. *The Astrophysical Journal* **542**:535–541.
- P. Goldreich & D. A. Keeley (1972). ‘Astrophysical masers. I. Source size and saturation’. *The Astrophysical Journal* **174**:517.
- J. Goodman & J. Weare (2010). ‘Ensemble samplers with affine invariance’. *Communications in applied mathematics and computational science* **5**(1):65–80.
- D. Green (2006). ‘A catalogue of Galactic Supernova Remnants (2006 April version). Astrophysics Group, Cavendish Laboratory, Cambridge’.
- B. Greig & A. Mesinger (2015). ‘21CMMC: an MCMC analysis tool enabling astrophysical parameter studies of the cosmic 21 cm signal’. *Monthly Notices of the Royal Astronomical Society* **449**(4):4246–4263.
- B. Greig & A. Mesinger (2017). ‘Simultaneously constraining the astrophysics of reionization and the epoch of heating with 21CMMC’. *Monthly Notices of the Royal Astronomical Society* **472**:2651–2669.

- B. Greig & A. Mesinger (2018). ‘21CMMC with a 3D light-cone: the impact of the co-evolution approximation on the astrophysics of reionization and cosmic dawn’. *Monthly Notices of the Royal Astronomical Society* **477**(3):3217–3229.
- J. E. Gunn & B. A. Peterson (1965). ‘On the Density of Neutral Hydrogen in Intergalactic Space.’. *The Astrophysical Journal* **142**:1633–1641.
- Z. Hamidi, et al. (2012). ‘Indication of radio frequency interference (RFI) sources for solar burst monitoring in Malaysia’. In *AIP Conference Proceedings*, vol. 1454, pp. 43–46. American Institute of Physics.
- G. J. Harker, et al. (2011). ‘An MCMC approach to extracting the global 21-cm signal during the cosmic dawn from sky-averaged radio observations’. *Monthly Notices of the Royal Astronomical Society* **419**(2):1070–1084.
- J. Harnois-Déraps, et al. (2013). ‘High-performance P<sup>3</sup>M N-body code: CUBEP<sup>3</sup>M’. *Monthly Notices of the Royal Astronomical Society* **436**:540–559.
- C. Haslam, et al. (1982). ‘A 408 MHz all-sky continuum survey. II-The atlas of contour maps’. *Astronomy and Astrophysics Supplement Series* **47**:1.
- S. Hassan, et al. (2017). ‘Epoch of reionization 21 cm forecasting from MCMC-constrained semi-numerical models’. *Monthly Notices of the Royal Astronomical Society* **468**(1):122–139.
- W. K. Hastings (1970). ‘Monte Carlo sampling methods using Markov chains and their applications’ .
- B. J. Hazelton, et al. (2013). ‘The Fundamental Multi-baseline Mode-mixing Foreground in 21 cm Epoch of Reionization Observations’. *ApJ* **770**:156.
- J. B. Hearnshaw (1992). ‘Doppler and Vogel—Two notable anniversaries in stellar astronomy’. *Vistas in astronomy* **35**:157–177.
- C. H. Heinrich, et al. (2017). ‘Complete reionization constraints from Planck 2015 polarization’. **95**(2):023513.

- A. Hewish, et al. (1968). ‘Observation of a rapidly pulsating radio source’. *Nature* **217**(5130):709–713.
- R. W. Hockney & J. W. Eastwood (1988). *Computer simulation using particles*. crc Press.
- H. Hsieh (1966). ‘Characteristics of ionospheric thermal radiation’. *Journal of Atmospheric and Terrestrial Physics* **28**(8):783–788.
- E. Hubble (1929). ‘A relation between distance and radial velocity among extragalactic nebulae’. *Proceedings of the National Academy of Sciences* **15**(3):168–173.
- I. T. Iliev, et al. (2014). ‘Simulating cosmic reionization: how large a volume is large enough?’. *Monthly Notices of the Royal Astronomical Society* **439**:725–743.
- I. T. Iliev, et al. (2007). ‘Self-regulated reionization’. *Monthly Notices of the Royal Astronomical Society* **376**:534–548.
- H. Intema, et al. (2009). ‘Ionospheric calibration of low frequency radio interferometric observations using the peeling scheme-I. Method description and first results’. *Astronomy & Astrophysics* **501**(3):1185–1205.
- H. Intema, et al. (2011). ‘Deep low-frequency radio observations of the NOAO Boötes field-I. Data reduction and catalog construction’. *Astronomy & Astrophysics* **535**:A38.
- H. T. Intema, et al. (2011). ‘Deep low-frequency radio observations of the NOAO Boötes field. I. Data reduction and catalog construction’. *Astronomy and Astrophysics* **535**:A38.
- C. Jackson (2005). ‘The Extragalactic Radio Sky at Faint Flux Densities’. *Publications of the Astronomical Society of Australia* **22**(1):36–48.
- C. Jackson & J. V. Wall (1999). ‘Extragalactic radio-source evolution under the dual-population unification scheme’. *Monthly Notices of the Royal Astronomical Society* **304**(1):160–174.

- D. C. Jacobs, et al. (2016). ‘The Murchison Widefield Array 21 cm power spectrum analysis methodology’. *The Astrophysical Journal* **825**(2):114.
- K. G. Jansky (1933). ‘Radio waves from outside the solar system’. *Nature* **132**(3323):66–66.
- V. Jelić, et al. (2010). ‘Realistic simulations of the Galactic polarized foreground: consequences for 21-cm reionization detection experiments’. *Monthly Notices of the Royal Astronomical Society* **409**(4):1647–1659.
- V. Jelić, et al. (2008). ‘Foreground simulations for the LOFAR-epoch of reionization experiment’. *MNRAS* **389**:1319–1335.
- V. Jelić, et al. (2008). ‘Foreground simulations for the LOFAR-epoch of reionization experiment’. *Monthly Notices of the Royal Astronomical Society* **389**(3):1319–1335.
- A. Jenkins, et al. (2001). ‘The mass function of dark matter haloes’. *Monthly Notices of the Royal Astronomical Society* **321**:372–384.
- H. Jensen, et al. (2013). ‘On the use of Ly $\alpha$  emitters as probes of reionization’. *Monthly Notices of the Royal Astronomical Society* **428**(2):1366–1381.
- J. L. Johnson & V. Bromm (2007). ‘The aftermath of the first stars: massive black holes’. *Monthly Notices of the Royal Astronomical Society* **374**(4):1557–1568.
- J. L. Johnson, et al. (2008). ‘Occurrence of metal-free galaxies in the early Universe’. *Monthly Notices of the Royal Astronomical Society* **388**(1):26–38.
- C. Jordan, et al. (2017). ‘Characterization of the ionosphere above the Murchison Radio Observatory using the Murchison Widefield Array’. *Monthly Notices of the Royal Astronomical Society* **471**(4):3974–3987.
- N. Katz (1992). ‘Dissipational galaxy formation. II-Effects of star formation’. *The Astrophysical Journal* **391**:502–517.

- N. S. Kern, et al. (2017). ‘Emulating Simulations of Cosmic Dawn for 21 cm Power Spectrum Constraints on Cosmology, Reionization, and X-Ray Heating’. *The Astrophysical Journal* **848**(1):23.
- N. S. Kern, et al. (2020). ‘Mitigating Internal Instrument Coupling for 21 cm Cosmology. II. A Method Demonstration with the Hydrogen Epoch of Reionization Array’. *The Astrophysical Journal* **888**(2):70.
- F.-S. Kitaura, et al. (2014). ‘Modelling baryon acoustic oscillations with perturbation theory and stochastic halo biasing’. *Monthly Notices of the Royal Astronomical Society* **439**:L21–L25.
- G. Knevitt, et al. (2014). ‘Heating and ionization of the primordial intergalactic medium by high-mass X-ray binaries’. *Monthly Notices of the Royal Astronomical Society* **445**(2):2034–2048.
- A. Kogut, et al. (2003). ‘First-Year Wilkinson Microwave Anisotropy Probe (WMAP) Observations: Temperature-Polarization Correlation’. *The Astrophysical Journal Supplement Series* **148**(1):161–173.
- E. W. Kolb & M. S. Turner (1981). ‘The early universe’. *Nature* **294**(5841):521–526.
- M. Kolopanis, et al. (2019). ‘A Simplified, Lossless Reanalysis of PAPER-64’. *The Astrophysical Journal* **883**(2):133.
- E. Komatsu, et al. (2009). ‘Five-Year Wilkinson Microwave Anisotropy Probe Observations: Cosmological Interpretation’. *The Astrophysical Journal Supplement Series* **180**:330–376.
- C. Lacey & S. Cole (1994). ‘Merger rates in hierarchical models of galaxy formation–II. Comparison with N-body simulations’. *Monthly Notices of the Royal Astronomical Society* **271**(3):676–692.
- R. Laing, et al. (1983). ‘Bright radio sources at 178 MHz-Flux densities, optical identifications and the cosmological evolution of powerful radio galaxies’. *Monthly Notices of the Royal Astronomical Society* **204**:151–187.

- G. Lemaître (1927). ‘Un Univers homogène de masse constante et de rayon croissant rendant compte de la vitesse radiale des nébuleuses extra-galactiques’. In *Annales de la Société scientifique de Bruxelles*, vol. 47, pp. 49–59.
- W. Li, et al. (2019a). ‘First Season MWA Phase II Epoch of Reionization Power Spectrum Results at Redshift 7’. *The Astrophysical Journal* **887**(2):141.
- W. Li, et al. (2019b). ‘Contribution of Radio Halos to the Foreground for SKA EoR Experiments’. *The Astrophysical Journal* **879**(2):104.
- A. Lidz (2016). *Physics of the Intergalactic Medium During the Epoch of Reionization*, vol. 423 of *Astrophysics and Space Science Library*, p. 23.
- S. Lim & J. Lee (2013). ‘An extended Zel’dovich model for the halo mass function’. **1**:19.
- A. Liu, et al. (2014). ‘Epoch of reionization window. II. Statistical methods for foreground wedge reduction’. **90**(2):023019.
- A. Liu & J. R. Shaw (2020). ‘Data Analysis for Precision 21 cm Cosmology’. **132**(1012):062001.
- C. J. Lonsdale, et al. (2009). ‘The Murchison widefield array: Design overview’. *Proceedings of the IEEE* **97**(8):1497–1506.
- Z. Lukić, et al. (2007). ‘The Halo Mass Function: High-Redshift Evolution and Universality’. *The Astrophysical Journal* **671**:1160–1181.
- D. J. MacKay (2003). *Information theory, inference and learning algorithms*. Cambridge university press.
- P. Madau & M. Dickinson (2014). ‘Cosmic Star-Formation History’. *Annual Review of Astronomy and Astrophysics* **52**:415–486.
- P. Madau, et al. (1997). ‘21 centimeter tomography of the intergalactic medium at high redshift’. *The Astrophysical Journal* **475**(2):429.
- P. Madau, et al. (2004). ‘Early reionization by miniquasars’. *The Astrophysical Journal* **604**(2):484.

- S. Majumdar, et al. (2018). ‘Quantifying the non-Gaussianity in the EoR 21-cm signal through bispectrum’. *Monthly Notices of the Royal Astronomical Society* **476**(3):4007–4024.
- B. Mandelbrot (1975). ‘Sur un modèle décomposable d’univers hiérarchisé: déduction des corrélations galactiques sur la sphère céleste.’. *CRASM* **280**(22):1551–1554.
- B. B. Mandelbrot (1977). ‘Lecture V Fractals and turbulence: Attractors and dispersion’. In *Turbulence Seminar*, pp. 83–93. Springer.
- M. Manera, et al. (2013). ‘The clustering of galaxies in the SDSS-III Baryon Oscillation Spectroscopic Survey: a large sample of mock galaxy catalogues’. *Monthly Notices of the Royal Astronomical Society* **428**:1036–1054.
- T. A. Matthews & A. R. Sandage (1963). ‘Optical identification of 3C 48, 3C 196, and 3C 286 with stellar objects’. Tech. rep., OWENS VALLEY RADIO OBSERVATORY PASADENA CA.
- T. Mauch & E. M. Sadler (2007). ‘Radio sources in the 6dFGS: local luminosity functions at 1.4 GHz for star-forming galaxies and radio-loud AGN’. *Monthly Notices of the Royal Astronomical Society* **375**(3):931–950.
- B. McKinley, et al. (2018). ‘Measuring the global 21-cm signal with the MWA-I: improved measurements of the Galactic synchrotron background using lunar occultation’. *Monthly Notices of the Royal Astronomical Society* **481**(4):5034–5045.
- B. McKinley, et al. (2012). ‘Low-frequency observations of the Moon with the Murchison widefield array’. *The Astronomical Journal* **145**(1):23.
- D. L. Meier (2002). ‘Grand unification of AGN and the accretion and spin paradigms’. *New Astronomy Reviews* **46**(2-7):247–255.
- G. Mellema, et al. (2013). ‘Reionization and the Cosmic Dawn with the Square Kilometre Array’. *Experimental Astronomy* **36**:235–318.

- F. Mertens, et al. (2020). ‘Improved upper limits on the 21 cm signal power spectrum of neutral hydrogen at  $z$  9.1 from LOFAR’. *Monthly Notices of the Royal Astronomical Society* **493**(2):1662–1685.
- A. Mesinger, et al. (2014). ‘Reionization and beyond: detecting the peaks of the cosmological 21 cm signal’. *Monthly Notices of the Royal Astronomical Society* **439**:3262–3274.
- A. Mesinger & S. Furlanetto (2007). ‘Efficient simulations of early structure formation and reionization’. *The Astrophysical Journal* **669**(2):663.
- A. Mesinger, et al. (2011). ‘21CMFAST: a fast, seminumerical simulation of the high-redshift 21-cm signal’. *Monthly Notices of the Royal Astronomical Society* **411**(2):955–972.
- A. Mesinger, et al. (2016). ‘The Evolution Of 21 cm Structure (EOS): public, large-scale simulations of Cosmic Dawn and reionization’. *Monthly Notices of the Royal Astronomical Society* **459**(3):2342–2353.
- N. Metropolis, et al. (1953). ‘Equation of state calculations by fast computing machines’. *The journal of chemical physics* **21**(6):1087–1092.
- M. Mevius, et al. (2016). ‘Probing ionospheric structures using the LOFAR radio telescope’. *Radio Science* **51**:927–941.
- A. A. Michelson (1890). ‘I. On the application of interference methods to astronomical measurements’. *The London, Edinburgh, and Dublin Philosophical Magazine and Journal of Science* **30**(182):1–21.
- A. A. Michelson & F. G. Pease (1921). ‘Measurement of the diameter of Alpha-Orionis by the interferometer’. *Proceedings of the National Academy of Sciences of the United States of America* **7**(5):143.
- J. Mirocha (2019). *Astrophysics from the 21-cm background*, p. 39.
- H. J. Mo & S. D. M. White (1996). ‘An analytic model for the spatial clustering of dark matter haloes’. *Monthly Notices of the Royal Astronomical Society* **282**:347–361.

- P. Monaco, et al. (2013). ‘An accurate tool for the fast generation of dark matter halo catalogues’. *Monthly Notices of the Royal Astronomical Society* **433**:2389–2402.
- P. Monaco, et al. (2002). ‘Predicting the Number, Spatial Distribution, and Merging History of Dark Matter Halos’. *The Astrophysical Journal* **564**:8–14.
- R. Mondal, et al. (2016). ‘Statistics of the epoch of reionization 21-cm signal - I. Power spectrum error-covariance’. *Monthly Notices of the Royal Astronomical Society* **456**(2):1936–1947.
- R. Mondal, et al. (2017). ‘Statistics of the epoch of reionization (EoR) 21-cm signal - II. The evolution of the power-spectrum error-covariance’. *Monthly Notices of the Royal Astronomical Society* **464**(3):2992–3004.
- R. Mondal, et al. (2015). ‘The effect of non-Gaussianity on error predictions for the Epoch of Reionization (EoR) 21-cm power spectrum.’. *Monthly Notices of the Royal Astronomical Society* **449**:L41–L45.
- R. A. Monsalve, et al. (2017). ‘Results from EDGES High-band. I. Constraints on phenomenological models for the global 21 cm signal’. *The Astrophysical Journal* **847**(1):64.
- M. F. Morales, et al. (2012). ‘Four fundamental foreground power spectrum shapes for 21 cm cosmology observations’. *The Astrophysical Journal* **752**(2):137.
- M. F. Morales & J. Hewitt (2004). ‘Toward Epoch of Reionization Measurements with Wide-Field Radio Observations’. *ApJ* **615**:7–18.
- M. F. Morales & J. S. B. Wyithe (2010). ‘Reionization and Cosmology with 21-cm Fluctuations’. *Annual review of astronomy and astrophysics* **48**:127–171.
- D. Mortlock (2016). *Quasars as Probes of Cosmological Reionization*, vol. 423 of *Astrophysics and Space Science Library*, p. 187.
- S. G. Murray (2018). ‘powerbox: A Python package for creating structured fields with isotropic power spectra’. *Journal of Open Source Software* **3**(28):850.

- S. G. Murray, et al. (2017). ‘An Improved Statistical Point-source Foreground Model for the Epoch of Reionization’. *The Astrophysical Journal* **845**(1):7.
- S. J. Mutch, et al. (2016). ‘Dark-ages reionization and galaxy formation simulation–III. Modelling galaxy formation and the epoch of reionization’. *Monthly Notices of the Royal Astronomical Society* **462**(1):250–276.
- A. Nasirudin, et al. (2020). ‘The Impact of Realistic Foreground and Instrument Models on 21 cm Epoch of Reionization Experiments’. *The Astrophysical Journal* **893**(2):118.
- P. Ocvirk, et al. (2016). ‘Cosmic Dawn (CoDa): the first radiation-hydrodynamics simulation of reionization and galaxy formation in the Local Universe’. *Monthly Notices of the Royal Astronomical Society* **463**(2):1462–1485.
- A. Offringa, et al. (2015). ‘The low-frequency environment of the Murchison Widefield Array: radio-frequency interference analysis and mitigation’. *Publications of the Astronomical Society of Australia* **32**.
- A. R. Offringa (2010). ‘AOFlagger: RFI Software’. Astrophysics Source Code Library.
- A. R. Offringa, et al. (2013). ‘The LOFAR radio environment’. *Astronomy and Astrophysics* **549**:A11.
- A. R. Offringa, et al. (2012). ‘A morphological algorithm for improved radio-frequency interference detection’. *A&A* **539**.
- S. P. Oh & Z. Haiman (2002). ‘Second-generation objects in the Universe: Radiative cooling and collapse of halos with virial temperatures above 104 K’. *The Astrophysical Journal* **569**(2):558.
- Y. Ono, et al. (2011). ‘Spectroscopic Confirmation of Three z-dropout Galaxies at  $z=6.844$ - $7.213$ : Demographics of Ly $\alpha$  Emission in  $z \sim 7$  Galaxies’. *The Astrophysical Journal* **744**(2):83.
- D. E. Osterbrock & G. J. Ferland (2006). *Astrophysics Of Gas Nebulae and Active Galactic Nuclei*. University science books.

- G. Paciga, et al. (2013). ‘A simulation-calibrated limit on the H i power spectrum from the GMRT Epoch of Reionization experiment’. *Monthly Notices of the Royal Astronomical Society* **433**(1):639–647.
- J. Park, et al. (2019). ‘Inferring the astrophysics of reionization and cosmic dawn from galaxy luminosity functions and the 21-cm signal’. *Monthly Notices of the Royal Astronomical Society* **484**(1):933–949.
- A. Parsons, et al. (2012). ‘A Sensitivity and Array-configuration Study for Measuring the Power Spectrum of 21 cm Emission from Reionization’. *ApJ* **753**:81.
- A. R. Parsons, et al. (2010). ‘The precision array for probing the epoch of reionization: Eight station results’. *The Astronomical Journal* **139**(4):1468.
- A. R. Parsons, et al. (2014). ‘New Limits on 21 cm Epoch of Reionization from PAPER-32 Consistent with an X-Ray Heated Intergalactic Medium at  $z = 7.7$ ’. *The Astrophysical Journal* **788**:106.
- A. Patil, et al. (2017). ‘Upper limits on the 21 cm epoch of reionization power spectrum from one night with LOFAR’. *The Astrophysical Journal* **838**(1):65.
- A. H. Patil, et al. (2014). ‘Constraining the epoch of reionization with the variance statistic: simulations of the LOFAR case’. *Monthly Notices of the Royal Astronomical Society* **443**(2):1113–1124.
- H. Payne, et al. (1989). ‘Stimulated emission of carbon recombination lines from cold clouds in the direction of Cassiopeia A’ .
- J. A. Peacock (1999). *Cosmological physics*. Cambridge university press.
- A. Pedlar, et al. (1978). ‘Studies of low-frequency recombination lines from the direction of the Galactic Centre and other galactic sources’. *Monthly Notices of the Royal Astronomical Society* **182**(3):473–488.
- P. J. E. Peebles (1980). *The large-scale structure of the universe*.
- P. J. E. Peebles (1993). *Principles of physical cosmology*. Princeton Series in Physics, Princeton, NJ: Princeton University Press, —c1993.

- A. A. Penzias & R. W. Wilson (1965). ‘A measurement of excess antenna temperature at 4080 Mc/s.’. *The Astrophysical Journal* **142**:419–421.
- S. Perlmutter, et al. (1999). ‘Measurements of  $\Omega$  and  $\Lambda$  from 42 high-redshift supernovae’. *The Astrophysical Journal* **517**(2):565.
- W. Peters, et al. (2011). ‘Radio recombination lines at decametre wavelengths—Prospects for the future’. *Astronomy & Astrophysics* **525**:A128.
- Planck Collaboration, et al. (2016). ‘Planck 2015 results. XIII. Cosmological parameters’. *Astronomy and Astrophysics* **594**:A13.
- Planck Collaboration, et al. (2020). ‘Planck 2018 results. VI. Cosmological parameters’. *Astronomy and Astrophysics* **641**:A6.
- J. C. Pober, et al. (2014). ‘What Next-generation 21 cm Power Spectrum Measurements can Teach us About the Epoch of Reionization’. *The Astrophysical Journal* **782**:66.
- J. C. Pober, et al. (2013). ‘The baryon acoustic oscillation broadband and broadband array: design overview and sensitivity forecasts’. *The Astronomical Journal* **145**(3):65.
- J. C. Pober, et al. (2012). ‘A technique for primary beam calibration of drift-scanning, wide-field antenna elements’. *The Astronomical Journal* **143**(2):53.
- R. J. Poulton, et al. (2020). ‘Extracting galaxy merger time-scales—I. Tracking haloes with WhereWolf and spinning orbits with OrbWeaver’. *Monthly Notices of the Royal Astronomical Society* **491**(3):3820–3837.
- W. H. Press & P. Schechter (1974). ‘Formation of Galaxies and Clusters of Galaxies by Self-Similar Gravitational Condensation’. *The Astrophysical Journal* **187**:425–438.
- J. R. Pritchard & A. Loeb (2012). ‘21 cm cosmology in the 21st century’. *Reports on Progress in Physics* **75**(8):086901.

- Y. Qin, et al. (2017a). ‘Dark-ages reionization and galaxy formation simulation–XIII. AGN quenching of high-redshift star formation in ZF-COSMOS-20115’. *Monthly Notices of the Royal Astronomical Society* **471**(4):4345–4354.
- Y. Qin, et al. (2017b). ‘Dark-ages reionization and galaxy formation simulation–X. The small contribution of quasars to reionization’. *Monthly Notices of the Royal Astronomical Society* **472**(2):2009–2027.
- Y. Qiu, et al. (2019). ‘Dark-age reionization and galaxy formation simulation–XIX. Predictions of infrared excess and cosmic star formation rate density from UV observations’. *Monthly Notices of the Royal Astronomical Society* **489**(1):1357–1372.
- D. S. Reed, et al. (2007). ‘The halo mass function from the dark ages through the present day’. *Monthly Notices of the Royal Astronomical Society* **374**:2–15.
- C. L. Reichardt (2016). *Observing the Epoch of Reionization with the Cosmic Microwave Background*, vol. 423 of *Astrophysics and Space Science Library*, p. 227.
- G. T. Richards, et al. (2006). ‘The sloan digital sky survey quasar survey: Quasar luminosity function from data release 3’. *The Astronomical Journal* **131**(6):2766.
- M. Ricotti & J. P. Ostriker (2004). ‘X-ray pre-ionization powered by accretion on the first black holes–I. A model for the WMAP polarization measurement’. *Monthly Notices of the Royal Astronomical Society* **352**(2):547–562.
- A. G. Riess, et al. (1998). ‘Observational evidence from supernovae for an accelerating universe and a cosmological constant’. *The Astronomical Journal* **116**(3):1009.
- V. C. Rubin & W. K. Ford Jr (1970). ‘Rotation of the Andromeda nebula from a spectroscopic survey of emission regions’. *The Astrophysical Journal* **159**:379.

- V. C. Rubin, et al. (1978). ‘Extended rotation curves of high-luminosity spiral galaxies. IV-Systematic dynamical properties, SA through SC’. *The Astrophysical Journal* **225**:L107–L111.
- G. B. Rybicki & A. P. Lightman (2008). *Radiative processes in astrophysics*. John Wiley & Sons.
- M. Ryle & D. Vonberg (1946). ‘Solar radiation on 175 Mc./s.’. In *Classics in Radio Astronomy*, pp. 184–187. Springer.
- W. C. Saslaw & A. J. S. Hamilton (1984). ‘Thermodynamics and galaxy clustering - Nonlinear theory of high order correlations’. *The Astrophysical Journal* **276**:13–25.
- M. Schmidt (1959). ‘The rate of star formation.’. *The Astrophysical Journal* **129**:243.
- M. Schmidt (1965). ‘Large Redshifts of Five Quasi-Stellar Sources.’. *The Astrophysical Journal* **141**:1295.
- C. J. Schmit & J. R. Pritchard (2018). ‘Neural Network Emulation of Reionization Simulations’ **333**:43–46.
- R. Scoccimarro & R. K. Sheth (2002). ‘PTHALOS: a fast method for generating mock galaxy distributions’. *Monthly Notices of the Royal Astronomical Society* **329**:629–640.
- P. A. Shaver, et al. (1999). ‘Can the reionization epoch be detected as a global signature in the cosmic background?’. *Astronomy and Astrophysics* **345**:380–390.
- A. K. Shaw, et al. (2019). ‘The impact of non-Gaussianity on the error covariance for observations of the Epoch of Reionization 21-cm power spectrum’. *Monthly Notices of the Royal Astronomical Society* **487**(4):4951–4964.
- R. K. Sheth (1995). ‘Press-Schechter, thermodynamics and gravitational clustering’. *Monthly Notices of the Royal Astronomical Society* **274**:213–220.

- R. K. Sheth & G. Tormen (1999). ‘Large-scale bias and the peak background split’. *Monthly Notices of the Royal Astronomical Society* **308**:119–126.
- H. Shimabukuro, et al. (2017). ‘Constraining the epoch-of-reionization model parameters with the 21-cm bispectrum’. *Monthly Notices of the Royal Astronomical Society* **468**:1542–1550.
- J. Silk (1977). ‘On the fragmentation of cosmic gas clouds. I-The formation of galaxies and the first generation of stars’. *The Astrophysical Journal* **211**:638–648.
- C. M. Simpson, et al. (2013). ‘The effect of feedback and reionization on star formation in low-mass dwarf galaxy haloes’. *Monthly Notices of the Royal Astronomical Society* **432**(3):1989–2011.
- P. H. Sims & J. C. Pober (2019). ‘Joint estimation of the Epoch of Reionization power spectrum and foregrounds’. *Monthly Notices of the Royal Astronomical Society* **488**(2):2904–2916.
- S. Singh, et al. (2017). ‘First results on the epoch of reionization from first light with SARAS 2’. *The Astrophysical Journal Letters* **845**(2):L12.
- V. Smolčić, et al. (2017). ‘The VLA-COSMOS 3 GHz Large Project: Cosmic evolution of radio AGN and implications for radio-mode feedback since  $z \sim 5$ ’. *Astronomy & Astrophysics* **602**:A6.
- E. Sobacchi & A. Mesinger (2014). ‘Inhomogeneous recombinations during cosmic reionization’. *Monthly Notices of the Royal Astronomical Society* **440**(2):1662–1673.
- M. Sokolowski, et al. (2015). ‘BIGHORNS-broadband instrument for global Hydrogen Reionisation signal’. *Publications of the Astronomical Society of Australia* **32**.
- R. S. Somerville & R. Davé (2015). ‘Physical models of galaxy formation in a cosmological framework’. *Annual Review of Astronomy and Astrophysics* **53**:51–113.

- R. S. Somerville & J. R. Primack (1999). ‘Semi-analytic modelling of galaxy formation: the local Universe’. *Monthly Notices of the Royal Astronomical Society* **310**(4):1087–1110.
- V. Springel (2005). ‘The cosmological simulation code GADGET-2’. *Monthly notices of the royal astronomical society* **364**(4):1105–1134.
- D. P. Stark, et al. (2010). ‘Keck spectroscopy of faint  $z_i \approx 7$  Lyman break galaxies–I. New constraints on cosmic reionization from the luminosity and redshift-dependent fraction of Lyman  $\alpha$  emission’. *Monthly Notices of the Royal Astronomical Society* **408**(3):1628–1648.
- D. P. Stark, et al. (2011). ‘Keck spectroscopy of faint  $z_i \approx 7$  Lyman break galaxies: a high fraction of line emitters at redshift six’. *The Astrophysical Journal Letters* **728**(1):L2.
- A. Sutinjo, et al. (2015a). ‘Understanding instrumental Stokes leakage in Murchison Widefield Array polarimetry’. *Radio Science* **50**(1):52–65.
- A. T. Sutinjo, et al. (2015b). ‘Characterization of a Low-Frequency Radio Astronomy Prototype Array in Western Australia’. *IEEE Transactions on Antennas and Propagation* **63**(12):5433–5442.
- G. Swarup, et al. (1991). ‘The giant metre-wave radio telescope’. *Current science* **60**(2):95–105.
- A. Taylor & B. Joachimi (2014). ‘Estimating cosmological parameter covariance’. *Monthly Notices of the Royal Astronomical Society* **442**(3):2728–2738.
- M. Tegmark (1997). ‘How to measure CMB power spectra without losing information’. **55**(10):5895–5907.
- R. A. Thompson, et al. (2017). *Interferometry and synthesis in radio astronomy*. Springer Nature.
- A. A. Thoul & D. H. Weinberg (1995). ‘Hydrodynamic Simulations of Galaxy Formation. I. Dissipation and the Maximum Mass of Galaxies’. *The Astrophysical Journal* **442**:480.

- N. Thyagarajan, et al. (2015a). ‘Foregrounds in wide-field redshifted 21 cm power spectra’. *The Astrophysical Journal* **804**(1):14.
- N. Thyagarajan, et al. (2015b). ‘Confirmation of wide-field signatures in redshifted 21 cm power spectra’. *The Astrophysical Journal Letters* **807**(2):L28.
- N. Thyagarajan, et al. (2013). ‘A Study of Fundamental Limitations to Statistical Detection of Redshifted H I from the Epoch of Reionization’. *ApJ* **776**:6.
- S. Tingay, et al. (2013). ‘The Murchison widefield array: The square kilometre array precursor at low radio frequencies’. *Publications of the Astronomical Society of Australia* **30**.
- G. Tormen (1996). ‘Hydrodynamic simulations of galaxy formation’. *Dark Matter in Cosmology, Quantum Measurement, Experimental Gravitation: Proceedings of the XXXIst Rencontre de Moriond, Les Arcs, Savoie, France, January 20-27, 1996* **91**:207.
- H. Trac, et al. (2008). ‘Imprint of inhomogeneous hydrogen reionization on the temperature distribution of the intergalactic medium’. *The Astrophysical Journal Letters* **689**(2):L81.
- H. Trac & N. Y. Gnedin (2011). ‘Computer simulations of cosmic reionization’. *Advanced Science Letters* **4**(2):228–243.
- M. Trenti & P. Hut (2008). ‘N-body simulations (gravitational)’. *Scholarpedia* **3**(5):3930. revision #91544.
- C. M. Trott, et al. (2020). ‘Deep multiredshift limits on Epoch of Reionization 21 cm power spectra from four seasons of Murchison Widefield Array observations’. *Monthly Notices of the Royal Astronomical Society* **493**(4):4711–4727.
- C. M. Trott, et al. (2018). ‘Assessment of Ionospheric Activity Tolerances for Epoch of Reionization Science with the Murchison Widefield Array’. *The Astrophysical Journal* **867**:15.
- C. M. Trott, et al. (2012). ‘The impact of point-source subtraction residuals on 21 cm epoch of reionization estimation’. *The Astrophysical Journal* **757**(1):101.

- J. E. Upjohn, et al. (2019). ‘The 1.4-GHz cosmic star formation history at  $z < 1.3$ ’. *Publications of the Astronomical Society of Australia* **36**:e012.
- M. P. van Haarlem, et al. (2013). ‘LOFAR: The LOw-Frequency ARray’. *Astronomy and Astrophysics* **556**:A2.
- H. Vedantham, et al. (2012). ‘Imaging the Epoch of Reionization: Limitations from Foreground Confusion and Imaging Algorithms’. *ApJ* **745**:176.
- H. K. Vedantham & L. V. E. Koopmans (2016). ‘Scintillation noise power spectrum and its impact on high-redshift 21-cm observations’. *Monthly Notices of the Royal Astronomical Society* **458**:3099–3117.
- A. Vilenkin (1985). ‘Classical and quantum cosmology of the Starobinsky inflationary model’. *Physical Review D* **32**(10):2511.
- E. Visbal, et al. (2014). ‘High-redshift star formation in a time-dependent Lyman-Werner background’. *Monthly Notices of the Royal Astronomical Society* **445**(1):107–114.
- J. Wang, et al. (2010). ‘How to identify and separate bright galaxy clusters from the low-frequency radio sky’. *The Astrophysical Journal* **723**(1):620.
- M. S. Warren, et al. (2006). ‘Precision Determination of the Mass Function of Dark Matter Halos’. *The Astrophysical Journal* **646**:881–885.
- W. A. Watson, et al. (2014). ‘Statistics of extreme objects in the Juropa Hubble Volume simulation’. *Monthly Notices of the Royal Astronomical Society* **437**:3776–3786.
- R. B. Wayth, et al. (2018). ‘The Phase II Murchison Widefield Array: Design overview’. *Publications of the Astronomical Society of Australia* **35**:33.
- M. H. Wieringa (1992). ‘An investigation of the telescope based calibration methods ‘redundancy’ and ‘self-cal’’. *Experimental Astronomy* **2**(4):203–225.
- S. J. Wijnholds, et al. (2010). ‘Calibration challenges for future radio telescopes’. *IEEE Signal Processing Magazine* **27**(1).

- M. J. Wilensky, et al. (2019). ‘Absolving the SSINS of Precision Interferometric Radio Data: A New Technique for Mitigating Faint Radio Frequency Interference’. *Publications of the Astronomical Society of the Pacific* **131**(1005):114507.
- R. Wilman, et al. (2008). ‘A semi-empirical simulation of the extragalactic radio continuum sky for next generation radio telescopes’. *Monthly Notices of the Royal Astronomical Society* **388**(3):1335–1348.
- C. Wolf, et al. (2003). ‘The evolution of faint AGN between  $z \sim 1$  and  $z \sim 5$  from the COMBO-17 survey’. *Astronomy and Astrophysics* **408**:499–514.
- S. Wouthuysen (1952). ‘On the excitation mechanism of the 21-cm (radio-frequency) interstellar hydrogen emission line.’. *aj* **57**:31–32.
- O. Zahn, et al. (2011). ‘Comparison of reionization models: radiative transfer simulations and approximate, seminumeric models’. *Monthly Notices of the Royal Astronomical Society* **414**(1):727–738.
- X. Zhang, et al. (2018). ‘Limits on radio emission from meteors using the MWA’. *Monthly Notices of the Royal Astronomical Society* **477**(4):5167–5176.
- F. Zwicky (1933). ‘Die rotverschiebung von extragalaktischen nebeln’. *Helvetica physica acta* **6**:110–127.

Every reasonable effort has been made to acknowledge the owners of copyright material. I would be pleased to hear from any copyright owner who has been omitted or incorrectly acknowledged.